Studies of a Modular Advanced Stellarator Reactor ASRA6C

G. Böhme, L.A. El-Guebaly, G.A. Emmert, G. Grieger, E.
Harmeyer, F. Herrnegger, J. Hübener, K. Jentzsch, J. Kisslinger,
P. Komarek, G.L. Kulcinski, E.M. Larsen, W. Maurer, F. Rau,
J.F. Santarius, M.E. Sawan, J.E. Scharer, I.N. Sviatoslavsky, W.F.
Vogelsang, P.L. Walstrom, L.J. Wittenberg and H. Wobig

May 1987

FPA-87-2

Abstract

This study is directed towards the clarification of critical issues of advanced modular stellarator reactors exploiting the inherent potential of steady state operation, and is not a point design study of a reactor. Critical technology issues arise from the three-dimensional magnetic field structure. The first wall, blanket and shield are more complex than those of axi-symmetric systems, but this is eased at moderate to large aspect ratio typical of stellarators. Several blanket options have been studied and a thin blanket (21 cm) was the first choice for the design. Super-conducting modular coils were investigated with respect to the conductor and mechanical supports. From the analysis of forces and stresses caused by the electromagnetic loads the coils are considered to be feasible, although shear stresses might pose a critical issue. Demountable intermagnetic support elements were designed for use at separation areas between the croystat modules. A scheme for remote reactor maintenance was also developed.

The plasma physics issues of different configurations were studied using extrapolations of transport behaviour and equilibrium from theory and present experiments. These studies in-dicate that the confinement and equilibrium behaviour is adequate for ignited operation at an average value of 5 % beta. Impurities may pose a critical issue. Several impurity control operations were investigated; a pumped limiter configuration utilizing the "ergodic layer" at the plasma edge was chosen for edge plasma and impurity control.

A general conclusion of the study is that the modular stellarator configuration offers interesting prospects regarding the development towards steady-state reactors.

STUDIES OF A MODULAR ADVANCED STELLARATOR REACTOR ASRA6C

G. Böhme[1], L.A. El-Guebaly[2], G.A. Emmert[2], G. Grieger[3], E. Harmeyer[3],
F. Herrnegger[3], J. Hübener[1], K. Jentzsch[1], J. Kißlinger[3], P. Komarek[1],
G.L. Kulcinski[2], E.M. Larsen[2], W. Maurer[1], F. Rau[3], J.F. Santarius[2], M.E. Sawan[2],
J.E. Scharer[2], I.N. Sviatoslavsky[2], W.F. Vogelsang[2], P.L. Walstrom[2], L.J. Wittenberg[2], H. Wobig[3]

1 Kernforschungszentrum Karlsruhe
2 Fusion Power Associates/University of Wisconsin
3 Max-Planck-Institut für Plasmaphysik, Garching, EURATOM-Association

STUDIES OF A MODULAR

ADVANCED STELLARATOR REACTOR ASRA6C

EXECUTIVE SUMMARY

Objectives and Framework of the ASRA6C Study

Advanced Stellarator Reactor studies were initiated at IPP–Garching during the construction of the WENDELSTEIN VII–AS experiment and the first scoping studies towards its "next step", the larger system WENDELSTEIN VII–X. Since this later experiment aims to demonstrate the potential of Stellarators towards their development of a fusion reactor, it was regarded as useful in this context to also study critical reactor issues of this concept.

This was done by starting from the W VII–AS geometry, although the W VII–AS device was built only for demonstrating the basic properties of Advanced Stellarators before optimizing the configuration for stable confinement of high-β plasmas. This optimization was done in parallel to the work presented in this report and, indeed, has yielded configurations capable of confining average values of $< \beta >$ of 9 %. The results of this optimization also support the working hypothesis that the modifications necessary to apply to the W VII–AS coils for achieving confinement of a high-β plasma are only small changes in coil geometry , so that basic reactor properties of Advanced Stellarator systems can indeed be studied by starting from the well–known W VII–AS configuration. The present ASRA6C study is directed towards the clarification of critical issues regarding such systems. It is therefore far from a point design of an Advanced Stellarator Reactor . Regarding future commercial power reactors of the Advanced Stellarator type, questions of economics, aspects of environmental impact, and inherent safety need also to be addressed.

The present study was initiated at IPP–Garching , and was extended in a co-operation between KfK–Karlsruhe and IPP–Garching in July 1983 to include questions of superconducting coils and reactor maintenance. The basis of this common work was then broadened early in 1985 by a group of Fusion Power Associates (FPA), entering the Advanced Stellarator Reactor field in the course of their co–operation with the Kernforschungszentrum Karlsruhe. Starting from the magnetic topology of WENDELSTEIN VII–AS, several earlier data sets for an Advanced Stellarator Reactor (ASR) were developed, considering NbTi for the superconducting coils. An Advanced Stellarator Burner experiment (ASB) was scaled from such an early version of an ASR by dispensing with tritium breeding and assuming a rather large magnetic induction, utilizing Nb_3Sn as superconductor. In Table I relevant data of these two systems are compared to those of the present reference case, ASRA6C , the most recent version of an ASR. In ASRA6C, as in several preceding Advanced Stellarator Reactor data sets, a small number of 6 coils per field period is chosen as a compromise between "magnetic field quality" and maintainability, and Nb_3Sn is foreseen as the superconductor.
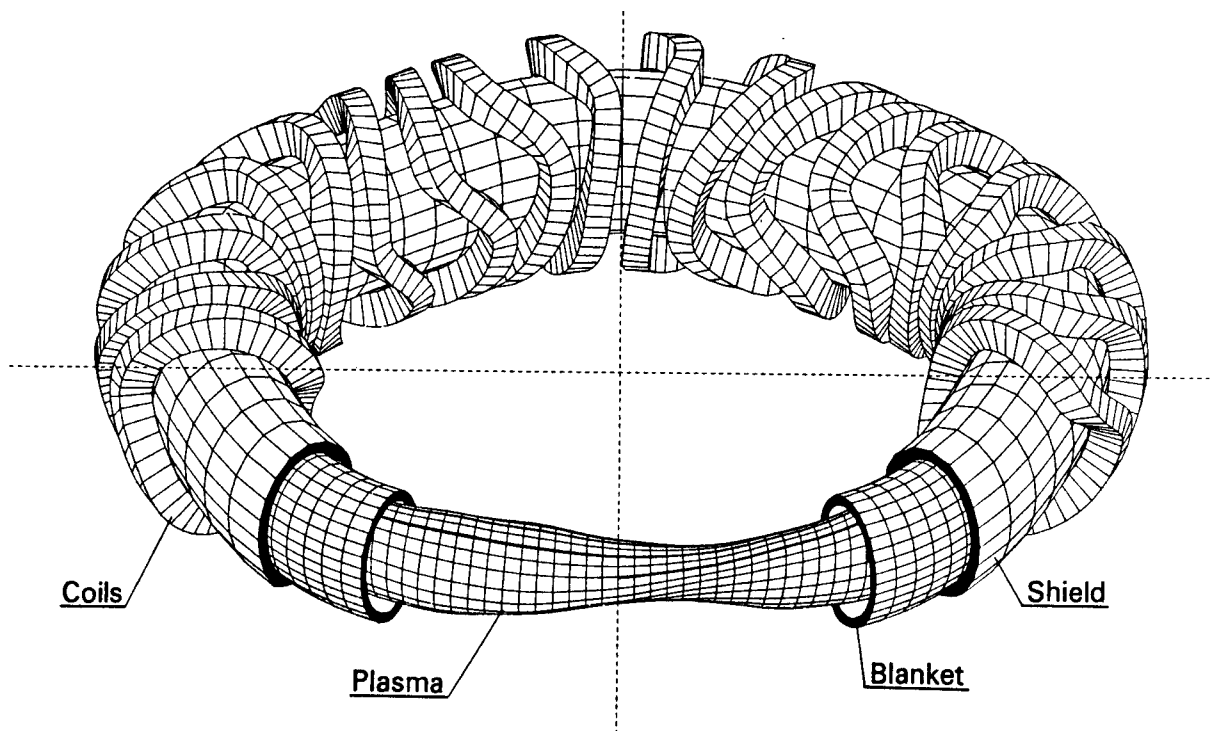
Table I : Characteristics of Advanced Stellarator Burner and Reactor Systems

Advanced Stellarator			Burner ASB06E	Reactor ASR25T7	Reactor ASRA6C
Average major radius	R_o	$[m]$	15.2	25.5	20.0
Average coil radius	r_c	$[m]$	3.24	5.24	4.57
Coils per field period			6	10	6
Conductor			Nb_3Sn	NbTi	Nb_3Sn
Effective current density	j_{eff}	$[MA/m^2]$	18	9.8	15
Maximum induction at coil	B_m	$[T]$	12.6	8.7	10.4
Stored magnetic energy	W_m	$[GJ]$	67	170	117
Induction on axis	B_o	$[T]$	7.0	5.3	5.3
Rotational transform	t_o		0.53	0.58	0.47
Average plasma radius	r_p	$[m]$	0.9	1.75	1.6
Distance to coils	Δ	$[m]$	1.2	>1.8	1.2
Average β	$<\beta>$	$[\%]$	2.5	5	5
Fusion power	P_f	$[GW]$	0.42	3.8	3.9

Reference Case ASRA6C

A schematic view of the general layout of ASRA6C is given in Figure 1, showing the contours of the non–planar modular coils for three of the 5 field periods, along with nested toroidal volumes representing the shield and the blanket, as well as the last closed magnetic surface. Due to the symmetry in the stellarator fields, i.e. a twofold mirror symmetry with respect to the beginning (or middle) of each of the field periods, there are three different coil shapes in the whole system. The characteristic difference of the reference case ASRA6C is a more compact system size, as compared to that of similar previous systems. This reduction in size is made possible by an advanced design for the blanket and shield of ASRA6C . Thus the critical distance Δ between the first wall of the system and the inner contour of the coil winding cross section is considerably reduced from the previously adopted value of $\Delta = 2.1\,m$ to $1.2\,m$. As a consequence, the major radius is changed from $R_o = 25\,m$ to a value of $20\,m$, and the average coil radius from $r_c = 5.22\,m$ to $4.57\,m$, keeping other parameters fixed, e.g. the average plasma radius $r_p = 1.6\,m$, an effective coil current density of $j_{eff} = 15\,MA/m^2$, and the induction at the magnetic axis of $B_o = 5.3\,T$. There are 30 coils with identical elliptical bores in the coil system. In each of the 5 field periods there are three coil pairs with different shapes of the toroidal excursion, placed at slightly different values of the major radius. All coils carry the same current of $18\,MA$ in their rectangular winding pack cross section. The maximum induction at the Nb_3Sn coils is $10.4\,T$, and the stored magnetic energy is $117\,GJ$ in the whole system.

The following reactor data of the reference case ASRA6C are results of one of the various transport calculations, made to evaluate start–up and steady state burn scenarios. Start-up to ignition is achieved by an effective heating power of $P_h = 30$ to $50\,MW$. The fusion power amounts typically to $P_f \approx 4\,GW$ at an average $< \beta >$ of $5\,\%$, where β is the plasma pressure normalized by the magnetic energy density. In this scenario, a radiative edge layer of $300\,MW$ can be sustained. It could effectively reduce the heat load to the pumped limiters.

Fig. 1: Advanced Stellarator Reactor:
    Schematic view of plasma, blanket, shield, and coils.

Magnetic Field Studies for an Advanced Stellarator

The characteristic feature of an Advanced Stellarator is a reduction of the secondary plasma currents and maintaining a global magnetic well in the vacuum fields. This reduction improves the confinement in the Pfirsch–Schlüter and plateau regimes of collisionality, and lowers the Shafranov–shift of the plasma at a finite β. A typical geometrical feature of an Advanced Stellarator is a variable shape of the magnetic surfaces along the toroidal direction, in contrast to the rotating ellipses of a standard $\ell = 2$ stellarator.

The magnetic topology of the reference configuration of this study, called ASRA6C, is computed from the coil currents, both for vacuum fields and also for finite values of β , up to an average value $< \beta > \approx 5\%$ which is near the critical β for equilibrium. Then the magnetic axis is shifted by approximately half of the plasma radius.

Heating and Burn Scenarios

Heating and burn scenarios for Advanced Stellarator Reactor systems are established in numerical computations as sequences of equilibria for neoclassical heat conduction and bremsstrahlung as losses, and including electric fields in the 1–D–code. For start-up, an effective heating power of 30 to 50 MW is sufficient. At an increased refuelling rate, the reactor is brought to full power, preferentially at a moderate temperature of $T = 12\,keV$ to $15\,keV$. In a different computation, an additional radiative power loss of 300 MW near the plasma edge can be tolerated at an increased fusion power of 3.9 GW. In this computation the electron heat losses are reduced by a factor of 2 in order to model the improved confinement properties of an Advanced Stellarator . The temperature is $T \approx 19\,keV$ and the average $< \beta >$ amounts to 5 % . Such β–values are also found by equilibrium calculations for the field of ASRA6C .

Blanket Design for ASRA6C

Four different blanket options have been investigated. A thin blanket of 21 cm thickness is proposed as preferred option for ASRA6C. The first wall is a structural part of the blanket and is shaped similar to the contours of the outer magnetic surfaces, or, preferentially, can have identical elliptic cross sections. In this case the average neutron load at the first wall is 1.4 MW/m^2 at a fusion power of $P_f = 3.8\,GW$ with local peaks up to 2.4 MW/m^2 . The local enhancement of the neutron load at the first wall is caused by the Shafranov–shift of the finite–β plasma. In addition to neutrons, the first wall is also loaded by radiation and plasma losses. The losses of trapped α–particles as well as the amount of local sputtering remain to be quantified. All these effects depend also on the efficiency of the pumped limiters.

The preferred blanket option uses slowly circulating $Li_{17}Pb_{83}$ as breeding material with Be as moderator and neutron multiplier, and He gas as coolant in a HT–9 ferritic steel structure. An overall breeding ratio of 1.05 (including penetrations) is computed. The required pumping power for the circulating breeding material is smaller than 0.5 % of the fusion power. A low tritium inventory of about 5 g in the coolant and breeder is

obtained. Tritium removal is accomplished in an external tritium oxide removal system from the slowly circulating breeder material and the helium coolant.

Shield Design and Optimization

The breeding ratio and the shielding of the superconducting coils are optimized by utilizing a composite system of materials: breeding, neutron multiplication and moderation in the $21\,cm$ thick blanket is aided by a $44.2\ cm$ thick HT–9 reflector inside of the $25.5\,cm$ thick B_4C and $6.3\,cm$ thick Pb shields. Local effects of the six He gas manifolds are seen within their poloidal angles of $10°$. They amount to a factor of 5 above the $0.11\,mW/cm^3$ of nuclear heating seen at the outside midplane where the first wall neutron load attains its local maximum value of $2.4\,MW/m^2$. At these particular positions, the fast neutron fluence amounts to $1.4 \times 10^{23}\,m^{-2}$ leading to a dose of $10^{10}\,rad$ in the GFF Polyimide insulator. The above numbers correspond to 20 full–power years.

Coil Engineering

Engineering considerations of the coils for the present Advanced Stellarator Reactor systems cover the evaluation of magnetic forces and optimization of the resulting stresses and strains by iterative improvement of the support system. The mutual support of mechanically connected coils is treated. Besides the forces caused by the toroidal geometry, a characteristic feature of non–planar coil systems is that there are lateral forces with local maximum values comparable to the maximum radial component. Within a field period the lateral forces are balanced.

The coils in ASRA6C provide an axis field of $B_o = 5.3\,T$; the total stored magnetic energy amounts to $W = 117\,GJ$. Local peak fields of $B_m = 10.4\,T$ exist in ASRA6C at particular points at the coil surface. The force distribution within the coils yields a local maximum force density of $155\,MN/m^3$. The mechanical stress and strain distributions are investigated inside the coils by finite–element calculations using the SAP V (2) program system. Using orthotropic material data of the LCT–coils, a maximum of the equivalent (von Mises) stress of $\sigma_{vM} = 135\,MPa$ is obtained, associated with a shear stress of $\sigma_{ST} = 50\,MPa$. The tangential strain amounts to about 0.2% for this case. Although these shear stresses are considerable, the coils seem to be feasible. The stresses in the coil housing and the mutual coil support elements are not found to be critical.

Coil Considerations

Coil considerations performed for the superconducting coils of ASRA6C have been concentrated on investigations of the conductor design, emphasizing the influence of the minimum bending radius. The associated strain imposed by the winding procedure might be kept within tolerable limits when using a cable–in–conduit conductor with comparatively small dimensions. An inside insulation is foreseen within a stainless steel mantle. A coil current of 18 kA is proposed as a compromise between the winding pack cross section and the turn number, when considering the peak field at the coil, its insulation in an emergency discharge, and the stationary cooling to counteract the nuclear heating. Laser welding of the compacted conductors are considered in the winding procedure.

General Layout and Maintenance

In the KfK design for the general layout of ASRA6C and its maintenance, a blanket option with variable thickness is used. The contour of the first wall is assumed at some distance outside of the last closed magnetic surface. The blanket accomodates space for structure and provides a breeding ratio of 1.05 without the use of Be as moderator/neutron multiplier. A system of many pumped limiters is chosen for edge control of the plasma. A high heat transfer rate is required at the regions of intense contact with the edge plasma. This heat load is assumed to be reduced by edge radiation. The choice of pumped limiters is a result of magnetic field studies near and outside of the separatrix of such systems where a rather complicated spatial structure of field lines outside of the last closed magnetic surface was found.

Note that Stellarators in principle allow a steady state burn, provided that refuelling and ash removal can be accomodated appropriately, and that the impurities in the system do not pose serious problems. After start–up the openings for the initial heating can be closed with shield material.

Maintenance of the ASRA6C reactor is assumed at regular intervals depending on the performance of the first wall. The pumped limiters are considered to be individually maintainable during short reactor shut–downs. Maintaining of the first wall and exchange of the blanket requires discharge of the magnets also. With the help of demountable cold intermagnetic support elements, the superconducting magnets can be kept at their operation temperature. One separation area per field period is considered for a short exchange time of the removable blanket units. After a radial motion of a whole field period, the two removable blanket units are replaced by new ones from both ends, utilizing appropriate service systems.

Conclusions

The Advanced Stellarator scheme offers interesting prospects regarding the development towards steady state reactors. For ASRA6C , the approach of a thin blanket has allowed a considerable reduction in the size and in the stored magnetic energy of the system as compared to previous systems.

Critical issues regarding technology may arise from the three–dimensional field structure. The influence of ferromagnetic material on the magnetic topology needs to be quantified. First wall, blanket, and shield may call for more complex structures as compared to those of axisymmetric systems, but this is eased at moderate to large aspect ratio. At separation areas between the cryostat modules demountable intermagnetic support elements between coils might pose a critical issue. Proposed solutions are under study.

Transport (heat conduction and particle losses) as extrapolated from present experiments and theory appears to be of the right order of magnitude for reactor–grade plasmas, but this needs experimental verification in large devices. As in the case of other steady state magnetic fusion systems with good confinement, impurities may pose a critical issue. Equilibrium–β values as obtained by modern 3D–codes are adequate for reactor operation; the experimental proof depends on the performance of forthcoming or planned machines. For ASRA6C the average β–value for equilibrium, $< \beta_{eq} >= 4.7\,\%$, is about the same as the computed value at reactor operation, $< \beta >= 5\%$, in a scenario where an additional edge radiation of 300 MW is included at a total fusion power of 3.9 GW.

Regarding the question of the stability–β in these systems, theory predicts lower values. Innovative configurations, called "HELIAS", have been published recently, which are stable up to a value $< \beta > \approx 9\ \%$ according to resistive interchange modes. Their geometrical characteristics are a helical magnetic axis and some indentation of the magnetic surfaces at those particular toroidal positions where the toroidal curvature has a maximum. Modular non–planar coils for such configurations are being developed. Detailed studies of critical reactor issues of these new configurations have still to be performed. It is pointed out, however, that the general results obtained in the above ASRA6C studies remain valid also for these innovative systems. This is due to the generic similarity of the non–planar modular coil systems which, by proper choice of their dimensions and shapes, introduce the respective magnetic topology.

1. Objectives and Framework of the Study

A steady state fusion reactor has attracted the attention of physicists from the beginning of fusion research in the fifties. Stellarators offer the chance of steady state operation. In early stellarator experiments helical windings were used. Large superconducting helical windings, however, seem to pose several difficulties for maintenance and repair under reactor conditions. The modular coil stellarator is an improvement to these early conventional stellarators. This holds true not only with respect to critical technical issues; it also allows a large variety of magnetic field configurations which are difficult to achieve with helical windings.

Reactor studies of modular stellarators have been published by various authors. Miller and Krakowski [1] have investigated a modular $\ell = 2$ stellarator MSR with reactor dimensions. The UWTOR–M study [2] considers the corresponding $\ell = 3$ version. Both reactor concepts are the equivalent to the continuous coil $\ell = 2$ or $\ell = 3$ stellarator. The divertor as means of impurity control was a key feature of the UWTOR–M concept.

The present study considers some special problems of the modular stellarator reactor based on the Advanced Stellarator principle. This principle will be studied in the WENDELSTEIN VII–AS experiment, which will start operation in Garching in 1987. The particular property of this configuration is the reduction of the secondary currents (Pfirsch–Schlüter currents) in order to minimize the particle drift and at the same time the radial Shafranov–shift of the plasma column. This reduction of secondary currents also improves plasma confinement. In terms of Fourier harmonics the magnetic field of the WENDELSTEIN VII–AS device is a superposition of $\ell = 0, 1, 2,$ and 3 components, which would be difficult to realize with conventional helical windings. With modular coils, however, such a superposition can be easily achieved.

In extrapolating the WENDELSTEIN VII–AS configuration to reactor dimensions several questions arise which are of particular interest for this specific type of magnetic field configurations :

- The available space for blanket and shield between plasma and coils;
- Geometry of the coils, maximum field at the coils, and forces and stresses in the coils;
- Maintenance procedure of blanket, shield, and coils;
- Boundary layer between plasma and first wall;
- Confinement properties of the plasma.

The question of plasma stability has not been given major importance in working out the configurations treated in this study. Theory predicts a comparatively low stability limit of $< \beta > \approx 2\,\%$ for the configuration realized in the experimental device WENDELSTEIN VII–AS which is too low for an economic fusion reactor. On the other hand, theoretical efforts have succeeded in finding stellarator configurations with much higher stability limits up to $< \beta > = 9\,\%$. These HELIAS configurations [3] exhibit many of the features of the WENDELSTEIN VII–AS configurations, in particular the use of non–planar modular coils. Therefore it is believed that many solutions found in investigating a reactor version of WENDELSTEIN VII–AS can be transferred to the HELIAS configuration, to the Bean–shaped Advanced Stellarator , or to any

other modular stellarator with high β-limits, and that the well-known W VII-AS configuration can be taken as basis for this study.

In extrapolating WENDELSTEIN VII-AS towards reactor dimensions, the condition for sufficient space for blanket and shield was the determining factor for the overall geometrical size. In a first concept, a minimum distance of 2.1 m between the plasma boundary and the coil winding pack led to a device with 25 m major radius, a value similar to that of other stellarator reactor designs like UWTOR-M or MSR. Compared to other concepts of fusion reactors such as tokamaks, these devices are rather large.

Therefore a major task of the present study was to reduce the main dimensions of the reactor by making use of a more compact blanket. This has led to the reference configuration ASRA6C . To a certain extent the blanket has to be adjusted to the geometry of the plasma and the coils, thus leading to a three-dimensional geometry. As will be described in chapter 5 , an appropriate three-dimensional blanket can be constructed with a breeding ratio above 1 . A solution could be found for exchanging the blanket on a routine basis with the interface between the blanket and shield being of constant elliptic cross section. This allows replacing the blanket in a torus section by horizontal movements only. It is hoped that the solution of the maintenance problem found for ASRA6C can also be applied to other Advanced Stellarators.

Another particular issue of the Advanced Stellarator reactor is the complex shape of the coils with strongly curved sections. The minimum radius of curvature is below 1 m in ASRA6C. This challenges the manufacturing of the coils and supporting the stress loads. These questions are addressed in Chapters 7 and 8.

In the field of plasma engineering, heating and steady state burn scenarios have been developed and several options of impurity control have been considered.

It is legitimate to scale the confinement in stellarators towards reactor size assuming neoclassical collisional processes, which are large for the electrons and just adequate to balance the fusion power production. Any anomalous processes must become rather large before they become comparable to the neoclassical processes and begin to deteriorate the confinement and aggravate ignition. Since neoclassical confinement depends critically on the details of the magnetic field, it is of particular interest to prove that the Advanced Stellarator reactor configuration meets the requirements of the ignition condition. Anomalous transport in stellarators is known experimentally only in a limited parameter range. Therefore it would be speculation to include anomalous transport coefficients in the heating and burn scenarios. In case that the scaling laws for anomalous transport found in the smaller WENDELSTEIN VII-A experiment remain valid in high temperature plasmas, this effect would be negligible at fusion temperatures.

Other critical issues are plasma wall interaction and impurity control. Since the last closed magnetic surface in an Advanced Stellarator reactor is surrounded by a layer of ergodic magnetic field lines rather than by a well defined open magnetic topology, a divertor with a well separated chamber can not be realized. Several options of controlling exhaust and impurity inflow are discussed in chapter 4; the main candidate for controlling plasma outflow is a pumped limiter system.

The present study concentrates mainly on the reference case ASRA6C, which among all versions of a modular Advanced Stellarator reactor studied so far seems to be an optimum with respect to geometric, magnetic, and mechanical parameters. The aim of

the study is to identify the critical issues of this reactor concept and to find solutions. Problems which are common to all toroidal fusion concepts are not evaluated in detail. The question of plasma stability has not been given major importance in working out the configurations treated in this study. Economic issues like mass utilization of the blanket and shield are discussed shortly in chapter 5. An overall analysis of the economics of a stellarator reactor, however, is beyond the scope of this study.

References to Chapter 1 :

[1]: Miller, R.L., Bathke, C.G., Krakowski, R.A., Heck, F.M., Green, L., et al.,
The Modular Stellarator Reactor: A Fusion Power Plant,
Los Alamos Nat. Lab. Report LA–9737–MS, Los Alamos (USA), (1983)

[2] : Badger, B., Sviatoslavsky, I.N., Van Sciver, S.W., Kulcinski, G.L.,
Emmert, G.A., et al., UWTOR-M, A Conceptual Modular Stellarator Power Reactor, University of Madison Report UWFDM–550, Madison, USA (1982)

[3] : J. Nührenberg, R. Zille, and S. P. Hirshman,
Resistively Stable Stellarator Equilibria by β Iteration,
8th Eur. Conf. on Comput. Physics, **10 D**, 57,
Eibsee, Germany, 1986

2.   Overview of the ASRA6C Reference Case

2.1. Introduction

This chapter gives an overview of the characteristic features and data for the reference case ASRA6C of an Advanced Stellarator Reactor, and a comparison to the preceding configuration ASRA6B. The main difference between these two data sets is the system size, which could be reduced in ASRA6C by employing an advanced design for the blanket and shield, keeping other parameters unchanged or adjusted appropriately.

In section 2.2 a short description of the physics data is given, including the geometrical dimensions and some information on the superconducting coils. The magnetic field properties of ASRA6C are briefly described in section 2.3. The vacuum fields are compared to those at $< \beta > \approx 5\,\%$, where $< \beta >$ is the average plasma pressure of the burn state normalized by the magnetic field energy density. In section 2.4, the reactor data of ASRA6C are derived by summarizing the results of heating and burn scenarios. In section 2.5 four options of the breeding blanket are listed, and the shield is described. The general lay–out of the reactor system is introduced in section 2.6.

2.2. Physics Data

A schematic view of an Advanced Stellarator Reactor, such as ASRA6C, is given in Fig. 2–1, showing the contours of the non–planar modular coils for three of the 5 field periods, along with nested toroidal volumes representing the shield and the blanket, as well as the last closed magnetic surface of this particular coil system. There are 6 coils per field period. Three different coil shapes are present in the whole system, if one considers the twofold mirror symmetry. This choice was made at an earlier stage of the considered interim versions of an Advanced Stellarator Reactor , and was also used in the larger system ASRA6B. In ASRA6C, a compact system size is made possible by introducing a modern design for the blanket and shield (see Chapter 5 and 6) by reducing the critical distance Δ between the first wall and the inner contour of the coil winding cross section from the previous value of $2.1\ m$ to $1.2\,m$. Consequently, the major radius can be changed from $R_o = 25\,m$ to a value of $20\,m$, and the average coil radius from $r_c = 5.22\,m$ to $4.57\,m$, keeping other parameters constant, e.g. the plasma radius $r_p = 1.6\,m$, the effective coil current density, and the induction at the magnetic axis.

The upper part in Fig. 2–2 shows the contours of single cryostats for the 6 coils of ASRA6C along with the shape of the last closed magnetic surface. The lower part of the picture is a cut through the mid–plane. It demonstrates the finite coil distance at the critical inside position. In ASRA6B these gaps are larger due to the increased dimensions.
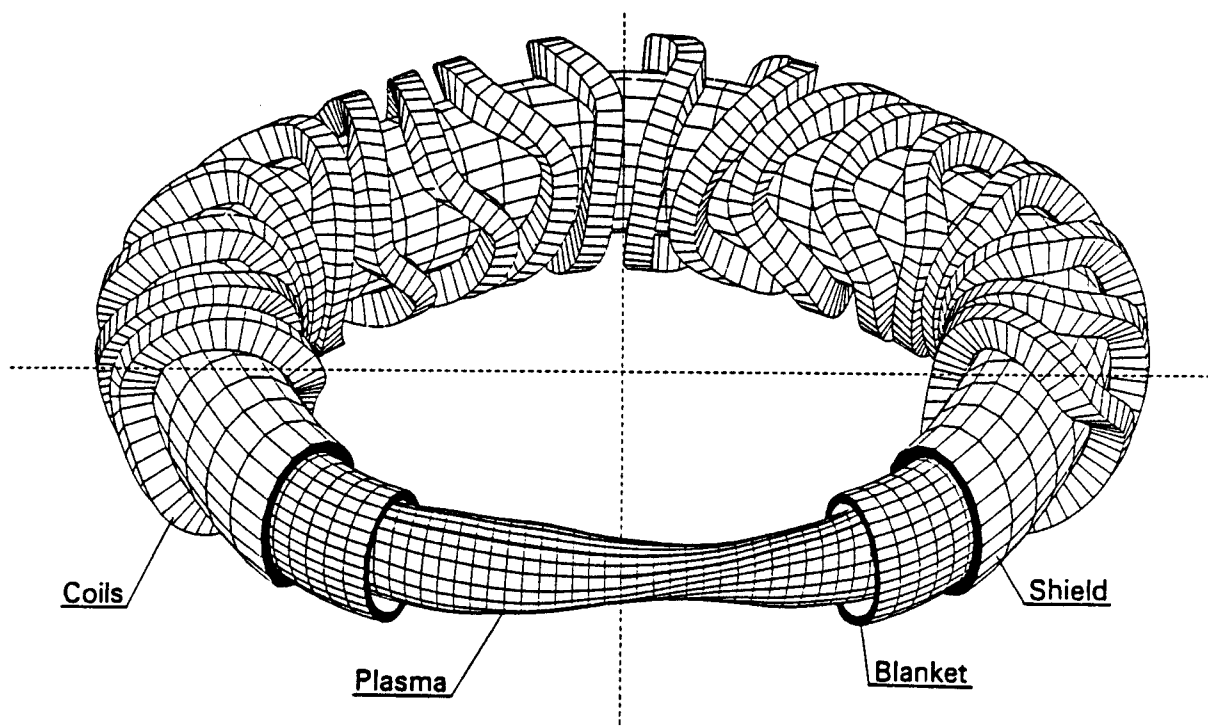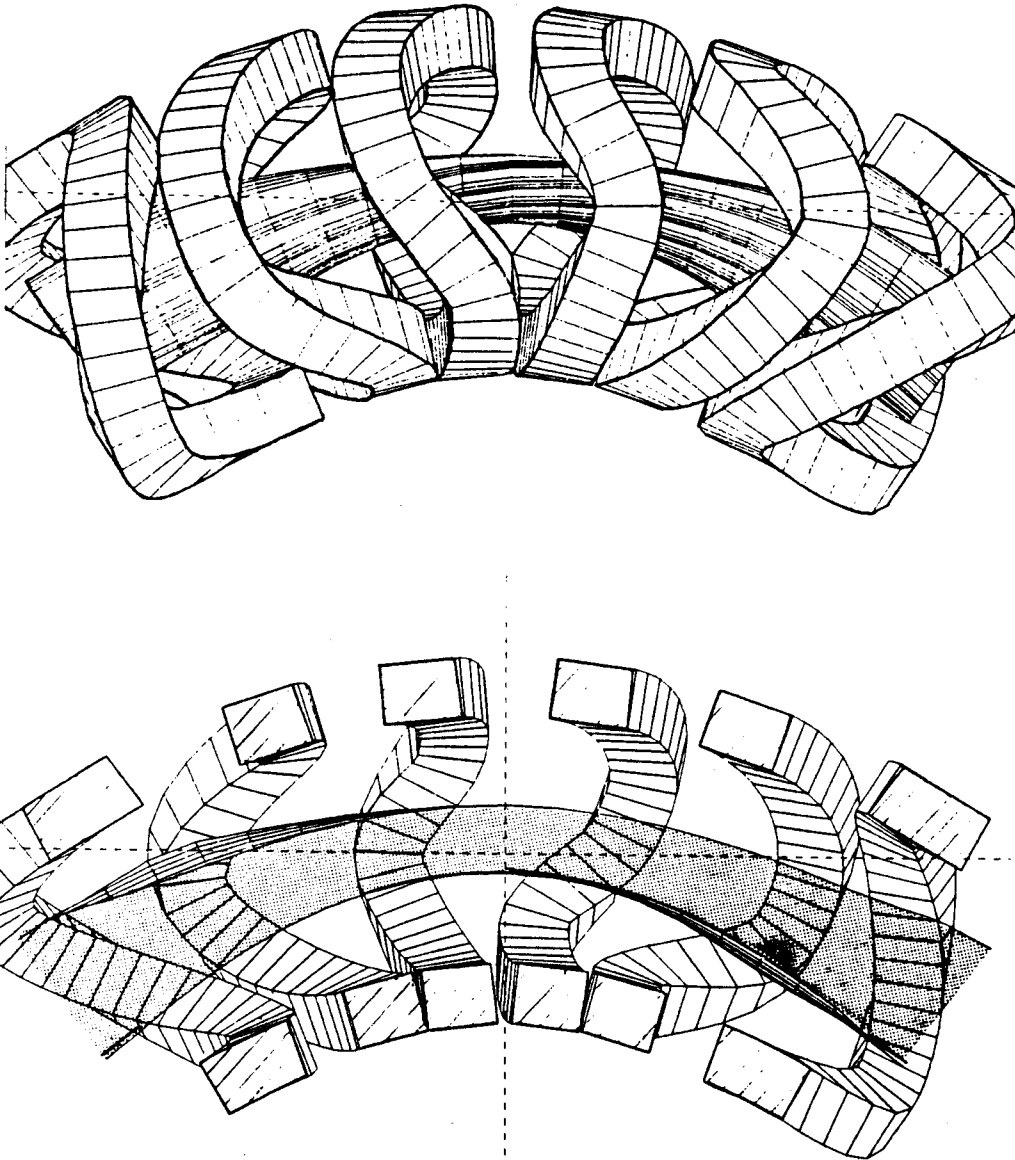
Coils

Shield

Plasma

Blanket

Fig. 2-1 :
Advanced Stellarator Reactor: schematic view of plasma, blanket, shield, and coils.

Fig. 2-2: Contours of single cryostats for ASRA6C
along with shape of last magnetic surface.
Upper half: top view, lower half: cut at mid-plane.

2.3. Magnetic Field

In the upper part of Fig. 2–3, the side and front views of one of the non–planar coils of ASRA6C are shown, along with the required coil housing. The lower part of the figure shows an unrolling of the coils in the φ, θ plane of angular coordinates, and an example of the system of mutual coil support. As detailed in Chapter 7, a considerable part of the finite–element stress and strain calculations is aimed at an optimization of this support.

Fig. 2–4 shows the magnetic topology of ASRA6C and the coil contours at three toroidal positions. The coil centers are at slightly different major radii. All coils have identical elliptic bores. The distance $\Delta = 1.2\,m$ is seen between the inner side of the coil and the dashed line outside of the last magnetic surface. This contour can be used as the shape of the first wall in one of the blanket options, see section 2.5. The right part of Fig. 2–4 shows for ASRA6C the system of magnetic surfaces at finite β, for an average value of $< \beta > \approx 5\,\%$. The shift of the magnetic surfaces is clearly visible. This shift can be taken as determining a 'soft' limit for the equilibrium–β. More details of the finite–β computations are given in Chapter 3, e.g. the deepening of the magnetic well as well as a reduction in the radial profile of the rotational transform for the net current free case.

2.4. Heating and Burn Scenarios

Heating to ignition and steady state burn of an Advanced Stellarator Reactor is investigated by a one–dimensional transport code. Typical values for ASRA6C are a fusion power $P_f \approx 4\,GW$ at an average $< \beta > = 5\%$. In the upper part of Fig. 2–5, the relation between the fusion power output and the peak values of $\beta(0)$ are given for the reference case ASRA6C under optimized conditions, versus the axis values of density and temperature. The lower part of the figure shows the dependence of these quantities on the external heating power P_i of start–up. These dynamic processes are treated in a series of computations as static equilibria. For ASRA6C, an effective heating power of 30 to 50 MW is sufficient for start–up. The two curves labelled by $P_i = 0$ characterize ignition and burn states at two different values of the magnetic induction.

By increasing the refuelling rate, the Advanced Stellarator reactor is brought to full power, preferentially at a moderate temperature $T = 12\,keV$ to $15\,keV$. In the ASRA6C reactor an additional radiative power loss of 300 MW can be tolerated at a fusion power of 3.9 GW if the ripple losses are reduced by a factor of 2 in order to account for the improved confinement properties of an Advanced Stellarator. In this computation $T \approx 19\,keV$ at a value of $< \beta_{eq} > = 5\,\%$.

The question of thermal stability of the operating points remains to be studied in further detail.

Side view   **Front view**

ASRA6C

SPULE 4-9

VERSION RG1#
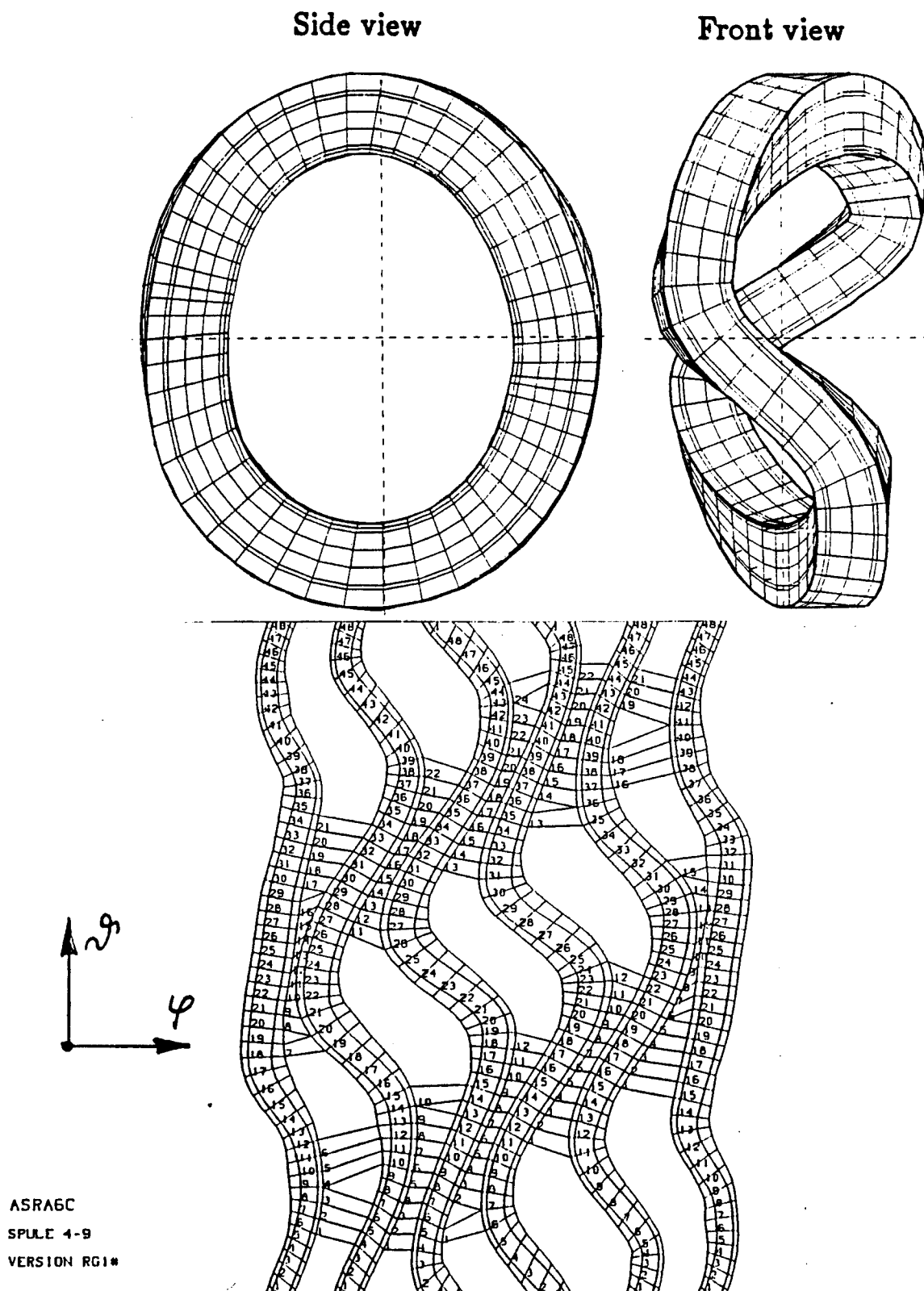
Fig. 2–3: Non–planar coil for ASRA6C with housing
and system of mutual support.
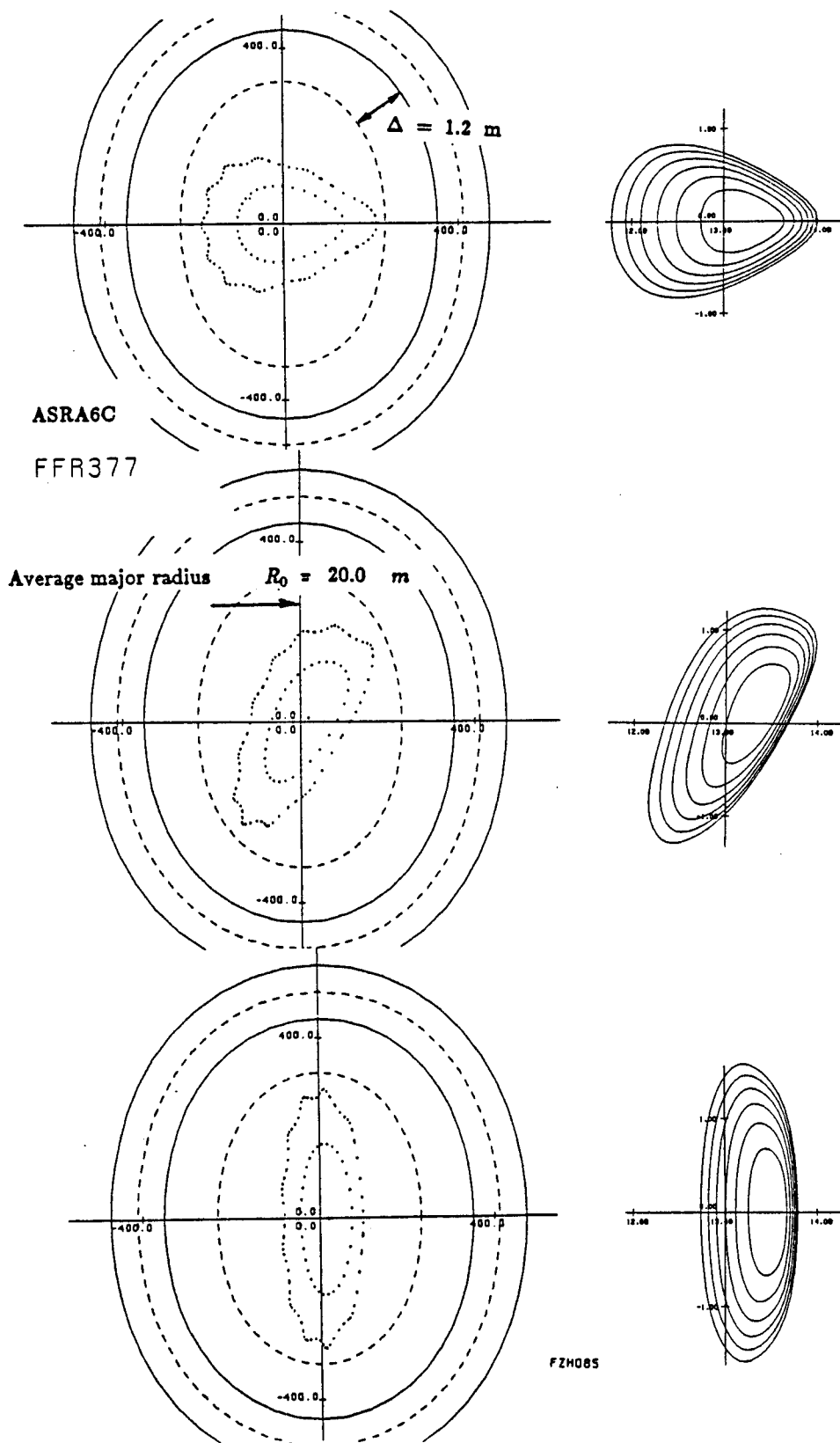
Fig. 2-4: Coil shape and system of magnetic surfaces for ASRA6C
along with the shape of elliptic contours at a distance
$\Delta = 1.2\,m$ inside of coils (left part);
magnetic surfaces at average value of $<\beta> = 4.7\,\%$
shown slightly enlarged in right part of the figure.
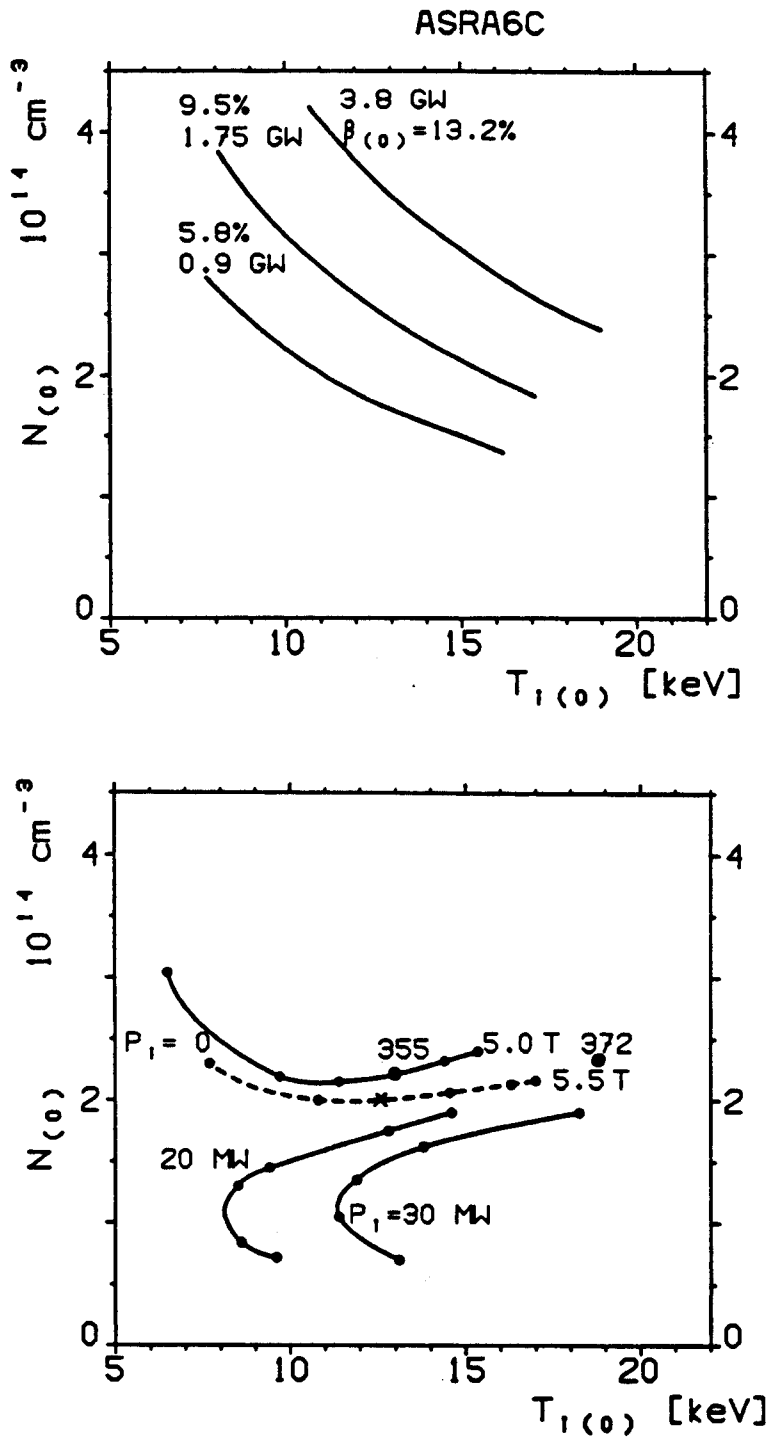
Fig. 2-5: Reference case ASRA6C.
Upper part: Fusion power output and peak values of $\beta(0)$.
Lower part: external heating power P_i of start-up and ignition curves at two different values of the magnetic induction versus the axis values of density and temperature.

2.5. Blanket and Shield

During the course of the study four blanket options have been considered for ASRA6C, as shown schematically in Fig. 2-6. The first option has a constant elliptical cross section and uniform thickness, utilizes $LiPb$ as the breeder, Be as the multiplier/moderator, He gas as the coolant and ferritic steel HT-9 as the structure. This option was selected on overall merits and is described in detail in Chapter 5. The second two options are similar to each other geometrically and utilize the same breeding, moderating, cooling and structural materials as in option I. These two options have a geometry which tracks the contour of the plasma and, therefore, has a helical twist in the poloidal direction. Option III uses denser shield materials in critical areas and in this way differs from option II. Finally, option IV is a design in which the inner surface of the blanket follows the contour of the plasma, but the outer surface is uniformly elliptical causing the blanket thickness to vary both in the poloidal as well toroidal directions. It also uses $LiPb$, HT-9 and He cooling but requires no Be multiplier. This option has been used by KfK in the maintenance analysis and thus appears in most of the figures.

The thin blanket design described in Chapter 5 is made possible by the use of the Be metal as the multiplier. It consists of a series of cells connected together which have semi-ellipsoidal walls for pressure containment, see Fig. 2-7. The Be is in a pebble bed configuration at a 55 % volumetric fraction and is surrounded by $LiPb$. The He coolant is at a $8\,MPa$ pressure and is contained within $1.0\,cm$ diameter tubes immersed in the $Be/LiPb$ mixture. We have selected HT-9 ferritic structure due to its resistance to swelling. The blanket is $21\,cm$ thick and is followed by a $44.2\,cm$ thick steel reflector. Peak neutron wall loading is $2.4\,MW/m^2$ and the average is $1.4\,MW/m^2$. The overall breeding ratio is 1.05 (including penetrations) and the overall energy multiplication is 1.2. Tritium is recovered by slowly circulating the $LiPb$, resulting in a total blanket inventory of $< 6\,g$. Blanket and reflector are cooled in series by the same He gas, and at the exit temperature of $575\,^oC$ the anticipated gross power cycle efficiency is 42.7 %. The tritium leakage through the single wall steam generator is $\sim 10\,Ci/d$.

An optimization study was performed to optimize the shield behind the thin $LiPb/Be$ blanket. The design driver for the shield was found to be the nuclear heating in the magnet. The results show that the optimum shield consists of $44.2\,cm$ HT-9 reflector, $25.5\,cm$ B_4C shield, and $6.3\,cm$ Pb shield. The radiation effects in the magnet vary poloidally and toroidally according to the variation in the neutron wall loading. The peak values occur behind the He manifolds. These are $1.4 \times 10^{23}\,m^{-2}$, $10^{10}\,rad$, and $5 \times 10^{-4}\,dpa/FPY$ for the fast neutron fluence, dose in the GFF insulator, and dpa-rate in the Cu stabilizer, respectively. The average nuclear heating in the front layer of the magnets is $0.13\,mW/cm^3$ and the total nuclear heating in the winding packs and coil cases amounts to $24\,kW$. Only 0.4 % of the gross electric power is needed to remove the nuclear heating from the magnets.

BLANKET OPTION I

BLANKET   UNIFORM THICKNESS
           ELLIPTICAL CROSS SECTION
           HT-9 STRUCTURE—LiPb BREEDER
           Be MODERATOR/MULTIPLIER—He GAS COOLING

REFLECTOR UNIFORM THICKNESS
& SHIELD   ELLIPTIC CROSS SECTION

BLANKET OPTION II

BLANKET   UNIFORM THICKNESS
           FOLLOWS PLASMA CONTOUR
           HT-9 STRUCTURE—LiPb BREEDER
           Be MODERATOR/MULTIPLIER—He GAS COOLED

REFLECTOR UNIFORM THICKNESS
& SHIELD   FOLLOWS PLASMA CONTOUR

BLANKET OPTION III

BLANKET   SEGMENTED, UNIFORM THICKNESS
           FOLLOWS PLASMA CONTOUR
           HT-9 STRUCTURE—LiPb BREEDER
           Be MODERATOR/MULTIPLIER—He GAS COOLED

REFLECTOR UNIFORM THICKNESS
& SHIELD   FOLLOWS PLASMA CONTOUR
           TUNGSTEN SHIELD USED AT
           STRATEGIC LOCATIONS

BLANKET OPTION IV

BLANKET   NONUNIFORM THICKNESS
           OUTSIDE SURFACE ELLIPTICAL
           INSIDE SURFACE FOLLOWS PLASMA CONTOUR
           HT-9 STRUCTURE—LiPb BREEDER
           He GAS COOLING

REFLECTOR UNIFORM THICKNESS
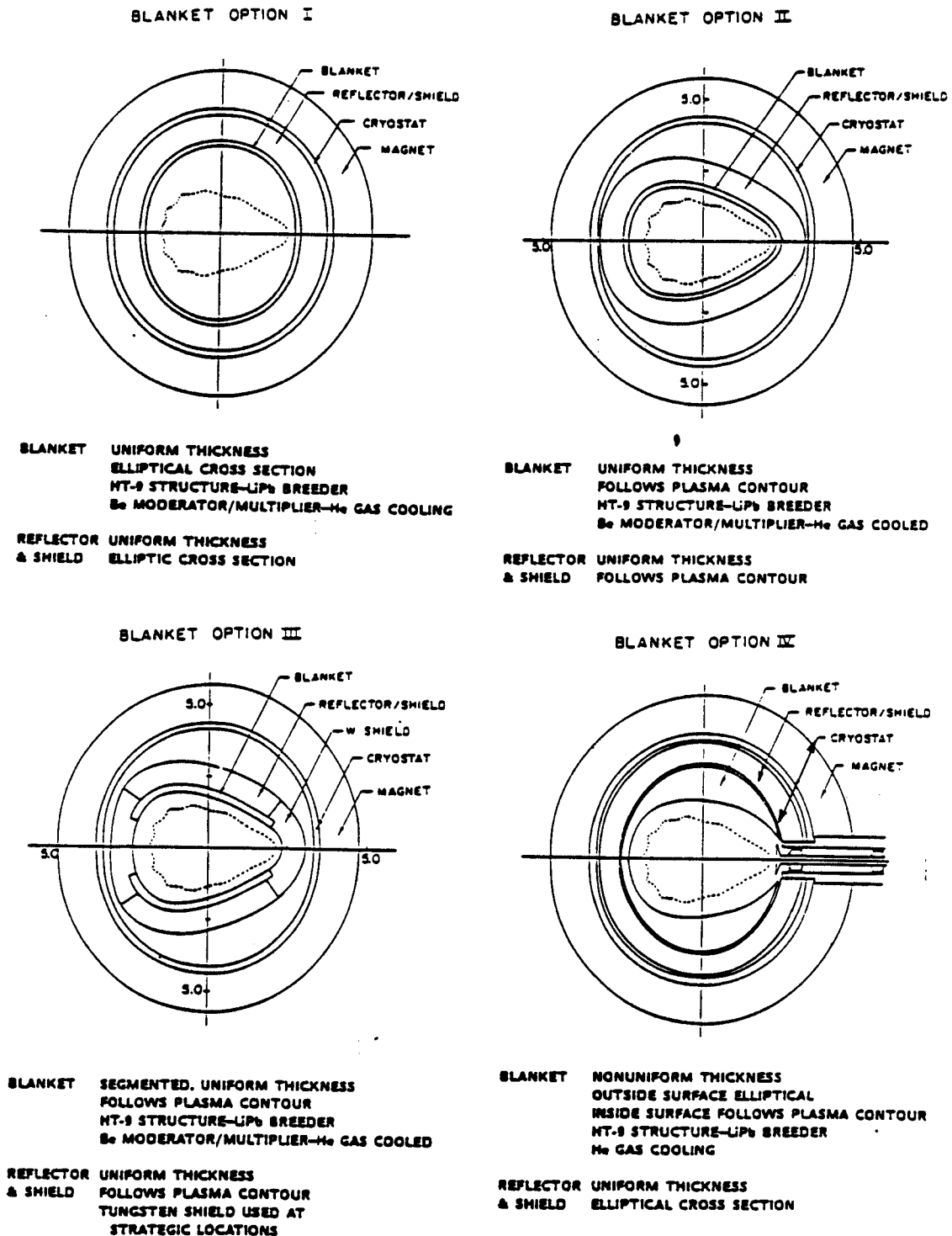& SHIELD   ELLIPTICAL CROSS SECTION

Fig. 2-6: Description of the four blanket options.

Fig. 2-7: Cross-section of a blanket cell.

2.6. Reactor Layout

The layout of the ASRA6C as a fusion reactor is described in more detail in Chapter 9. In the two cross sections of Fig. 2-8, the contour of the first wall is assumed at some distance outside of the last closed magnetic surface. Thus, a blanket with variable thickness is foreseen, accommodating space for structure. A system of many pumped limiters is chosen for edge control of the plasma. Their heat load is assumed to be reduced by edge radiation. The choice of pumped limiters is a result of magnetic field studies near and outside of the separatrix of such systems, see Chapter 3. This study shows a rather complicated radial structure of field lines started at some distance outside of the last closed magnetic surface.

The cross-hatched area outside of the blanket region provides volume for reflector and shield. The outer elliptical contours enclose the superconducting coils and their cryostats. Open space between the radial arrangement of reactor elements is available for assembly and maintenance. The upper part of the figure is at the beginning of the field period, the lower half applies for some adjacent toroidal position.

In Fig. 2-9, a plan view of a field period plus the two adjacent coils is shown schematically, cut at the vertical mid-plane. The positions of the many pumped limiters are indicated. Fig. 2-10 gives a cross section along the direction of neutral beam injection, which is one of the options for reactor start-up. Note that stellarators in principle allow a steady state burn, provided that refuelling and ash removal can be accommodated appropriately, and the impurities in the system do not pose serious problems. Then, after start-up, the openings for the initial heating can be closed with shield material.
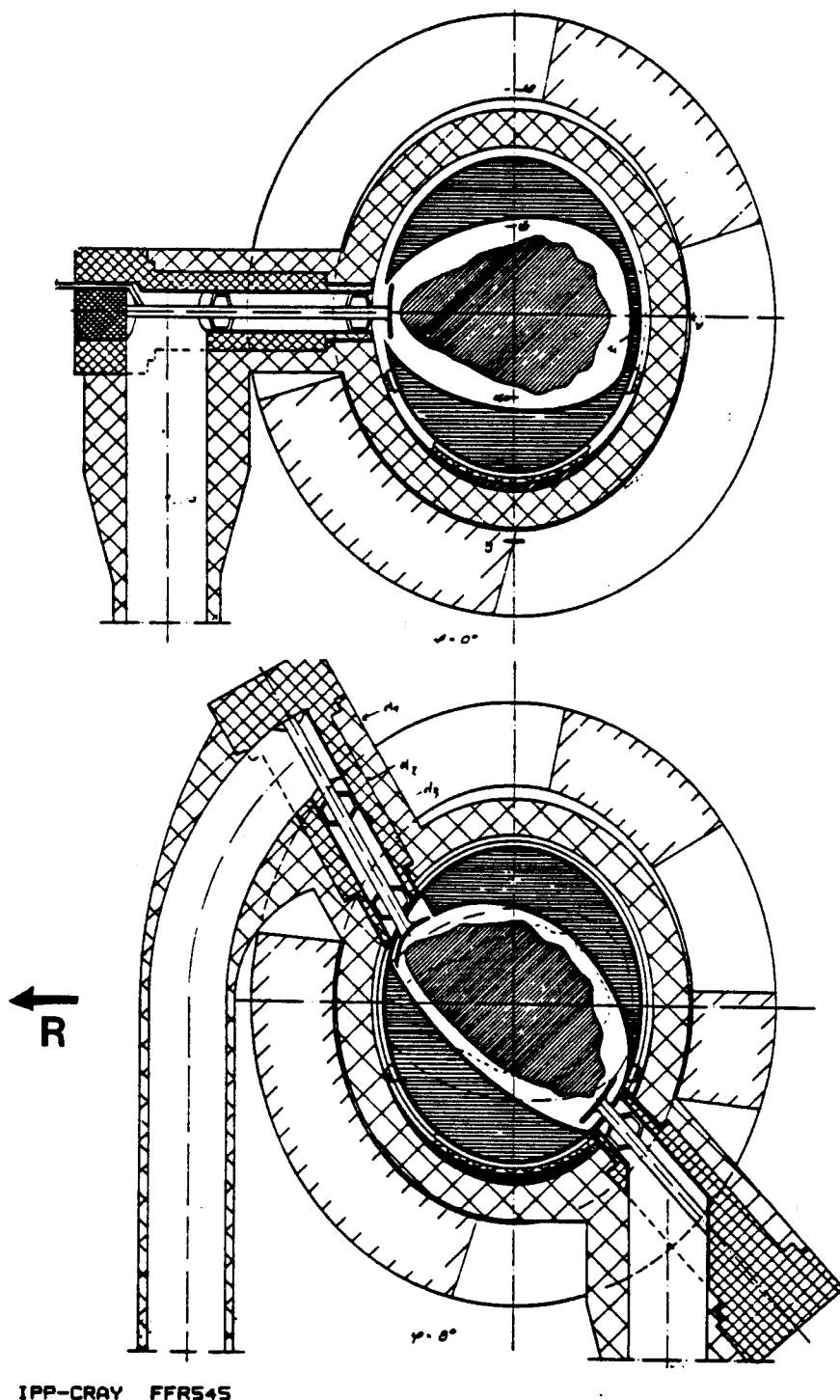
IPP–CRAY FFRS4S

Fig. 2–8: ASRA6C as fusion reactor
shown at beginning of field period and at some toroidal position.
KfK design to study construction and maintenance.

Neutral Injection System

ASRA6C
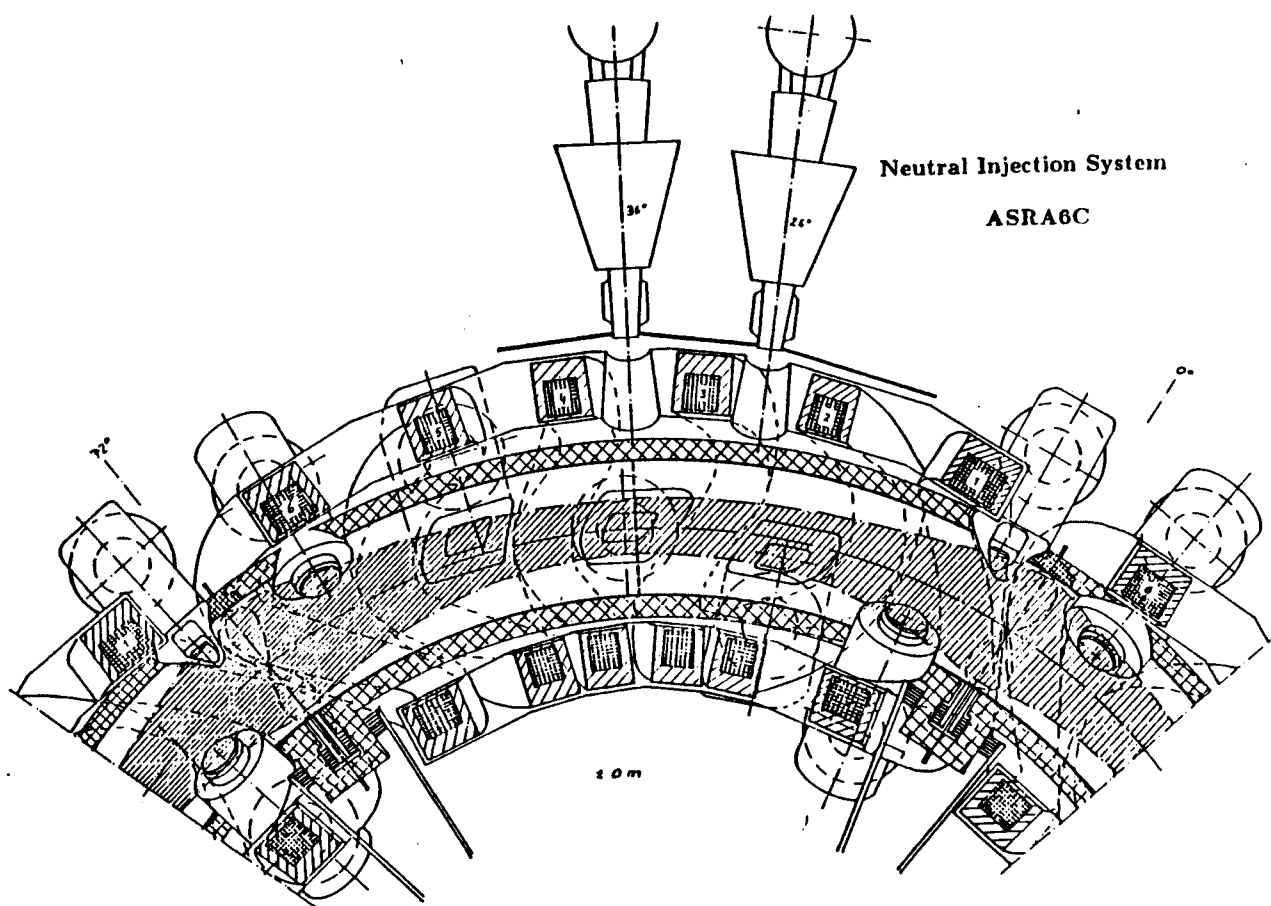
Fig. 2-9: Plan view of same design, cut at vertical mid-plane;
one field period plus adjacent coils.
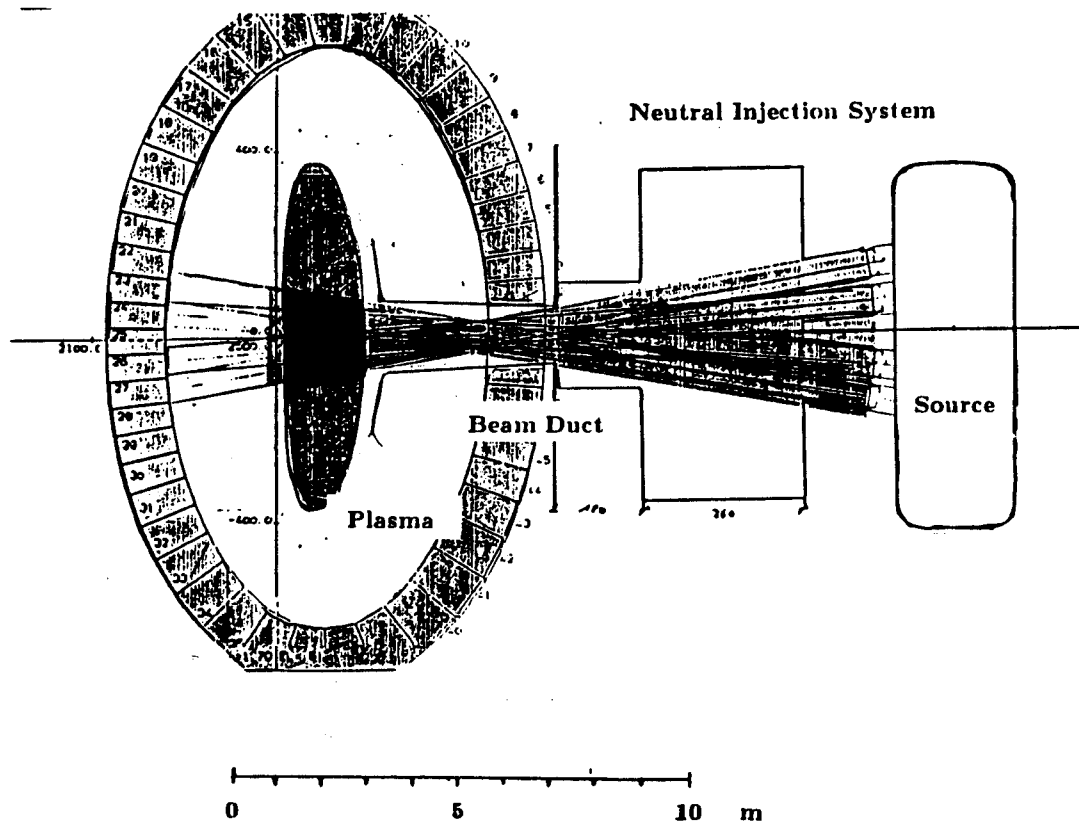
Fig. 2-10: Schematic view of neutral injection port.
Not shown : blanket/shield module to be closed
after stationary power is attained.

3. Magnetic Field Studies of Advanced Stellarators

3.1. Introduction

Stellarator fusion reactors with continuous helical windings or those using systems of non–planar modular coils constitute viable options for their development towards an alternative to tokamak reactors. Start–up from existing magnetic surfaces and the possibility of a steady–state burn in the absence of dangerous disruptions are distinct advantages of stellarators. The prospect for continuous operation of the reactor allows different approaches for the coil engineering and avoids problems associated with the cyclic loads of pulsed systems, especially in the first wall and in the coils with their support structure. Furthermore, less circulating power is required in stationary systems. A moderate aspect ratio alleviates problems regarding the first wall power loading, although, in general, small systems offer advantages due to a scaling of costs with magnet size or with stored magnetic energy. Modular systems of non–planar coils avoid problems which result from the geometry of interlinked coils present in certain stellarators with continuous helices as well as in most tokamaks.

The coil topology of modular non–planar coils of Advanced Stellarator Reactors (ASR) and Burner (ASB) configurations is derived from magnetic vacuum field studies, starting from the fields of the Garching Advanced Stellarator experiment WENDELSTEIN VII–AS, which is characterized by a reduction of the secondary plasma currents as compared to those of a standard stellarator.

Numerical and analytic winding laws are used for the contours of the coils. There are 5 field periods. The number of coils is varied between 18 and 4 coils per field period. An optimum is seen at 6 coils per field period, compromising between magnetic field quality (reduction of secondary currents, magnetic well, plasma aspect ratio, field modulation) and requirements of accessibility and maintenance of such coils.

The rotational transform $\iota = 0.4$ to 0.6 at the magnetic axis is determined mainly by the minor coil radius and by the specific coil contours, i.e. the shapes of the coil cross section and of the toroidal excursions. These, and the radial position of the coil centers influence the field quality. Rational ι–values of low order are to be avoided within the plasma, because of the formation of magnetic islands. Such islands exist in ASRA6C also outside of the separatrix in its vicinity. The behaviour of field lines started outside of the last closed surface lead to the choice of pumped limiters for control of the edge plasma in the presently considered ASR systems.

Magnetic field calculations at finite plasma pressure are performed for the reference configuration ASRA6C up to an average value of $< \beta_{eq} >= 4.7\,\%$ for the equilibrium–β, yielding a relative shift of the magnetic axis up to about 50 % of the radial distance to the edge, with a considerable deepening of the average magnetic well.

Section 3.2 contains a short description of the main properties of Advanced Stellarators. Section 3.3 briefly summarizes the development of several earlier Advanced Stellarator Reactor and Burner systems. In section 3.4, two Advanced Stellarator Reactor configurations, ASRA6B and ASRA6C are introduced, which are described by analytical coil winding laws. Effects of perturbation fields are briefly mentioned.

Section 3.5 summarizes the results of computations of the finite–beta fields for the reference configuration ASRA6C. In section 3.6, a short summary gives the main conclusions regarding coil topologies and magnetic fields of Advanced Stellarator Reactors as studied so far.

3.2. Properties of Advanced Stellarators

Advanced Stellarators are distinguished from standard ones by a reduction of the secondary plasma currents for all magnetic surfaces of the system, and a magnetic well between the magnetic axis and the last closed surface of the vacuum fields, combined with reasonable values of the aspect ratio and of the rotational transform. Thus, the associated neoclassical particle and energy losses as well as the deformation of the magnetic surfaces by a finite plasma pressure (Shafranov–shift) are reduced, and the drift surfaces of circulating charged particles deviate less from the magnetic surfaces, in comparison to the respective results for standard stellarators. The principles of optimization to arrive at an Advanced Stellarator topology are given in [1]. They consist of a reduction of the poloidal variation of $\int dl/B$, as taken for different poloidal starting points on a magnetic surface, and integrating along one field period. A difficult side condition is to maintain a magnetic well in a configuration with a reasonably low aspect ratio. This optimization is performed by a proper combination of poloidal fields, which also influence the rotational transform t and the shear.

Modular coils are essential to produce such Advanced Stellarator fields. The Garching experimental device WENDELSTEIN VII–AS (with a major radius 2 m, a plasma radius 0.2 m, and a magnetic induction of 3 T) is the first Advanced Stellarator to be built and is expected to begin operation in 1987. It has 5 toroidal field periods (FP) and is equipped with 9 non–planar modular coils per FP. Details of its design and of the expected parameter range are given in [2].

The value of the rotational transform t can be varied considerably in this experimental device. This is done by the fields of a separate set of 10 planar coils superposed on the fields of the modular coils. A fusion reactor is expected to be built for operation at optimized conditions, e.g. at optimized t, and does not require such additional toroidal field coils. Furthermore, as was seen in the scoping considerations for modular coils of the future experiment WENDELSTEIN VII–X, a certain change of t can also be provided by appropriate design of the non–planar coils.

3.3. Vacuum Fields of Advanced Stellarators

Starting from the magnetic field topology of the Garching Advanced Stellarator WENDELSTEIN VII–AS and enlarging the dimensions and fields to values of a fusion reactor or a burner experiment, several coil sets are derived with average major radii $R_o \approx 25\,m$ for the Advanced Stellarator Reactor (ASR), and about 15 m for the Advanced Stellarator Burner experiment (ASB), respectively. In the present study, the number of coils of each of the 5 field periods is varied between 18 and 4, as can be seen in Fig. 3–1, which shows the top view of the coil arrangements of three different

earlier ASR and of one ASB with 18, 9 or 6 coils per field period, drawn in the same scale. As is clearly visible in the figure, the major radii of the coil positions vary in the toroidal direction with fivefold periodicity. The spatial curves describing the coil centers are obtained numerically using procedures developed for the design of the coils for WENDELSTEIN VII–AS [2]. The average value of the induction on the magnetic axis is set to $B_o = 5.3\,T$ for ASR, and to a larger value of $7\,T$ for ASB. In the two systems with 10 coils per FP, the current densities and coil cross sections are matched to keep the maximum value of the magnetic induction at values $B_m < 9\,T$ at the coil surface, in order to stay within the limits of $NbTi$ as superconducting material and operating at the temperature of liquid helium.

The case ASR254E with 4 coils per FP offers distinct advantages for assembly and maintenance, but shows a large value for the peak induction of $10.1\,T$ at the coils in contrast to $8.8\,T$ for ASR2510, as detailed in [3], although the effective current density is larger in the latter case. Furthermore, the modulation of the induction (magnetic field ripple) between the axis and the last closed surface is considerably increased in ASR254E , see Fig. 3–2. In the trace of the magnetic induction along the axis (top), a periodicity with each of the $m = 5$ field periods is visible. An increased value of this helical ripple is responsible for larger neoclassical energy and particle losses, see Chapter 4. Therefore this data set is rejected.

As shown in the lower left of Fig. 3–1, a coil configuration ASR25T7 is derived, which produces the same average value of the induction on the magnetic axis, $B_o = 5.3\,T$, using smaller coils at increased current density. Simultaneously, the rotational transform ι is raised to a value of about 0.6 in order to achieve a larger value of the equilibrium–beta. In a standard or 'classical' stellarator, this quantity roughly scales as $< \beta_{eq} > \approx \iota^2 / A$, where the aspect ratio $A = R_o/r_p$ and $r_p \approx 1.6\,m$ is the plasma radius. Note that for an Advanced Stellarator a larger value of the equilibrium–β applies, due to the reduction of the secondary currents and the smaller vertical fields which then cause a smaller Shafranov–shift in the configuration.

The configuration ASR25T7 has about the same value of the magnetic field ripple, $\delta B/B = (B_{max} - B_{min}) / (B_{max} + B_{min})$ as the data set ASR2510.

The magnetic field quality of these Advanced Stellarator reactors is demonstrated in Fig. 3–3, which shows the maximum absolute values of $|j_{\|}/j_{\perp}|$ versus the rotational transform ι, where $j_{\|}$ and $j_{\perp}$ are the parallel and diamagnetic current densities, respectively. The dots characterize the ASR data sets with values close to those computed for the Garching Advanced Stellarator experiment WENDELSTEIN VII–AS; the upper curve labelled by $2/\iota$ characterizes a standard stellarator. The secondary currents $j_{\|}$ are reduced by a factor of about 2 in W VII–AS and in these ASR configurations, compared to those of a standard stellarator.

A similar improvement of the behavior of the drift surfaces is seen in these Advanced Stellarator configurations by analyzing the drift surfaces of charged particles. The deviation Δ^*/ρ is found to be about half of the value of $1/\iota$ which is expected for a standard stellarator with the same rotational transform ι, where Δ^* is the radial offset of the guiding center of charged particles from the corresponding magnetic surface, and ρ is the Larmor radius. An example of drift surfaces for fusion α particles with an energy of $3.5\,MeV$ is given in Fig. 3–4 for the magnetic field configuration of ASR25T7.

The coil configurations for the burner experiments ASB (right part of Fig. 3–1) are derived from the data set ASR25T7 by a reduction of the major radius to a value of $15\,m$, and by doubling the coil current density to $j_{eff} = 18\,MA/m^2$, where this number is the effective value averaged over the whole winding cross section, i.e. including superconductor, stabilizer, internal structure, as well as insulation and helium channels. The magnetic induction at the axis is increased to $B_o = 7\,T$ in order to achieve ignition at the comparatively small plasma radius of $r_p = 0.9\,m$. Associated with the increased axis induction, a large value of the induction B_m results at the coil surface, calling for Nb_3Sn as superconductor.

The number of coils per field period is changed from 18 to 9 and 6 in the ASB configurations in order to see the effect on the peak induction at the coils, as well as the influence on the field quality of the Advanced Stellarator. Some quantitative information is given in Table 3–I which compares the data sets ASR25T7 with the three ASB cases at 18, 9 and 6 coils per field period. In the three ASB cases the peak values of the magnetic induction at the coils increases for a lower coil number when keeping the axis values of the magnetic induction and the current density in the coils unchanged. This is caused by the increased coil width at a low coil number.

Comparing the axis and edge values of the rotational transform, t_o and t_a, a negative shear is introduced in the data set with 6 coils per FP, and the depth of the magnetic well is about half the value of the cases with 9 or 18 coils per FP.

The general properties of an Advanced Stellarator are maintained, however. Therefore, data sets with 6 coils per field period are developed to reactor dimensions, since this number of coils per FP is considered as a reasonable compromise between field quality and prospects for assembly and maintenance.

The coil shapes for these ASR and ASB data sets vary along the field period. This is visible in Fig. 3–5, showing the contours of the adjacent coils at toroidal positions at the beginning and half of a field period, together with the system of nested magnetic surfaces of the vacuum field. Outside of the drawn magnetic surface, a number of 10 dots is visible. Here, the value of the rotational transform $t = 5/10 = 1/2$ is a low–order rational number. As described in detail in [4], such low–order rational t–values should be avoided. This can be easily realized in vacuum fields with small shear.

Due to the non–planar shape of the coils there exists a complicated spatial distribution of the magnetic forces. Integrating the magnetic forces over one field period yields the net radial force which characterizes a toroidal arrangement of planar coils. Further details of the magnetic forces and their dependence on the large number of parameters describing the coils are given in Chapter 7 for the data sets ASRA6B and ASRA6C.

ASR2510

ASB18D

ASR254E

ASB09D

ASR25T7

ASB06E
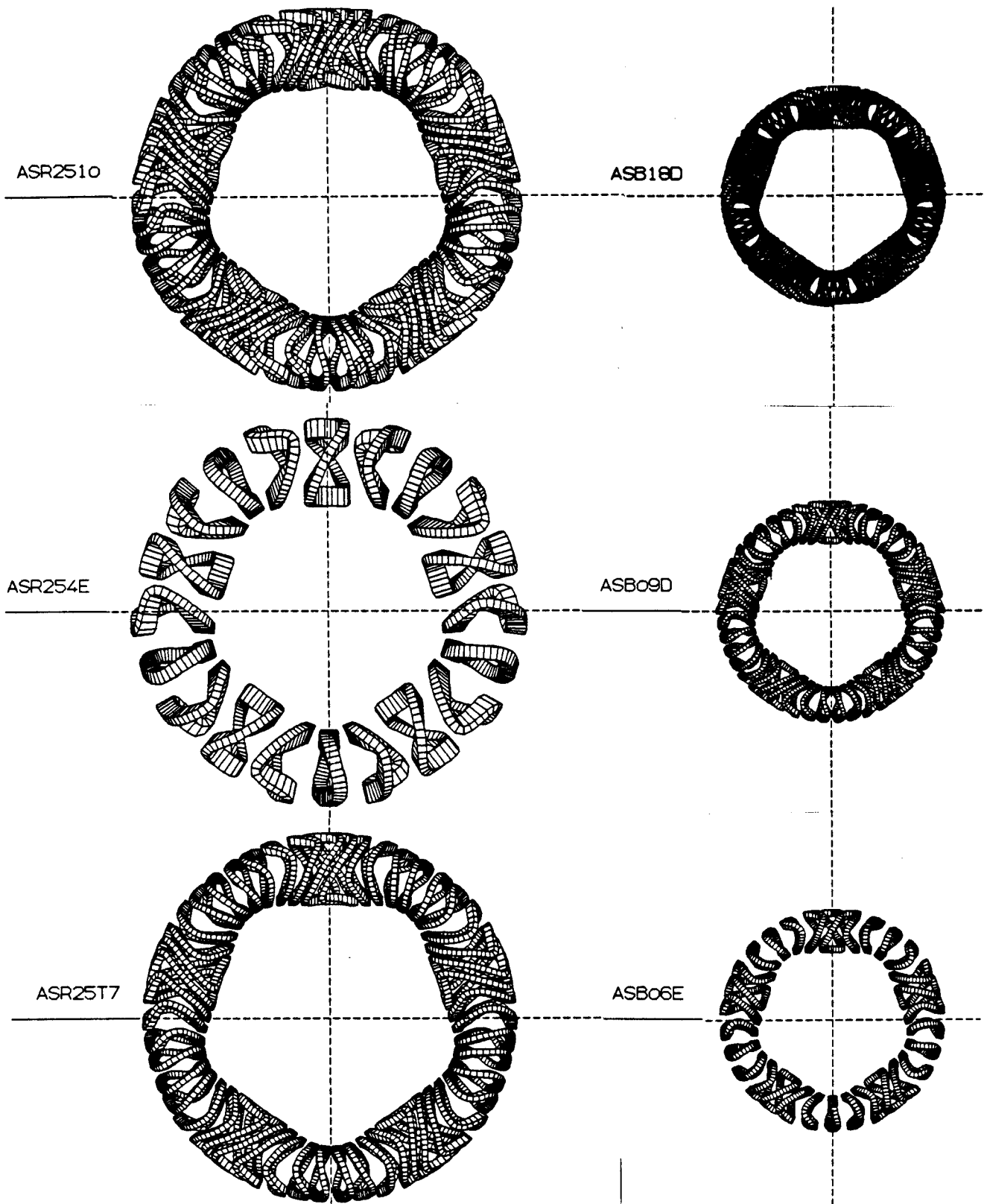
Fig. 3-1: Coil configurations of Advanced Stellarator
Reactor and Burner systems with different numbers
of coils per field period shown in same scale.

ASR2510   ASR254E
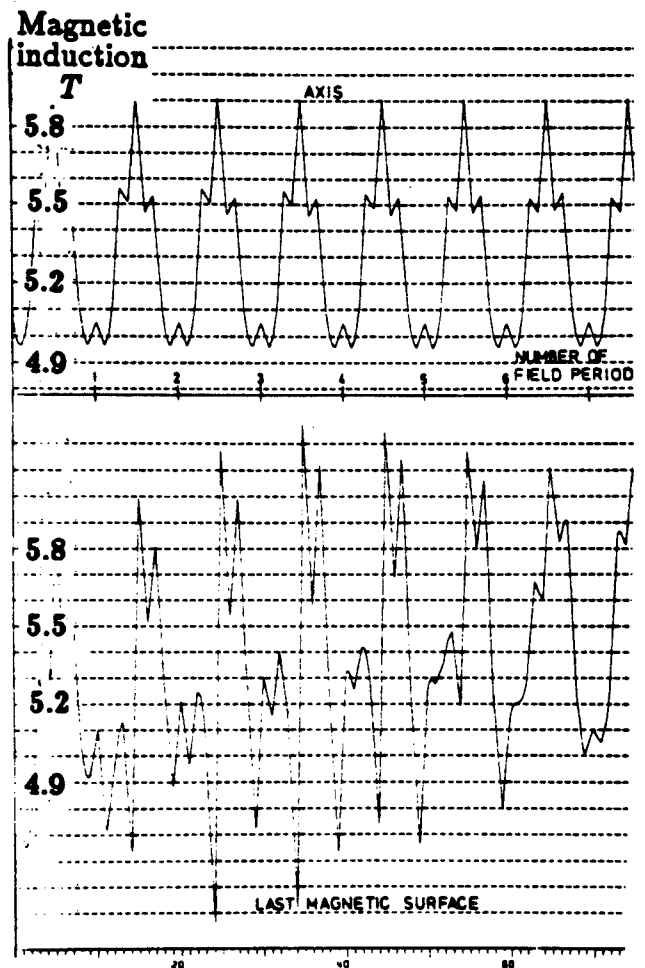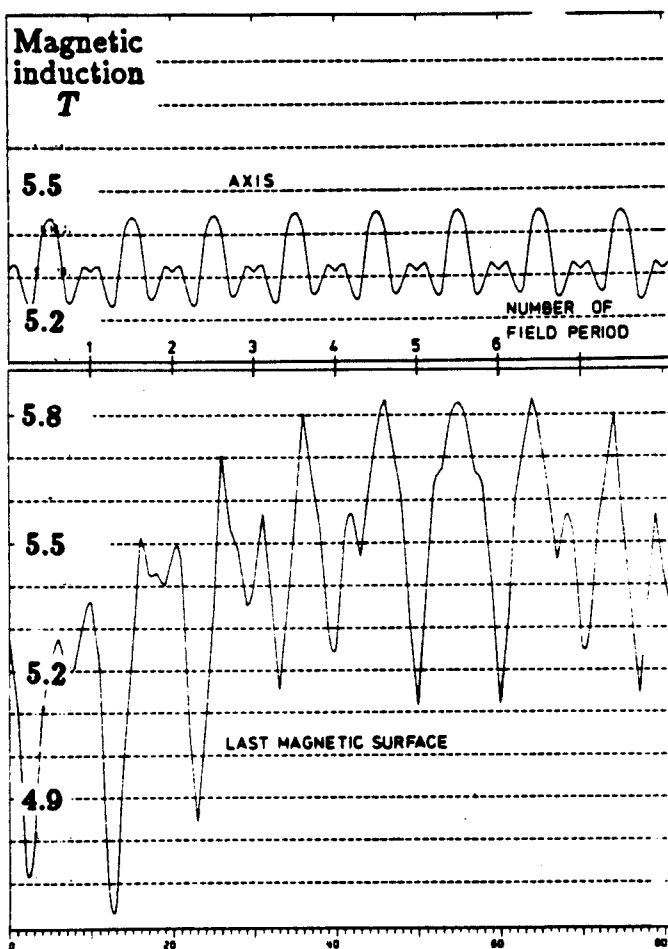
Fig. 3-2: Magnetic induction along the axis (top)
and for the last closed surface of the vacuum field (bottom)
showing an increased field ripple for ASR254E
with 4 coils per FP (right part),
in comparison to ASR2510 with 10 coils per FP.
The abscissae extend over 8 field periods .
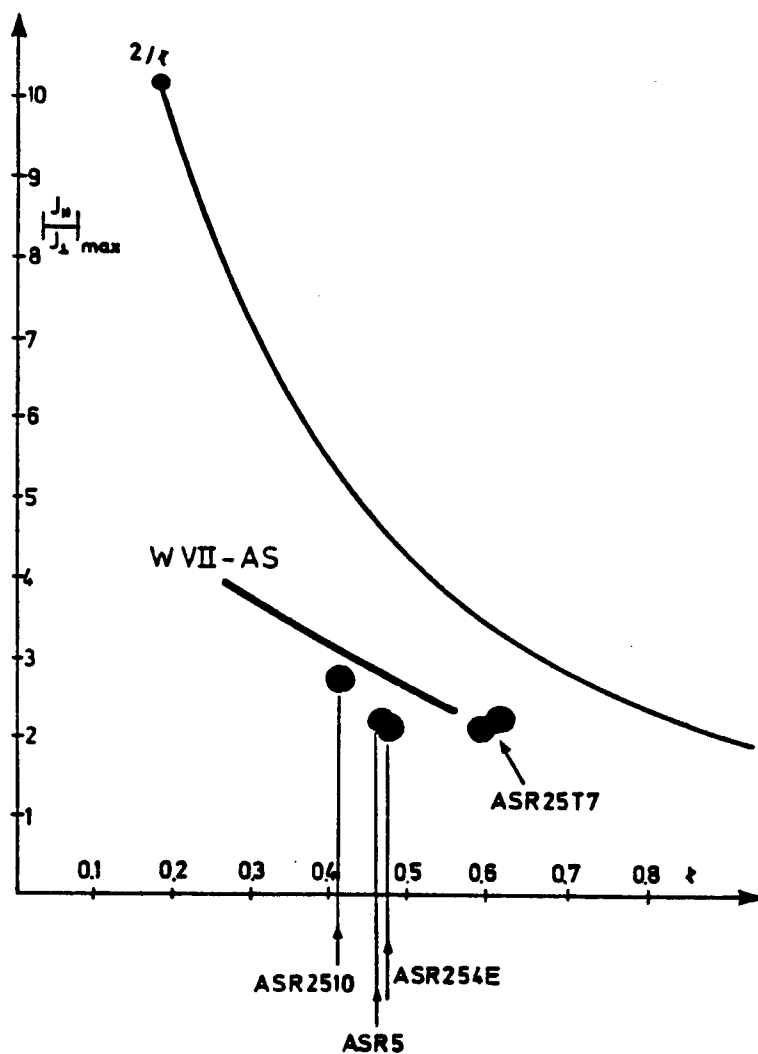
Fig. 3-3: Maximum values of $|j_{||}/j_{\perp}|$ versus the rotational transform ℓ for several Advanced Stellarator Reactor configurations in comparison to data for WVII-AS and standard stellarators, the latter being described by the curve labelled $2/\ell$.

Z

200.0

PASSING α PARTICLES

$V_{\shortparallel}$

$V_{\uparrow\downarrow}$

0.0

2100.0   2300.0   2500.0   START

2700.0

3.5 MeV → ρ=5cm

$\varphi = 0$

$V_\perp/_V = 0.71$

4Δ

30 cm

Z

$\Delta^{\bullet}/_\rho = {}^{1.5}_{0.8}$ at $\varphi = {}^{0}_{\frac{1}{2}}$ F.P.

$1/_\tau = 1.7$

200.0

0.0

2100.0   2300.0   2500.0   2700.0

$\varphi = 1/2$ F. P.

-200.0

4Δ

16 cm
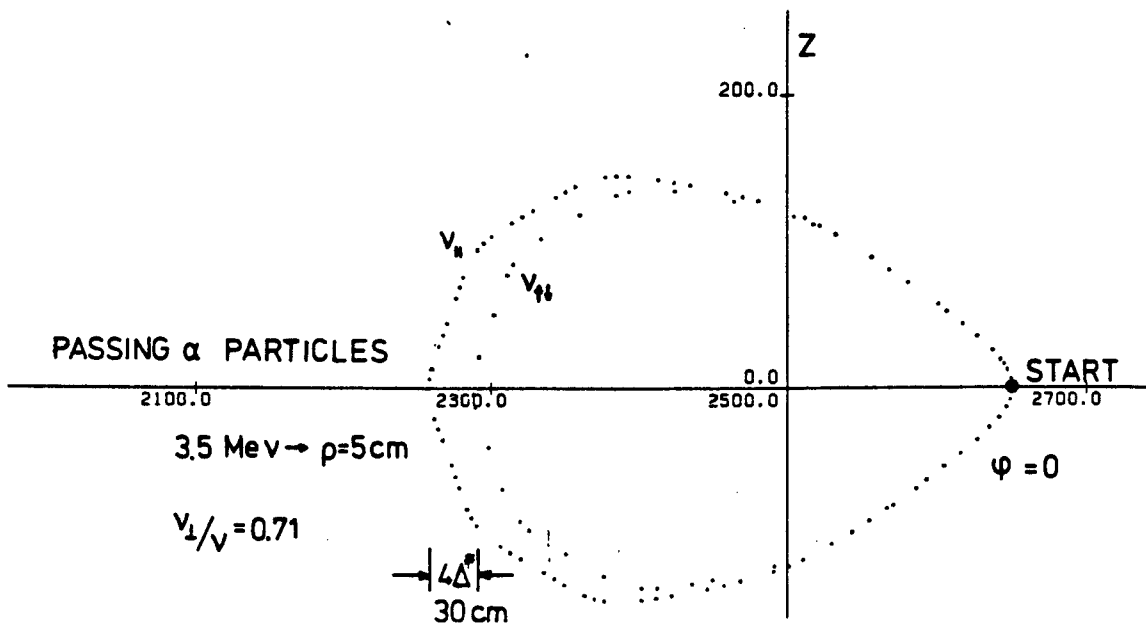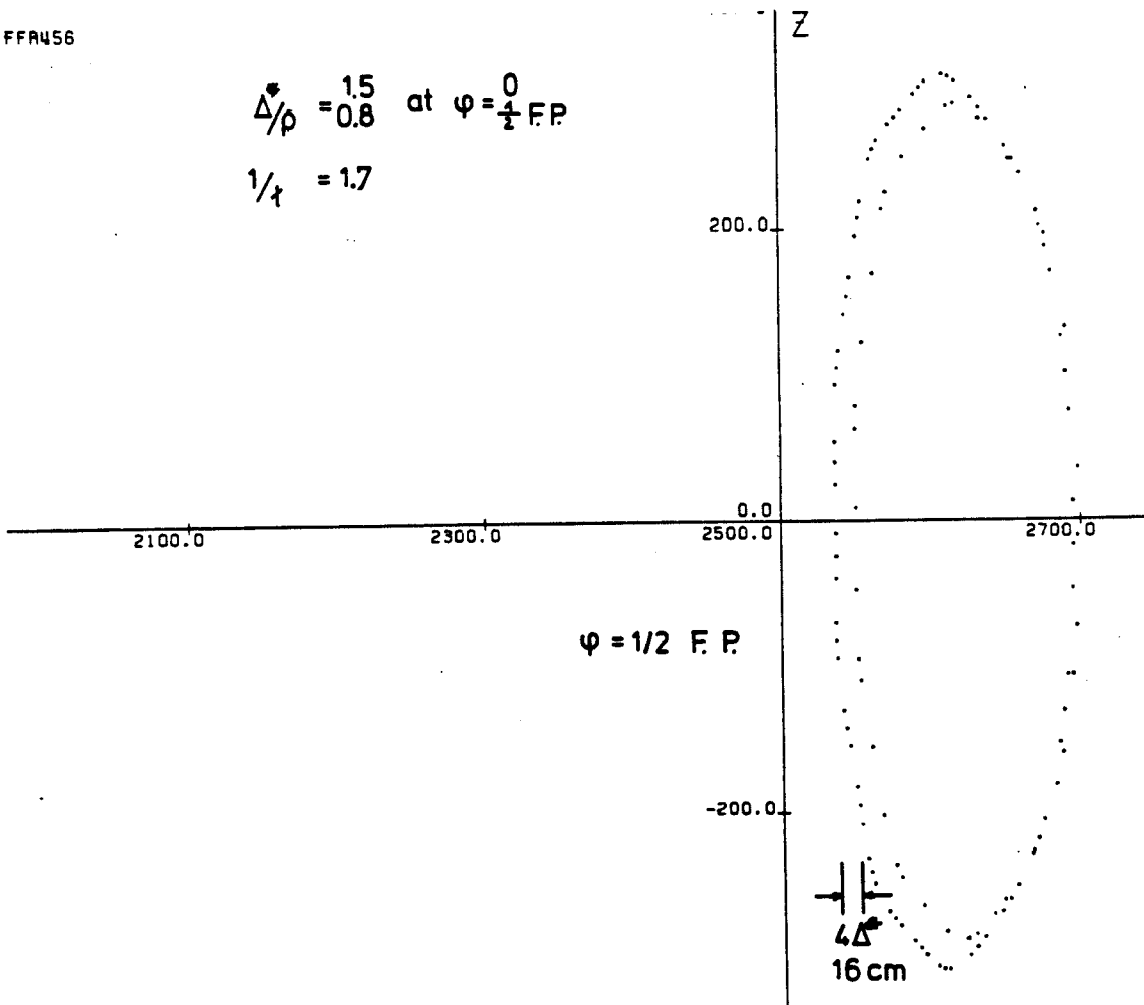
Fig. 3–4: Drift surfaces of "passing" α particles in ASR25T7

<u>TABLE 3-I</u>

Characteristic data of ASR25T7 and of three ASB configurations.

System			ASR25T7	ASB18D	ASB09D	ASB06E
Average major radius	R_o	$[m]$	25.5	15.2	15.2	15.2
Average coil radius	r_c	$[m]$	5.24	3.24	3.24	3.24
Coil number/FP			10	18	9	6
Conductor			NbTi	Nb_3Sn	Nb_3Sn	Nb_3Sn
Effect. current density	j_{eff}	$[MA/m^2]$	9.8	18	18	18
Max. induction at coil	B_m	$[T]$	8.7	10.3	11.0	12.6
Induction on axis	B_o	$[T]$	5.3	7.0	7.0	7.0
Rotat. transf. on axis	t_o		0.58	0.51	0.50	0.53
Rotat. transf. at edge	t_a		0.61	0.52	0.51	0.51
Magn. well depth	V''	%	-0.1	-0.1	-0.08	-0.04
Aver. plasma radius	r_p	$[m]$	1.75	0.9	0.9	0.9
Distance to coils	Δ	$[m]$	> 1.8	1.2	1.2	1.2

$r_p = 0.9\,m$

$\Delta = 1.2\,m$
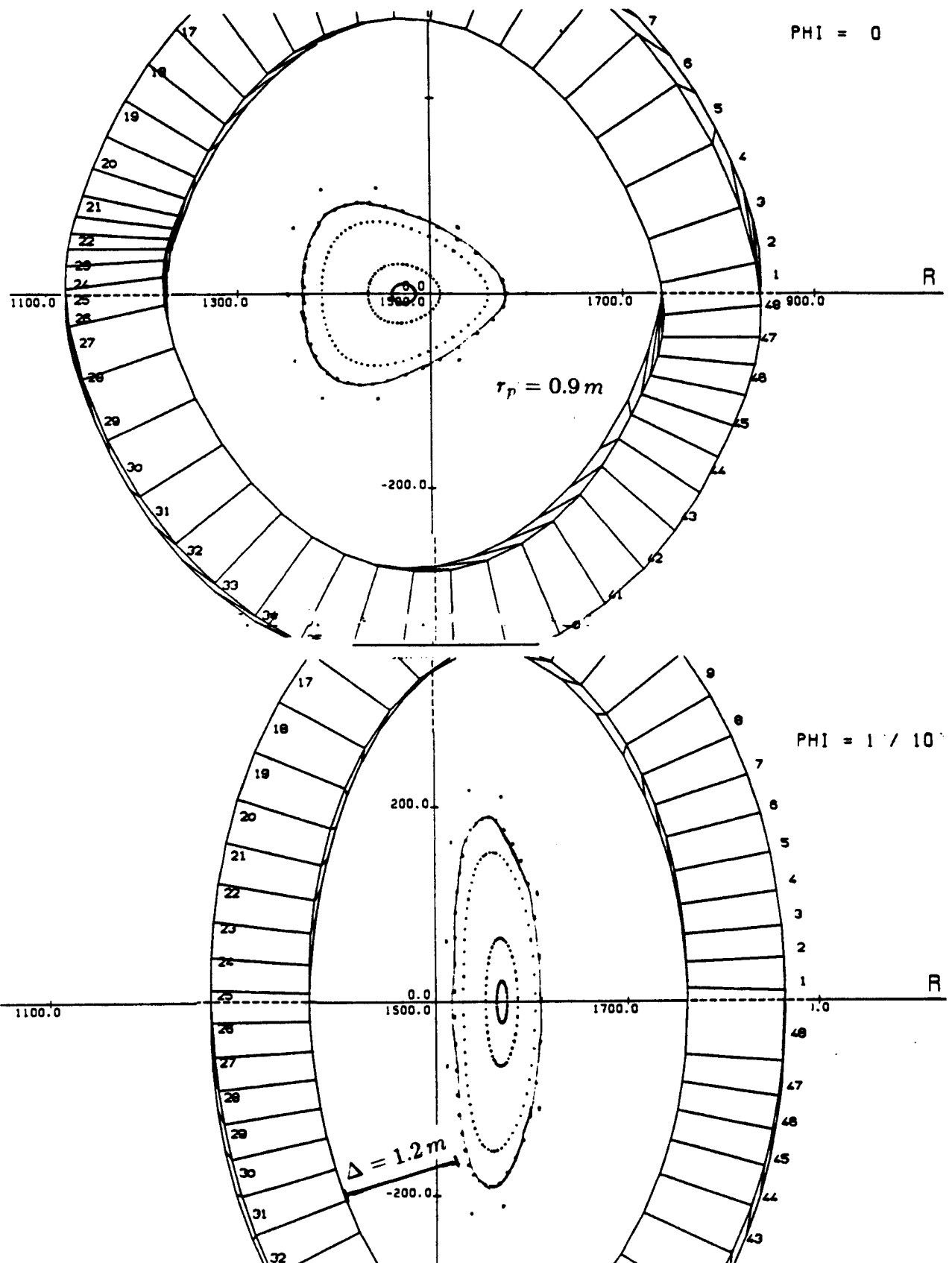
Fig. 3–5: Coil shape and nested system of magnetic vacuum field
for the Advanced Stellarator Burner ASB06E
at toroidal angles 0 and at 1/2 of the field period.

3.4. Advanced Stellarator Systems ASRA6B and ASRA6C

Using a flexible system for describing the spatial curves of the coil center lines with an analytic "winding law", applicable for arbitrary position and orientation of the modular coils as detailed in [5], the two coil systems ASRA6B and ASRA6C are derived. The abbreviations of these data sets stand for <u>A</u>dvanced <u>S</u>tellarator <u>R</u>eactors with coils described by an <u>A</u>nalytic winding law and <u>6</u> coils per field period, version B and C. The label C indicates a more compact version than the preceding data set ASRA6B. This is made possible by introducing a modern design for the blanket and shield (see Chapters 5 and 6), reducing the critical distance Δ between the first wall of the system and the inner contour of the coil winding from the previous value of $2.1\,m$ to $1.2\,m$. As a consequence, the major radii can be changed from $R_o = 25\,m$ in ASRA6B to a value of $20\,m$ in ASRA6C, keeping other parameters unchanged. Other data of this system are given in <u>Table 3–II</u> and compared to those of ASRA6B as well as to data of the previous configuration ASR25T7 and of the Garching Advanced Stellarator experiment WENDELSTEIN VII–AS. Note the remarkable decrease in the magnetic energy when reducing the size of ASRA6B to that of the compact system ASRA6C.

The coil geometry of both cases is shown in <u>Fig. 3–6</u>. There are 6 coils per FP and three different coil shapes are present in the complete coil system, if one considers the twofold mirror symmetry. All coil apertures are of the same elliptic cross section centered at major radii according to $R(\varphi) = R_o(1 - k\cos(5\varphi))$, where $k = 0.016$ for both cases and φ is the toroidal angle. <u>Fig. 3–7</u> shows the contours of the coils at the beginning and half of a field period, together with the nested system of the magnetic surfaces of the vacuum field. The varying contours of the magnetic surfaces and the radially undulating axis position are geometric characteristics of an Advanced Stellarator. Outside the last closed magnetic surface (the separatrix) an "ergodic" region is seen with 11 small magnetic islands at a rational value of the rotational transform, $\iota = 5/11$. Inside the separatrix, no low–order rational ι–values are present. The modulation of the induction along a field line is demonstrated in <u>Fig. 3–8</u> for the magnetic axis and the last closed surface of ASRA6C.

It is easy to adjust the rotational transform to irrational values by a proper choice of the minor coil radii, see top part of <u>Fig. 3–9</u>, once the shape of the center line of the modular coils is fixed. The amount of toroidal excursion also changes the value of ι, and the higher harmonics present in the winding law of the coil centers influence the degree of reduction of the secondary currents. The amplitudes of these higher harmonics differ for the three coil shapes present in the ASRA6 data sets. As to be seen in the lower half of <u>Fig. 3–9</u>, the effective radius of the last closed magnetic surface is smaller at rational ι. This is caused by N "natural" magnetic islands which are found at rational $\iota = m/N$ in such Advanced Stellarators inside of and near the separatrix, see also [2] and [4]. In these references, more information on these islands is given and their sensitivity to external perturbation fields is studied. ASRA6C allows a comparatively large value of such a perturbation, $B_y/B_o = 0.2\,\%$, see <u>Fig. 3–10</u>. The system of outer islands vanishes and the average radius of the last closed surfaces is reduced by a relatively small amount of about 10 %.

TABLE 3-II

Characteristic data of WVII–AS and ASR25T7 compared to those of the more recent data sets ASRA6B and ASRA6C

System			WVII–AS	ASR25T7	ASRA6B	ASRA6C
Average major radius	R_o	$[m]$	2.0	25.5	25.0	20.0
Average coil radius	r_c	$[m]$	0.48	5.24	5.22	4.57
Conductor			Cu	NbTi	Nb_3Sn	Nb_3Sn
Coils / FP			8+1	10	6	6
Coil current	I_c	$[MA]$	0.6/1.5	13.7	22.5	18
Effect. current density	j_{eff}	$[MA/m^2]$	27	9.8	15	15
Max. induction at coil	B_m	$[T]$	5.2	8.7	11.0	10.4
Stored mag. energy	W_m	$[GJ]$	0.04	170	193	117
Induction on axis	B_o	$[T]$	3.0	5.3	5.3	5.3
Rotat. transform	t_o		0.39	0.58	0.39	0.47
Aver. plasma radius	r_p	$[m]$	0.2	1.75	1.6	1.6
Distance to coils	Δ	$[m]$		> 1.8	2.1	1.2
Average β	$< \beta >$	$[\%]$		5	5	5
Fusion power	P_f	$[GW]$		3.6	4	4
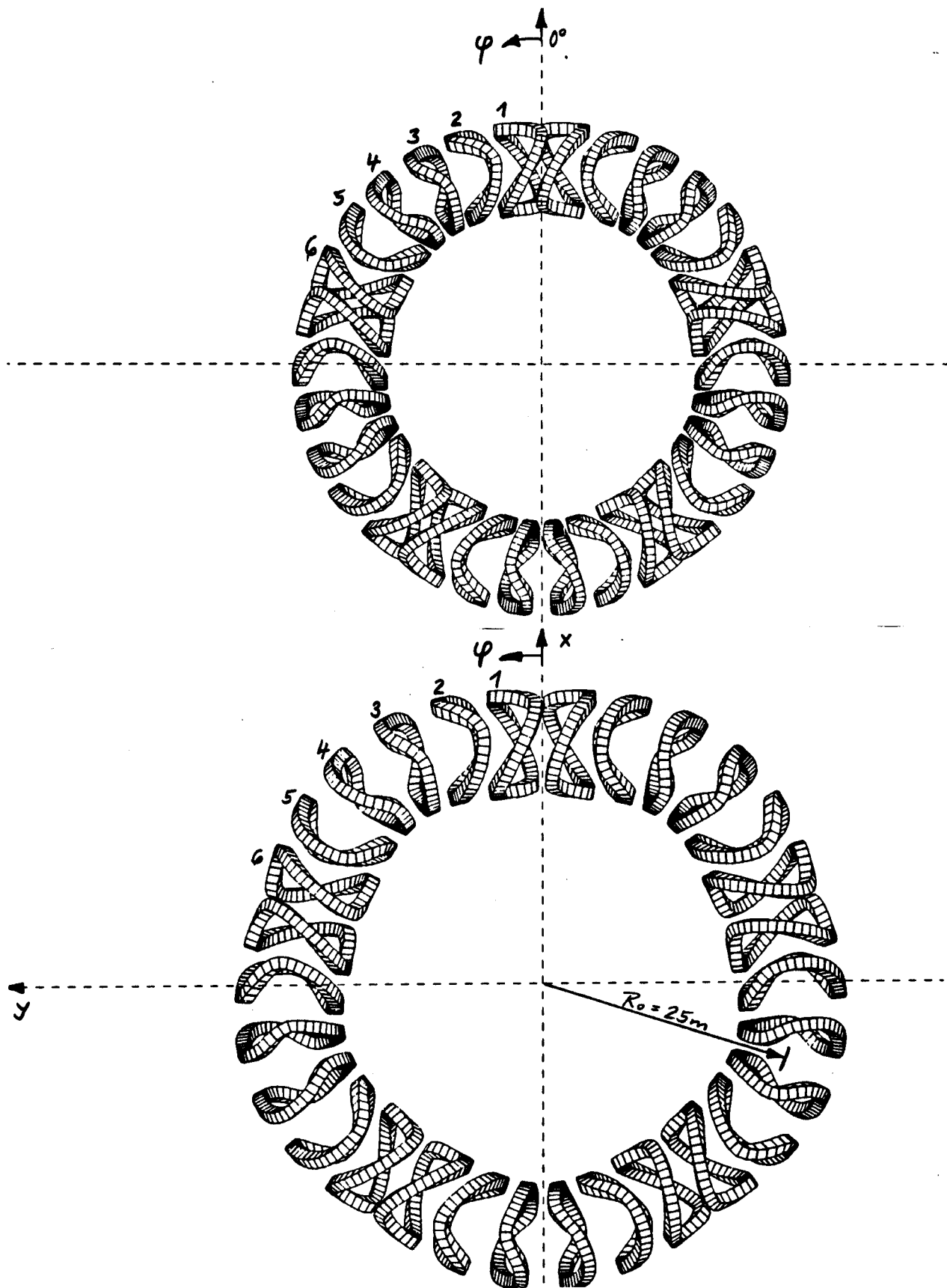
Fig. 3-6: Top view on winding packs for the coil sets
of ASRA6C (upper part) and ASRA6B (lower part)
shown in the same scale.
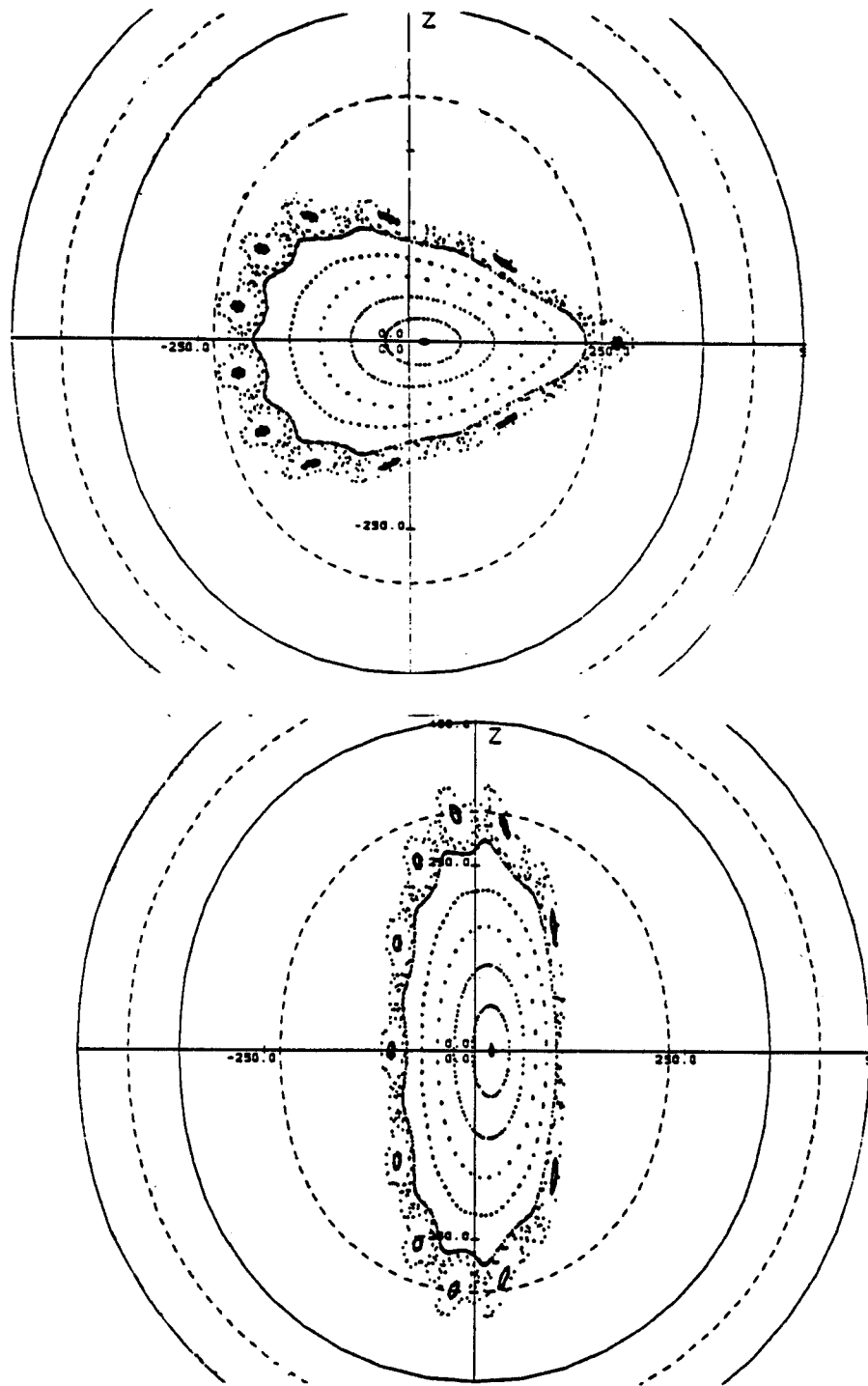
Fig. 3-7: Advanced Stellarator Reactor ASRA6C.
Coil shape and nested system of magnetic vacuum field
at toroidal angles 0 and 1/2 of the field period.
Outside of the last closed flux surface an "ergodic" region
is present with magnetic islands at $t = 5/11$.
The inner dashed line is at a distance $\Delta = 1.2\,m$ from coil bore.
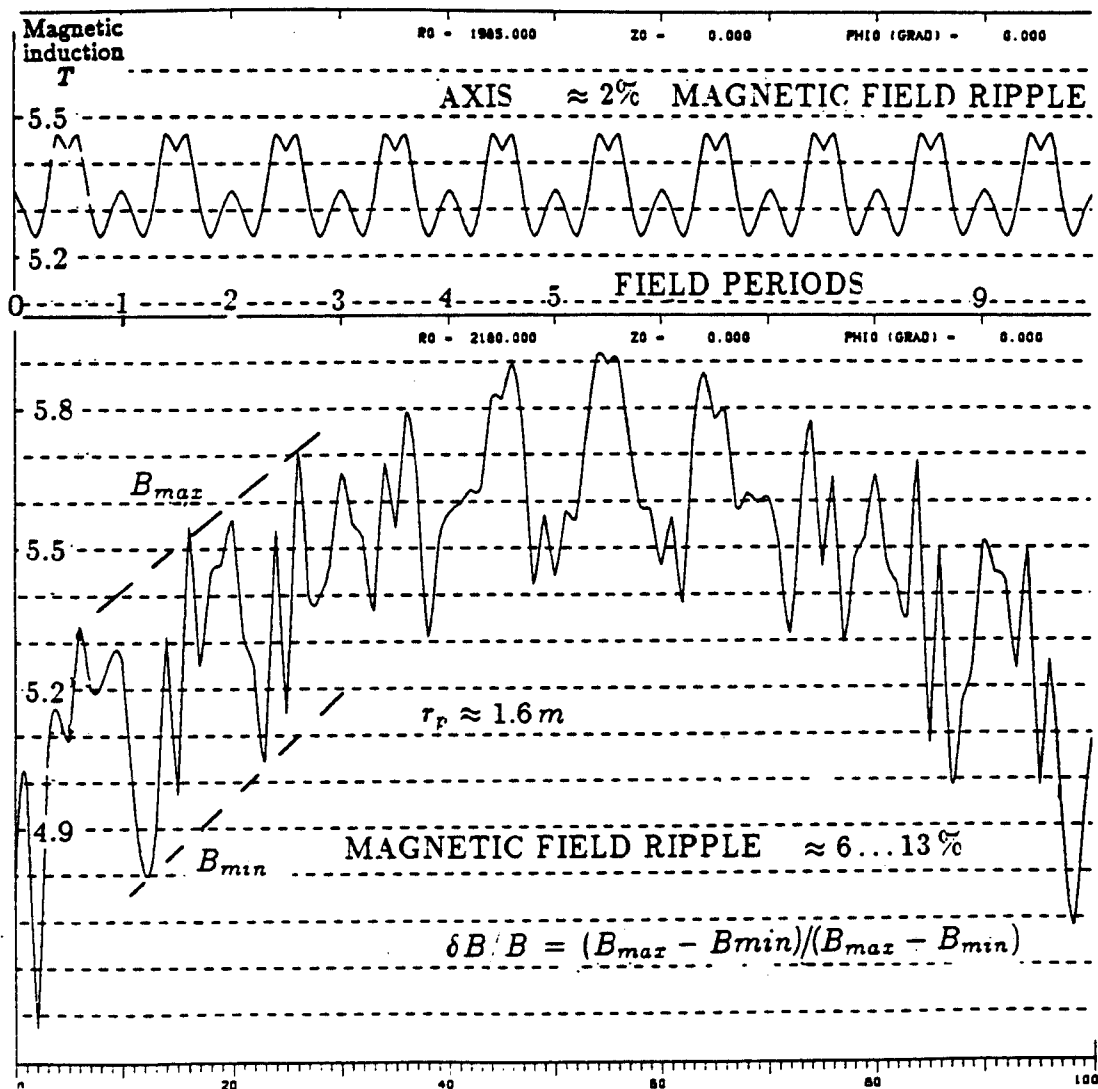
Fig. 3–8: Magnetic induction along the axis (top)
and for the last closed surface of the vacuum field (bottom)
for ASRA6C with 6 coils per field period,
showing a magnetic ripple of 2 % near the axis
which increases to 6 to 13 % for the last closed surface.
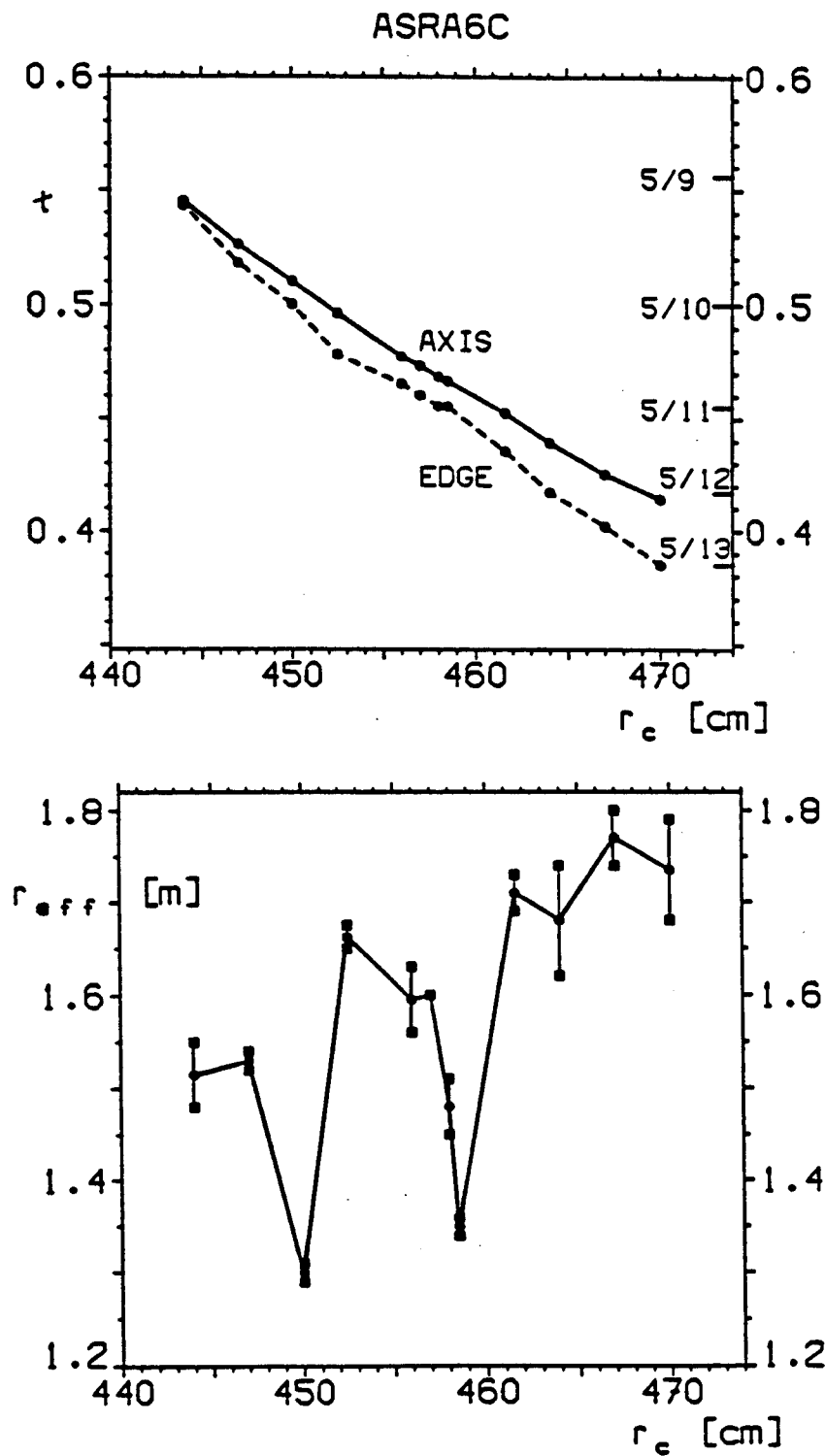
Fig. 3-9: Dependence of rotational transform ι on the coil radius
for the data set ASRA6C (top)
and effective radius of the last closed surface (bottom).
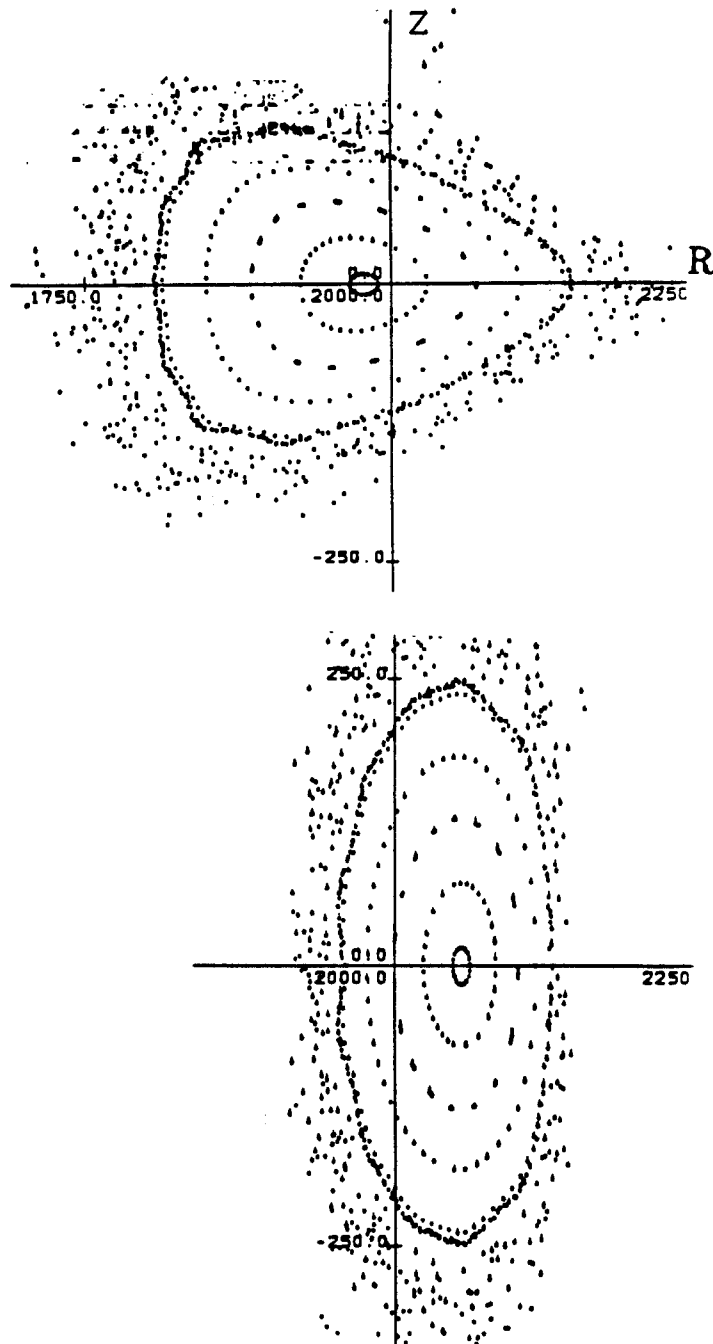
Fig. 3–10: ASRA6C with superimposed horizontal perturbation field
$\overline{B_y/B_o} = 0.2\%$.

3.5. Finite–Beta Fields in ASRA6C

Magnetic field computations for a finite value of the plasma pressure are done so far for one of the reference configurations, ASRA6C, up to values of the average plasma pressure normalized by the magnetic field energy density, $< \beta > \approx 5\,\%$. As is shown in Chapter 4, an average $< \beta > \approx 5\,\%$ is typical for the operation regime of the reactor.

The shapes of the magnetic surfaces of the vacuum field and at $< \beta > = 4.7\,\%$ are shown in Fig. 3–11 at toroidal positions of the beginning, one quarter and one half of a field period. The solid curve of the vacuum field contours is used as a fixed boundary for the computations. At finite β–values, the inner surfaces and especially the magnetic axis are radially shifted. This axis shift (Shafranov–shift) amounts to about 50 % of the average minor radius. Such a value of the axis shift is regarded as determining the upper limit of the equilibrium–β. A parabolic pressure profile is used in the computations presented here.

In addition to the radial Shafranov–shift, a slight helical offset of the magnetic axis is also visible. The magnitude of the axis shift is obtained by varying the number of grid points used in the code and extrapolating to zero mesh size, see Fig. 3–12. Here, three curves are shown for different peak values of $\beta_o = 1.9, 3.7,$ and $6.9\,\%$; the point marked by 'x' corresponds to the result of the previous figure.

The upper part of Fig. 3–13 shows the dependence of this radial shift versus the peak value of β_o. Simultaneously, a considerable deepening of the magnetic well is obtained, as shown in the lower part of the figure. The dashed curves give the result of a net current free computation, whereas the solid curves apply for a flux conserving case, yielding nearly the same results. A difference is seen in the radial profile of the rotational transform, $t(r)$, as demonstrated in Fig. 3–14. In the flux conserving case, the initial profile of the rotational transform of the vacuum field with low shear is maintained, whereas the net current free computations show a decrease of the rotational transform in the region of the plasma edge.

The shift of the magnetic surfaces found in the above computation can be taken as determining a 'soft' limit for the equilibrium–β. Regarding the critical value for stability, β_{stab}, theory predicts lower numbers for this type of configuration. In this respect, interesting new configurations, 'HELIAS', were recently published in [6] and [7], with stable values of $< \beta_{stab} >$ up to $9\,\%$, considering resistive interchange modes. The geometrical characteristics of a HELIAS configuration are a helical magnetic axis and some indentation of the magnetic surfaces at those particular toroidal positions where the toroidal curvature has a maximum. Bean–shaped Advanced Stellarators with a nearly planar magnetic axis are described in [8] . Modular non–planar coils for such configurations are being developed in the studies towards WENDELSTEIN VII–X, the future large Advanced Stellarator experimental device at IPP–Garching .
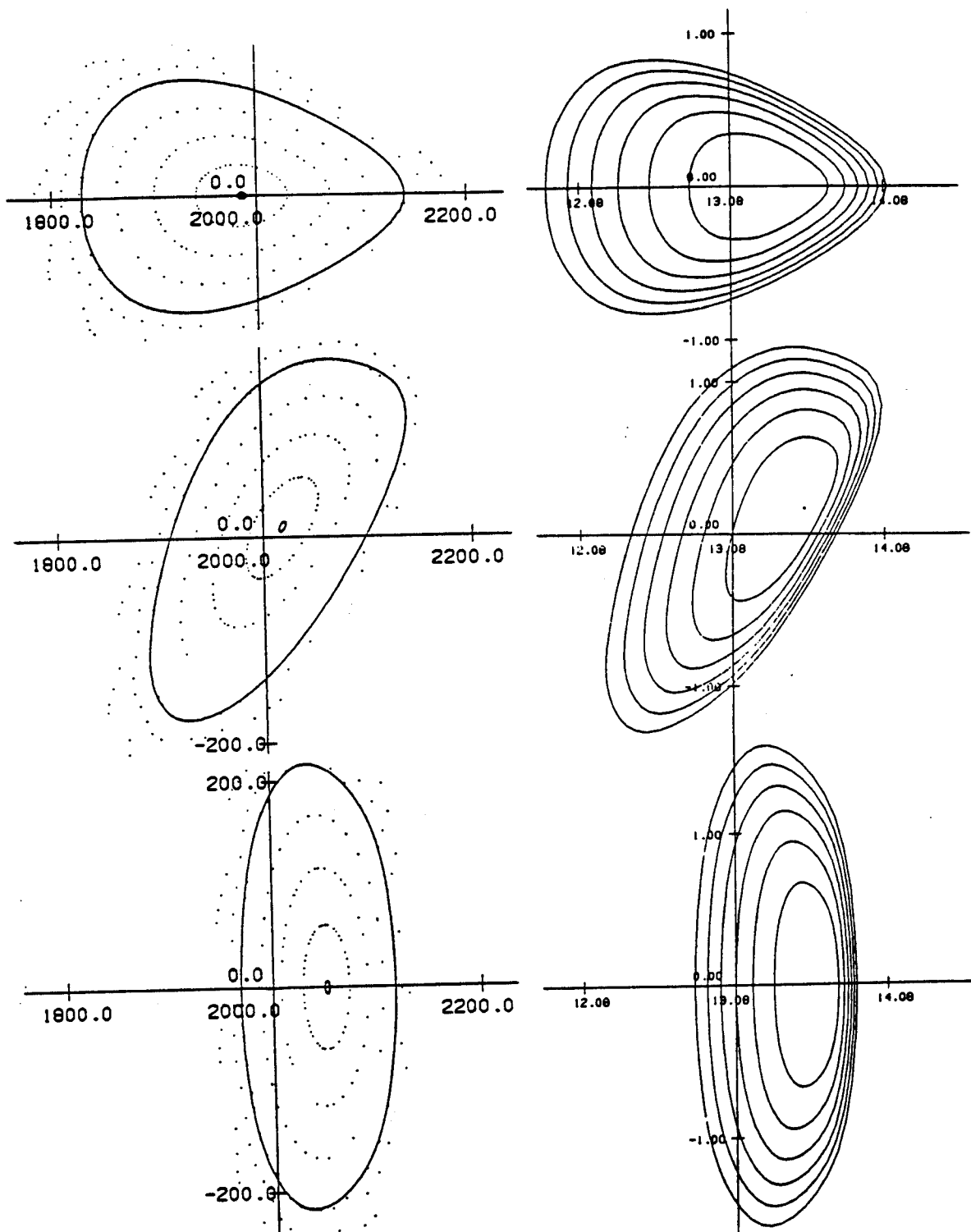
Fig. 3-11: Magnetic surfaces of ASRA6C.

Left part: initial vacuum field with fixed boundary close to separatrix; right part: final configuration at $< \beta_{eq} > \approx 5\%$, showing a value of about 50 % for the Shafranov shift.

Fig. 3-12: Dependence of the axis shift on the grid size
for different peak values of $\beta_o = 1.9$, 3.7, and 6.9%.
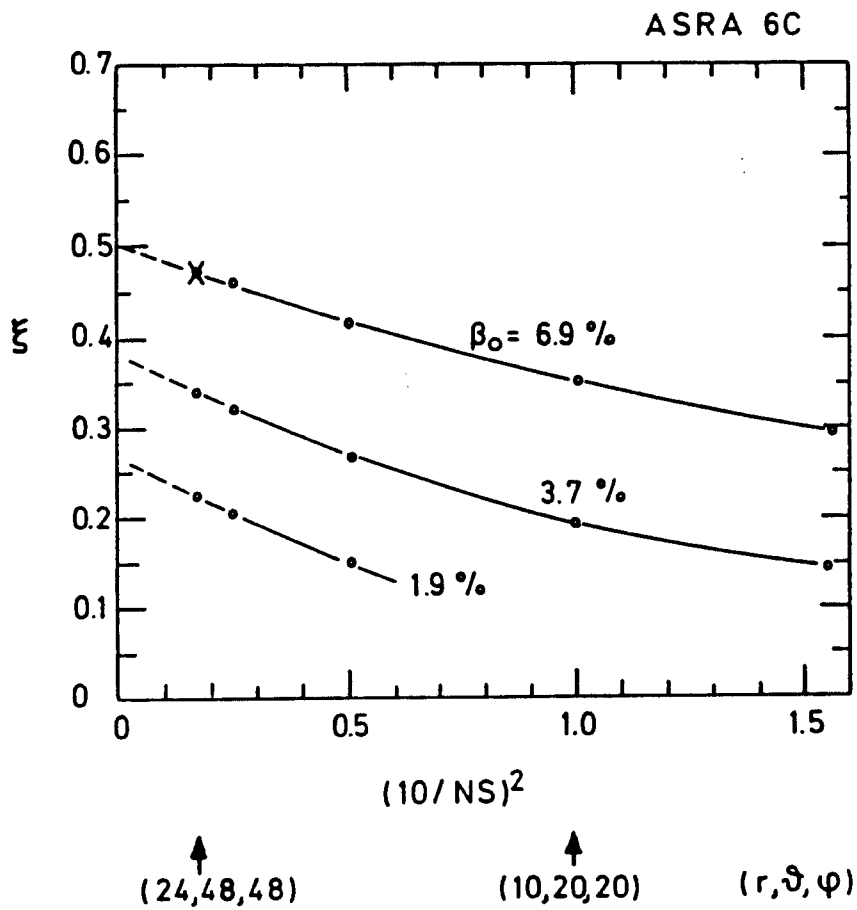The point marked by 'x' corresponds to the result
of the previous figure.
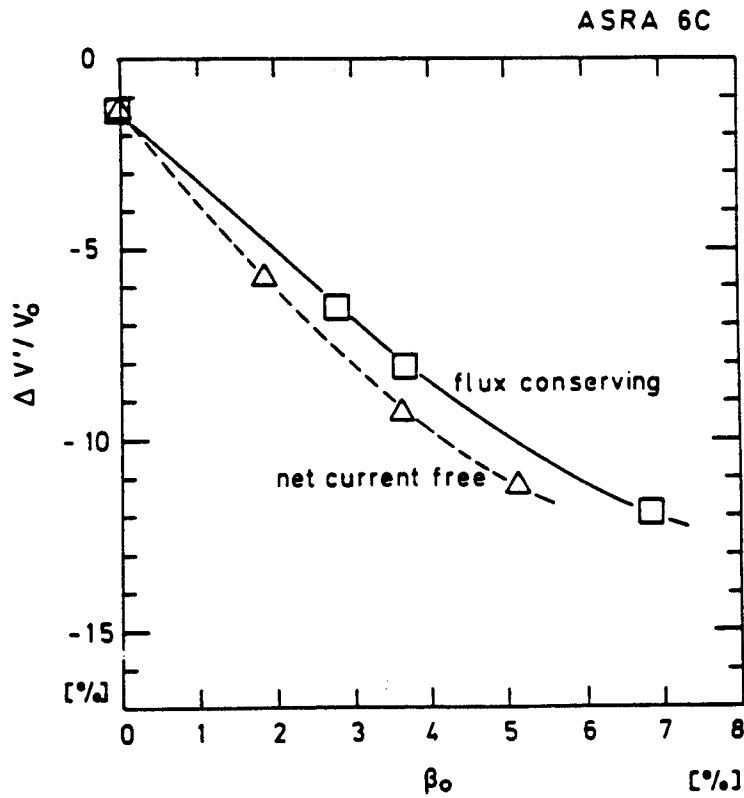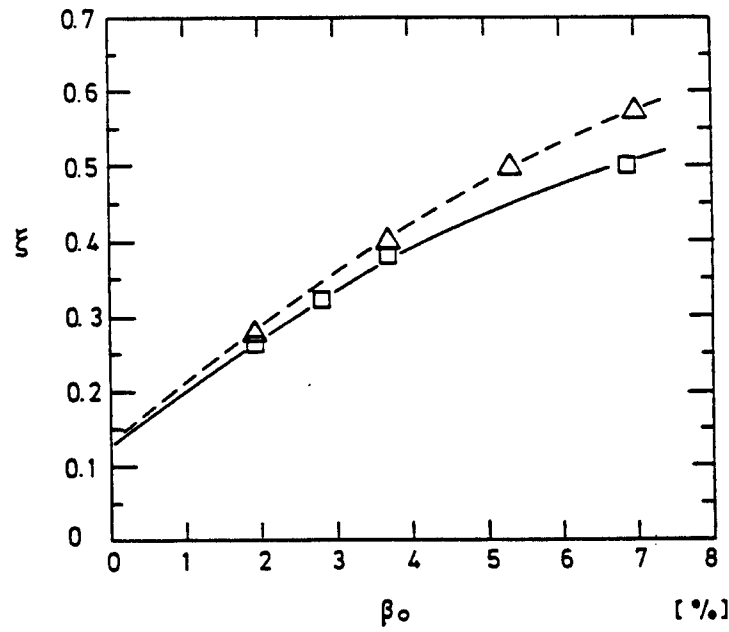
Fig. 3-13: Dependence of the radial axis shift (upper part) on β_o and considerable deepening of the magnetic well (lower part). Dashed curve: result of a net current free computation; the solid curve is a flux conserving case with nearly identical results.

ASRA 6C
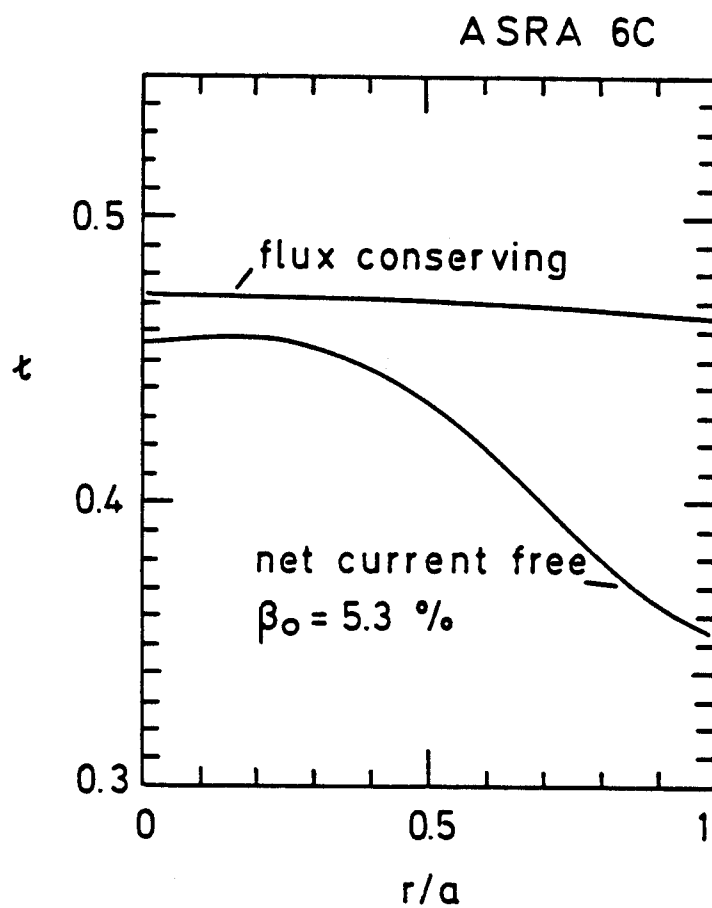
Fig. 3-14: Radial profile of the rotational transform ι.
Flux conserving and current free computations,
a is the average minor radius of the fixed boundary.

3.6. Summary and Conclusions

For magnetic field studies for Advanced Stellarator Reactors and Burner systems numerical and analytic relations for the positions and contours of the non–planar coils are used. Starting from topologies similar to those of the Garching Advanced Stellarator experiment WENDELSTEIN VII–AS, considerable progress is made in the two data sets ASRA6B and ASRA6C regarding the simplicity of the coil system.

The compact system ASRA6C is obtained by reducing the size of ASRA6B from a value of the major radius from $R_o = 25\,m$ to $20\,m$, correlated with a change of the magnetic energy from $W_m = 193\,GJ$ to a value of $117\,GJ$. This reduction of system size is made possible by use of a modern approach of a thin blanket with appropriate reflector and shield. Using the same average current density in the coils of both data sets and adjusting the same average induction at the magnetic axis, the peak field at the coils is moderately reduced in ASRA6C. The minor plasma radius remains unchanged.

Magnetic field computations at finite plasma pressure are done for ASRA6C at an average $< \beta >$ up to $5\,\%$, yielding a considerable deepening of the magnetic well and a still tolerable shift of the magnetic surfaces. Regarding the critical β–value for stability, β_{stab}, theory predicts lower numbers for this type of configuration. However, an interesting innovative configuration, 'HELIAS', and also Bean–shaped Advanced Stellarators were recently published. Non–planar modular coils for such systems are being developed. The detailed reactor properties of these new configurations remain to be studied. From the experience gained in the ongoing investigations it can be concluded that such new configurations do not require qualitatively new and differing engineering approaches.

References to Chapter 3

[1]: R. Chodura, W. Dommaschk, W. Lotz, J. Nührenberg, A. Schlüter,
Three–Dimensional MHD Equilibrium Studies,
Proc. Plasma Phys. and Contr. Nucl. Fusion Research Brussels 1980
Vol. I, 807, (1981).

[2]: U. Brossmann, W. Dommaschk, F. Herrnegger, G. Grieger,
J. Kisslinger, W. Lotz, J. Nührenberg, F. Rau, H. Renner,
H. Ringler, J. Sapper, A. Schlüter, H. Wobig,
Concept of an Advanced Stellarator,
Proc. Plasma Phys. and Contr. Nucl. Fusion Research
Baltimore 1982, Vol. III, 141, (1983).

[3]: E. Harmeyer, U. Brossmann, H. Gorenflo, J. Kisslinger,
S. Mukherjee, J. Raeder, F. Rau, H. Wobig,
On Modular Coil Systems of the WENDELSTEIN VII–AS Type
with Reactor Dimensions, IPP Garching Report IPP 2/269 , (1983).

[4]: E. Harmeyer, J. Kisslinger, F. Rau, H. Wobig,
Magnetic Field Studies Near Separatrix,
13th Eur. Conf. on Contr. Fusion and Plasma Heating, **10 C**, 323,
Schliersee, Germany (1986).

[5]: E. Harmeyer, J. Kisslinger, F. Rau, H. Wobig,
A General Winding Law of Modular Stellarator Coils,
IPP Garching Report IPP 2/274 , (1985).

[6]: J. Nührenberg and R. Zille,
Stable Stellarators with Medium β and Aspect Ratio,
Physics Letters 114A, 129, (1986).

[7]: J. Nührenberg, R. Zille, and S. P. Hirshman,
Resistively Stable Stellarator Equibilbria by β Iteration,
8th Eur. Conf. on Comput. Physics, **10 D**, 57,
Eibsee, Germany, (1986).

[8]: F. Herrnegger and F. Rau,
Bean–Shaped Advanced Stellarators with Modular Coil Systems,
13th Eur. Conf. on Contr. Fusion and Plasma Heating, **10 C**, 307,
Schliersee, Germany, (1986).

4. Plasma Engineering

4.1. Introduction

An essential advantage of Stellarators with regard to their prospects for development towards economically competitive fusion reactors is their possibility of steady state operation. This possibility stems from the property of Stellarators to allow plasma start-up from existing magnetic surfaces of the vacuum magnetic field, which provide a stable confinement of plasmas up to a certain value of β, the plasma pressure normalized by the energy density of the magnetic field used for confinement. For the numerical investigation of heating and burn scenarios in Advanced Stellarator Reactor (ASR) and Advanced Stellarator Burner (ASB) systems, steady state conditons are assumed in the burn state. The start-up procedure is treated as a sequence of such steady states, called equilibria, with the external heating power and its radial profile as input. The question of thermal stability of such equilibria remains to be studied in detail, however.

A one-dimensional numerical transport code is used to solve the coupled equations of particle and energy transport (heat conduction and bremsstrahlung) for electrons and ions in the presence of electric fields. The complicated structure of the magnetic fields in ASR and ASB is modelled by an effective ripple ranging from 2 % to about 10 % between the magnetic axis and the edge.

For start-up, an effective heating power of 30 to 50 MW is sufficient. By increased refuelling, ASR is brought up to full power, preferentially at a moderate temperature $T = 12\,keV$ to $15\,keV$ at the plasma center. The fusion power amounts to typically $P_f \approx 4\,GW$ for ASR, whereas ASB stays at about 10 % of this value. For ASR6C, central radiation losses up to 300 MW can be tolerated if the fusion power output is increased by an increased refuelling rate. Particle input fluxes Φ_o of 1.0 to $1.1 \cdot 10^{23}\,s^{-1}$ are required in the two cases without and with radiation, yielding values of the average $<\beta>$ of 5.3 and 6.4 % at a fusion power of 3.8 and 5.6 GW. In a different computation for a radiative power loss of 300 MW near the plasma edge and a refuelling rate of $1.1 \cdot 10^{23}\,s^{-1}$, a total fusion power of 3.9 GW is obtained at an average $<\beta>$ of 5 %. The peak temperature is $T \approx 19\,keV$. In this case the ripple losses are reduced by a factor of two, in order to take account of the improved confinement of an Advanced Stellarator, see [1], and the field is raised to 5.5 T at the axis.

In section 4.2 of this Chapter, the transport model and assumptions made in the one-dimensional code calculations are discussed. In the third section earlier findings [2] are summarized, comparing an ASR with an ASB. In section 4.4, heating and refuelling methods are described. In section 4.5, results are given as obtained for the presently considered reference data set ASRA6C. Radiation losses in addition to bremsstrahlung are considered. The influence of the smaller major radius of ASRA6C, $R_o = 20\,m$, as compared to a previous value of 25 m on the required start-up power and the operation regime is pointed out. In section 4.6, impurity control options are treated, considering pumped limiters and RF impurity control as an alternative. The Chapter ends with summary and conclusions in section 4.7.

4.2. Transport Model and Boundary Conditions

The computations of the start–up and of the burning conditions in ASR and ASB are done with the use of a one–dimensional transport code. The coupled equations of particle and energy transport are solved for neoclassical diffusion and heat conduction of electrons and ions. Corrections to account for the varying shape of the magnetic surfaces are neglected. The system of equations is

$$-\frac{1}{r}\frac{\partial}{\partial r} r\, n\, \chi_e\, \frac{\partial T_e}{\partial r} = Q_e(r) + Q_{e,\alpha} - P_{rad} - P_{ei} \tag{1}$$

$$-\frac{1}{r}\frac{\partial}{\partial r} r n \chi_i\, \frac{\partial T_i}{\partial r} = Q_i(r) + Q_{i,\alpha} + P_{ei} \tag{2}$$

$$-\frac{1}{r}\frac{\partial}{\partial r} r\, D\, \frac{\partial n}{\partial r} = Q_D(r) \tag{3}$$

In these equations χ_e and χ_i are the coefficients of thermal conductivity and D is the particle diffusion coefficient. In our model neoclassical transport coefficients as given by Shaing and Houlberg are used. To the neoclassical terms the anomalous electron thermal conductivity found in ohmically heated plasmas in W VII-A is added [3].

The coefficients of thermal conductivity are given in Fig. 4–1 for ASRA6C at half radius. The abscissa is the inverse collisionality $\lambda t/R$, where λ is the mean free path between collisions, $t = 1/q$ is the rotational transform, with q being the safety factor of a Tokamak with comparable toroidal and poloidal fields and equal major radius R. Four curves at constant temperatures $T = 8$, 10, 13, and $16\,keV$ are entered in each of the four parts of the figures, which apply for electrons (ions) in the left (right) part of the figure; the top half is without radial electric field, in the lower half a normalized field equal to the temperature gradient is assumed. The thermal conductivity increases with temperature at all collisionalities. For electrons there is a continuous increase in the thermal conduction coefficient with $\lambda t/R$, depending on the amplitude ϵ of the magnetic field modulation. This 'ripple' is about 2 % at the magnetic axis of ASRA6C and rises to 6 to 13 % near the plasma edge, see Chapter 3, Fig. 3–8. An edge ripple of $\epsilon_1 = 15\%$ is assumed in the above computation; thus the effect of the trapped particles is overestimated.

The thermal ion conduction coefficient at large values of $\lambda t/R$, decreases again, due to the depletion of the distribution function, since the loss rate of trapped ions is faster than the scattering in velocity space. A loss cone develops in addition to the drift term included in the analytical formula for the ion thermal conduction coefficient.

Note that the radial electric field plays a major role only for the ions in the reactor relevant regime of $\lambda t/R \approx 100-1000$, and effectively reduces the conduction coefficient, typically by a factor of about 5. A larger radial field would yield a still larger reduction. So far, a self–consistent radial electric field, depending on the radial position, such as to locally balance the electron and ion particle loss rates is beyond the scope of our code.

For start–up, electrons and ions are heated by the input powers Q_e and Q_i, respectively. The particle refuelling rate Q_D enters only in the third equation; it is required during start–up and steady state burn. The above quantities are given as radial profiles, peaked either at the center or near the edge. The α–particle heating power to electrons and ions, $Q_{e,\alpha}$ and $Q_{i,\alpha}$, respectively, are obtained from the temperature–dependent reaction rate $< \sigma v >$ of the D–T process. In the transport equations, the quantity P_{ei} is the electron–ion Coulomb interaction, which enters the electron and ion equations with opposite sign. The term P_{rad} in the electron equation consists of the bremsstrahlung, and can be increased by an optional radiative loss simulating the effects of impurity radiation. This radiative loss can be chosen either within the whole cross section or as a radiative layer near the plasma edge, choosing an appropriate radial profile.

The transport code is operated iteratively, starting from an initial radial density profile. Other boundary conditions are fixed values of the electron and ion temperature and density, $T_e(a)$, $T_i(a)$, and $n(a)$, respectively, at the edge radius a. Prompt α–particle losses are neglected. The refuelling rate and its radial profile are essential input data for the stationary burn state. The start–up computations are determined by the applied heating power, in addition to the refuelling.

THERMAL CONDUCTION COEFFICIENTS (CM**2/S)
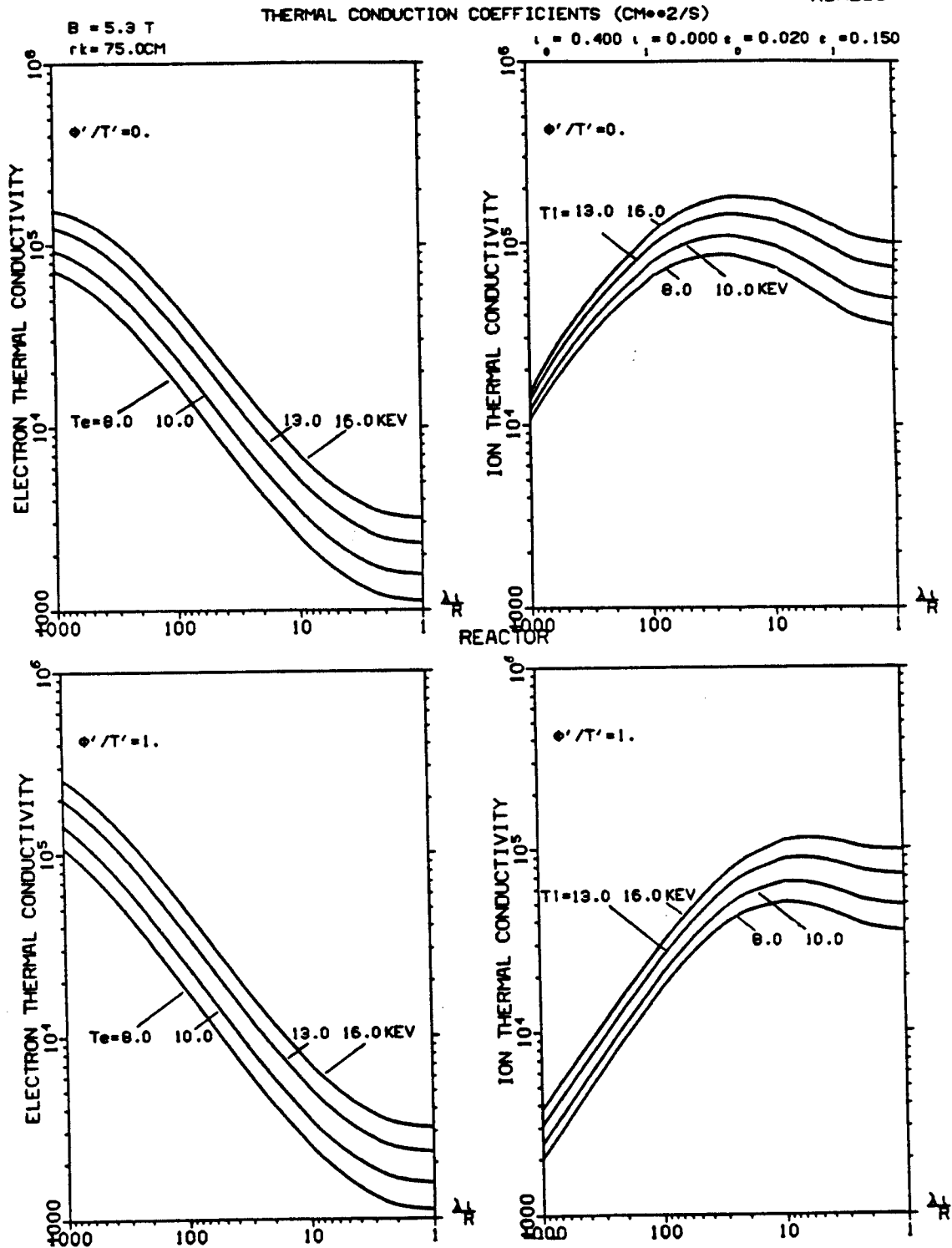
Fig. 4-1: Calculated thermal conductivity coefficients for ASRA6C
versus the inverse collisionality $\lambda t/R$
without and with radial electric field (top and bottom parts),
for electrons and ions (left and right parts), respectively.

## 4.3. Heating and Burn Scenarios for ASR and ASB

Computations of the burning conditions for a typical Advanced Stellarator Reactor (ASR) and an Advanced Stellarator Burner (ASB) are given in [2]. The results of these considerations are summarized here. The following dimensions and fields are used in the systems of ASR and ASB : major radii of $R_o = 25$ and $15\,m$, with plasma radii of $r_p = 1.6$ and $0.9\,m$, at an average magnetic induction of $B_o = 5.3$ and $7.0\,T$, respectively.

Using the transport code with a radial electric field and an effective helical ripple of 2 % amplitude at the axis and 7 % at the plasma edge, a net heating power of $30\,MW$ is found for ASR, as well as for ASB, to reach ignition. This is shown in the lower part of Fig. 4-2 for ASR. Curves of constant heating power are shown which cross a saddle point near $20\,MW$ coupled to the plasma. At ignition, the fusion power amounts to $P_f = 0.6$ and $0.4\,GW$, in ASR and ASB, respectively, at values of the average β of about 2 and 2.5 %. At these comparatively low β-values the neutron load on the first wall is still moderate. In ASR the ports for the start-up power can be closed after ignition and the neutron streaming reduced.

The reactor power is increased by raising the input flux of particles, e.g. of injected pellets. Two different scenarios are envisaged, central refuelling and a refuelling profile which is peaked near the plasma edge.

In the top left part of Fig. 4-2, several radial profiles are given: in the left part the electron and ion temperatures T_e and T_i, and in the right part the density n and the refuelling rate Q_d, respectively. The refuelling is peaked at the plasma center. The curves pertain to the ignited state of ASR. Increasing the refuelling rate for a central deposition profile raises the temperatures, and thus the fusion output to values above $P_f > 3\,GW$. As demonstrated in the upper right part of Fig. 4-2, a refuelling profile peaked near the edge of ASR broadens the density profile and allows for a power production of $P_f = 3.2\,GW$ at temperatures close to those of the ignition state with central refuelling. Increasing the refuelling rate to a value of $\Phi_o = 3 \cdot 10^{23}\,s^{-1}$ brings the system to full power $(3.6\,GW)$ at average temperatures of $T_i = 10\,keV$ and $T_e = 12\,keV$ for ions and electrons, respectively. The average β amounts to 5.3 %. The power flow diagram of this state is given in Fig. 4-3 at an average density of $1.4 \cdot 10^{20}\,m^{-3}$.

Thus, a change of the radial deposition of refuelling constitutes a viable option for increasing the power of the reactor after ignition without an essential temperature rise. This is done by adjusting the pellet velocity or the pellet size, and keeps the neoclassical heat conduction losses limited.
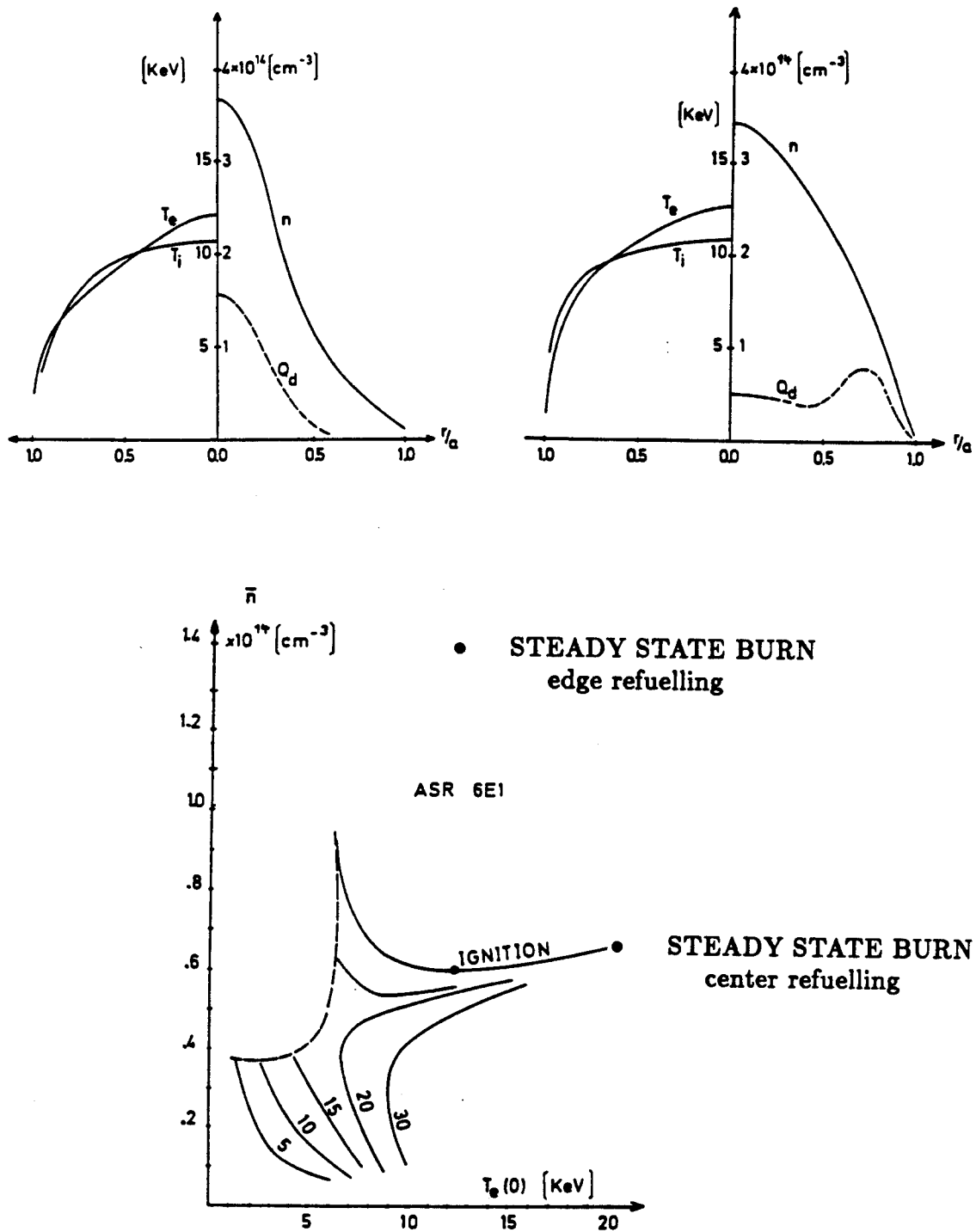
Fig. 4-2: Profiles of temperature and density in ASR
for different radial refuelling at ignition
and burn states (upper left and right parts)
and heating scenario (lower part)
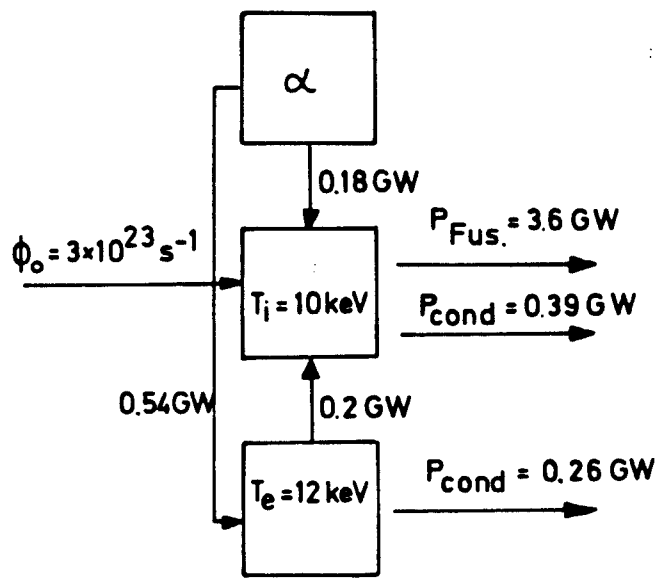
Fig. 4-3: Power flow diagram for ASR as given in [2].

4.4. Heating and Refuelling Methods

The plasma engineering methods envisaged for heating and refuelling of the plasma in ASRA6C are ion cyclotron heating and/or neutral particle injection, and pellet injection, respectively. Since there exists far more experience in the WENDELSTEIN team at Garching with neutral injection as the heating method, ion cyclotron heating will not be discussed in the following, although smaller penetrations through the blanket and shield might be possible.

A target plasma in ASRA6C is to be produced by electron cyclotron waves at a frequency of $150\,GHz$, compatible with the electron cyclotron resonance for $B_{res} = 5.3\,T$, which is equal to the magnetic induction on the axis in ASRA6C. Plasma build–up and heating with an electron cyclotron resonance system has been tested successfully in the small stellarator experiment WENDELSTEIN VII–A at an induction of $B = 2.5\,T$ up to the cut–off density of $n \approx 6 \cdot 10^{19}\,m^{-3}$, using a gyrotron of $200\,kW$. It was possible to raise the stored plasma energy by subsequent application of neutral beam heating of about $1\,MW$. Heating of the ASRA6C plasma by neutral beams with a power of $P_i = 30$ to $50\,MW$ requires typically 4 to 6 injector systems with a power of $8.4\,MW$ in each unit, similar to that of the neutral injectors used in the JET tokamak. A schematic for the ASRA6C neutral injection scheme is shown in Fig. 2–9 and Fig. 2–10 of Chapter 2. The injection is at a cross section where the magnetic surfaces have the smallest radial dimension of about $80\,cm$ between the magnetic axis and the plasma edge. This value is comparable with the penetration length of neutral particles at an injection energy of 70 to $80\,keV$, as is presently being used in the JET neutral injection system. For ASRA6C, beam ducts of a typical size of $1.8\,m$ height and $1\,m$ width are estimated from the dimension of the sources and their beam divergence.

An important advantage of stellarator fusion reactors is that they allow steady state operation in principle. Ignition in an Advanced Stellarator reactor occurs preferentially at a low to moderate β–values of the plasma, as demonstrated in the preceding section. Then the fusion power is low, hence the neutron load and damage of the injection systems are considered to be tolerable. After reaching ignition, the start–up power can be turned down and appropriate shielding are introduced into the respective ports, in order to avoid problems of neutron streaming. Such movable shielding plugs are omitted in the above figure. The shielding of the neutral injection ports without such plugs is analyzed in Chapter 6.4 .

The density increase and the continuous refuelling of the ignited plasma is conceived to be done by pellet injection. The pellet injectors are also to be placed at the toroidal position where the magnetic surfaces have a small radial dimension. The pellet velocity should be matched to a deposition outside but near the axis of the ignited low–β plasma. By increased refuelling the density is increased and the deposition profile is shifted towards edge refuelling as discussed in the above section. The reactor is thus brought to full power. Then particle fluxes of the order of $\Phi = (1 - 3) \cdot 10^{23}\,s^{-1}$ are calculated. The necessary penetrations in the blanket and shield systems are comparatively small. Several pellet injection systems might have to be provided, since the particle fluxes are above those achievable at present. Development is required

regarding the pellet velocity, possibly also regarding an adjustment of the velocity during the transition from the ignited state to the full power operation of the reactor.

4.5. Results for the Reference Case ASRA6C

In [2], heating and burn scenarios for a system with $R_o = 25\,m$ as well as for an Advanced Stellarator Burner with $R_o = 15\,m$ at an increased magnetic induction were published, as described in the above sections. More recent results are given in this section for ASRA6C, including also the effect of an additional radiative loss. These findings are summarized in Table 4-I and are elaborated in more detail in the following. The smaller major radius of the data set ASRA6C, $R_o = 20\,m$, introduces a more difficult situation regarding start–up and stationary burn of the reactor.

In Fig. 4-4, upper part, the relation between the fusion power output and the peak values of $\beta(0)$ are given versus the axis values of density and temperature. The middle and lower parts of the figure show the dependence of these quantities on the external heating power P_i of start–up. In the middle part of the figure, the magnetic field is $B_o = 5.3\,T$, and the ripple losses are as given in [2], with a magnetic ripple amplitude up to about 10 %, as to be seen in Chapter 3, Fig. 3-8. Under these circumstances, ignition is possible at an effective heating power $P_i \approx 50\,MW$ with center densities of $N(0) \approx 3 \cdot 10^{14}\,cm^{-3}$, and temperatures of $T_i(0) \approx 10\,keV$, respectively. A full power operation point is found at a particle input flux $\Phi = 1 \cdot 10^{23}\,s^{-1}$, characterized by an average β of 5.3 % and a fusion power of $P_f = 3.8\,GW$. This data point is labelled '400' in the middle part of the figure. Introducing an additional radiative loss with a broad centered profile and amounting to $P_{rad} = 0.3\,GW$, the fusion power is to be increased to $P_f = 5.6\,GW$ at an average $\beta = 6.4\,\%$, by an increased input flux $\Phi = 1.1 \cdot 10^{23}\,s^{-1}$, as shown by the point marked '406'. Such radiation losses with a centered broad distribution should be avoided in order to keep the total power output within reasonable limits.

In the lower part of Fig. 4-4, the improved confinement properties of an Advanced Stellarator are modelled by a reduction of the ripple losses by a factor of 2. The magnetic field is also varied to values of 5.0 and 5.5 T, the larger field being indicated by the dashed curve. In these cases, an effective heating power of 30 MW is sufficient to reach ignition, as is the case with the larger systems at $R_o = 25\,m$. In ASRA6C with reduced ripple losses, ignition occurs at a peak ion temperature of about $10\,keV$ and central densities around $2.2 \cdot 10^{14}\,cm^{-3}$, with little dependence on the magnitude of the magnetic field.

Two examples of the various operation points for ASRA6C are shown in the Figures 4-5 and 4-6, using input rates of $\Phi_o = 0.9$ and $1.1 \cdot 10^{23}\,s^{-1}$, respectively. The first case is without radiation; in Fig. 4-6 a radiative loss of 300 MW is assumed near the boundary, as to be seen in the lower right of the figure. In the lower right part of Figures 4-5 and 4-6, the two other curves indicate the α–particle heating power densities to ions and electrons, respectively. Due to the larger electron heat conduction, $Q_{e,\alpha} > Q_{i,\alpha}$. The radial profiles of the thermal conduction coefficients are given in the upper right part of the figures. The largest contribution is by the ripple term,

whereas the anomalous coefficient found in the W VII-A experiments is important only at the plasma edge.

For the two examples shown in the Figures 4-5 and 4-6, the total fusion power amounts to $P_f = 2.0$ and $3.9\,GW$ with average β–values of 3.6 and 5 %, respectively. The density and temperature profiles (upper and lower left part of the figures) are comparatively broad and reveal steep gradients near the plasma edge, set at $r_p = 1.5\,m$. Peak values are 2.1 and $2.3{\cdot}10^{20}\,m^{-3}$ for the density, and $T = 15\,keV$ to $19\,keV$ for the temperatures, respectively, as can be seen in the left parts of the figures. The data point with the radiative loss of 300 MW at a fusion power of 3.9 GW is labelled '372' in the lower part of Fig. 4-4. The average value of $\beta = 5\%$ agrees well with the computed $\beta_{eq} = 4.7\%$ for the finite–β fields of ASRA6C , see Chapter 3.5.

Note that the edge physics in laboratory or fusion reactor plasmas is not described by the equations used in the transport model. If one assumes a pumped limiter system, assisted by an efficient radiative outer layer, other terms are to be included. Furthermore, the electric field, which ensures equal particle loss rates of electrons and ions for all radial positions, is not yet treated selfconsistently. The three–dimensional topology of the stellarator fields, modified by the Shafranov–shift at the different finite β–values of the start–up and burning plasma states, introduces further geometrical corrections. Furthermore, the thermal stability of these operation points needs to be analysed.

TABLE 4-I

Results of the Transport Code for ASRA6C :

job no.	Φ_o 10^{23} s^{-1}	$T_e(0)$ keV	$T_i(0)$ keV	$n(0)$ 10^{20} m^{-3}	$\beta(0)$ %	$\langle\beta\rangle$ %	$\langle n\rangle\tau$ 10^{20} $m^{-3}s$	P_α GW	P_f GW	P_{rad} MW	B T	f_χ
400	1.0	15.1	13.7	3.2	13.3	5.3	1.75	0.75	3.80	0	5.3	1.0
406	1.1	15.7	14.6	3.7	15.8	6.4		1.13	5.63	300	5.3	1.0
161	1.2	15.8	15.3	3.0	13.2	5.1	1.44	0.57	2.83	0	5.3	1.0
355	0.8	14.3	13.1	2.2	9.2	4.0	1.95	0.33	1.64	0	5.0	0.5
383	0.4	12.0	10.7	2.0	6.0	2.5	2.76	0.16	1.60	0	5.5	0.5
392	0.7	14.8	13.6	2.0	7.7	3.2	1.89	0.30	1.52	0	5.5	0.5
391	0.9	16.0	15.4	2.1	8.8	3.6	1.63	0.40	2.02	0	5.5	0.5
393	0.9	16.6	16.0	2.2	9.4	4.0	1.59	0.49	2.45	100	5.5	0.5
388	0.9	17.5	17.2	2.3	10.5	4.7	1.53	0.68	3.38	300	5.5	0.5
387	1.1	18.4	18.9	2.3	11.4	5.0	1.38	0.78	3.88	300	5.5	0.5

Legend :

The different computations are labelled by a three-digit job number in the first column of the Table. The following symbols are used in the other columns:

Φ_o : refuelling flux, peaked near the edge;

$T_e(0)$, $T_i(0)$: axis values of electron and ion temperature, respectively;

$n(0)$, $\beta(0)$: axis values of density and plasma pressure, respectively;

$\langle\beta\rangle$, $\langle n\rangle\tau$: average values of β and density times confinement time, respectively;

P_α , P_f , P_{rad} : powers of α-particles, fusion output, and radiative loss,

B : average magnetic induction in the plasma

f_χ : multiplication factor of heat conduction loss.
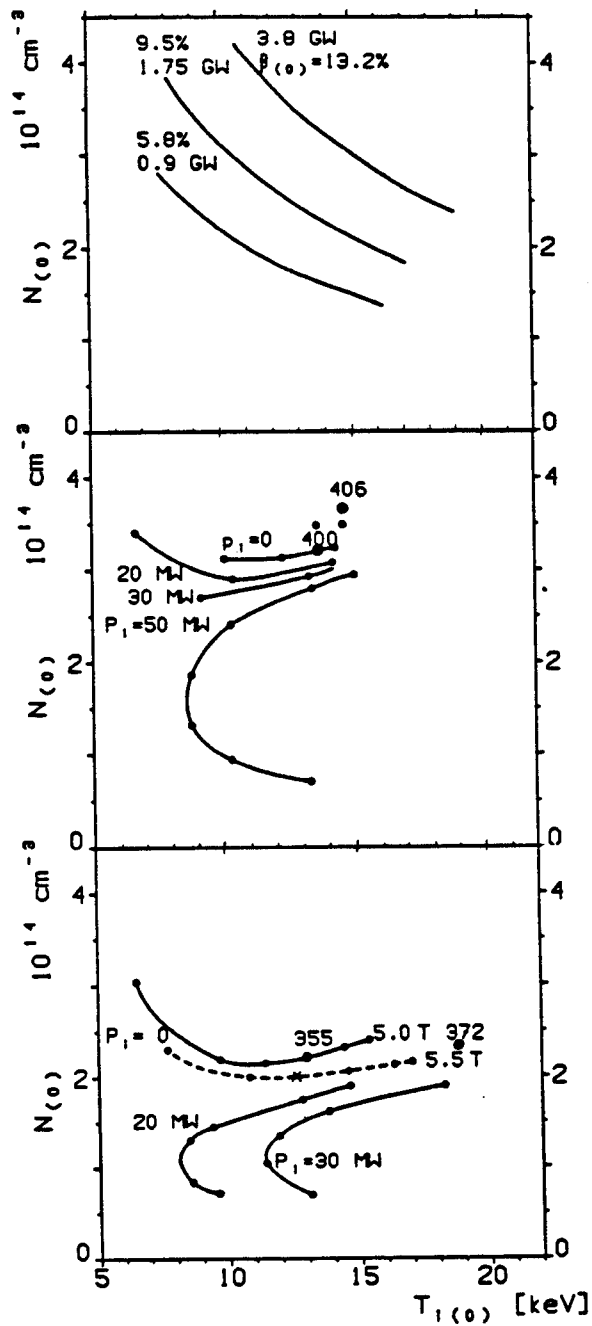
Fig. 4-4: Heating and burn scenarios for ASRA6C;
   top part: fusion power and center values $\beta(0)$;
   middle and lower parts: curves of constant external power P_i
   at full and reduced value of the ripple heat conduction
   coefficient; several operation points are indicated.

DENSITY PROFILES (10**13CM**-3)
INITIAL DENSITY_ _

$\Phi_o = 0.9 \cdot 10^{23} s^{-1}$

$< \beta > = 3.6\%$

$P_{th} = 2.0\,GW$

THERMAL CONDUCTION COEFF. (CM**2/S)

TEMPERATURE PROFILES (KEV) μ 2.5
IONS —— , ELECTRONS – – –   ň 2.30E+14

HEATING POWER (W/CM**3)
IONS —— , ELECTRONS – – –   LAMBDA 90.0

$P_{rad} = 0$
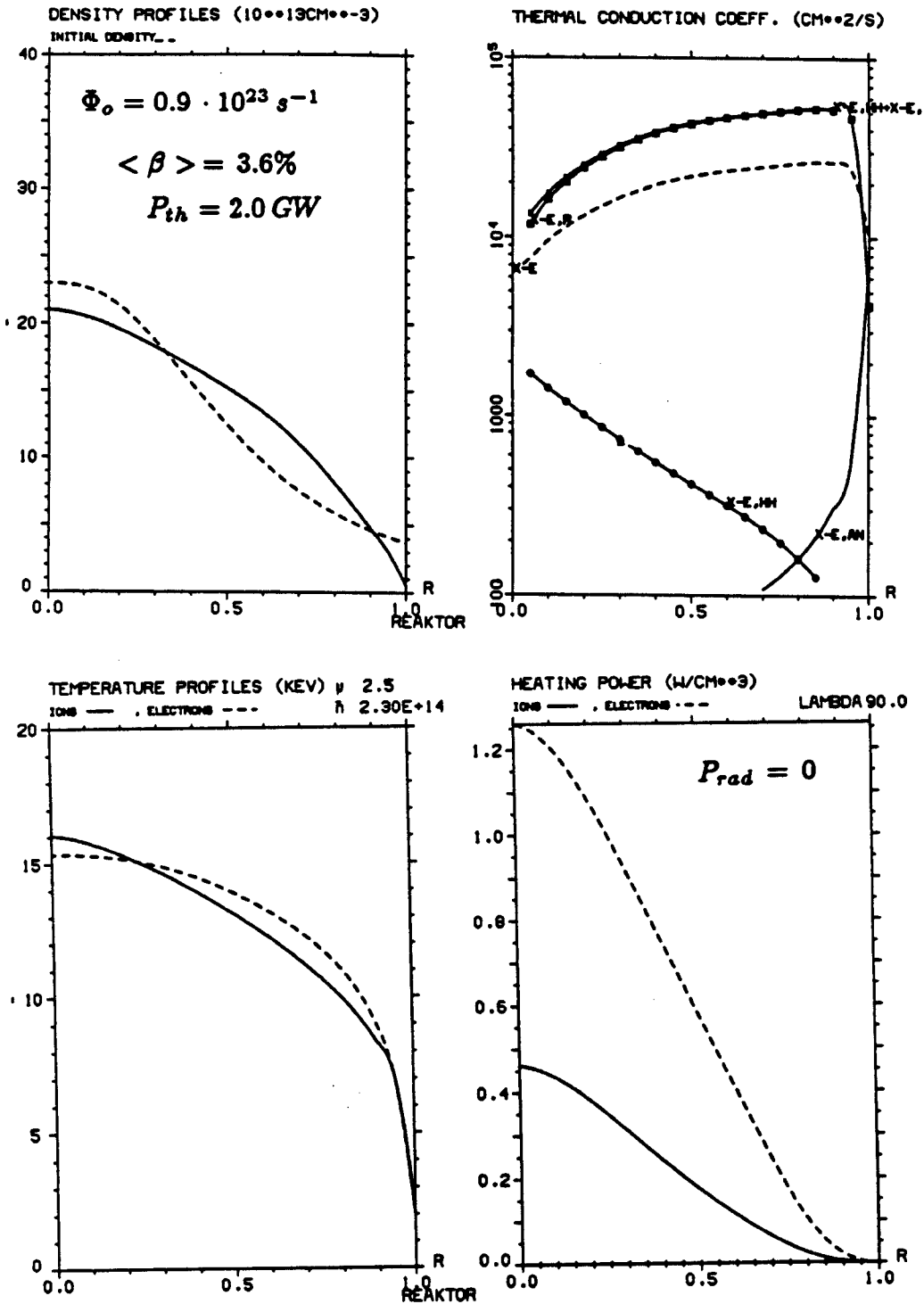
Fig. 4–5: Radial profiles for ASRA6C operated at $P_f = 2.0\,GW$.
Top left: initial (dashed) and final densities;
lower left: electron (dashed) and ion temperatures;
top right: thermal conduction coefficients;
lower right: electron (dashed) and ion heating powers.
Radiatvive losses: only bremsstrahlung.

DENSITY PROFILES (10••13CM••-3)

INITIAL DENSITY _

$$\Phi_o = 1.1 \cdot 10^{23}\, s^{-1}$$

$$<\beta> = 5.0\%$$

$$P_{th} = 3.9\, GW$$

THERMAL CONDUCTION COEFF. (CM••2/S)

TEMPERATURE PROFILES (KEV) µ 2.5

IONS —— , ELECTRONS – – –   ħ 2.30E+14

RADIATION DENSITY (W/CM••3)
HEATING POWER (W/CM••3)

IONS —— , ELECTRONS – – –   LAMBDA 90.0

$$P_{rad} = 300\, MW$$

Fig. 4–6: Radial profiles for ASRA6C operated at $P_f = 3.9\,GW$;
  $300\,MW$ radiation included beyond bremsstrahlung,
  as indicated by the radial profile in the lower right part.
  Other items of the figure are as in Fig. 4–5.

4.6 Impurity Control Options

Impurity control studies for ASRA6C have focused on the development of a system which provides for the following requirements: 1) Adequate removal of the heat transported across the last closed magnetic surface by the escaping plasma, 2) pumping of helium produced in the reacting plasma, 3) minimal production of impurities by sputtering at a target plate where the ions leaving the plasma are neutralized, and 4) shielding of the core plasma from incident impurities and fast D and T atoms. In addition, we have investigated RF techniques for actively removing impurities from the core plasma as an additional method of impurity control. In Section 4.6.1 we consider the plasma outside the last closed magnetic surface and its interaction with a target plate with the resulting recycling of neutral gas and the requirements for vacuum pumping. In Section 4.6.2 RF techniques for impurity control are considered.

4.6.1 The Edge Plasma

The magnetic field topology outside the last closed surface of ASRA6C has been shown in Section 3.3 to be "ergodic" with some indications of weak magnetic i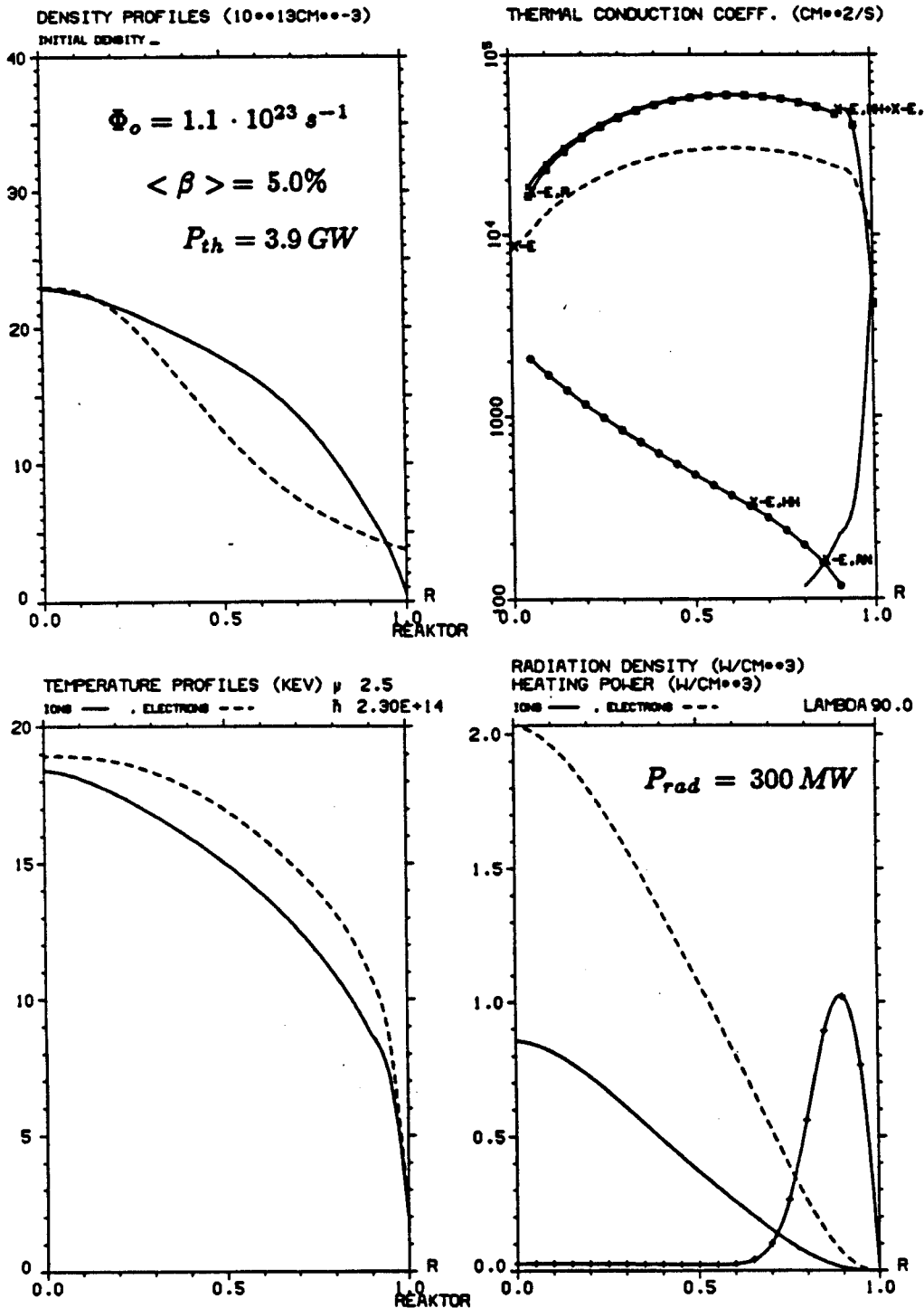slands. The islands, however, are believed to be sensitive to magnetic field errors caused by plasma currents and/or small errors in magnetic coil manufacture and assembly. These errors would erode the islands further and lead to increased ergodic behavior of the magnetic field. For the impurity control studies, we have therefore considered the edge magnetic field to be ergodic in a region about 20 cm wide just outside the last closed magnetic flux surface.

Ergodic magnetic limiters[1] have been considered for tokamaks as a way of spreading the charged particle power over a large surface area. If the 760 MW of alpha power in ASRA6C were spread uniformly over the surface of the first wall, the resulting heat load would be 30 W/cm^2, which exceeds the limit of about 20 W/cm^2, imposed by the maximum temperature of the first wall. Consequently, with the present blanket design, at least 40% of the power (charged particle plus radiation) escaping the plasma must be directed to surfaces designed to take a high heat flux. This leads us to consider an edge plasma which impinges on a target plate, as in the usual divertor or limiter, and operates in a high recycling mode so that the plasma at the target plate is cool ($\sim$ 10 eV) and dense. Production of impurities by sputtering is minimized by the resulting low sheath potential and pumping of neutral gas is enhanced because the localized recycling leads to high neutral pressure in the vicinity

of the pump ducts. The edge plasma can shield the core plasma from incident neutral particles and impurities if it is sufficiently dense. Unlike a tokamak, the edge plasma is in an ergodic magnetic field which enhances radial transport in the edge region and reduces the peaking of the heat flux on the target plates.

The plasma temperature at the target plate is determined by the power input P_H to the edge plasma, the power radiated in the edge plasma, the amount of recycling, and the sheath boundary condition at the plate. We define the recycle ratio R to be the ratio of the ion flux hitting the target plate to the ion flux Γ_H out of the core plasma. In the discussion we treat P_H to be a parameter varying from 50% to 100% of the alpha power (this can be influenced by the amount of impurity radiation coming from the core plasma), but restrict Γ_H to the core refueling rate of 1.2×10^{23} ions/s. A power balance on the edge plasma yields the equation,

$$P_H = [2\,T_b + 5.5\,T_b(1 - R_e) + W_i + R_n a_f(1.5\,T_b)$$

$$(4.6\text{-}1)$$

$$+ (1 - R_n)\,a_m(T_b + \tfrac{1}{3}\,E_{FC})]\,R\Gamma_H + W_{ex}(R - 1)\,\Gamma_H$$

where T_b is the plasma temperature at the plate, R_n and R_e are the particle and energy reflection coefficients, respectively, for ions hitting the plate at energy $5.5\,T_b$ (this includes the effect of acceleration across the sheath evaluated for a D-T plasma), a_f and a_m are the albedo for fast atoms and molecules incident on the plasma, W_i is the ionization potential and W_{ex} is the energy lost[2] by atomic and molecular excitation per ion pair created. E_{FC} is the Franck-Condon energy, which we take to be 3 eV. The albedo terms in Eq. (4.6.1) incorporate the energy loss due to charge exchange. The dominant terms in P_H are the power carried by the ions and electrons hitting the target plate; charge exchange and radiation only account for a small fraction of the power. In this analysis we assume that the plasma is sufficiently collisional that the ion and electron temperatures are equal throughout the ergodic layer. The power deposited on the plate is not only that carried by the ions and electrons hitting the plate; the plate also receives 50% of the energy released by recombination at the plate and about 50% of the power radiated by atomic excitation since the excitation occurs primarily in front of the plate. Shown in Fig. 4.6-1 is the required recycle ratio for a given plasma tempera-
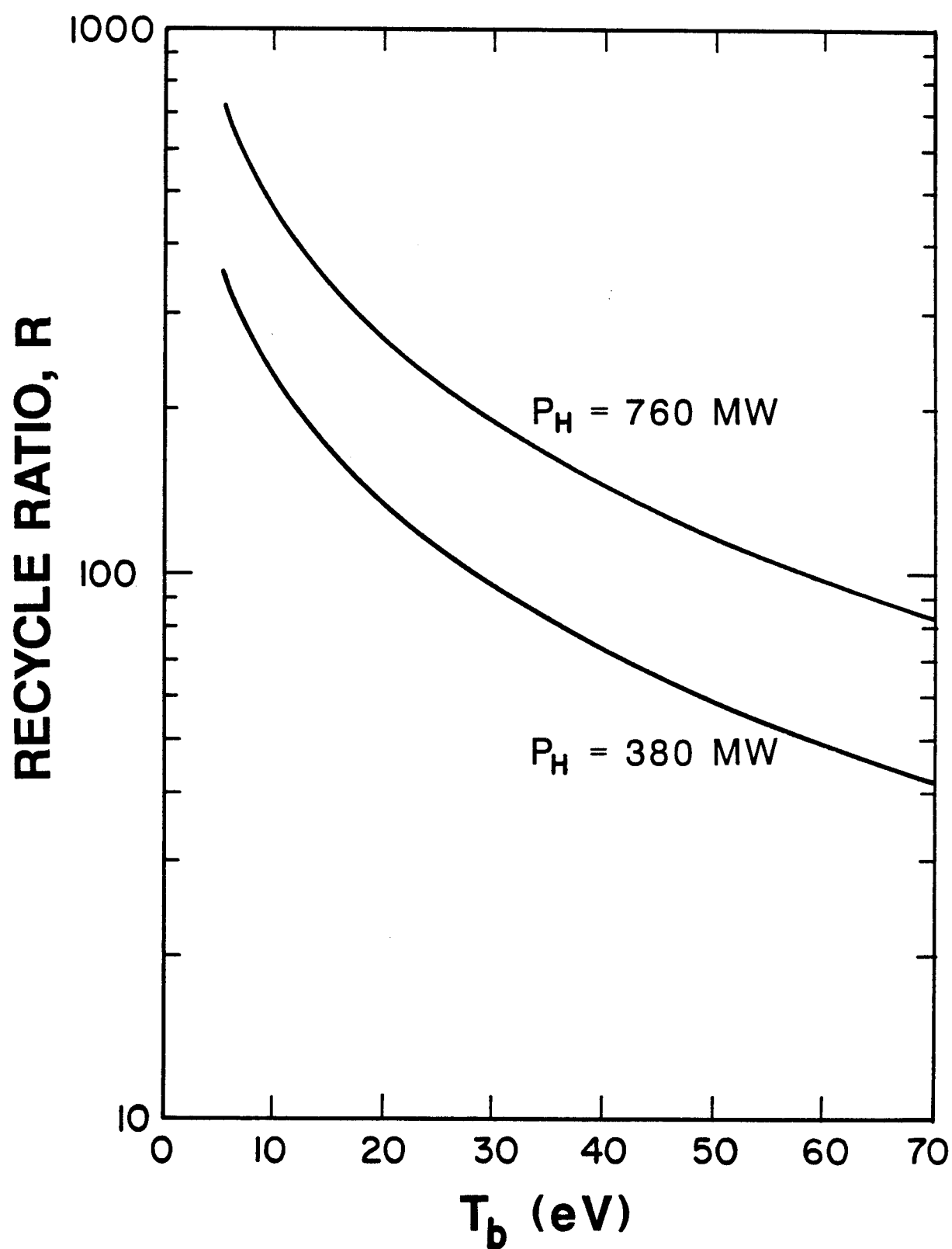
Fig. 4.6-1. Recycle ratio, R, versus plasma temperature, T_b at the target.

ture at the plate. We see that recycle ratios on the order of several hundred are required to reduce the plasma temperature at the plate to the 10-20 eV range. Shown in Fig. 4.6-2 is the ratio of P_t, the power incident on the plate to P_H, the power leaving the hot core plasma; P_t is given by

$$P_t = [2 T_b + 5.5 T_b(1 - R_e) + \frac{1}{2} W_i + R_n a_f(1.5 T_b)$$

$$+ (1 - R_n) a_m(T_b + \frac{1}{3} E_{FC})]R\Gamma_H + \frac{1}{2} W_{ex} (R - 1) \Gamma_H . \tag{4.6-2}$$

We see that about 10-20% of the power entering the edge plasma is converted to radiation in the edge plasma by the recycling process itself and is incident on the walls. An equal amount of radiation is incident on the target plate. The plasma density n_b at the plate is determined by the condition that the ion flow velocity along the magnetic field at the sheath edge is the ion acoustic velocity. This yields

$$n_b = R\Gamma_H q/(c_s P_t \sin \theta) \tag{4.6-3}$$

where q is the heat flux on the plate, θ is the angle of inclination of the plate relative to the magnetic field, and c_s is the ion acoustic velocity. It is desirable to maximize the ion density; this makes the edge plasma opaque to energetic neutral atoms and impurities and improves the shielding property of the edge plasma. We see from Eq. (4.6-3) that we want to make θ as small as possible since q is limited by heat transfer limits and mechanical design con- siderations. Shown in Fig. 4.6-3 is the ion density for q = 3 MW/m^2 and 5 MW/m^2 and θ = 10°. The density is also increased by high recycling, leading to low T_b.

The heat flow along the magnetic field from the core plasma to the plate is determined primarily by electron heat conduction. Integrating the expres- sion,

$$q_{\parallel} = -2.15 \times 10^{13} \frac{d}{ds} (T_e^{7/2}) \qquad W/m^2$$

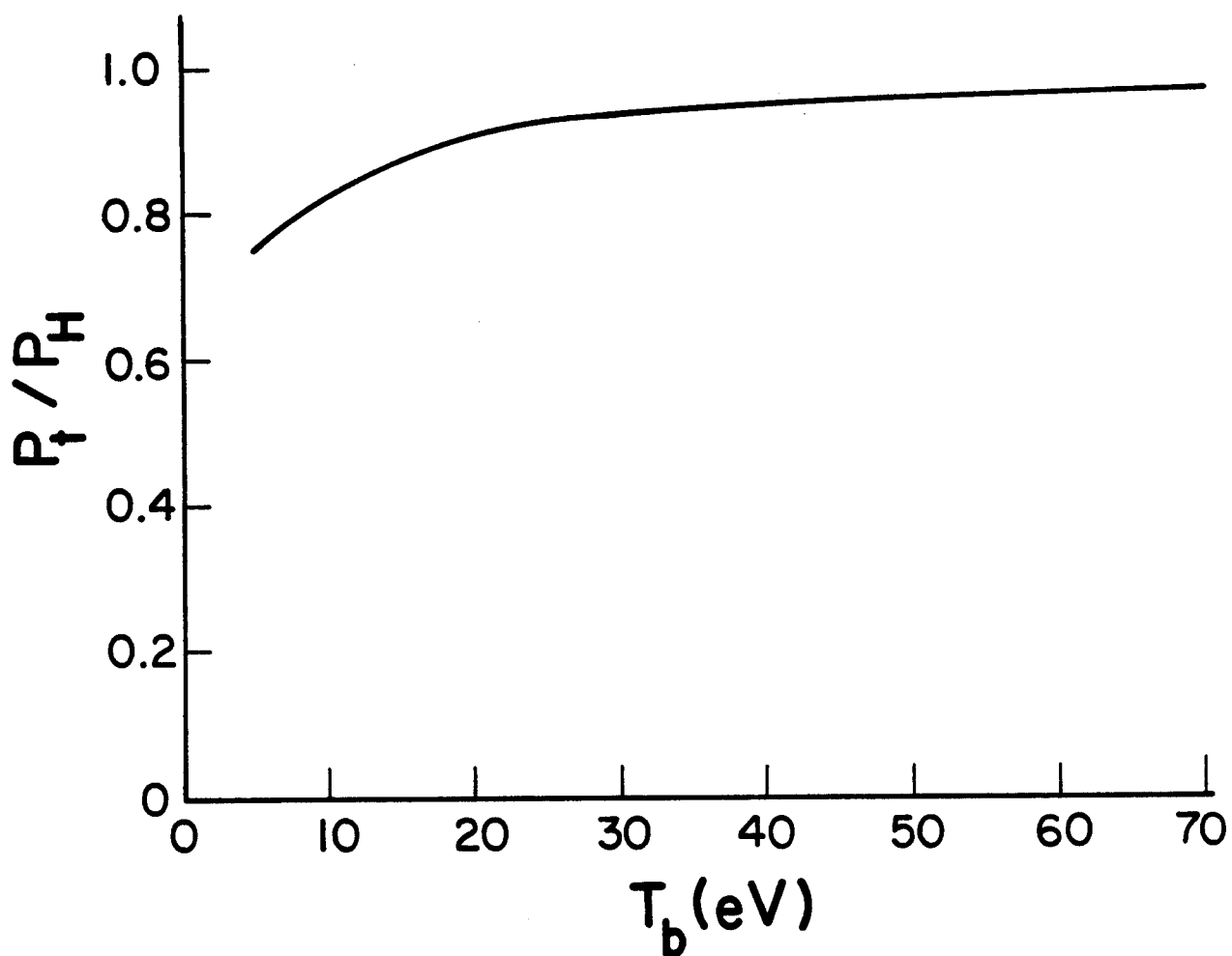along the field line gives the electron temperature, T_0, at the edge of the core plasma:

Fig. 4.6-2. The ratio of the power incident on the target, P_t, to the power entering the ergodic layer, P_H, versus plasma temperature, T_b, at the target.
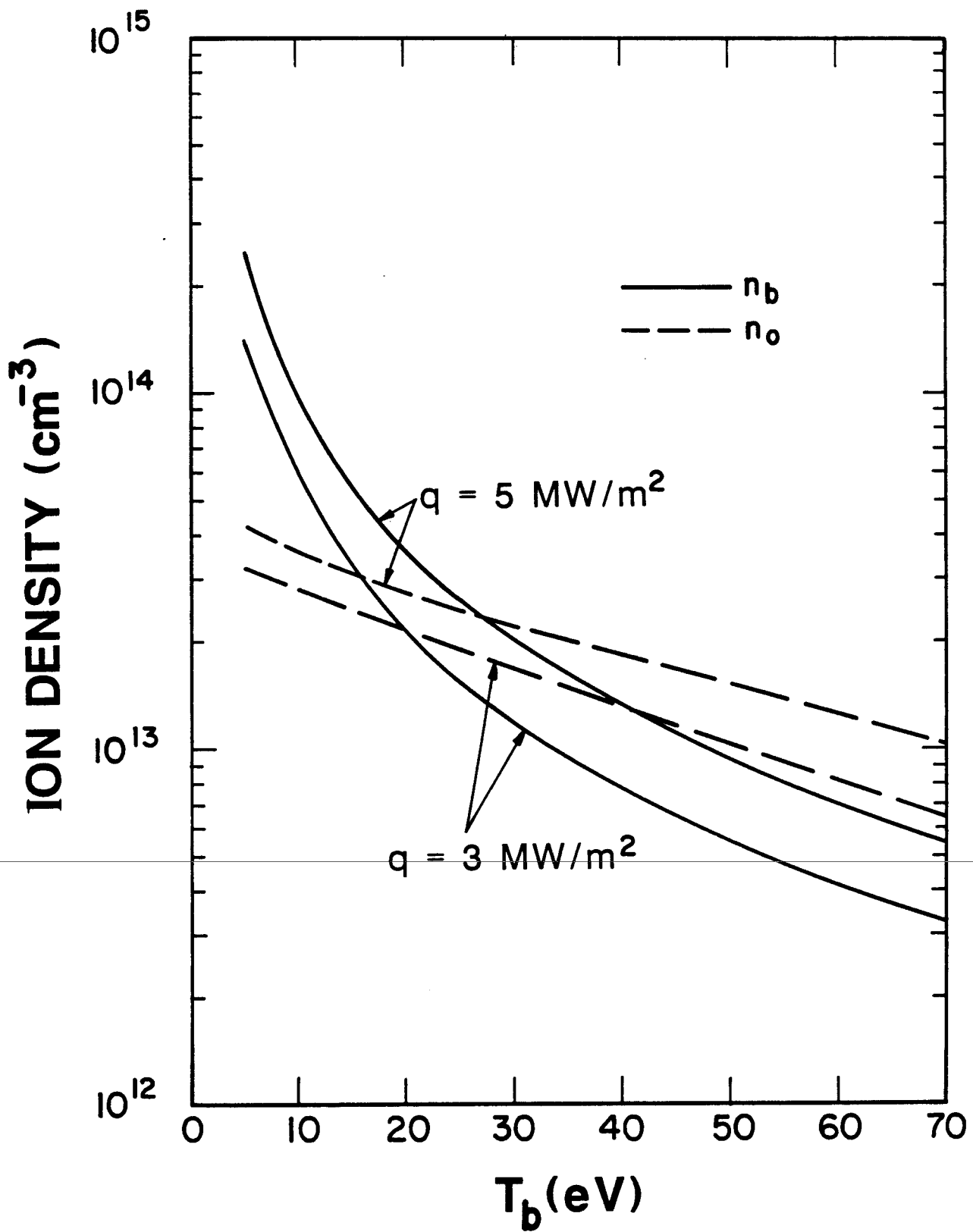
Fig. 4.6-3. Ion density at the target, n_b, and in the ergodic layer, n_0, versus plasma temperature at the target, T_b, for different heat fluxes, q, at the target.

$$T_0 = (T_b^{7/2} + P_H L/(4.3 \times 10^{13} A \sin \theta)^{2/7}) \tag{4.6-4}$$

where A is the target plate area and L is the average length along the field line from the edge to the target plate. In this expression, MKS units are used except that T_0 is in keV. We choose L such that (AL sin θ) is the volume of the ergodic layer. This leads to rather short lengths in comparison with poloidal divertors and reduces the temperature at the boundary of the core plasma. Because of the 2/7 power, the temperature is not very sensitive to the choice for L.

Shown in Fig. 4.6-4 is T_0 versus T_b for different values of q and P_H. At low T_b the temperature T_0 exceeds T_b by a large amount; in this limit the heat flow along the field is primarily by electron heat conduction. At higher T_b, energy transport is primarily by convection and the conduction model used here is not very good, but it still gives the right asymptotic limit of $T_0 = T_b$. In the intermediate region, the real difference between T_0 and T_b is less than that shown in this figure. This error is not significant since we are primarily interested in operating in the high recycling limit with low T_b. The upturn in T_0 as T_b drops below 25 eV is due to the reduction of P_t, because of excitation radiation, for a given P_H. At constant q, this causes the target area to decrease and the effective length L to increase.

The ion density, n_0, at the edge of the core plasma is given by a momentum balance along the magnetic field, accounting for the acceleration of the plasma to the ion sound speed as it nears the sheath at the target. This yields[3]

$$n_0 \cong \frac{2 \, n_b T_b}{T_0} \propto \frac{R \Gamma_H T_b}{P_t} \left(\frac{P_t}{P_H}\right)^{2/7} \left(\frac{q}{\sin \theta}\right)^{5/7} . \tag{4.6-5}$$

Increasing q and reducing T_b (by increasing the recycle ratio) increases n_0 and improves the shielding effectiveness of the ergodic layer. Shown in Fig. 4.6-3 is the density n_0 versus T_b. Note that in the conduction limit ($T_b \ll T_0$), the density n_0 is less than n_b, but in the convection limit ($T_b = T_0$) n_0 is twice n_b, as is well known from collisionless presheath theory.[4]

The ability of the ergodic layer to screen out impurities and neutral gas can be ascertained by estimating the mean free path of cold and energetic neutral atoms near the target plate and near the edge of the core plasma. For the case of P_H = 380 MW, T_b = 10 eV, and q = 3 MW/m^2, the density at the tar-
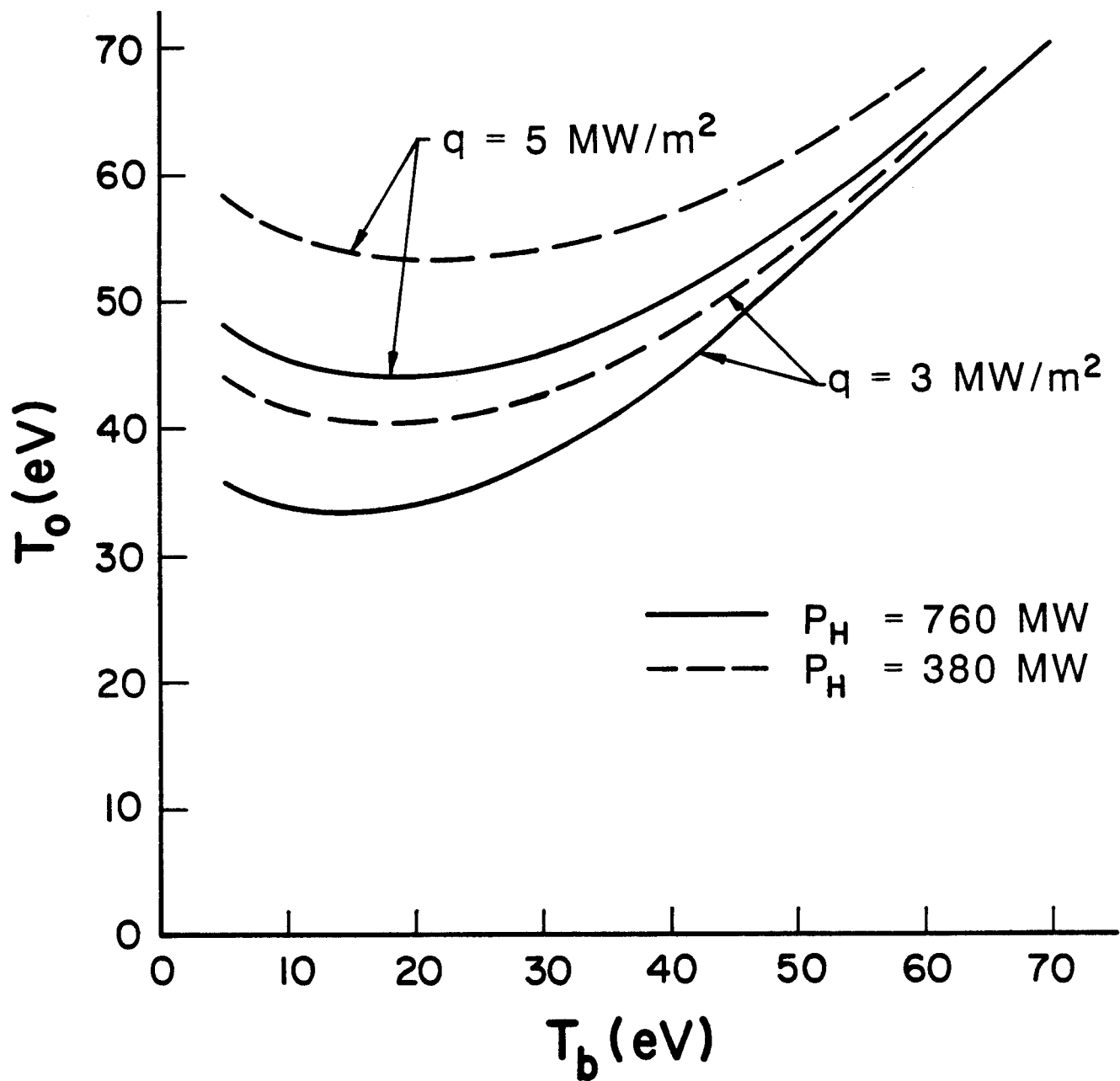
Fig. 4.6-4. Plasma temperature in the ergodic layer, T_0, versus plasma temperature at the target, T_b.

get plate is 6×10^{13} cm^{-3}; energetic atoms with a mean energy of 30 eV can be formed by reflection of ions accelerated across the sheath. These atoms would have a charge exchange mean free path of about 3 cm and a net mean free path (i.e., a neutral atom density scale length due to the combined effects of charge exchange and ionization) of about 4 cm. Consequently, most of them are screened out before they can reach the edge of the core plasma, which is still not very hot. Near the last closed magnetic surface, the plasma is less dense ($\sim 3 \times 10^{13}$ cm^{-3}) and warmer ($\sim$ 40 eV); the charge exchange mean free path is increased to 4.5 cm, but the net mean free path is still only about 4.5 cm because of the higher ionization probability. A cold neutral atom ($\sim$ 3 eV) formed by the Franck-Condon process would have a net mean free path of 1.8 cm near the plate and 1 cm near the last closed magnetic surface. Consequently, it appears from these simple estimates that an adequate shielding probability against gas, and therefore also impurity atoms, can be obtained if we can operate in this high recycling mode. Note also that the temperature at the last closed magnetic surface is not very high; energetic fuel atoms getting this far into the plasma still do not produce a flux of atoms on the target plate with enough energy to cause significant sputtering of the plate.

The discussion above indicates that a cool, dense plasma in the edge region can be obtained if the recycle ratio can be made to be about 200 or more. Up to now the discussion has been fairly generic and not strongly dependent on the detailed design of the target plate where the recycling takes place. We now turn to the target plate and consider whether this degree of recycling is obtainable and consistent with vacuum pumping requirements.

A possible target plate concept is the vented plate utilized in the TIBER ETR[5] design; this is shown schematically in Fig. 4.6-5. The vented plate is essentially opaque to ions since they hit the plate at near grazing angles. The particles are partly reflected as energetic neutral atoms and partly as molecules; this creates a neutral gas layer in front of the plate which charge exchanges with the incoming ions. About half of the neutral flux is directed towards the plate with a roughly isotropic angular distribution. The vented plate is more transparent to neutrals because of the nearly normal incidence. A fraction f_t passes through the plate and creates a neutral gas pressure in the plenum behind the target plate. This plenum is connected to pumping ducts leading to the vacuum pumps. For TIBER the neutral gas is pumped at the rather high pressure of 10^5 bar, which reduces the size of the penetrations
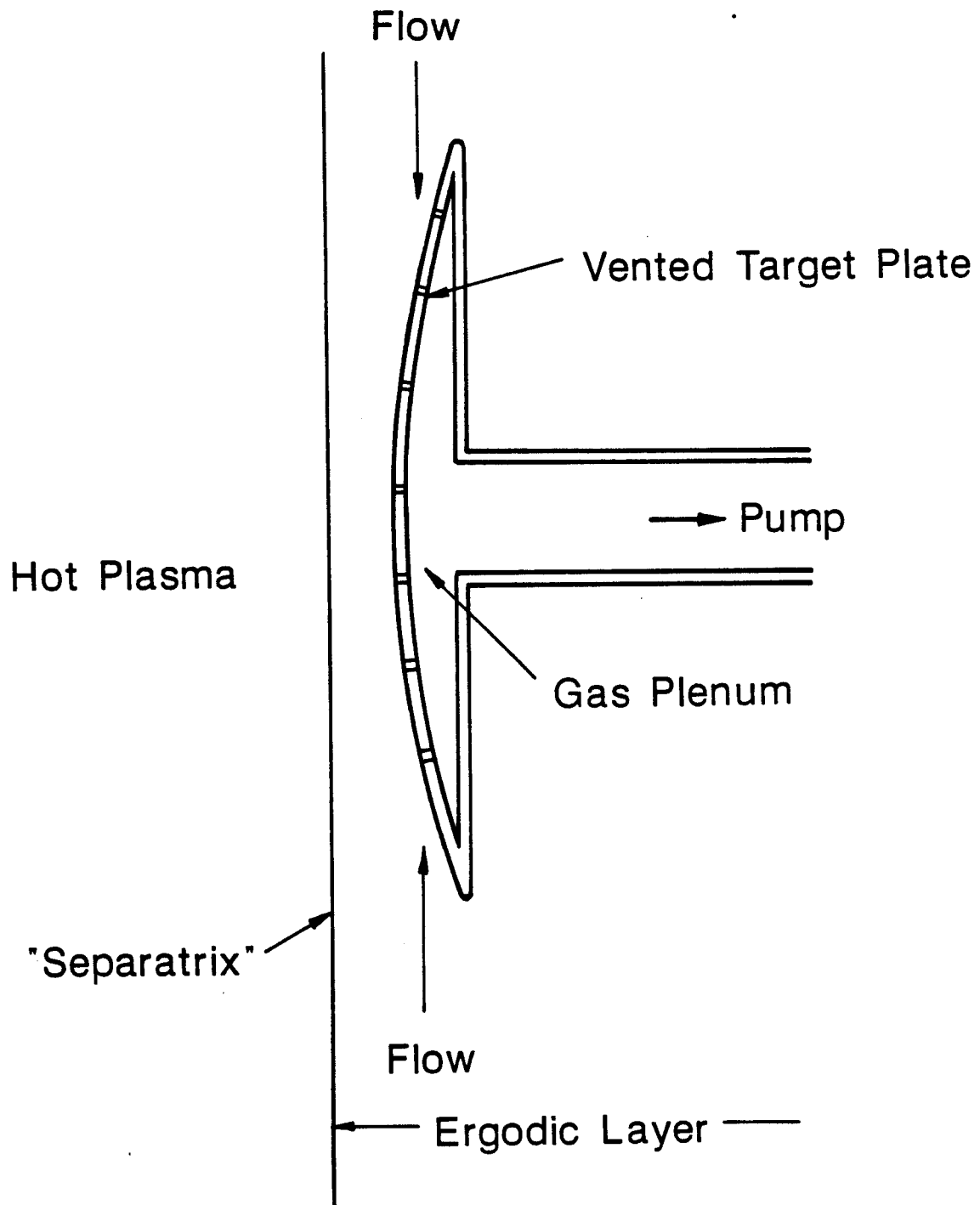
VENTED TARGET PLATE

Fig. 4.6-5. Schematic of the vented target plate.

required in the blanket for vacuum pumping ducts. In comparison, the pumped limiter designs utilized in NET[6] and INTOR[7] pump the gas at about 1 mbar and therefore require a proportionally larger area for pump ducts. Note that the pump duct area is determined by the gas throughput and the pressure at which it is pumped. This is unrelated to the target area which is determined by heat transfer considerations and plasma flow.

A particle balance on the plasma in the ergodic layer yields the following equation for the transparency factor f_t required to achieve a given recycle ratio R:

$$f_t = \frac{1 - a_n}{a_n(R - 1)} \qquad (4.6\text{-}6)$$

where a_n is the albedo (ratio of the neutral flux reflected by the plasma to the neutral flux entering the plasma) of the neutral gas. The albedo depends on the energy spectrum of the neutrals incident on the plasma as well as the plasma temperature. For T_b = 10 eV, about 50% of the ions hitting the target plate recycle as molecules which have an albedo of 0.3.[8] If we assume that the energetic reflected atoms penetrate further and don't recycle to the target plate, then the effective albedo is 0.15. For R = 200, the required f_t is about 0.03. Hence, the plate is about 3% transparent. This is only a rough estimate to indicate the principle; the transparency can easily be adjusted for a more refined calculation of the albedo and three-dimensional effects. In any case, the plate has a low transparency.

Since the plasma conditions are similar to those in TIBER, it is reasonable to expect the gas pressure in the plenum to be about 10^5 bar. This pressure is also in the same range as seen in a number of tokamaks where the neutral pressure has been measured in scoop limiters.

A final concern for this concept is whether it will pump helium from the vacuum chamber. A helium ion impinging on the target plate hits the plate with energy of about 90 eV, if doubly ionized, or 55 eV if singly ionized. The reflection coefficient is about 0.4; hence 60% of the helium recycles as cold atoms. A cold helium atom in a 6×10^{13} cm^{-3}, 10 eV plasma has a mean free path for ionization of 1.2 cm and a mean free path of 2.5 cm for elastic scattering[9] with the incoming deuterium and tritium. The elastic scattering will cause the helium to be returned to the plate and a portion of it will enter the plenum and produce a helium gas pressure driving a flow towards the

pumps. Ionization, however, will cause the helium to be converted to ions which, like the deuterium and tritium ions, can't get through the ports. We have to consider ionization to be a competing process which inhibits the pumping action of the ports in the target plate. We can easily control, however, the amount of ionization by small changes in the electron temperature at the plate. If the temperature is reduced to 5 eV, then the ionization mean free path is 10 times longer than the mean free path for elastic scattering. In this case, one might anticipate a substantial reflux of neutral helium incident on the target plate and some degree of pumping of helium. An adequate analysis of this problem is beyond the scope of this study, however.

In conclusion, we have seen that a high recycling mode of operation in which a cool, dense plasma at the target plate is produced, can be obtained. Furthermore, the plasma temperature near the edge of the core plasma is still not very hot and the plasma is sufficiently dense that there should not be a problem with a flux of more energetic atoms producing excessive erosion and impurity generation by sputtering. Calculations for the TIBER study indicate that a gas pressure of 10^5 bar at the entrance to the pump ducts can be produced; this gives adequate gas flow to the pumps with rather small penetrations through the blanket and shield. Helium pumping by this concept has not been thoroughly addressed, but elastic scattering by fuel ions is a possible process for helium pumping if the electron temperature near the target plate is reduced to about 5-10 eV.

4.6.2 ICRF Method for Active Impurity Control

We consider the use of localized ICRF (Ion Cyclotron Range of Frequencies) heating in the ASRA6C stellarator reactor to reduce impurity transport from the ergodic region into the hot reacting plasma core. The basic principle has been put forth by Ohkawa[10] in his work on the prevention of impurity accumulation in classical tokamaks. He has proposed the use of poloidal ion density inhomogeneities caused by trapped ions produced by ICRF heating to produce a poloidal electric field which leads to an azimuthal variation for the impurity ion distribution and produces a flux-averaged impurity radial flow reversal in circular or noncircular tokamaks. The resulting poloidal electric field which leads to an azimuthal variation for the impurity ion distribution and produces a flux-averaged impurity radial flow reversal in circular or noncircular tokamaks. The resulting poloidal electric field and the poloidal variation of the impurity ion distribution can be averaged over a

flux surface to yield the net radial flux for impurity species Z when the trapped particle ion density is

$$n_t/n_e > 3 \; \varepsilon_t (1 + Z_{eff})/Z \qquad (4.6\text{-}7)$$

where ε_t is the inverse aspect ratio for the machine; this process is most effective on medium and high Z impurities. If we apply this to ASRA6C parameters with $Z_{eff} = 2$, $\varepsilon_t = 0.08$ and $Z_{Fe} = 26$ we obtain a two percent variation in ion concentration to reverse the ion impurity radial influx.

Recent works on ICRF heating in stellarators[11] and an analysis of ICRF heating for the Heliotron E and ATF torsatrons[12] have been carried out. Preliminary ICRF heating experiments have also been carried out on the L-2 stellarator and Heliotron E torsatron.

Fokker-Planck calculations for poloidal ion density variations due to banana trapped ions in an ICRF heated tokamak reactor have been calculated by Harvey et al.[13] and have been observed in moderate power ICRF experiments on PLT.[14] Our concept is to locally heat the ASRA6C stellarator reactor in a region somewhat inside (30 cm) the last closed magnetic flux surface by means of ICRF heating.

Questions which we will address for ASRA6C include the frequency required to heat the bulk deuterium or seeded small concentration (5%) of hydrogen, the ICRF wave coupling efficiency through the ergodic layer edge plasma, the required power density in the heating zone and total supplementary power required. The poloidal and toroidal dependence of the ICRF induced equilibrium electric fields are briefly addressed. This work should be considered a preliminary investigation of the concept and factors which determine a successful active ICRF impurity control concept.

The ergodic layer of 20 cm extent with a high density $n = 3 \times 10^{13}/cm^3$ plasma, relatively cool T = 40 eV plasma is an ideal region which allows good coupling through it without a substantial evanescent wave zone for the 80 MHz ICRF wave. The cooler edge temperatures will allow improved antenna performance, should reduce impurity production, and could provide enhanced energy confinement times.

The mod B and flux surface plots for ASRA6C at different field periods show that the most convenient region for localized ICRF heating would be at a 1/2 field period corresponding to a toroidal angle of 36° where the flux sur-

faces are vertically elongated ellipses and the mod B surfaces are nearly vertical over a large portion of the central plasma zone. The ICRF radiation would be focused over the central portion of the 5.2 T mod B surface on the low field side of the stellarator axis as shown in Figs. 4.6-6 and 4.6-7. This corresponds to a fundamental deuterium cyclotron frequency of 40 MHz and a fundamental seeded hydrogen (< 5% concentration) cyclotron frequency of 80 MHz. The first few harmonics of the cyclotron frequency can be considered (n < 3) with good single pass absorption expected at the 10 keV ion temperatures and $7 \times 10^{13}/cm^3$ deuterium density in this region obtained from equilibrium ignited transport code results for ASRA6C. ASRA6C is particularly well suited to harmonic ICRF heating since its large aspect ratio R/a = 12.5 insures that a single ion cyclotron harmonic can be isolated in the confined stellarator flux volume for harmonics below n = 3 for deuterium and n = 4 for tritium.

The choice for which harmonic or ion species to heat and trap is one of convenience for the compact design of the ICRF waveguide or antenna coupler consistent with the ASRA6C wall, magnet, blanket and shield design. There is also the physics issue of which heating mode produces the most trapped ions for the least amount of auxiliary RF power. Previous experimental and theoretical research for tokamaks[15] suggests that a fundamental minority ion population produces the strongest ion tail formation for a given amount of power absorbed and that a substantial trapping fraction can be obtained at moderate powers. One can consider the seeding of the plasma with the required concentration of hydrogen to accomplish this (< 5%), but this sacrifices the D-T fusion power output. If one heats the second or third harmonic of the deuterium bulk distribution, then higher amounts of auxiliary power will be required to achieve a given trapped ion population.

An estimate of the power required can be obtained by using the results of Harvey et al.[13] for a D-T tokamak reactor heated by second harmonic deuterium heating. The bounce average Fokker-Planck equilibrium code shows that 1 W/cm^3 yields a 3% poloidal ion density variation with the heating on axis, an electron density of $1 \times 10^{14} \text{ cm}^3$ and 10 keV background ion and electron temperatures. One can anticipate that heating off axis as is proposed here would reduce the required absorbed power density levels. This is because the heating off axis would deposit a substantial amount of power in a region tangent to the local flux surface which increases the amount of time the pass-
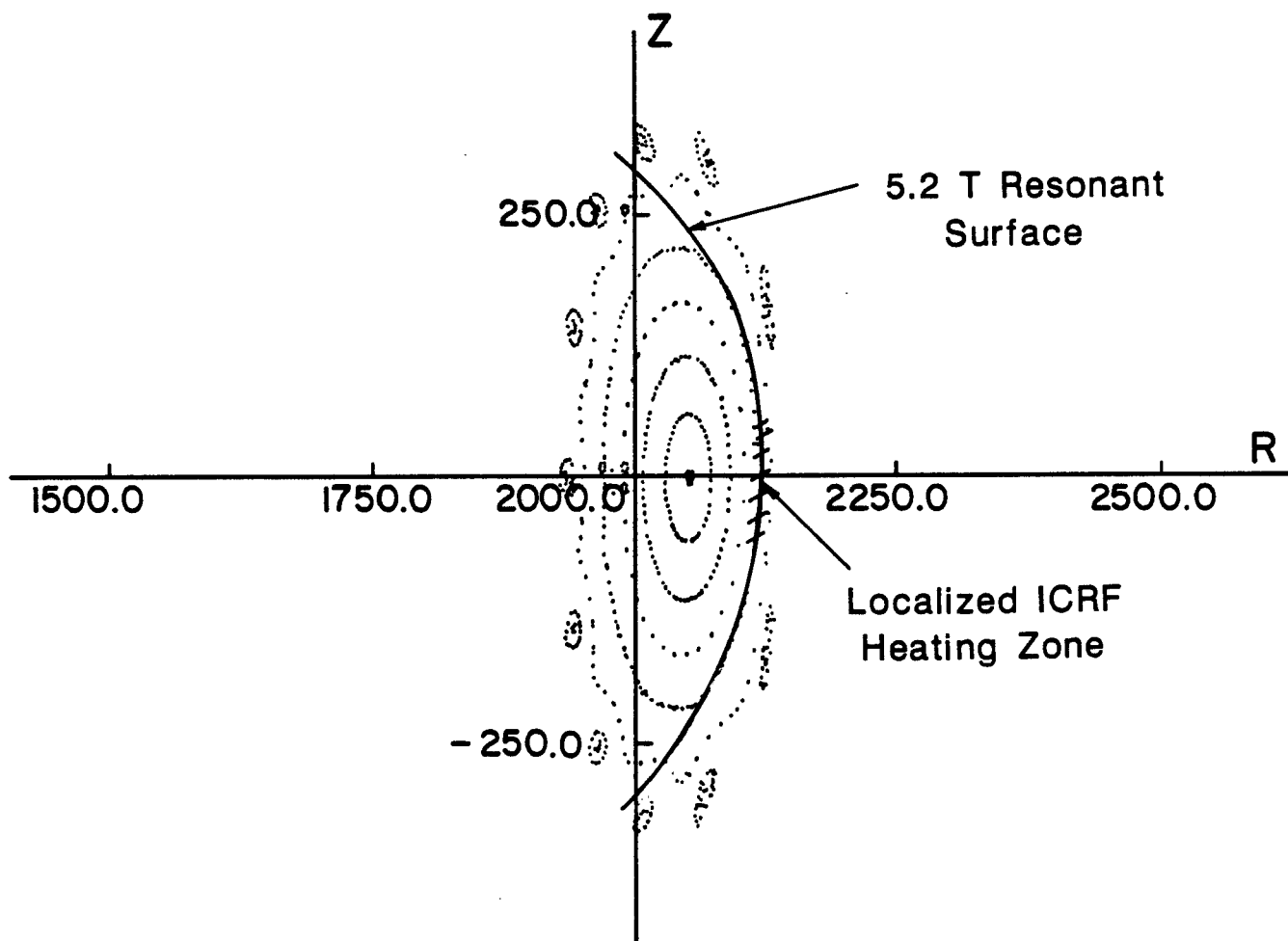
Flux Surface and Mod B Resonance Surface at φ = 36°, 1/2 Field Period

Fig. 4.6-6. Flux surfaces and mod B resonance surface at φ = 36°, 1/2 field period.
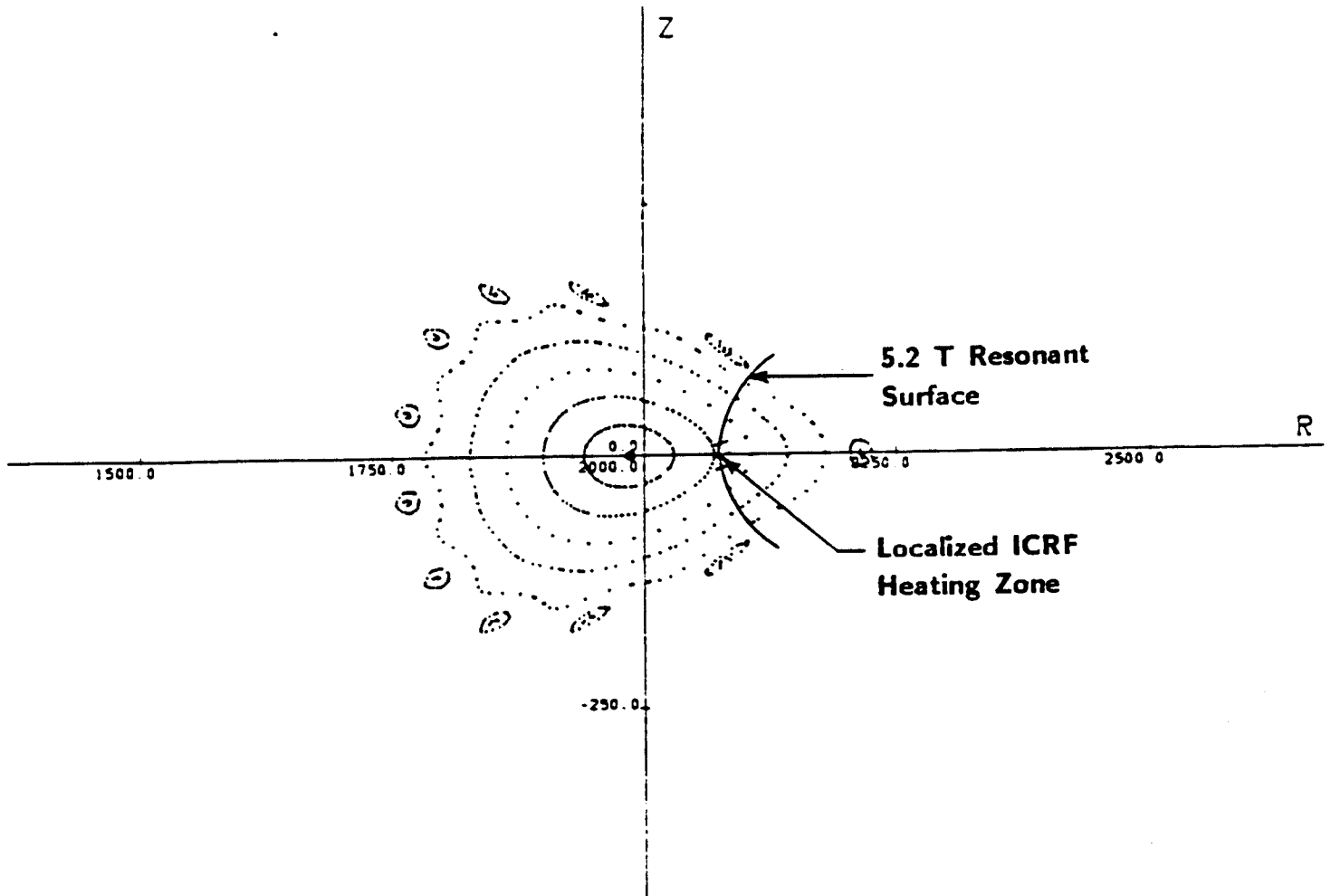
Flux Surfaces and Mod B Resonance Surface at $\phi = 0°$, 0 Field Period

Fig. 4.6-7. Flux surfaces and mod B resonance surface at $\phi = 0°$, 0 field period.

ing particles have to interact with the ICRF wave and become trapped. The absorption profile of 1/50th of the total poloidal cross-sectional area yields an <u>upper limit</u> power requirement over the <u>whole machine</u> of P_{max} = 1.0 W/cm^3 x 1760 cm^2 x 2 x π x 2000 cm = 22 MW. As one moves to different regions in the toroidal direction, the 5.2 tesla mod B resonance surface deforms from weakly convex outward at ϕ = 36° to more sharply concave outward at ϕ = 18° and 0° but always lies on the outboard region of the cross section and would be most accessible to antennas located on the outboard side of the torus.

If ICRF heating were applied only in the five toroidal field periods in the neighborhood of the ϕ = 36° toroidal angle and subsequent zones where the flux surfaces repeat their shape, then the amount of additional power might be reduced since impurity ions would traverse these zones many times during their slower radial drift. The mapping of the broader heating zone at ϕ = 36° where the flux surfaces are vertical ellipses to regions where the flux surfaces are more triangular would have the effect of an increased localization of the potential formed by trapped ions on the vertically compressed resonant mod B surfaces at those points. Since a discrete number of toroidal heating zones (5) makes sense from a point of a discrete set of heating antennas, a higher value of poloidal electric field would have to be introduced there to compensate for adjacent regions where the poloidal electric field giving rise to impurity flow reversal is reduced due to fewer trapped ions. Since the heating zones would have a toroidal extent and the trapped ion banana orbits execute toroidal drifts, an extended region where the potential is produced is evident. The effect of ICRF heating and the production of helical ripple trapped ions which would produce localized potentials should also be addressed.

The ergodic layer of 20 cm extent with a high density n = 3 x 10^{13}/cm^3 plasma, relatively cool T = 40 eV plasma is an ideal region which allows good coupling without a substantial evanescent wave zone for the 80 MHz ICRF wave. The cooler edge temperatures will allow improved antenna performance and will reduce impurity production.

References for Section 4.6

1. W. Feneberg, Proc. 8th Europ. Conf. on Controlled Fusion and Plasma Phys., Vol. 1, p. 3 (1977).

2. M.F.A. Harrison, P.J. Harbour, E.S. Hotston, "Plasma Characteristics and Gas Transport in the Single-Null Poloidal Divertor of INTOR," Culham Laboratory Report CLM-P688 (1982).

3. M. Kaufmann, K. Lackner, J. Neuhauser, H. Vernickel, Nucl. Fusion 25, 89 (1985).

4. P. Stangeby, "The Plasma Sheath," in Physics of Plasma-Wall Interactions in Controlled Fusion, edited by D.E. Post and R. Behrisch, Plenum Press, 1986.

5. C.D. Henning, "TIBER - Tokamak Ignition/Burn Experimental Research," Lawrence Livermore National Laboratory, UCID-20589 (1985).

6. "Next European Torus Status Report 1985," NET Report 51, C.E.C., Brussels (1985).

7. "International Tokamak Reactor - Phase Two A," Part II, I.A.E.A., Vienna (1986).

8. B.Q. Deng, G.A. Emmert, J.F. Santarius, "The Effect of Edge Molecular Processes on Neutral Transport in the Tandem Mirror Halo Plasma," University of Wisconsin Fusion Technology Institute Report UWFDM-696 (1986).

9. J.H.H.M. Potters and W.J. Goedheer, Nuclear Fusion 25, 779 (1985).

10. T. Ohkawa, "Prevention of Impurity Accumulation in Classical Tokamaks," GA Technology Report GA-A17719 (1984).

11. L. Kovrizhnykh and P. Moroz, "Enhancement of Cyclotron Absorption of a Fast Magnetosonic Wave in Stellarators," Proc. 10th Conf. on Plasma Physics and Controlled Nuclear Fusion Research, London, IAEA-CX1-44-F-IV-7, Vol. I, pp. 633-642, (1985).

12. A. Fukuyama et al., "Propagation and Absorption of ICRF Waves in Helical Plasmas," Nuclear Fusion 26, 151 (1986).

13. Harvey et al., "ICRF Fusion Reactivity Enhancement in Tokamaks," Nuclear Fusion 26, 43 (1985).

14. J. Hosea, private communication.

15. J. Scharer et al., "Fokker-Planck Calculations for JET ICRF Heating Scenarios," Nuclear Fusion 25, 435 (1985).

4.7. Summary and Conclusions

Although there are several open question regarding the transport model as described above, especially regarding the very edge region of the plasma, it can be concluded that essential features of the start–up and burn conditions of an Advanced Stellarator Reactor (ASR) or Burner system (ASB) can be described appropriately.

Under neoclassical conditions, the plasma confinement is dominated by the effect of trapped particles and the associated ripple transport. A radial electric field reduces the losses by decreasing the ion heat conduction. The heat conduction coefficients, increasing with temperature, introduce relatively broad temperature and density profiles.

The fusion power amounts to typically $P_f \approx 4\,GW$ for ASR, whereas ASB stays at about 10 % of this value. For the reference configuration ASR6C, a radiative power loss of 300 MW near the plasma edge and a fusion power of 3.9 GW is obtained at an average β of 5.0 % , at a refuelling rate of $1.1 \cdot 10^{23}\,s^{-1}$. The peak temperature is $T \approx 19\,keV$. In this case the ripple losses are reduced by a factor of two in order to take account of the improved confinement of an Advanced Stellarator, and the field is raised to 5.5 T at the axis.

For start–up, an effective heating power of $P_i = 30$ to $50\,MW$ is sufficient for ASB and ASR. Larger major radii, e.g. a value of $R_o = 25$ instead of $20\,m$, ease the requirements for start–up and allow a larger difference in the β–values of the ignition and the burn points. Since stellarators can, in principle, operate steady state, the start–up power can be turned down after reaching ignition, and appropriate shielding can be introduced into the respective ports, in order to avoid problems of neutron streaming.

Furthermore, continuous operation of the reactor is an essential advantage regarding the material stresses and lifetimes. Due to the absence of cyclic loads a longer operation at full power is possible in a stationary system than in a pulsed reactor.

The ergodic layer at the separatrix combines some of the features of magnetic divertors with the simplicity of pumped limiters. This allows the edge plasma to operate in a high recycling mode which produces low plasma temperature ($\sim 10\,eV$) at the target plate. The use of RF to induce net outward impurity transport is an interesting option for the impurity control, but requires further study to fully assess its feasibility.

References to Chapter 4

[1]: R. Chodura, W. Dommaschk, W. Lotz, J. Nührenberg, A. Schlüter,
Three–dimensional MHD Equilibrium Studies,
Proc. Plasma Phys. and Contr. Nucl. Fusion Research Brussels 1980,
Vol. I, 807, (1981).

[2]: E. Harmeyer, J. Kisslinger, F. Rau, H. Wobig,
Some Aspects of Modular Stellarator Reactors,
Proc. Plasma Phys. and Contr. Nucl. Fusion Research,
London 1984, Vol. III, 363, (1985).

[3]: H. Wobig and WVII–A Team,
A Transport Model of ECR–Heated Plasmas in WVII–A,
13th Eur. Conf. on Contr. Fusion and Plasma Heating, **10** C, 291,
Schliersee, Germany, (1986).

5. BLANKET AND REFLECTOR DESIGN

5.1 Blanket Options
5.1.1 Motivation

In the past several years there has been a trend in conceptual fusion power reactor designs toward more compact systems, primarily motivated by economic considerations. The blanket thickness directly impacts the size and mass of the components immediately behind it, ultimately determining the size of the magnets, which constitute a major fraction of the cost of the nuclear island. The effect is not as dramatic for tokamaks, where only the inboard side of the reactor chamber must have a limitation on the blanket thickness. In linear geometry tandem mirrors and high aspect ratio stellarators, where the magnets follow immediately behind the shield the effect is much more pronounced.

Obviously the nuclear performance of the blanket cannot be compromised at the expense of the thickness. The blanket must be capable of breeding tritium, giving a high energy multiplication and producing thermal energy which can be converted to electricity at a reasonably high efficiency. The thinnest blanket which can achieve all these goals is one which makes use of Be metal as a multiplier/moderator. Such a blanket has been proposed as the base case for ASRA6C. It is a He gas cooled design utilizing LiPb as the breeding material, Be metal as a multiplier/moderator and the ferritic steel HT-9 as the structure.

In the case of ASRA6C, the blanket thickness is only one aspect for consideration. Since the plasma in a stellarator has a helical twist in the toroidal direction, the question arises as to whether the blanket shape should conform to the plasma or be made independent of the plasma shape. Further, because impurity control is a major requirement in a reactor grade plasma, placement and accommodation of collection plates and pump ports is an important consideration.

It was determined early in the study that the plasma in ASRA6C can be contained in an elliptical chamber of uniform cross section when viewed in the toroidal direction. A thin blanket with a uniform elliptical cross section and constant thickness would avoid complicated shapes and be the simplest to fabricate. Nevertheless, it was important to determine whether a blanket which conformed to the shape of the plasma made it possible to reduce the size

of the magnets, achieving a more attractive reactor from the cost standpoint. For this reason it was decided to do a trade study comparing suitable blanket options on the basis of neutronics performance, configuration, maintainability, mass utilization and economics. The four blanket options selected for comparison are described in the next section.

5.1.2 Description of Blanket Options

The initial intent of the trade study was to compare two blanket options: a uniformly elliptical blanket of constant thickness, and a blanket which followed the contour of the plasma on the inner surface, had a uniformly elliptical shape on the outside surface and was, consequently, of non-constant thickness. As the study progressed, it became apparent that using the thin blanket in configurations other than uniformly elliptical may have some economic advantages. The study finally settled on comparing four blanket options, three utilizing variations of the thin blanket of constant thickness and a fourth option, the non-constant thickness blanket mentioned above.

Figure 5.1-1 is a schematic representation of the four blanket options and has a short description of each. In the following sections a more detailed description is given.

Option I

The blanket, reflector, and shield are uniformly elliptical in the toroidal direction. Dimensions are selected to insure that the plasma, which changes shape in the toroidal direction always fits within the provided envelope and has a minimum scrapeoff layer of 22 cm between it and the first wall.

The blanket consists of cells which circumvent the plasma poloidally and are joined together to form a RBU (Removable Blanket Unit). External structure and coolant tubes are made of the ferritic steel HT-9. The coolant tubes spiral within the cells and are immersed in a matrix of Be balls and the remaining spaces are filled with $Li_{17}Pb_{83}$. Helium gas at 80 atm is circulated through the tubes as the coolant. The $Li_{17}Pb_{83}$ is slowly circulated for T_2 recovery.

The reflector is made of modified 9CrlMo and is cooled in series with the blanket using the same helium gas. It is followed by a shield composed of layers of B_4C and Pb and cooled with water.

BLANKET OPTION I

BLANKET OPTION II

BLANKET   UNIFORM THICKNESS
           ELLIPTICAL CROSS SECTION
           HT-9 STRUCTURE–LiPb BREEDER
           Be MODERATOR/MULTIPLIER–He GAS COOLING

REFLECTOR UNIFORM THICKNESS
& SHIELD   ELLIPTIC CROSS SECTION

BLANKET   UNIFORM THICKNESS
           FOLLOWS PLASMA CONTOUR
           HT-9 STRUCTURE–LiPb BREEDER
           Be MODERATOR/MULTIPLIER–He GAS COOLED

REFLECTOR UNIFORM THICKNESS
& SHIELD   FOLLOWS PLASMA CONTOUR

BLANKET OPTION III

BLANKET OPTION IV

BLANKET   SEGMENTED, UNIFORM THICKNESS
           FOLLOWS PLASMA CONTOUR
           HT-9 STRUCTURE–LiPb BREEDER
           Be MODERATOR/MULTIPLIER–He GAS COOLED

REFLECTOR UNIFORM THICKNESS
& SHIELD   FOLLOWS PLASMA CONTOUR
           TUNGSTEN SHIELD USED AT
             STRATEGIC LOCATIONS

BLANKET   NONUNIFORM THICKNESS
           OUTSIDE SURFACE ELLIPTICAL
           INSIDE SURFACE FOLLOWS PLASMA CONTOUR
           HT-9 STRUCTURE–LiPb BREEDER
           He GAS COOLING

REFLECTOR UNIFORM THICKNESS
& SHIELD   ELLIPTICAL CROSS SECTION

Fig. 5.2-1. Description of the four blanket options.

Option II

This design is a variation of Option I with the difference being in the geometry only. Here the blanket follows the contour of the plasma and thus has a helical twist in the toroidal direction, repeating the same shape every field period. Although the blanket thickness is the same everywhere, and it circumvents the plasma, it is of non-uniform cross section when viewed in the toroidal direction. The reflector and shield also conform to the shape of the plasma but are made of the same materials as in Option I and are cooled in the same way.

Option III

This design is yet another variation of Option I. Here it was decided to use a denser shield at the points where the plasma makes its closest approach to the coils. To do this, it was necessary to segment the blanket in order to take maximum advantage of the denser shield at these locations. Geometrically the configuration is the same as in Option II with the difference being that the blanket does not completely circumvent the plasma, but is rather segmented. The reflector and shield behind the blanket are the same as in the previous two options, but are segmented. The denser shield is composed of a He cooled tungsten layer, followed by water cooled layers of B_4C and Pb.

Option IV

In this option the first wall, which is integral with the blanket, follows the contour of the plasma, but the back surface of the blanket is uniformly elliptical. For this reason, the blanket thickness varies both in the poloidal as well as the toroidal direction. Because in places the blanket thickness was as high as 110 cm, it was decided not to use Be and instead adopt a He gas cooled $Li_{17}Pb_{83}$ blanket. As in the other options, the blanket structure and tubes are made of HT-9, the coolant is He gas at 80 atm and the breeding material is $Li_{17}Pb_{83}$.

The reflector and shield are of constant thickness and uniformly elliptical. They are composed of the same materials as in Option I and II, and are cooled in the same way.

Table 5.1-1 gives the physical parameters of the four blanket options.

Table 5.1-1. Physical Parameters of Blanket Options

BLANKET	UNITS	O P T I O N S			
		I	II	III	IV
FW Surface Area	m^2	2280	1780	1780	> 1780
Fraction of Penetration Area	%	3	4	4	~ 4
Blanket Composition					
Breeder/vol/o		LiPb/14	LiPb/14	LiPb/13.5	LiPb/80
Multiplier/vol/o		Be/53	Be/53	Be/62.5	Pb in LiPb
Structure/vol/o		HT-9/11	HT-9/11	HT-9/9	HT-9/10
Coolant, Void/vol/o		He/22	He/22	He/15	He/10
Blanket Thickness	cm	17.5	17.5	24	15-110
Blanket Coverage Fraction	%	97	96	74.7	96
Reflector &					
Shield Thickness	cm	80	80	100	68 + 10*
Reflector:					
Thickness	cm	46.4	46.4	81.4;58.1	35.3 + 10*
Composition		HT-9/He	HT-9/He	W/He; HT-9/He	HT-9/He
	v/o	90/10	90/10	90/10	90/10
B_4C Shield:					
Thickness	cm	27	27	16.6;33.6	26.2
Composition		$B_4C/Fe1422/H_2O$		same	same
	v/o	80/10/10			
PbShield:					
Thickness	cm	6.6	6.6	2;8.3	6.5
Composition		$Pb/Fe1422/H_2O$		same	same
	v/o	80/10/10			

*for blanket support

5.2 Blanket Comparison

The common design criteria for all the options are as follows:

Overall T_2 breeding ratio	1.05 - 1.10
Average nuclear heating in front layer of superconductor	~ 0.1 mW/cm^3
Peak fast neutron fluence (E > 0.1 MeV) in Nb$_3$Sn	1.5×10^{19} n/cm^2
Reactor lifetime	20 FPY

Neutron wall loading distribution for the two different blanket geometries has been determined and is presented in Figs. 6.1-1 and 6.1-2 of Chapter 6.

5.2.1 Configuration and Maintainability

In order to compare the options on the basis of configuration and construction complexity, it was necessary to have a scoping design. Figure 5.2-1 shows possible configurations of the four options. Option I is represented with top view of an RBU only, since this design is described in detail in Section 5. The remaining options are shown as isometrics of RBUs with the plasma outlines superimposed. Because all four blankets are cooled with He gas at 80 atm, it is necessary to design them with the capability of withstanding this pressure in case a leak develops in a coolant tube. For this reason the containment structures are in the form of small elliptical cells joined together to form a complete RBU. In Options I, II and III, all the cells are of constant thickness and circumvent the plasma poloidally. In Option IV, the individual cells are of constant thickness and circumvent the plasma in a helical spiral. There are four RBUs in each field period and each RBU has three supply and three return coolant connections.

Table 5.2-1 gives a relative judgmental evaluation of the four options with respect to configuration and maintainability. Configuration is judged on design and construction complexity and the ability of the design to accommodate penetration. Maintainability is judged on the ease of extracting an RBU from the reflector and on the mass of the drained RBU.

As far as design and construction complexity is concerned, Option I is superior due to its simpler geometry. It is equally difficult to accommodate large penetrations in all four options. In Option III, a penetration falling between blanket segments can be accommodated easier.

Table 5.2-1 Configuration and Maintenance

	I	II	III	IV
Design/construction complexity	Moderate	Difficult	Difficult	Difficult
Penetration accommodation	Difficult	Difficult	Difficult	Difficult
Mass of Drained RBU (tonnes)	38	27	32	58
Ease of Extraction	Moderate	V. Difficult	V. Difficult	Moderate

POSSIBLE BLANKET DESIGN
OPTION I
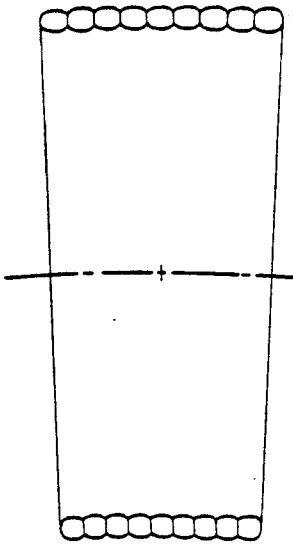
POSSIBLE BLANKET DESIGN
OPTION II
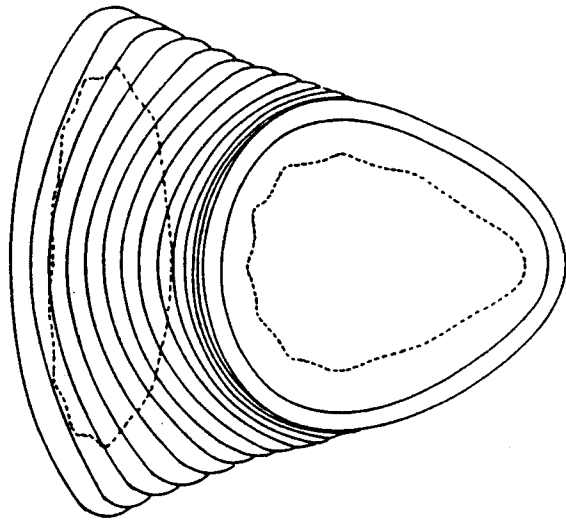
POSSIBLE BLANKET DESIGN
OPTION III
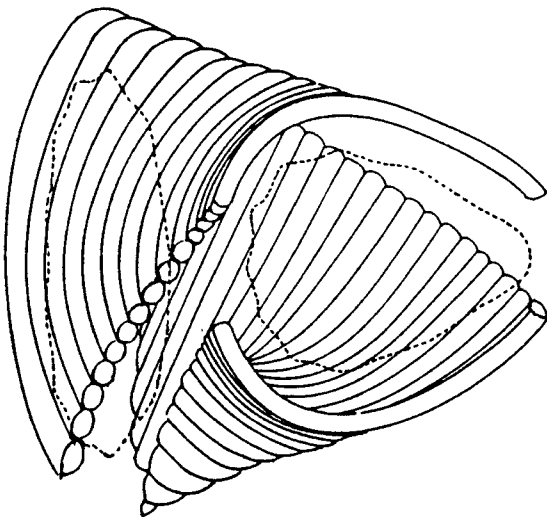
POSSIBLE BLANKET DESIGN
OPTION IV
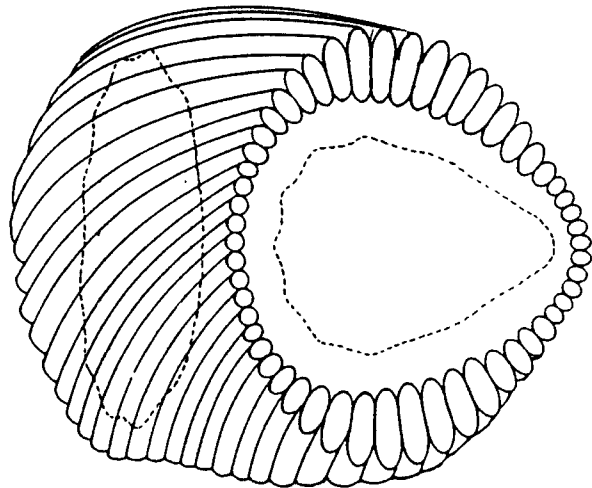
Fig. 5.2-1. Possible design of the four blanket options.

With respect to maintenance, Options I and IV are clearly ahead. Because they have a uniformly elliptical interface between the RBU and the reflector, they can be extracted from each other. The drained mass of the RBU in Option I is 38 tonnes as compared with 58 for Option IV.

5.2.2 Neutronics Comparison

The neutronic comparison is summarized in Table 5.2-2. The neutron wall loading distribution was calculated for Options I and II (see section 6.1 for more details). The peak wall loading occurs at the midplane of the outboard side of the reactor for Option I and slightly above the midplane in the other options. The wall loading is higher for Option II since the first wall is closer to the plasma. The first wall shape in Option III is exactly the same as that of Option II while in Option IV the first wall is located between the walls of Options I and II and, consequently, the wall loading is expected to have values between those of Options I and II.

The comparison was carried out for an early design of ASRA6C where the fraction of the penetration area amounts to 3-4% of the first wall surface area. The local tritium breeding ratio (TBR) and energy multiplication (M) calculated using a one-dimensional code were scaled down by the blanket coverage fraction (96-97%) in order to get the overall values. The final design calls for a higher penetration area (~ 10%) and a rigorous analysis was performed for the final blanket design to assess the effect of the increase in the penetration area on the TBR and M (see section 5.2.3).

In Options I, II and III, the blanket thickness is determined such that it yields an overall TBR in the range of 1.05-1.1. Blanket III is thicker than blankets I and II to compensate for the decrease in breeding due to the loss in blanket coverage. The blanket thickness for Option IV was predetermined and ranges between 15 cm at the midplane and 110 cm at the top and bottom. The energy multiplication is based on the energy recovered from both blanket and reflector. According to this neutronics analysis, all blankets will be self-sufficient in tritium and Option I gives the highest energy multiplication which may lead to the lowest cost of electricity.

The reflector and shield are designed to minimize the peak nuclear heating in the magnet and their thicknesses are determined from the optimization study of section 6.3. The peak radiation effects in the magnets are listed in Table 5.2-2 and the poloidal variation of the nuclear heating and fluence are shown in Figs. 5.2-2 and 5.2-3 for the four options. In Option I,

Table 5.2-2. Neutronics Comparison of the Four Options

	Units	I	II	III	IV
Peak/Av. Neutron Wall Loading	MW/m²	2.4/1.41	2.55/1.84	2.55/1.84	~ 2.5/~ 1.6
Fraction of Penetration	%	3	4	4	~ 4
Blanket Thickness	cm	17.5	17.5	24	15 - 110
Blanket Coverage Fraction	%	97	96	74.7	96
Local/Overall TBR		1.14/1.1	1.14/1.09	1.5/1.1	1.17/1.12
Local/Overall Energy Multiplication		1.42/1.38	1.42/1.36	1.38/1.33	1.18/1.13
HT-9 Reflector Thickness	cm	46.4	46.4	81.4; 58.1 W; HT-9	35.3 + 10*
B_4C/Pb Shield Thickness	cm	33.6	33.6	18.6; 41.9	32.7

*The 10 cm is the blanket support structure.

| Radiation Effects in S/C Magnet:	Units	I	II	III	IV
Peak Nuclear Heating (in innermost / Av. Nuclear Heating layer)	mW/cm³ / mW/cm³	0.5*/0.1	0.1/0.08	0.0042/< 0.001	0.11/0.03
Peak Fast Neutron Fluence in Nb_3Sn	n/cm² @ 20 FPY	1 E19*	2.3 E18	1 E17	2.0 E18
Peak Dose in GFF Polyimide	rad @ 20 FPY	1 E10*	2.1 E9	8 E7	1.88 E9
Peak dpa in Cu Stabilizer	dpa/FPY	4.5 E-4*	1 E-4	4.5 E-6	8.3 E-5
Potential for Magnet IR Reduction	cm	-	10	28	10

*For cross section through 10 cm thick He manifolds.
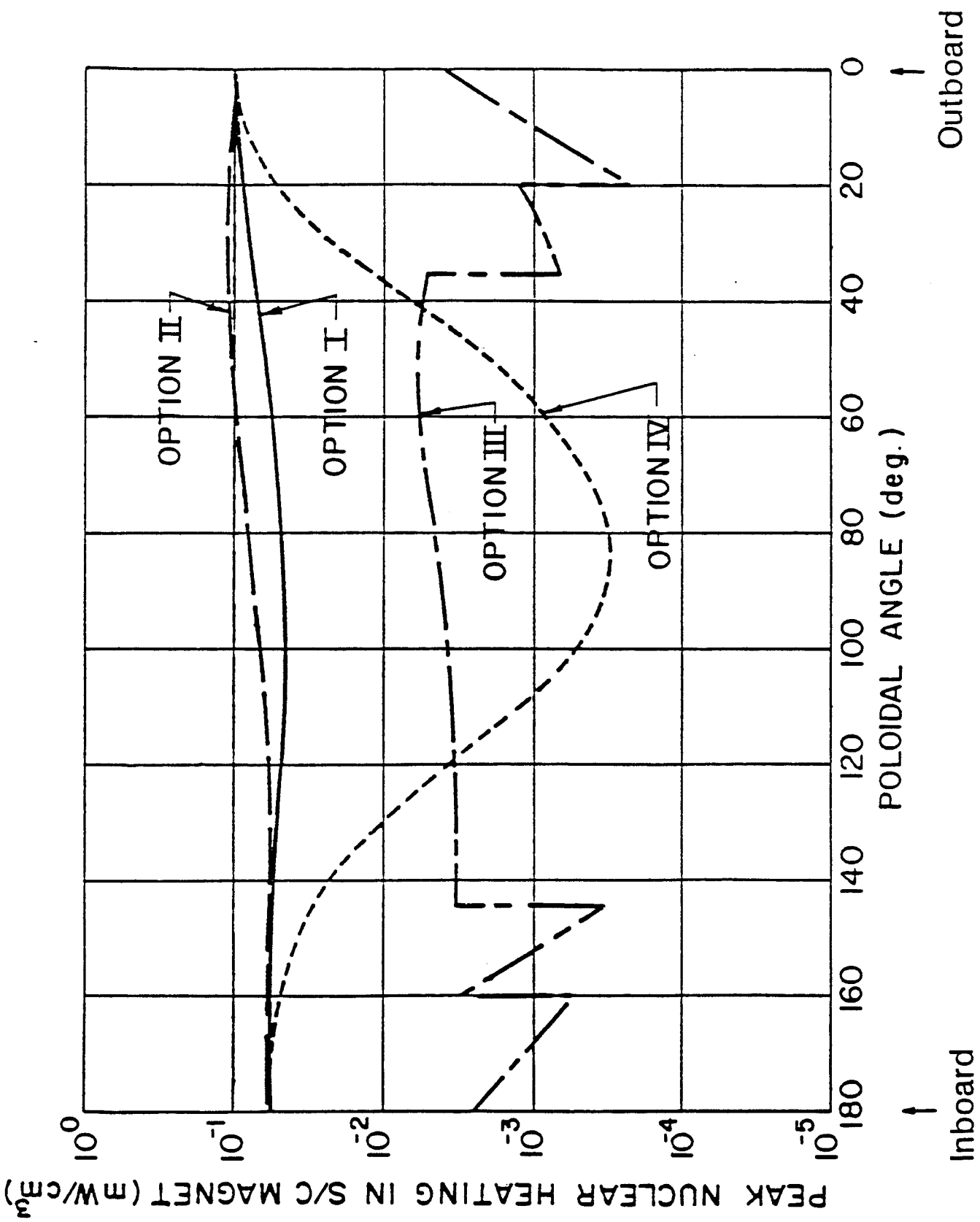
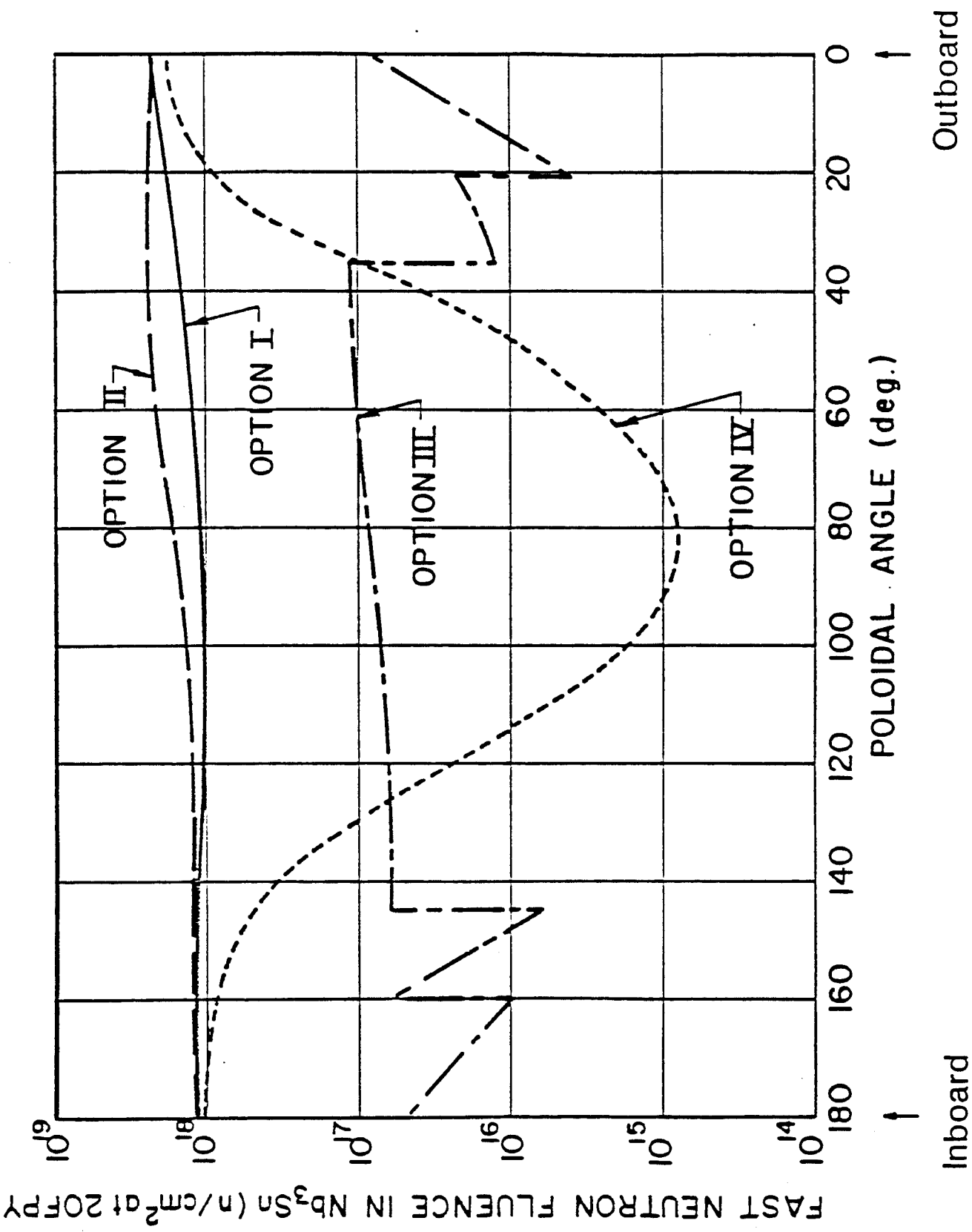Fig. 5.2-2. Poloidal variation of the peak nuclear heating in the S/C magnet at toroidal location $\phi = 0$.

Fig. 5.2-3. Poloidal variation of the peak fast neutron fluence at the S/C magnet at toroidal location $\phi = 0$.

the He manifolds replace some parts of the reflector. As a result, the damage in the magnet behind the He manifolds increases by a factor of ~ 5 over the nominal values. In Options II and III, the He manifolds could be arranged in the available space between the shield and the magnets and, therefore, are not expected to raise the damage in the magnets. In all cases, the magnet radiation limits are all met. It is interesting to notice that in Options II, III, and IV the S/C magnets are overprotected. Therefore, the shield thickness and, thus, the inner bore dimensions of the magnets can be reduced by 10, 28, and 10 cm, respectively, and all the limits are still satisfied.

It should be pointed out that in order to accommodate a 10% penetration area in the final design of ASRA6C the blanket should have a local TBR of 1.4, as will be shown later. This would require 21, 21 and ~ 34 cm thick blankets for Options I, II and III, respectively, to achieve an overall TBR of 1.05. With the current design of Option IV, the blanket will not be self-sufficient in tritium since the overall TBR amounts to 0.9 for 10% penetration area. A feasible solution is to replace the 5 cm thick first wall and the extra 10 cm of the shield by blanket materials. This results in a local TBR of 1.46 and an overall TBR of 1.1.

5.2.3 Economics and Mass Utilization

In order to perform an economics comparison of the four blanket options, it was necessary to adopt a set of unit costs. To allow for the more complex construction in Option II, III & IV, the fabricated cost of the structure was taken higher than in Option I. Filler material such as Be, LiPb, B_4C, Pb and W has the same unit cost in all the options. Table 5.2-3 gives the unit costs used for the various options.

Table 5.2-4 summarizes the economics and mass utilization for the four options. The table lists the mass in tonnes and the cost in 10^6 for the blanket, reflector, shield, and totals. It also lists the thermal power using the energy multiplication obtained in the neutronics analysis and the net electric power using a net efficiency of 38%. From these quantities we can obtain the total direct cost based on the blanket, reflector and shield in $/kWe and the mass utilization based on the drained mass of the blanket, reflector and shield in kWe/tonne. It should be noted that in order not to penalize Option IV for the use of the large amount of LiPb, the mass utilization is based on the drained mass as given in Table 5.2-4.

Table 5.2-3. Unit Costs Used in the Economic Comparison ($/kg)

	I	II	III	IV
Blanket				
Structure	45	80	80	80
Be	440	440	440	-
LiPb	14	14	14	14
Reflector	20	40	40	20
W	-	-	70	-
Shield				
Structure	20	40	40	20
B_4C	50	50	50	50
Pb	4	4	4	4

Table 5.2-4. Economics and Mass Utilization

	Option I mass/cost (tonnes/$x10^6)	Option II mass/cost (tonnes/$x10^6)	Option III mass/cost (tonnes/$x10^6)	Option IV mass/cost (tonnes/($x10^6)
Blanket (total)	1259/175	996/151	1064/183	8937/215
Reflector	8713/174	5756/230	3761/150	6121/122
W Shield			6095/427	
B_4C Shield	1809/74	1361/64	1365/55.7	1412/57.5
Pb Shield	1746/9	1374/9.4	1046/8.6	1436/7.5
Total	13527/432	9487/454	13331/824	17906/402
Drained Mass (tonnes)	13087	9080	12906	10129
Thermal Power (MWth)	4271	4180	4089	3542
Net Electric Power (MWe)	1623	1588	1554	1346
Total Direct Costs ($/kWe)*	266	286	530	299
Mass Utilization (kWe/tonne)**	124	175	117	133

* Based on direct cost of only the blanket, reflector and shield.

** Based on the drained mass of only the blanket, reflector and shield.

5.2.4 Comparison of Results

We can now list the first and second choices in each one of the comparison categories:

Configuration:	Option I, Option IV
Maintainability:	Option I, Option IV
Neutronics:	All four options will perform
Economics:	Option I, Option II
Mass Utilization:	Option II, Option IV

Given that the four options perform neutronically, the choice must be made on the basis of the remaining categories. Option I wins three of the four categories.

It is, therefore, concluded that the thin blanket of constant thickness and of uniformly elliptical cross section is the best choice under the circumstances.

5.3 Thin Blanket Design

5.3.1 Introduction

The blanket in a fusion reactor should not be viewed as an entity in itself, but rather as a constituent in a series of components, namely blanket, reflector and shield which together breed fuel, convert nuclear energy into heat and protect the superconducting magnets. Further, since the blanket suffers radiation damage and must be replaced periodically, it would be advantageous to have the capability of separating it from the reflector, thus minimizing the quantity of structure that must be replaced. At the same time, it is beneficial to recover useful energy from the reflector and use it at maximum efficiency in the power cycle. These kinds of considerations that have been motivating the design of the thin blanket which comes close to satisfying the requirements mentioned above.

Having decided to use $Li_{17}Pb_{83}$ as the breeding material for ASRA6C we were faced with the choice between a self-cooled blanket and a separately cooled blanket. Although self-cooled blankets have some attractive features, they have four major drawbacks:

1. High MHD losses due to pumping of liquid metals across magnetic field lines.
2. Potential for corrosion product transport in the primary loop.
3. Large and heavy piping needed in the primary loop.
4. Double walled steam generator tubes needed to alleviate T_2 diffusion into the steam cycle.

Separately cooled blankets manage to avoid these problems. However, the question arises as to what is the best coolant to use. The choices are basically limited to water (steam), molten salt or helium gas. We have generally avoided the use of water in close proximity to a liquid metal for safety reasons. Further, achieving a reasonable efficiency with a water cooled blanket is difficult and one is also faced with the problem of T_2 recovery from water. Molten salts have the potential of low pressure operation but have problems with corrosion, corrosion product transport and T_2 recovery from the molten salt. The major disadvantage of helium gas cooling is the need for operating at a high pressure. Nevertheless, taken overall, a helium gas cooled blanket has enough advantages to overcome this drawback, and for this reason we have opted to use it.

An important factor in the thin blanket is the use of Be metal as a moderator/multiplier. By cooling the blanket and reflector in series, using the same He gas, the energy in the reflector is recovered at a high temperature with a resulting improvement in the power cycle efficiency. This improvement is achieved while maintaining a low temperature at the interface between the breeding material and the structure. The salient features for the ASRA6C blanket are summarized in Table 5.3-1.

5.3.2 Description and Mechanical Design

The ASRA6C blanket is a He gas cooled design utilizing $Li_{17}Pb_{83}$ (LiPb) breeder, ferritic steel HT-9 structure and Be metal as moderator/multiplier. Over the years, there have been many He gas cooled blankets proposed for fusion reactors. In most of them the gas flows through channels in the first wall, then emerges into the blanket, cooling the breeding material, which is contained in tubes, on the way out. Since the blanket outer structure in such designs acts as a pressure vessel, it continuously operates at a high level of stress. We have avoided this condition in ASRA6C by keeping the He gas in small tubes which are immersed in a close-packed matrix of Be balls with the voids filled with LiPb. The result is a compact blanket 21 cm thick in which only the tubes are in a stressed condition. Nevertheless, the blanket outer structure is designed to withstand a leak in one or more of the He gas coolant tubes.

The question of corrosion product transport is ever present in any circulating liquid metal system. A self-cooled liquid metal blanket is particularly susceptible to this problem since there is continuous dissolution in the hot zone, namely the blanket, with deposition in the cold zone, usually the steam generator. In this design we have avoided the problem in three ways. First, the maximum liquid metal/structure interface temperature is maintained low. Second, the LiPb is circulated at a very slow rate for T_2 recovery and is essentially static. Finally, the LiPb remains isothermal in the T_2 recovery system preventing any deposition of corrosion products.

The reaction chamber in ASRA6C is toroidal with a major radius of 20 m. The cross section of the vacuum chamber is uniformly elliptical in the toroidal direction with a vertical dimension of 6.4 m and a horizontal dimension of 4.6 m. There is a total of 30 coils in the reactor with six coils completing a field period. Each field period extends 25.12 m toroidally along the axis

Table 5.3-1. Salient Features of ASRA6C Blanket

The blanket is He gas cooled, utilizes LiPb breeder, HT-9 structure and Be multiplier/moderator and is only 21 cm thick.

It is backed up by a 44.2 cm thick reflector made of modified 9Cr1Mo the energy of which is directly used in the power cycle.

The overall breeding ratio is 1.05, the overall energy multiplication is 1.2 and the gross power cycle efficiency is 42.7%.

The T_2 is recovered from a slowly circulated LiPb stream and the total T_2 inventory in the blanket is < 6 g.

T_2 leakage through a single wall steam generator is ~ 10 Ci/day.

of the ellipse. There are four RBU in each field period with a length on axis of 6.28 m.

Figure 5.3-1 is a top view of a RBU where its curvature indicates that it is a segment of a torus. The radial lines indicate the joints between cells while the circumferential lines indicate coolant manifolds. Figure 5.3-2 is a cross section looking in the toroidal direction showing the elliptical configuration of the blanket. In this figure the manifolds are shown as ellipses attached to the outer surface of the blanket. There are three double supply manifolds and three double return manifolds. The internal flow distribution is discussed in the thermal hydraulics section. Each double manifold set will have a single radial header, either supplying or returning coolant gas to or from it.

Each RBU is divided into 28 cells oriented circumferentially in the toroidal direction. The cells are wider (24.0 cm) at the outer perimeter of the RBU than on the inner perimeter (19.5 cm), thus creating the toroidal shape needed. A cross section of a cell is shown in Fig. 5.3-3. Note that the outer walls of the cell are shaped semi-ellipsoidally to make them capable of withstanding a He gas leak in one or more cooling tubes. This figure shows the cooling tubes surrounded by a matrix of Be metal balls which in turn are surrounded with molten LiPb. Each cell has individual cooling tubes and only communicates with the adjacent cells through the common manifolds.

The cooling tubes are 1.0 cm internal diameter and have a wall thickness of 0.5 mm. There are two types of cooling tubes in this blanket, the outer and inner tubes. The outer tubes provide cooling for the first wall and absorb a large fraction of the nuclear heating in the front zone of the blanket. These tubes spiral around the inside of the cell coming in contact with the first wall. Each outer tube makes only seven loops inside the cell before returning to the exit manifold. There are also inner tubes which cool the central part of the cell. These tubes, of which there are three, perform a small radius large pitch spiral, traveling the full length of a cell quadrant. All the inner and outer tubes are the same length and thus present an equal impedance to the flow of He gas.

Figure 5.3-4 is a cross section through a portion of a cell, showing outer and inner tubes as well as a single set of supply and return manifolds. It shows the He gas supply manifold connected to the tubes at a manifold flange. The tubes travel one-sixth of the circumference in both directions
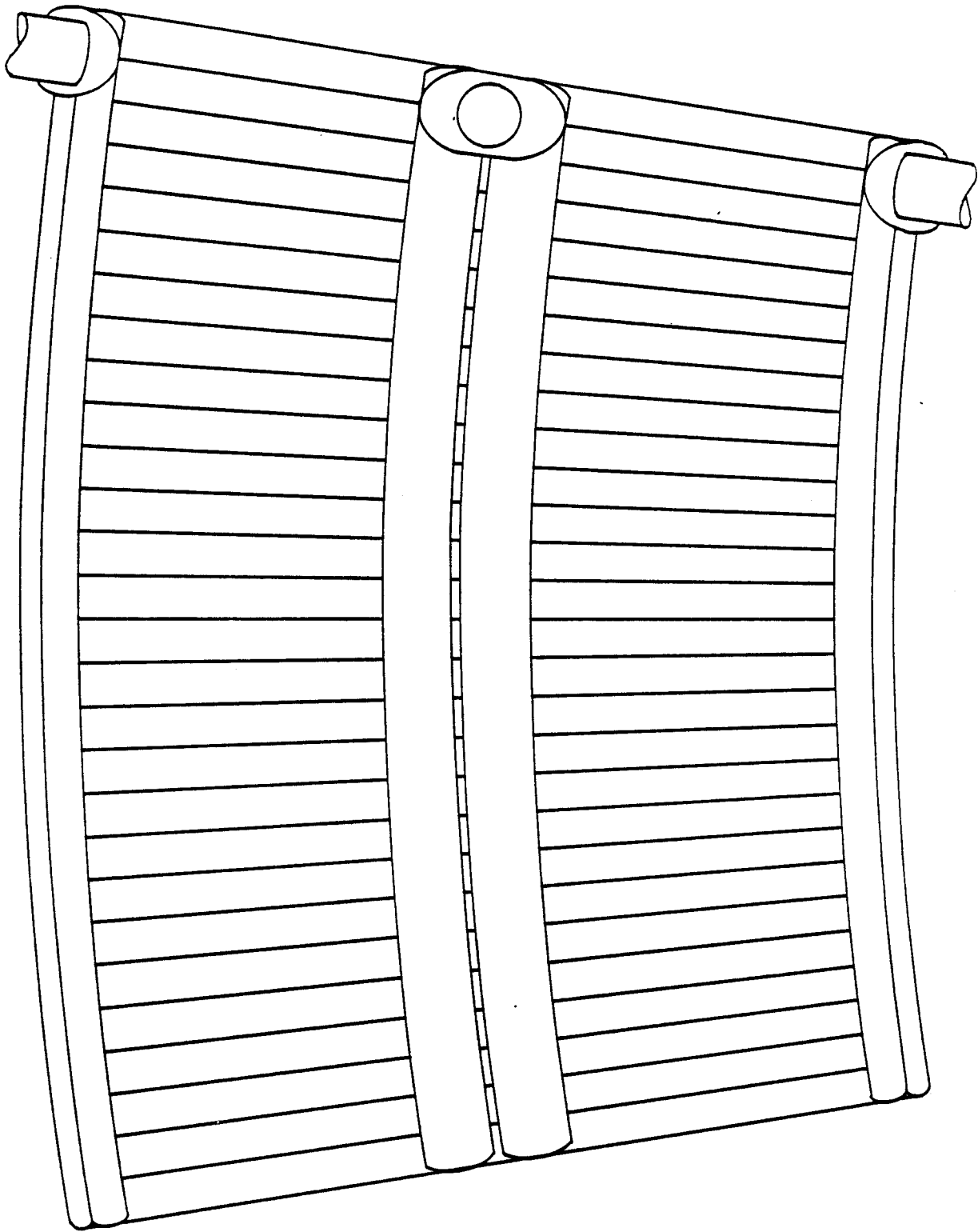
Fig. 5.3-1.   Top view of RBU.
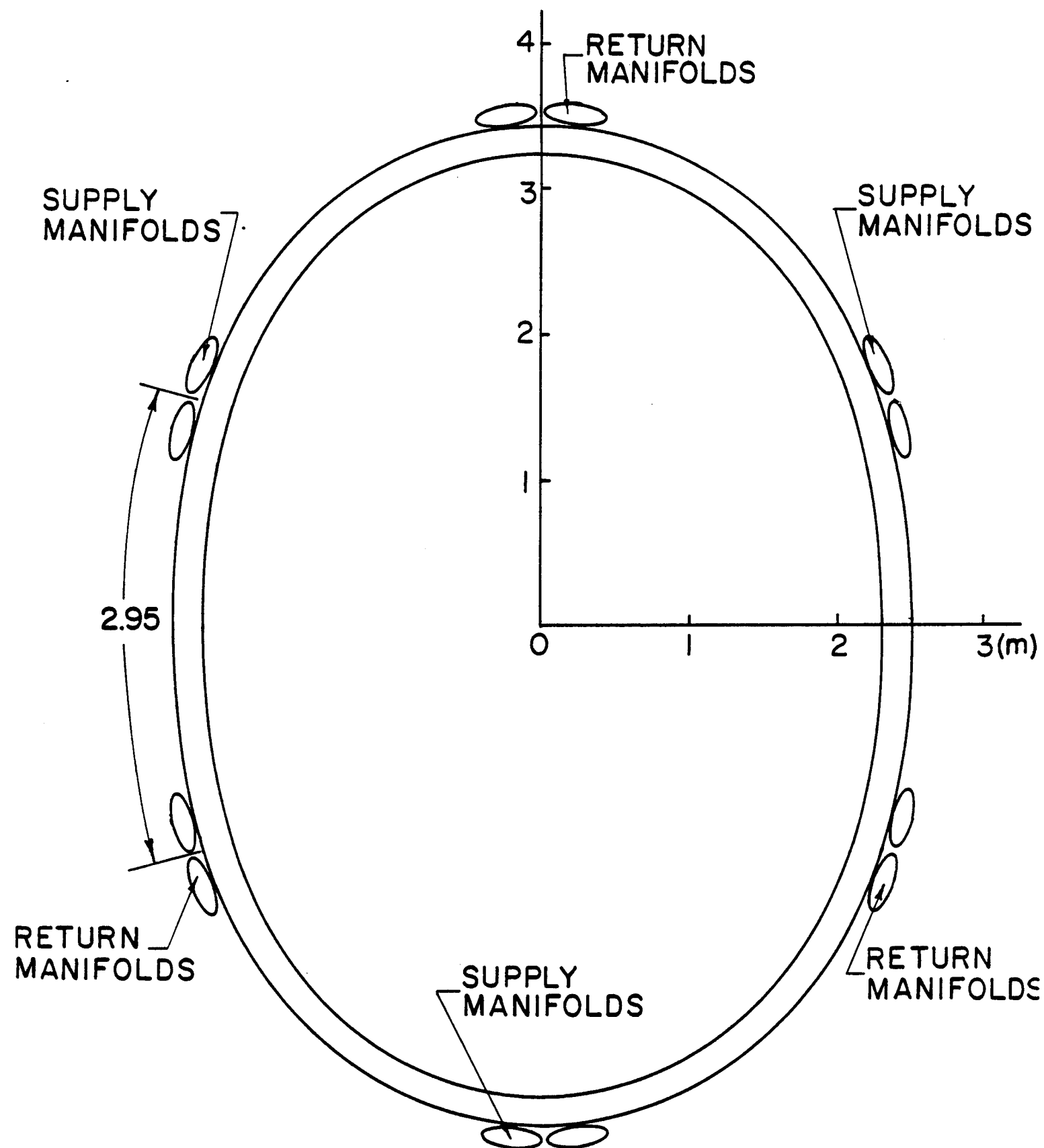
Fig. 5.3-2.   Cross section of RBU looking in toroidal direction.
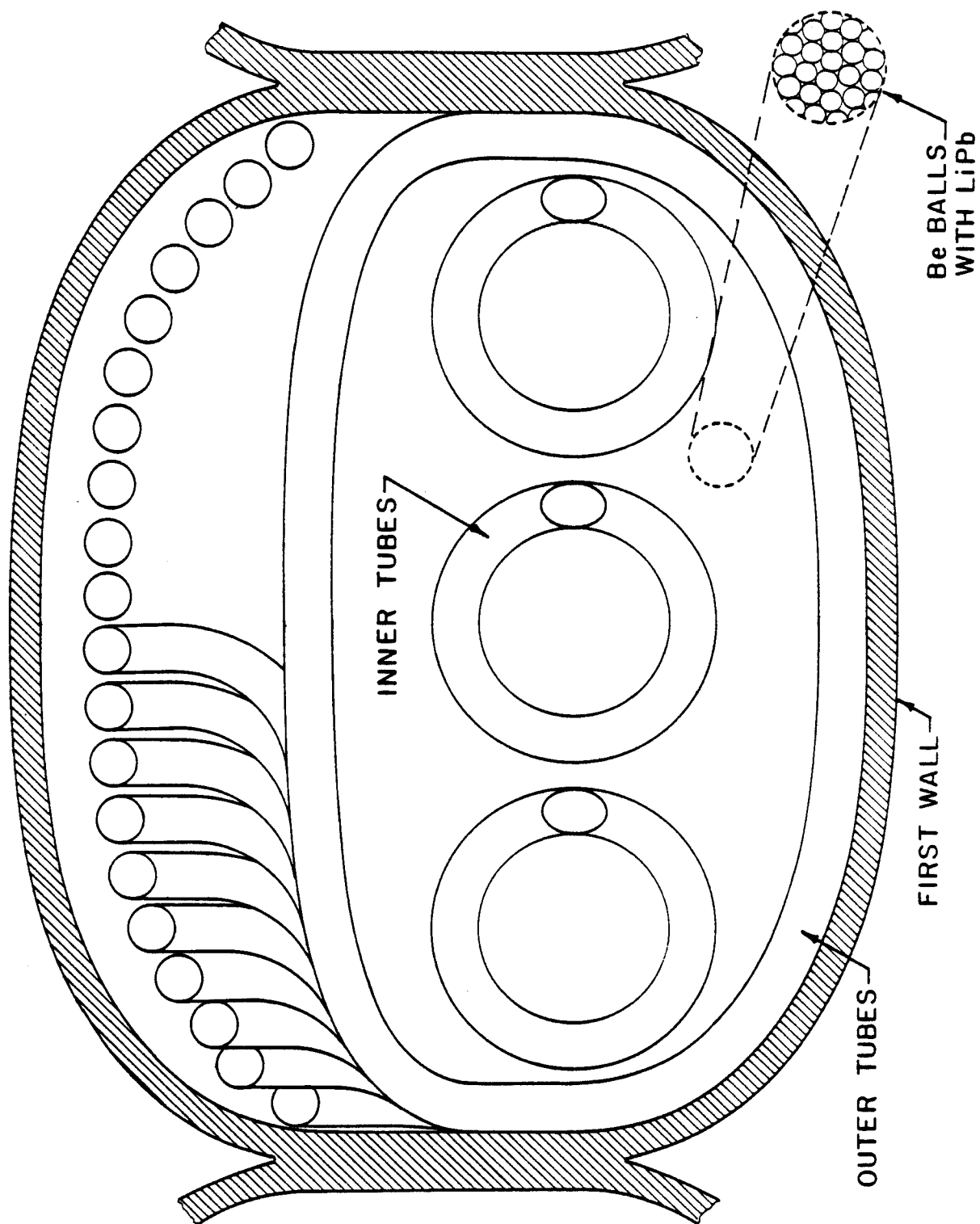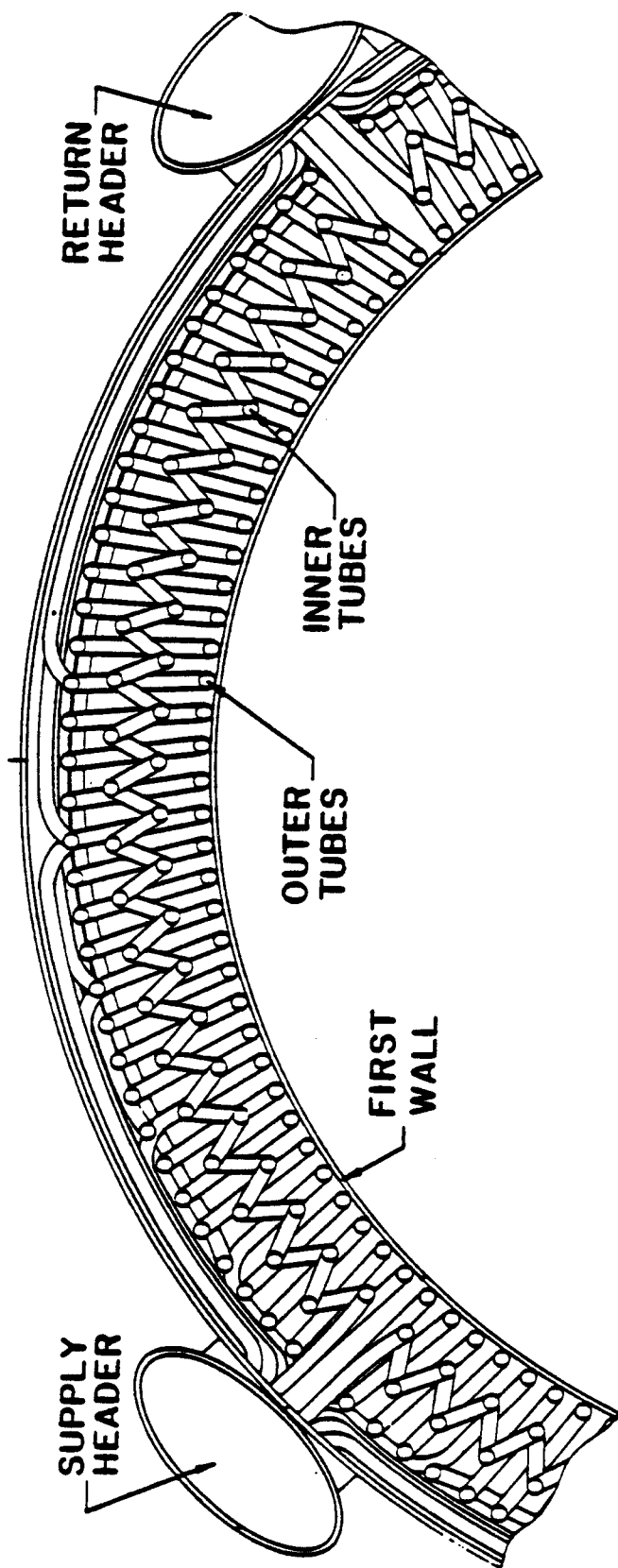
Be BALLS WITH LiPb

INNER TUBES

FIRST WALL

OUTER TUBES

Fig. 5.3-3. Cross section of a blanket cell.

RETURN HEADER

INNER TUBES

OUTER TUBES

FIRST WALL

SUPPLY HEADER

Fig. 5.3-4. Longitudinal cross section through cell segment.

and are then connected to a return manifold. This figure shows that each outer tube executes only seven complete loops within the cell before travelling the remaining distance to the return header in the rear zone of the blanket.

It is important at this point to explain why two manifolds are used as a set and why they are shaped elliptically. To minimize the He gas pumping power, it is necessary to limit the maximum gas velocity in the manifolds to < 100 m/s. Since the header connection to the manifolds is always made on one side of the RBU, the manifolds must be sized to be capable of delivering gas the whole length of the RBU to the last cell. Further, the extent to which the manifold penetrates into the space of the reflector determines the hot spot in the nuclear heating of the superconducting coil. To satisfy these requirements it was decided to use two manifolds at every supply and return point, each feeding alternate cells, and to make the manifolds elliptical, to limit their protrusion into the reflector space. This makes it possible to supply an RBU which is up to 6 m long from one end, while maintaining reasonably low gas velocities.

After the coolant gas leaves the blanket through the return manifolds, it is routed through the reflector. Each set of two return manifolds is connected to a single coupling which directs the He gas flow into the reflector. It should be noted that the supply headers and the blanket/reflector couplings are all located on one end of a RBU to make it possible to slide out the RBU from its reflector from one end.

The flow path of the He gas through the blanket/reflector can be summarized in the following way:
1. He gas comes in through three supply headers.
2. Each header is attached to an elliptical connecting pipe which feeds a set of two supply manifolds.
3. From the supply manifolds the He gas travels through the cooling tubes ending at the return manifolds.
4. From the two return manifolds the gas goes through another elliptical connecting pipe which is attached to the blanket/reflector coupling.
5. The He gas then travels through the reflector and finally exits the reflector through three return headers.

Finally the question of penetrations has to be addressed. Penetrations extending 40 cm in the toroidal direction and up to 2 m poloidally can be

Table 5.3-2. Pertinent ASRA6C Option I Blanket Parameters

First wall radius (cm)	232-322
Blanket thickness (cm)	21
Reflector thickness (cm)	44.2
Shield thickness (cm)	31.8
Volumetric fraction in the blanket	
HT-9 (v/o)	10.3
He + void (v/o)	20
Be (90% density) (v/o)	55.7
LiPb (v/o)	14
Overall breeding ratio	1.05
Overall blanket multiplication	1.20
No. of RBUs in reactor	20
No. of cells per RBU	28
Cell width	19.5 - 24.0
Cooling tube ID (cm)	1.0
Cooling tube OD (cm)	1.10
First wall and rear wall thickness (cm)	0.6
No. of cooling tubes per cell	138
No. of coolant supply manifolds per RBU	6
No. of coolant return manifolds per RBU	6
Dimensions of manifolds	15 x 40
Mass of LiPb in reactor (tonnes)	635
Mass of Be in reactor (tonnes)	436
Mass of HT-9 in blanket (tonnes)	372
Mass of 9Cr1Mo in reflector (tonnes)	8300

easily accommodated by fitting them within two cells as shown in Fig. 5.3-5. The figure shows the tubes shunted over to the sides of the cells to make room for a frame which surrounds the penetration. The poloidal extent of the penetration can be quite large and is only limited by the spacing between manifolds.

Penetrations which must extend more than 40 cm toroidally will be more difficult to accommodate. Such penetrations will have to terminate near manifolds, or possibly, manifolds will have to be specially located. Table 5.3-2 lists the pertinent parameters of the ASRA6C Option I blanket.

5.3.3 Thermal Hydraulics

The primary aim of thermal hydraulic analysis is to ensure that the blanket structures are adequately cooled and that the temperatures on the first wall or elsewhere do not exceed recommended design limits for the materials at those conditions.

The blanket in ASRA6C is cooled with He gas at 80 atm. Helium cooled blankets have a general reputation for requiring a high pumping power. Pumping power is a function of the volumetric flow rate and the pressure drop, and is therefore directly dependent on the pressure of the coolant. Most He cooled blanket designs have used 50 atm as the coolant pressure, because the gas was contained within the structural shell of the blanket. Since the He gas in this blanket is contained in small tubes, we have been able to operate at a higher pressure. At the higher pressure, volumetric flow is lower for the same mass throughput and the velocity is lower, therefore the pressure drop is lower, directly reducing the pumping power. We have found that 80 atm seems to be the pressure at which the benefits of lower pumping power begin to be offset by the increased structure in the blanket.

In this design the He gas enters the blanket at 275°C, exits at 510°C, then is routed to the steel reflector and exits at 575°C, finally going to the steam generator. As mentioned earlier, there are two kinds of cooling tubes in the blanket identified as the outer and inner tubes. These tubes are 1.0 cm internal diameter and 1.10 cm external diameter. Each sextant of each blanket cell has twenty outer tubes and three inner tubes. The outer tubes cool the front zone of the blanket including the first wall. On entering the blanket, each outer tube executes only seven loops inside the cell, then travels the remaining distance to the exit manifold in the rear (low nuclear heating zone) of the blanket. The next outer tube crosses over the seven
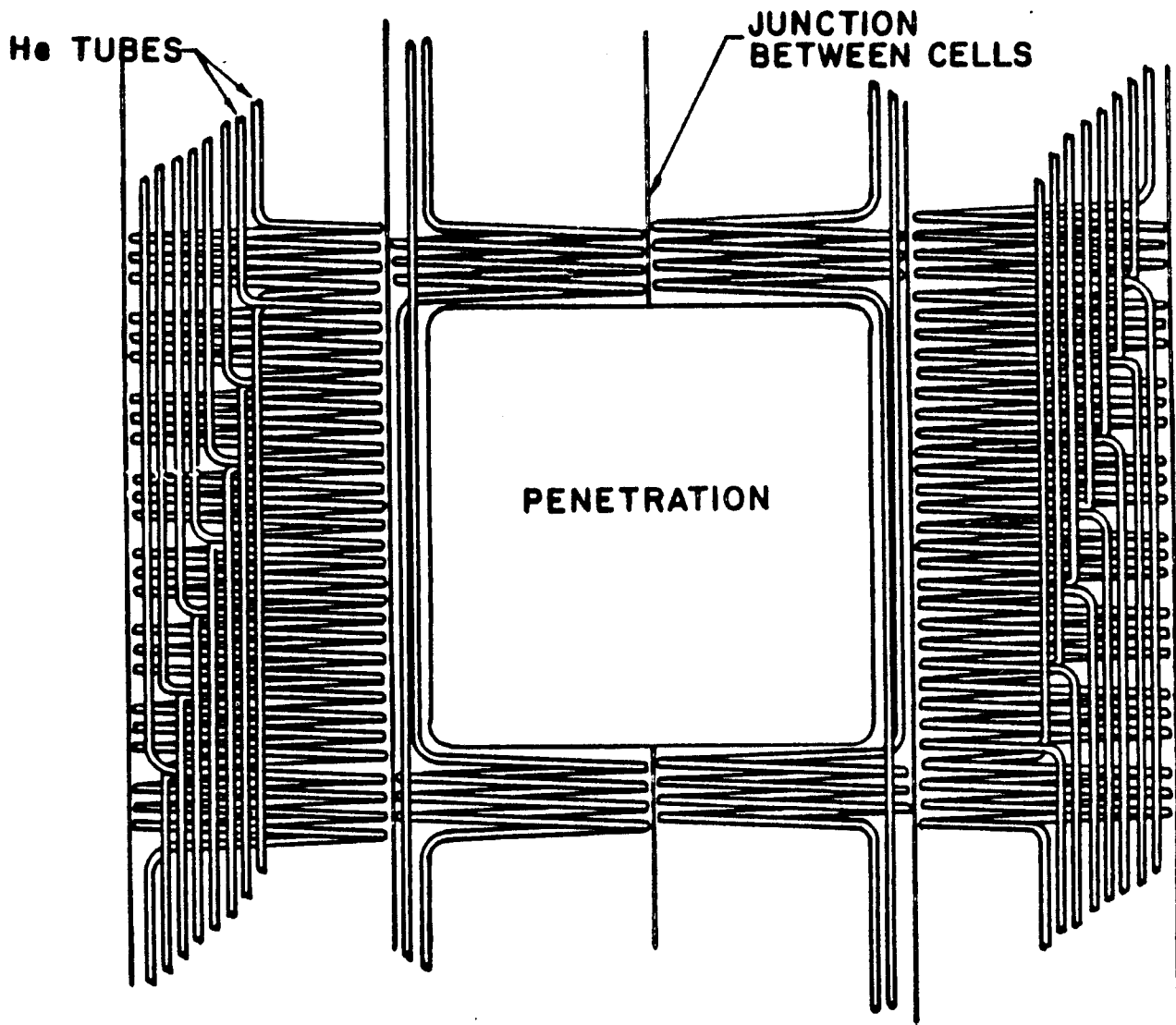
Fig. 5.3-5.   Typical blanket penetration showing tube routing.

loops of the preceding tube, then executes seven loops of its own before exiting to the return manifold. From the plasma side, it appears as if only one tube spirals around the circumference of the cell, but in fact there are many. This design is unique because the length of all the tubes is the same, 626 cm, therefore, the pressure drop and mass flow rate are the same.

The inner tubes, of which there are three per cell quadrant, travel the full length of the quadrant executing a large-pitch small radius spiral. They provide a heat sink in the center of the cell and are also 626 cm long, the same as the outer tubes. Neglecting the small inertia effects due to the different pitch between the inner and outer tubes, the pressure drop in all the tubes will be the same, ensuring that the mass flow rate in them will also be the same.

The average nuclear heating in the first wall is 11 W/cm^3, in the rear wall it is 3.3 W/cm^3 and in the bulk it varies from 11.4 W/cm^3 at the front to 4.7 W/cm^3 at the rear. At the outer midplane, nuclear heating peaks by a factor of 1.7 and at that point, the above values go up by this factor. The number of outer cooling tubes used has to be adjusted poloidally to accommodate the nuclear peaking. However, the thermal hydraulic parameters will be based on the average nuclear heating.

The total thermal power in the blanket consists of nuclear heating and radiant surface heating. Nuclear heating consists of 80% of the fusion power multiplied by the overall blanket multiplication. The total radiant surface heating depends on impurity control assumption and can vary from a lower limit of 228 MW to an upper limit of 494 MW. Using the upper limit we obtain as the total thermal power 3648 + 494 = 4142 MW_{th}. Of this amount, 76% of the nuclear heat and all the radiant heat ends up in the blanket or 3266 MW_{th}. The power in the reflector is only 876 MW_{th}.

To determine the maximum temperature at the first wall it is necessary to obtain the bulk coolant temperature profile in the outer tubes. Since the He gas circulates in a spiraling motion within the outer tubes which are in contact with the first wall, it is the coolant bulk temperature which will determine the hot spot on the first wall. We write steady state one dimensional energy balance equations for the He gas and for the blanket materials (Be and LiPb) along the circumferential length neglecting circumferential conduction and all convection. This approach is conservative in that it predicts slightly higher circumferential temperature gradients in the coolant and the blanket

materials. The results are plotted Fig. 5.3-6 where the He gas temperature profile is plotted as a function of the tube length for the first and the last outer tubes in any cell sextant. The He gas temperature as it leaves the last point of contact with the first wall is 495°C. To this must be added the cumulative temperature rise through the gas film on the inside of the coolant tube, conduction through the tube wall, the Be-LiPb and finally the temperature rise across the first wall due to surface and nuclear heating.

The average velocity in the tubes is 76 m/s and the heat transfer coefficient 0.71 W/cm^{2}K. For the average condition where the tube spacing at the first wall is 1.09 cm, the heat flux on the coolant tube on the side in contact with the first wall is 23.6 W/cm^2. This heat flux can be made to be the same at peak nuclear heating locations by simply adding tubes and decreasing the spacing between them.

The temperature drop across the first wall depends on the surface heat load which is dependent on the impurity removal assumption and to a lower degree on the nuclear heating. Using the lower limit gives a surface heat load of 10 W/cm^2 while the upper limit yields 20.5 W/cm^2. Assuming the lower limit of surface heat load and average nuclear heating gives an average first wall temperature of 544°C. The same surface heating at the peak nuclear heating gives an average first wall temperature of 548°C. If, however, the upper limit of surface heat load is used, the corresponding average first wall temperatures would be 554°C and 558°C respectively for the average and the peak nuclear heating zones. These values assume no heat transfer in the circumferential direction and are therefore conservative.

The total He gas mass throughput through the reactor is 2600 kg/s. The pressure drop in the blanket tubes and the manifolds is calculated using the equation:

$$\Delta p = \frac{2 f \rho v^2 L}{gD}$$

where f is a friction factor, ρ the density, v the velocity, L the length, g acceleration due to gravity and D the diameter. The friction factor is obtained from:

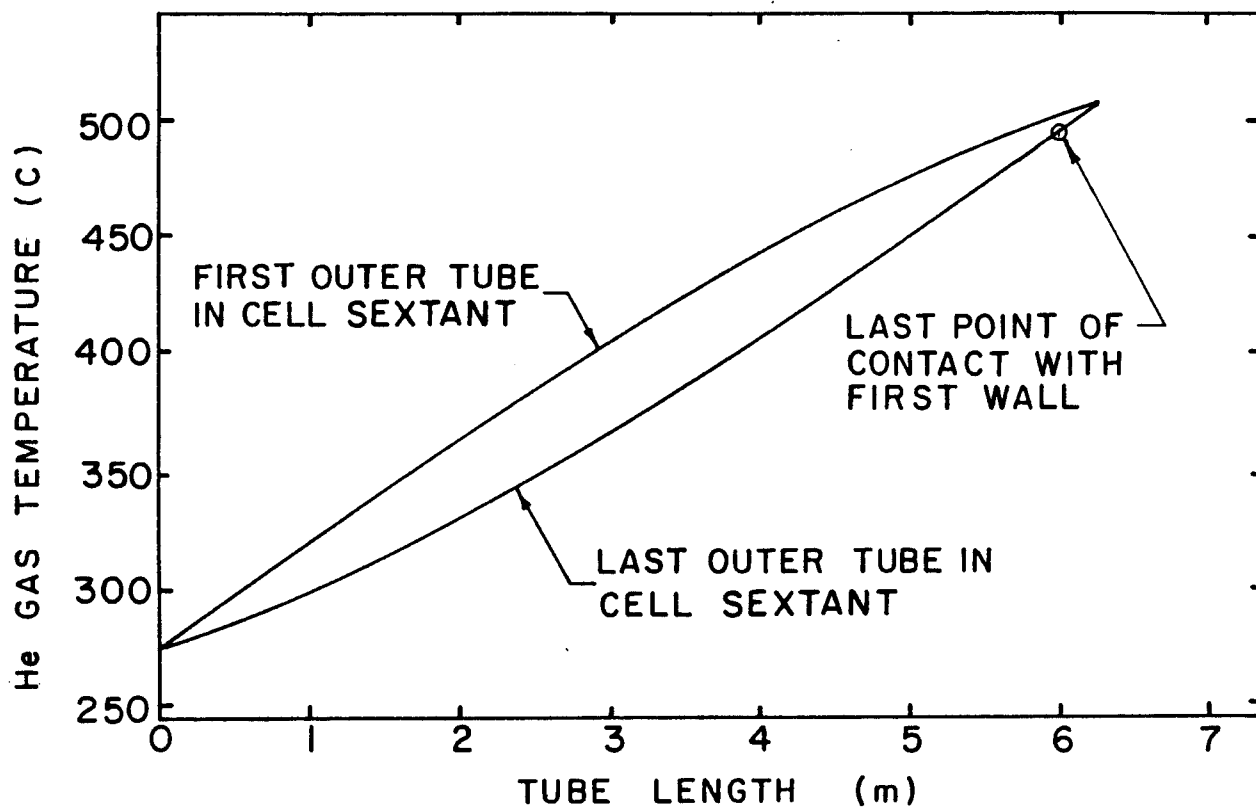$$f = 0.0024 + 0.125 \left(\frac{Dv\rho}{\mu}\right)^{-0.32}$$

Fig. 5.3-6.   Temperature profile in coolant tubes.

where μ is the gas viscosity. The calculated friction factor is .004 and Δp is equal to 1770 g/cm^2.

Pumping power is then equal to VΔp where V is the volumetric throughput. Using the volumetric throughput at the average gas density we obtain a pumping power of 77 MW for the blanket.

Table 5.3-3 gives the thermal hydraulic parameters of the blanket.

5.3.4 Blanket Stresses

During normal operation the blanket outer structural shell operates at a low pressure and consequently a negligible pressure stress. The blanket, however, is designed to withstand a leak in one or more coolant tubes, in which case the shell will experience a pressure of 8 MPa. The cooling tubes, however, are constantly subjected to the high pressure and for this reason we have designed them with a higher margin of safety.

Figure 5.3-7[1] gives the recommended design stress values for HT-9 ferritic steels as a function of temperature. There is a discontinuity in the curve where the design stress criterion changes from a fraction of the yield strength to creep rupture in 10^5 hours. This discontinuity occurs at ~ 535°C. From the previous section we determine that the maximum average temperature in a coolant tube is ~ 550°C and of the first wall 558°C. The corresponding recommended design stress values are 128 MPa and 125 MPa, respectively.

The maximum stresses in the coolant tubes are circumferential, which for a thin walled cylindrical vessel are:

$$\sigma = \frac{Pr}{t}$$

where P is the pressure, r is the average radius and t the wall thickness. For the coolant tubes of 1.0 cm internal diameter and 0.05 cm wall thickness the stress is 85 MPa. This is only 2/3 of the recommended design stress at this temperature.

The stresses in the semi-ellipsoidal toroidal shell which make up the front and the rear surfaces of a blanket cell are:[2]

In the center of the semi-ellipse:

Longitudinal stress $\qquad \sigma_L = \frac{PR^2}{2th}$

Table 5.3-3. Thermal Hydraulic Parameters of the Blanket

|	
Fusion power (MW)	3800
Total thermal power (MW_{th})	4142
Thermal power in the blanket (MW_{th})	3266
He gas inlet temperature (°C)	275
He gas outlet temperature from blanket (°C)	510
He gas outlet temperature from reflector (°C)	575
He gas pressure (MPa)	8.1
He gas mass throughput (kg/s)	2660
Heat flux on front surface of outer tubes (W/cm^2)	23.6
Avg. nuclear heat in FW (W/cm^3)	11
Peak nuclear heat in FW (W/cm^3)	18.7
Lower limit surface heat (W/cm^2)	10
Upper limit surface heat (W/cm^2)	20
Avg. FW temp. at peak nuclear heating (°C)	548
Avg. FW temp. at peak nuclear heat and max. surface heat (°C)	558
Max. temp. of coolant tube (°C)	550
Avg. He gas velocity in coolant tube (m/s)	76
Avg. heat transfer coefficient in coolant tube (W/cm^2K)	0.71
Avg. He gas velocity in supply manifold (m/s)	33.6
Avg. He gas velocity in return manifold (m/s)	47
Max. stress in coolant tubes (MPa)	85
Max. thermal stress in FW (MPa)	± 80
Min. Thermal stress in FW (MPa)	± 40
He gas pressure drop in the blanket (MPa)	0.173
Total pumping power for the blanket (MW)	77
LiPb pumping power (kW)	~ 700
Gross power cycle efficiency (%)	42.7
Gross electric power output (MWe)	1770
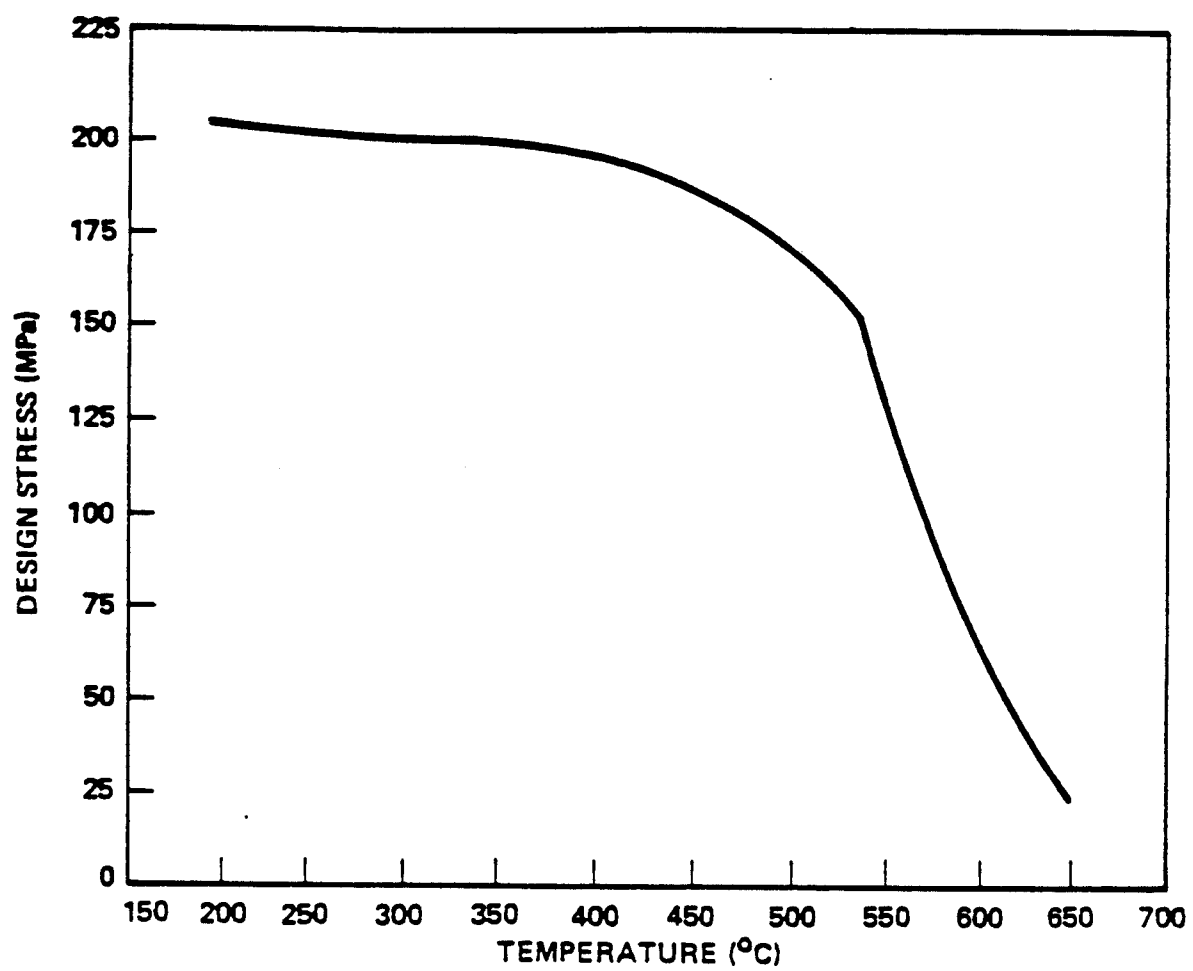
Fig. 5.3-7. Allowable design stresses in HT-9.

Tangential stress $\qquad \sigma_t = \dfrac{PR_t}{2t} = \dfrac{PR^2}{2th}$

In the knuckle:

Longitudinal stress $\qquad \sigma_L = \dfrac{PR}{2t}$

Tangential stress $\qquad \sigma_t = \dfrac{PR}{t}$

where P is the pressure, R is the half width of the major dimension of the semi-ellipse, t the wall thickness, h the half width of the minor dimension of the semi-ellipse and R_t the radius of curvature of the front of the semi-ellipse. For this blanket P is 8.1 MPa, and R is 10.7 cm, h is 5.4 cm at the widest portion of the cell. In a semi-ellipsoidal toroidal shell, the dominant stresses are the longitudinal and tangential stresses in the center of the shell and are equal to 143 MPa in this case. As mentioned, in the worst case (upper limit of surface heating and peak nuclear heating) the recommended design stress value based on creep rupture in 10^5 hours is 125 MPa. It should be repeated that this stress will be felt in the toroidal shell only in the event of a leak in a coolant tube. We expect that a leak can be detected within minutes, the plasma shut down and the blanket depressurized. The equilibrated temperature of the blanket at shutdown is only 435°C which will also be the temperature of the first wall and the recommended design stress at this temperature is 185 MPa. At these conditions, low pressure He gas can be circulated indefinitely to absorb afterheat.

The thermal stress in the first wall is calculated by the following formula:

$$\sigma_{th} = \pm \frac{\alpha}{2} \frac{E}{k(1-\nu)} \left[q_s t + \frac{q_n}{2} t^2 \right]$$

where α is the coefficient of expansion, E the modulus of elasticity, k the thermal conductivity, ν Poisson's ratio, q_s surface heating, q_n nuclear heating and t the wall thickness. For HT-9 at 550°C and using the lower limit surface heat and average nuclear heating we obtain $\sigma_{th} = \pm 42$ MPa while for the upper limit surface heat and peak nuclear heating, $\sigma_{th} = \pm 80$ MPa. This

means that the front surface of the first wall will be in compression and the rear surface in tension.

It is important to understand the significance of the thermal stress. Structure that has not experienced radiation creep will have the thermal stress in it as soon as the plasma is turned on. Thermal and radiation creep, however, will anneal the thermal stress out. This means that the structure, after a certain amount of radiation exposure, will have no thermal stress as long as there is surface and nuclear heating. However, when the plasma is turned off, the thermal stress reappears in reverse, namely the front surface of the first wall will be in tension and the rear surface in compression. Assuming the higher value of thermal stress, the implication of this is that in the event of a coolant line leak and plasma shutdown, the first wall will have a tensile stress of 223 MPa on the front surface and 63 MPa on the rear surface until the blanket is depressurized. Again we feel this is tolerable for a few minutes, in view of the fact that yield strength of HT-9 at 550°C is > 300 MPa.

5.3.5 Reflector Design

The reflector in ASRA6C is an important component in the reactor since it acts as a part of the shield and its energy is used directly in the power cycle to improve the overall thermal efficiency. It is cooled in series with the blanket, using the same He gas.

The reflector is made of the modified 9Cr1Mo ferritic steel which has been normalized and tempered. The modification is done by the addition of 0.06-0.1% Nb and 0.18-0.25 V to the original composition of 9Cr1Mo.[3] In this composition this alloy has creep strength which exceeds that of standard 9Cr1Mo for the temperature range 427-704°C. The total elongation and reduction of area values for all test temperatures and rupture times up to 22,500 hours exceed 15% and 70% respectively. Estimated design allowable stress values are considerably higher than the standard alloy, being a factor of two higher at 550°C. Figure 5.3-8 gives the allowable design stress value as a function of temperature for the range 550°C to 640°C. These values have been obtained from V. Sikka's paper.[3]

The reflector is built up of concentric ellipses which have cooling channels machined into them prior to assembly. Figure 5.3-9 shows an end view of the reflector and a cross section at plane A-A. The details show the manifold
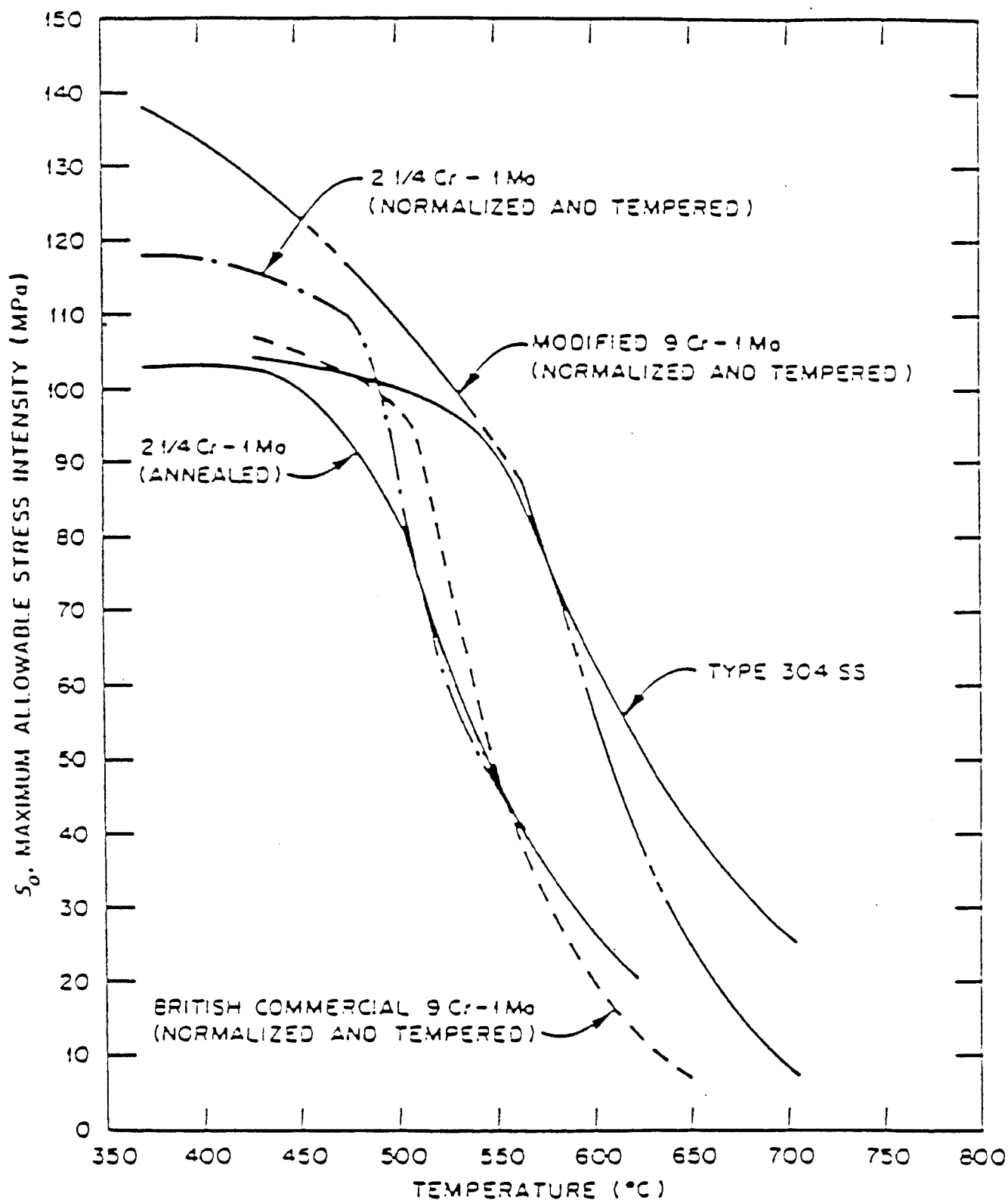
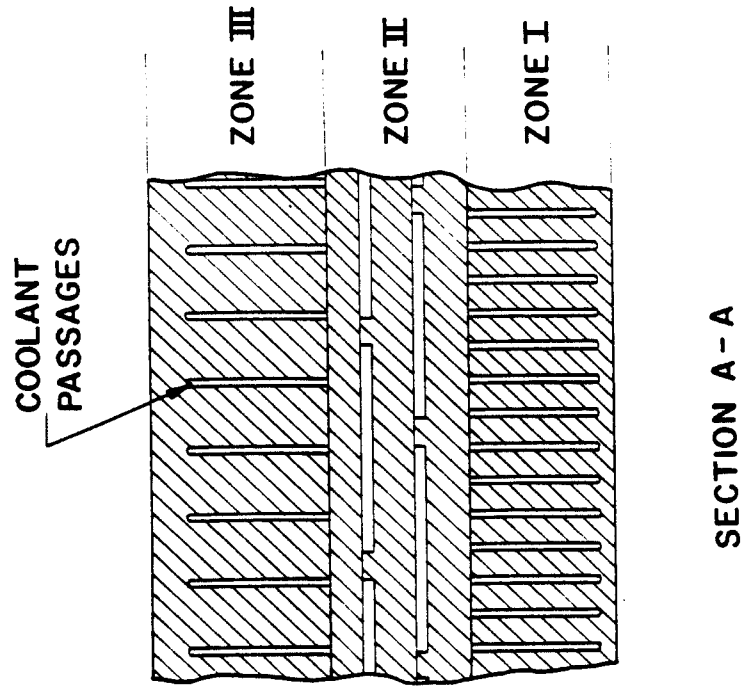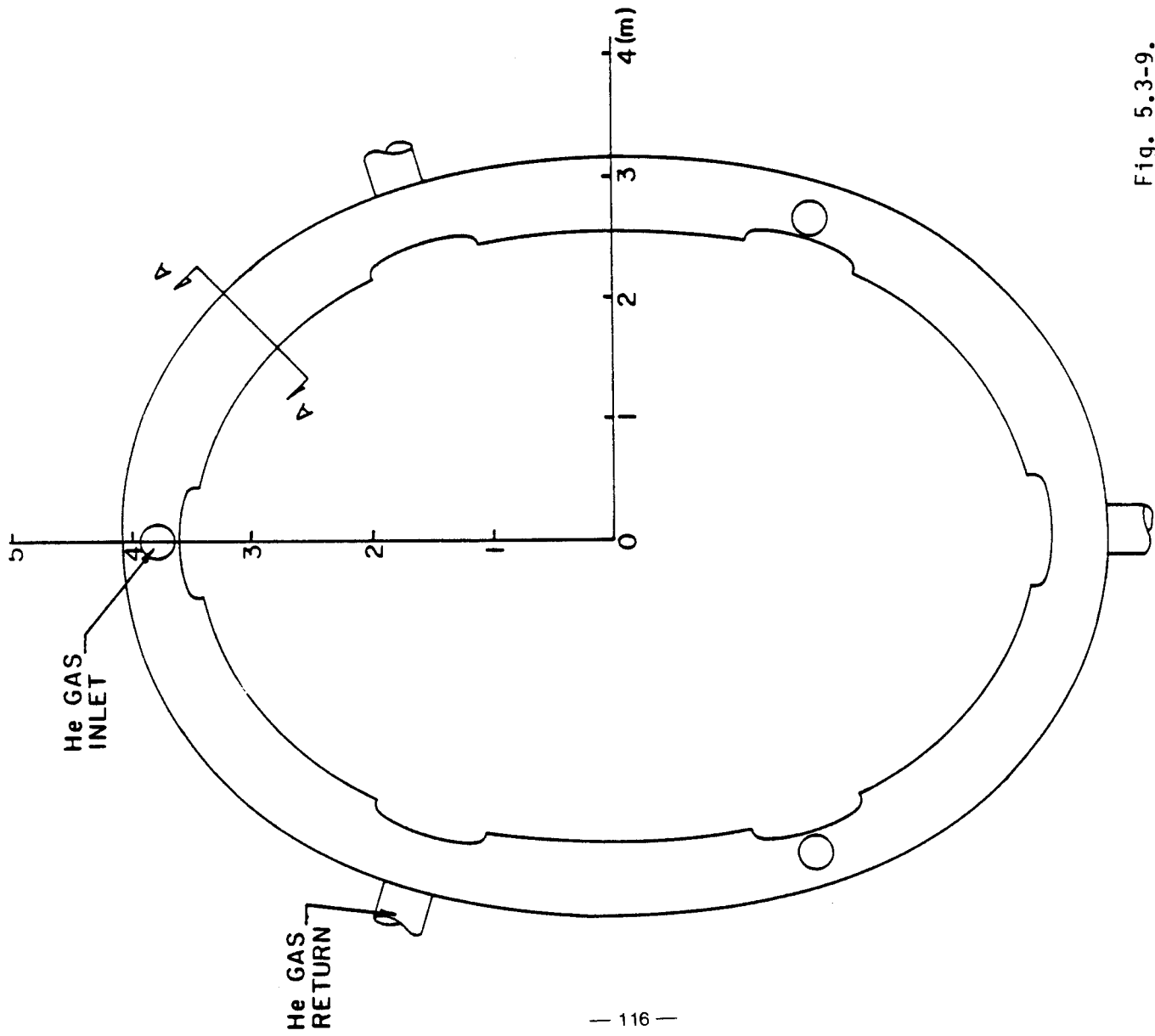Fig. 5.3-8.   Allowable design stresses in modified 9Cr1Mo.

ZONE Ⅲ

ZONE Ⅱ

ZONE Ⅰ

COOLANT
PASSAGES

SECTION A-A

4(m)

3

2

1

0

He GAS
INLET

He GAS
RETURN

REFLECTOR END VIEW

Fig. 5.3-9. End view and cross section of reflector.

cutouts on the inner surface of the elliptical reflector and also the three He gas inlet ports. The cross-section at A-A shows the reflector as consisting of three zones used for thermal hydraulic analysis. The first zone consists of a single ellipse 13.6 cm thick which is deeply grooved on the back side. The grooves are 0.5 cm thick and 12.6 cm deep, coming to within a centimeter of the front surface. This is done to reduce the effect of thermal stress while keeping the hoop stresses low. The second zone consists of an assembly of three ellipses with cooling grooves machined into them. These ellipses carry the longitudinal force in the reflector. Finally, the last zone is another heavy walled ellipse with grooves machined on the inside surface.

The He gas flow path in the reflector is chosen to minimize high temperature buildup and the coolant channel distribution is consistent with the nuclear heating in the reflector.

The reflector is cooled with He gas at 80 atm in series with the blanket. It receives gas from the blanket at 510°C and discharges it to the steam generator at 575°C, giving up 876 MW of thermal energy in the process.

Figure 5.3-10 is a segment of the same end view as in Fig. 5.3-9 but has the He gas flow path indicated on it. He gas enters the three ports, travels axially and then splits in half and travels circumferentially through the grooves in Zone I. Notice that there is countercurrent flow of gas through alternate grooves in this zone, designed specifically to average temperatures out. A considerable amount of energy recirculation takes place from the countercurrent flow; however, no energy is wasted. After going through Zone I the gas then goes through Zone II also flowing countercurrent but in grooves at two different radii. This is done for a very special reason. The nuclear heating in the first row of grooves in Zone II is greater than in the second row. Thus the gas flowing in the first row will end up at a slightly higher temperature than that in the second row. The last zone has only singular flow of gas in it before the two streams coming from opposite sides combine and exit together from the back of the reflector.

Helium gas temperatures are determined from energy and mass flow balance equations, and heat transfer coefficients are calculated using average gas velocities and properties for each zone. The results are presented in Table 5.3-4.

Table 5.3-4. Thermal Hydraulic and Stress Parameters of Reflector

	Zone I	Zone II	Zone III
Zone thickness (cm)	13.5	13.4	17.3
Inner radius at midplane (cm)	255	268.5	281.9
Outer radius at midplane (cm)	268.5	281.9	299.2
Local zone void fraction (%)	13.1	13.3	5.1
Overall void fraction (%)	4	4	2
Nuclear heating (MW)	560	237	79
Mass flow per 1/3 reflector (kg/s)	887	887	887
Inlet He gas temperature (°C)	510	551	569
Outlet He gas temperature (°C)	551	569	575
Characteristic channel width (cm)	0.5	1.0	0.5
Average He velocity (m/s)	45	43	50
Average heat transfer coefficient (W/cm^2-K)	0.40	0.40	0.40
Temperature of outer wall surface (°C)	560	N/A*	590
Temperature of inner wall surface (°C)	551	N/A*	586
Average cylinder temperature (°C)	555	565	594
Recommended design stress (MPa)	92	85	64
Thermal stress (MPa)	± 14	N/A*	± 2.8
Pressure stress (MPa)	55	32	55
Maximum stress (MPa)	69	32	58
Average stress (MPa)	55	32	55
Pressure drop (MPa)	0.032	0.025	0.023

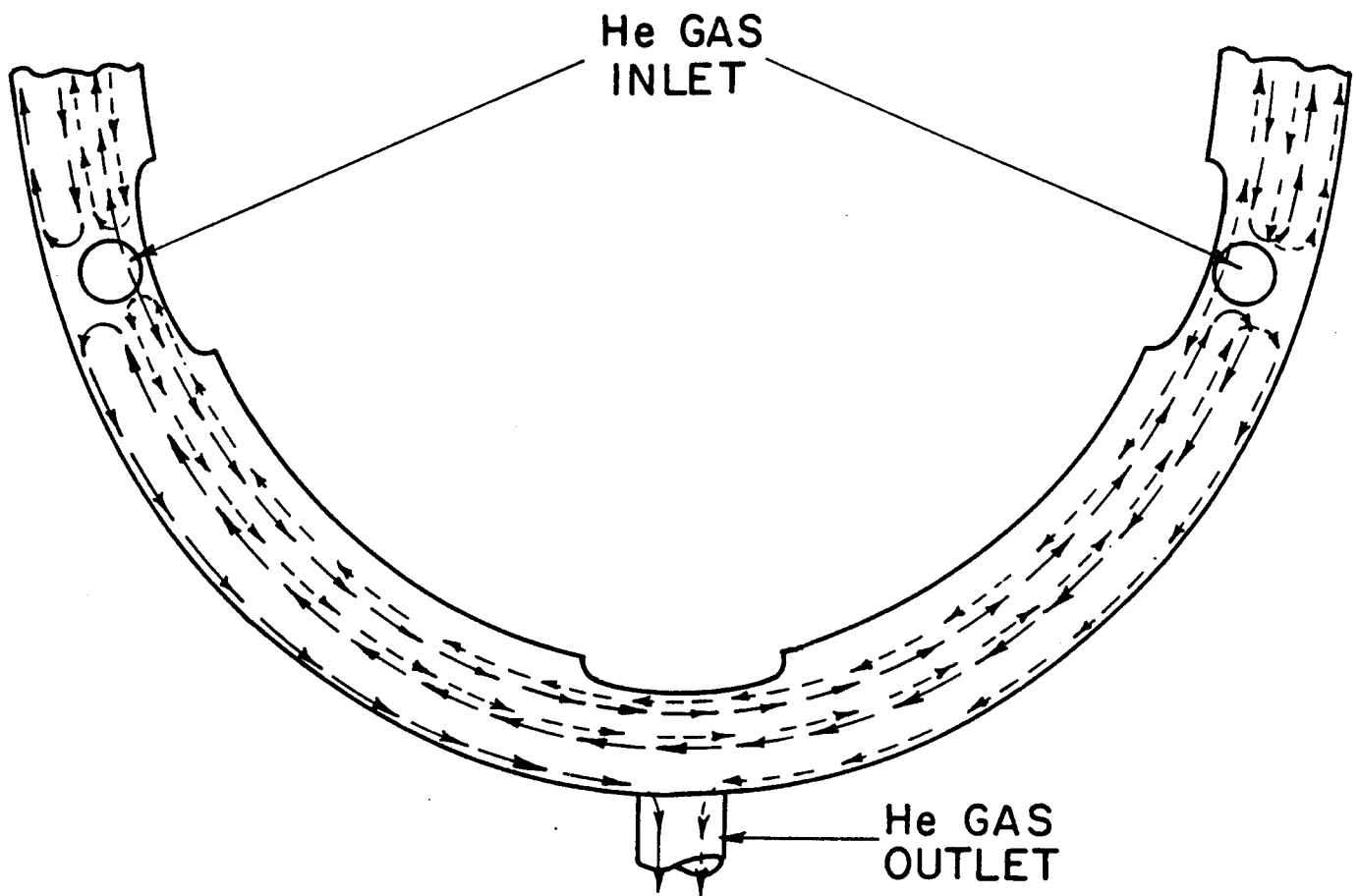*N/A means not applicable

He GAS
INLET

He GAS
OUTLET

Fig. 5.3-10. Helium gas flow path in reflector.

Thermal stresses are fairly low because all the heating is relatively low nuclear heating. They are calculated using thick walled vessel formulae. To calculate the pressure stress, we assume the whole reflector acts as a unit, since all the layers are in contact with each other. Here again we use the thick walled vessel equations. The stresses in Zone II are mostly due to longitudinal forces.

The total pressure drop in the reflector is equal to 0.08 MPa giving a pumping power requirement of 45 MW. Thus the total pumping power requirement for the blanket and reflector is 122 MW not counting the pressure drop through the steam generator. This is 6.9% of the gross electric power and 2.9% of the total thermal power.

References for Section 5.3

1. J.D. Gordon, J.K. Garvey (TRW), N.M. Ghoniem (UCLA) and J.F. Parmer (General Dynamics), "Ferritic Steel Application in the MARS High Temperature Blanket," Proceedings of Topical Conference on Ferritic Alloys for Use in Nuclear Energy Technologies, Snowbird, Utah, June 1983.

2. H.H. Bedner, PE, "Pressure Vessel Design Handbook," Van Nostrand Reinhold Co. (1981).

3. V.K. Sikka, "Development of Modified 9Cr-1Mo Steel for Elevated Temperature Service," (ORNL), Proceedings of Topical Conference on Ferritic Alloys for Use in Nuclear Energy Technologies, Snowbird, Utah, June 1983.

5.4 Blanket Neutronics Analysis

5.4.1 Introduction

The main function of the blanket in a D-T fusion reactor is to breed tritium, and recover and multiply the neutron energy. In addition, it cooperates with the reflector and shield in providing adequate radiation protection for the superconducting (S/C) magnets. However, the blanket has less shielding performance and keeping its thickness to a minimum reduces the sizes of the reflector, shield, and magnet, and, thus, decreases the overall reactor cost. Other advantages for thin blankets include reduced tritium and Li inventories, and light weight modules which greatly ease the replacement and maintenance process of the blanket.

Lithium lead ($Li_{17}Pb_{83}$) is an attractive choice for the breeding material where the breeder and multiplier are intermixed. It has other attractive features regarding reactor safety, tritium breeding, tritium extraction, and energy multiplication. The need for a thin blanket design provided a driving force to improve the performance of the LiPb-type blanket through adding a moderator to the breeder to soften the neutron spectrum and, thus, enhance the tritium breeding. Almost all the tritium breeding in such a system results from the $^6Li(n,\alpha)T$ reaction and, therefore, it is beneficial to highly enrich the Li in ^6Li. An overall tritium breeding ratio (TBR) of 1.05 is a design goal for the ASRA6C blanket and as large an energy multiplication (M) as possible is highly desirable to improve the reactor economics.

5.4.2 Moderator Choice

The description of how the choice of the moderator affects the TBR, M, and the blanket thickness is thoroughly covered in Ref. 1 and only a summary of the analysis is given here. Candidate moderators are hydrogen compounds, graphite and beryllium. Hydrides are good neutron moderators. However, beryllium has the dual advantage of acting as moderator and multiplier. Basically, two generic configurations were examined; the moderator in the first is TiH_2, while in the second is Be. The results of the two cases were then compared to the case of a pure LiPb blanket. All the calculations were carried out in one-dimensional (1-D) cylindrical geometry using the discrete ordinates transport code ONEDANT[2] with the LANL nuclear data library (30 neutron and 12 gamma groups) which is based on the ENDF/B-V evaluation. In the analysis, we considered 10 vol% coolant and 10 vol% HT-9 structure in all blankets. A meter thick He cooled HT-9 reflector was placed behind the

blanket to reflect some of the leaked neutrons and intercept most of their energy. The results of the analysis show that a 0.275 m thick LiPb blanket yields a TBR of 1.05 and M of 1.32. The TiH_2 (at 80% theoretical density) was gradually added to the LiPb blanket (trading LiPb for TiH_2). The optimum mixture that maximizes the TBR consists of 10 vol% TiH_2 and 70 vol% LiPb yielding TBR and M of 1.37 and 1.23, respectively. In order to get a TBR of 1.05, the $LiPb/TiH_2$ blanket thickness was reduced to 0.145 m. This corresponds to almost half of the LiPb blanket thickness and results in an M of 1.28. Although the performance of the TiH_2 is acceptable from the neutronics standpoint, the decomposition of the TiH_2 at elevated temperatures limits its use in the blanket.

The alternative option is to use beryllium as a moderator. Beryllium is not only an excellent moderator, but it is also an effective neutron multiplier. It increases the total number of neutrons through a high (n,2n) reaction cross section with a relatively low threshold energy at 1.7 MeV (compared to 6.7 MeV for Pb). The effect of Be is demonstrated upon adding the Be (at 90% theoretical density) to the 0.275 m thick LiPb blanket (trading LiPb for Be). The TBR peaks at 70 vol% Be and 10 vol% LiPb at a value of 1.68 and the corresponding value of M is 1.56. The 0.275 m thick LiPb/Be blanket gives excessive breeding and a 0.137 m thick LiPb/Be blanket was found to give a TBR of 1.05 and M of 1.57.

Clearly, the LiPb/Be concept yields the thinnest breeding blanket with the largest energy multiplication. Two important factors must be considered in the design of a LiPb/Be blanket, however. Firstly, due to the small LiPb inventory in the thin LiPb/Be blanket, the Li will be depleted rapidly and the TBR will decrease during reactor operation. Therefore, during the process of slowly circulating the LiPb for tritium removal, Li replenishment must be done continuously in order to maintain a constant ^6Li concentration in the breeder. Secondly, at the ASRA6C flux level, the Be swells by 10 vol% at the end of the 5 FPY design lifetime of the blanket.[3] At that time the blanket will be changed and the Be must be reprocessed.

5.4.3 Tritium Breeding Requirements

In ASRA6C, the NBI and pumping ports subtend ~ 10% of the total solid angle seen by the source neutrons. The direct loss of the 14.1 MeV source neutrons through the penetrations is predicted to be 10%. One would expect that the local TBR drops by 10% and a value of 1.17 results in an overall TBR

of 1.05. Unfortunately, this is not the case because the lower energy neutrons that are moderated in the blanket and reflected back into the plasma chamber will also stream through the ports and as a result the TBR and M decrease more rapidly than the loss of blanket coverage. Meier[4] performed 3-D calculations to analyze the effects of the penetrations on the neutron leakage and the blanket performance. The analysis was carried out for an Inertial Confinement Fusion (ICF) spherical geometry, natural ^{6}Li in $Li_{17}Pb_{83}$, 10 vol% structure content, and 70 cm thick blanket. The conclusion was that the number of neutrons per D-T fusion reaction that reenter the plasma chamber is 7.8 neutrons per D-T neutron. Moreover, the total neutron leakage through the penetrations is a factor of 6-7 higher than the direct loss. As a result of the enhanced neutron leakage, the TBR and M decrease at 3.5-4.5 and 2.5-3.5 times the expected rate, respectively, with the high and low ends of this range corresponding to solid angles < 2% and 10%, respectively. The results are shown in Figs. 5.4-1 and 5.4-2. The $T_T(0)$ and $E_D(0)$ are the TBR and M for the case without penetrations.

In order to scale from Meier's results, a run was made for the ASRA6C thin LiPb/Be blanket with cylindrical geometry, in which the number of reentering neutrons to the plasma chamber was calculated. This number was found to be 3.5 neutrons per D-T neutron. Scaling from Meier's results we determined that the ratios of the overall to local TBR and M are 0.76 and 0.83, respectively, for the ASRA6C blanket with 10% penetrations as shown in Figs. 5.4-1 and 5.4-2. This means that a local TBR of 1.4 must be achieved to meet the design goal for the tritium breeding in ASRA6C.

It should be mentioned that the required local TBR is conservatively estimated for two reasons. Firstly, there is a difference in the angular distribution of the source neutron incident on the first wall between ICF and magnetic fusion. The distribution is forward peaked in the ICF and results in a complete loss of the source neutrons streaming through the penetrations. Secondly, in ASRA6C there are numerous small penetrations while Meier carried out the analysis for two large penetrations. These two differences lead to a larger chance for the streaming neutrons to enter the blanket from the penetration walls and contribute to the breeding in the ASRA6C blanket.
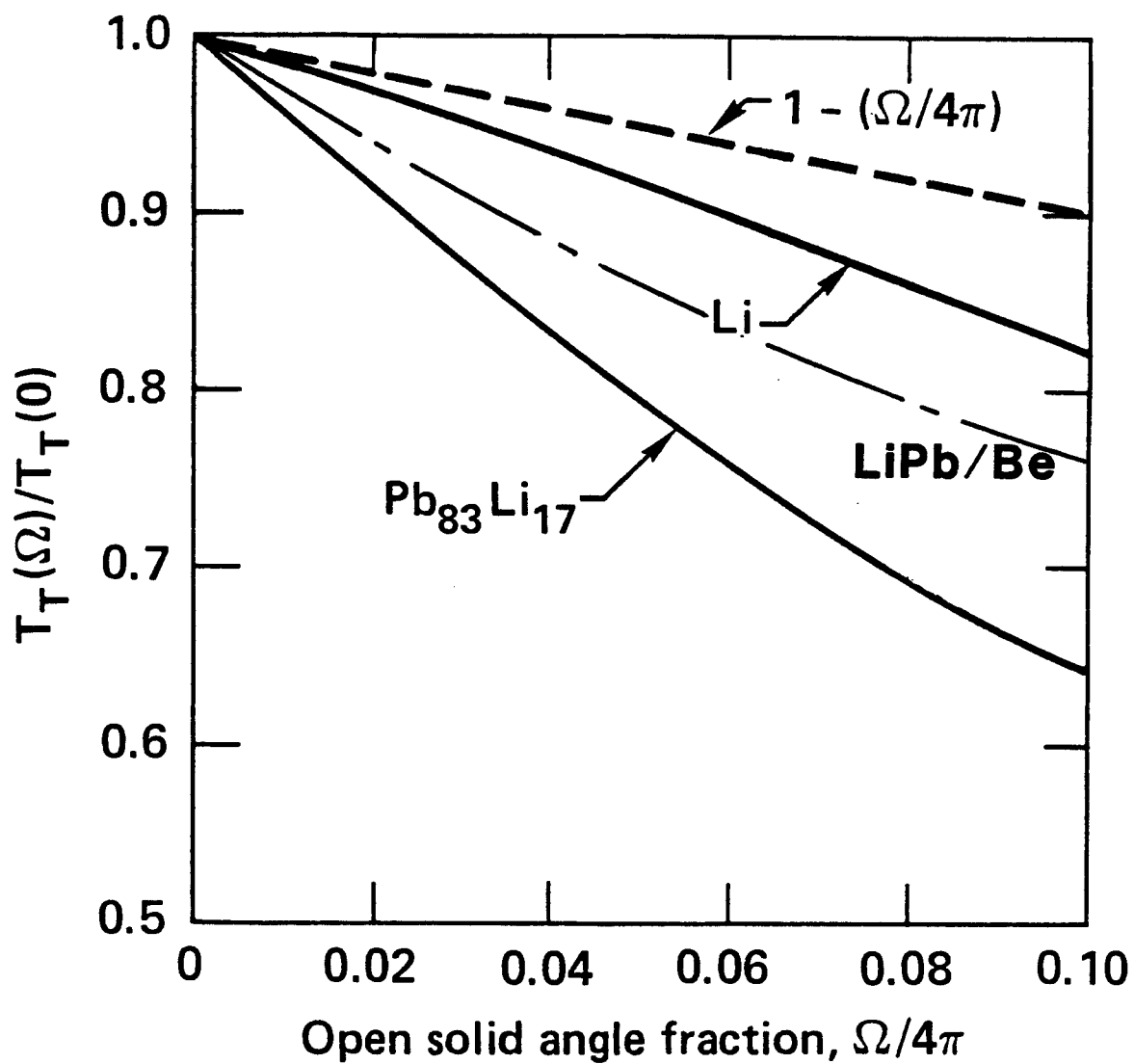
Fig. 5.4-1. Normalized TBR as a function of the open solid angle fraction;
the dashed line is the geometrically predicted scaling (Ref. 4).
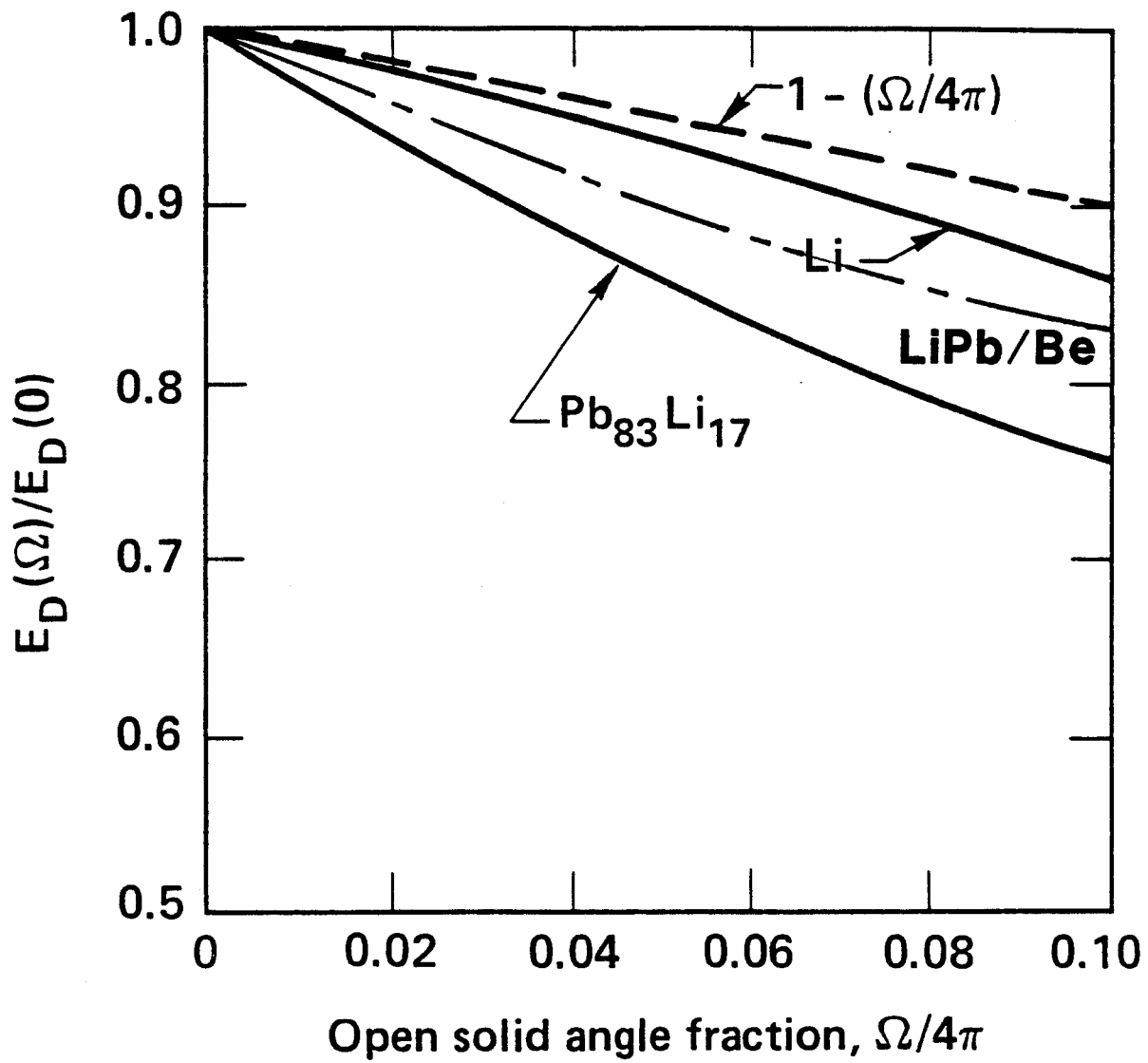The chain-dashed line is our estimate for the thin LiPb/Be
blanket of ASRA6C.

Fig. 5.4-2. Normalized M as a function of the open solid angle fraction; the dashed line is the geometrically predicted scaling (Ref. 4). The chain-dashed line is our estimate for the thin LiPb/Be blanket of ASRA6C.

5.4.4 Final Blanket Design

In the above scoping analysis, we have considered 10 vol% coolant and 10 vol% structure that were invariant with the blanket thickness. In the actual design, these quantities vary according to the blanket thickness in order to meet the mechanical and thermal hydraulics requirements. With the constraint of 1.4 local TBR, many iterations were performed to determine the blanket thickness and content that satisfy all requirements for neutronics, thermal hydraulics, and mechanical design. The LiPb to Be ratio was reoptimized for the thin blanket with the TBR being maximized. The variation of the TBR with the total blanket thickness is given in Fig. 5.4-3. The results show that the required blanket thickness is 0.21 m and consists of 14 vol% LiPb, 55.7 vol% Be, 10.3 vol% HT-9 with the balance being void and He coolant. Only 0.04% of the TBR is contributed by the ^{7}Li(n,n'α)T reaction.

The energy multiplication depends on the thickness of the reflector as the energy is recovered from both blanket and reflector. In ASRA6C, the reflector acts as the first layer of the magnet shield and its thickness depends on the shield materials, the allowable radiation limits in the magnet, and the neutron wall loading. An extensive study has been performed to optimize the shield and determine the thickness that adequately protects the magnet. As shown later, the optimal shield consists of 58.1% steel-shield, 33.6% B_4C-shield, and 8.3% Pb-shield. The values indicate percentage of the total reflector and shield thickness which is 0.76 m. The reflector thickness is, therefore, 0.442 m and the corresponding value for the local energy multiplication is 1.45.

The energy in the blanket amounts to 76% of the total and the neutron heating contributes 80% of blanket energy, whereas in the reflector the energy is mostly produced by gamma rays. Appropriate reflector cutouts are used to accommodate the He manifolds implying that the reflector thickness is reduced by 0.15 m at the poloidal locations where the manifolds are located. The manifolds cover 30% of the reflector area and reduce M to 1.43. As mentioned before, the 10% penetrations result in an overall M that is 83% of the full coverage value. Therefore, the overall energy multiplication in ASRA6C is 1.2.
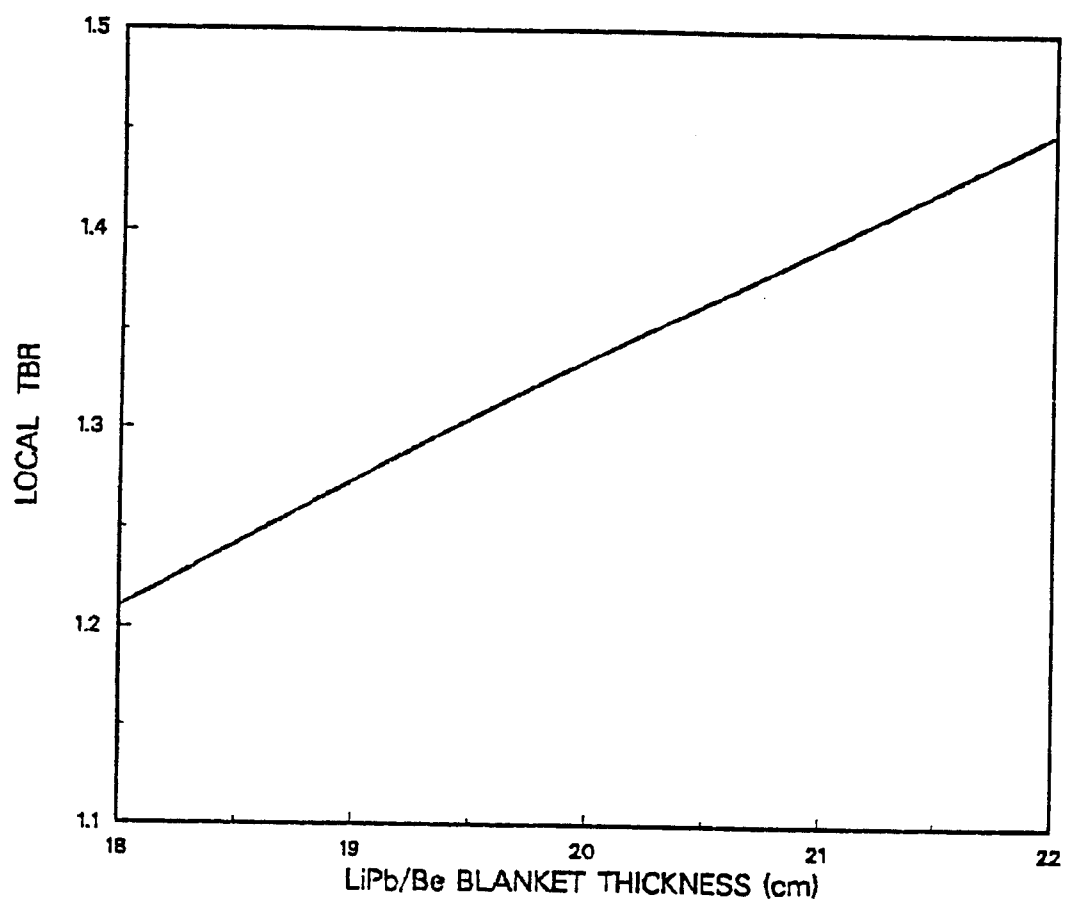
Fig. 5.4-3. Variation of the local TBR with the LiPb/Be blanket thickness.
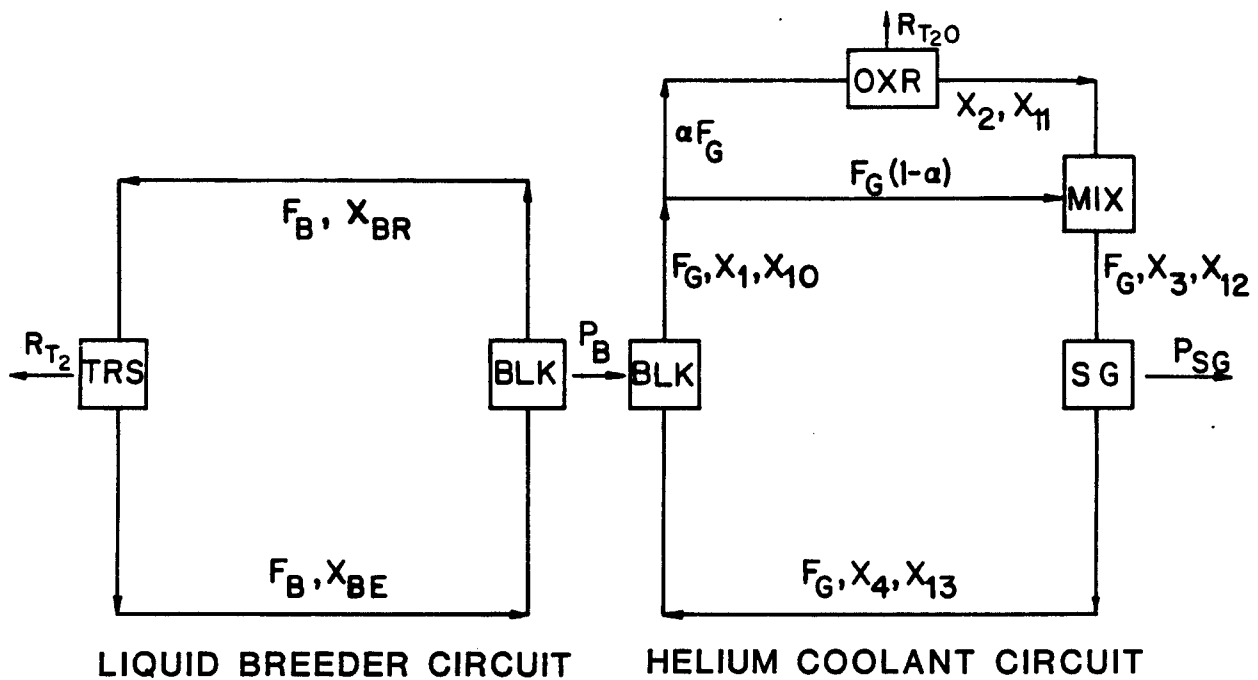
References for Section 5.4

1. L.A. El-Guebaly, "A Thin LiPb/Be Helium Cooled Blanket for MINIMARS: Neutronics Analysis," Fusion Technology, to be published in 1986.

2. R.D. O'Dell et al., "User's Manual for ONEDANT: A Code Package for One-Dimensional, Diffusion-Accelerated, Neutral Particle Transport," LA-9184-M, Los Alamos National Laboratory (Feb. 1982).

3. L.G. Miller and J.M. Beeston, "Radiation Damage Experiments and Lifetime Estimates for Beryllium Components in Fusion Systems," Fusion Technology 8, Number 1, Part 2B, 1152 (1985).

4. W.R. Meier, "Neutron Leakage through Fusion Chamber Ports: A Comparison of Lithium and Lead-Lithium Blanket," Lawrence Livermore National Laboratory, UCRL-87331 (Feb. 1982).

5.5 Tritium Removal from the Breeder Blanket

5.5.1 Introduction

The liquid breeder alloy, $Li_{17}Pb_{83}$, together with Be spheres are contained within the blanket for the thin blanket design. Tubes containing flowing helium are interspersed within the blanket for heat removal. Tritium removal from the breeder can be accomplished by either (1) slow circulation of the liquid breeder to an external Tritium Removal System (TRS), or (2) noncirculation of the liquid breeder so that the tritium permeates from the breeder into the coolant from which it is removed (see Fig. 5.5-1). The primary advantage of the former system is that the tritium concentration in the liquid breeder can be more easily controlled by variations in the recycle rate, while the static system has the advantages that the MHD pressure opposing the flowing liquid metal in the complex magnetic field of the stellarator is eliminated and corrosive effects caused by the flowing liquid are reduced. Both tritium removal schemes were briefly analyzed.

Both tritium removal schemes allow some tritium to permeate from the breeder into the helium coolant. A technique must be used to lower the T_2 pressure in the helium coolant so that the tritium permeation is not excessive in the steam generator (SG) where it can be lost to the environment. The tritium partial pressure is reduced, therefore, by the addition of oxygen into the helium so that T_2O is formed. While the uncatalyzed reaction rate for the oxidation of hydrogen is low, recent experimental studies[1] indicate that, when tritium permeates through a steel tube which is externally coated with an oxidized surface, greater than 95% of the tritium is converted to the oxidized form. For this study we assume that 99% of the tritium can be oxidized with careful oxidation of the steel. Additionally, investigators[2] conclude that an oxidized steel surface retards the permeation of hydrogen as compared to an unoxidized surface. This retardation effect increases as the hydrogen partial pressure decreases, as shown in Fig. 5.5-2 for an oxidized surface on ferritic steel. At the T_2 partial pressure in the helium typical of that found in the steam generator (SG), the permeation rate decreases approximately 10^3 times as compared to the unoxidized surface in which the permeation rate is a function of the square root of the hydrogen pressure. Additionally, the permeation rate for T_2 is decreased by a factor of 10 to 10^2 at 10^3 $Pa(T_2)$ which is the typical T_2 pressure in the liquid breeder alloy. These retardation effects were utilized in this study.

LIQUID BREEDER CIRCUIT **HELIUM COOLANT CIRCUIT**

Diagram labels:

R_{T_2O}

OXR X_2, X_{11}

αF_G

$F_G(1-\alpha)$ MIX

F_B, X_{BR}

F_G, X_1, X_{10} F_G, X_3, X_{12}

R_{T_2} TRS BLK P_B BLK SG P_{SG}

F_B, X_{BE} F_G, X_4, X_{13}

F_B = flow rate of breeder
F_G = flow rate of coolant gas
α = fraction of gas flow to OXR
X_1, X_2, X_3, X_4 = mole fraction T_2 in He
$X_{10}, X_{11}, X_{12}, X_{13}$ = mole fraction of T_2O in He

R_{T_2O} = rate of T_2O removal
R_{T_2} = rate of T_2 removal

X_{BR}, X_{BE} = g atoms T/mole of $Li_{17}Pb_{83}$
P_B = tritium permeation rate to the coolant gas
P_{SG} = tritium permeation rate to the steam circuit

BLK = breeder blanket
OXR = tritium oxide removal system
TRS = tritium removal system for liquid breeder
SG = steam generator
MIX = mixer for gas streams

Fig. 5.5-1. Flow diagram for tritium removal from the helium and the liquid metal breeder circuits. For the nonconvective breeder concept only the helium coolant circuit is used. Both circuits are used for the circulating breeder concept.
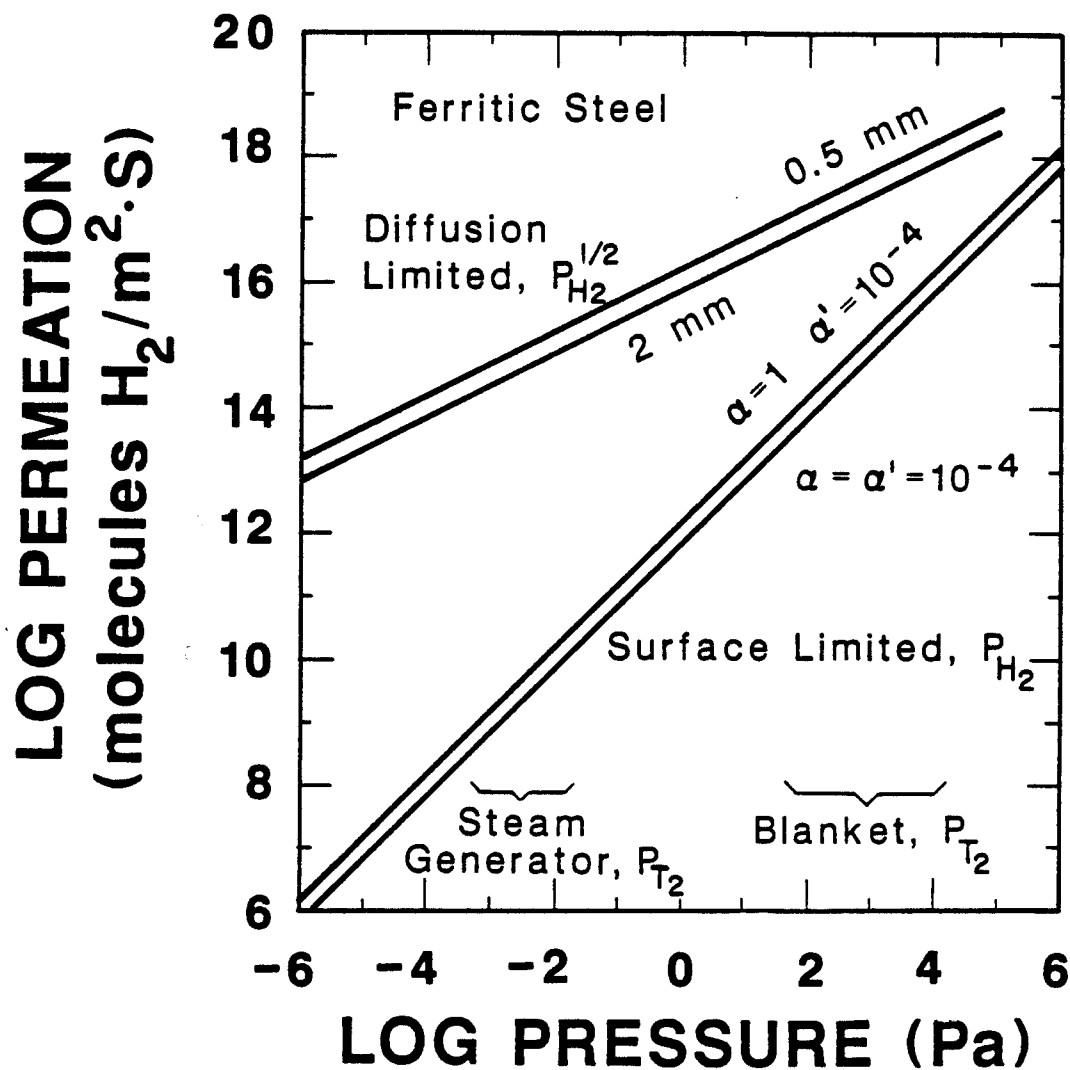
Fig. 5.5-2. H_2 permeation through ferritic steel as a function of pressure, for diffusion limited and surface limited permeation. The sticking coefficients α and α' for the inner and outer tube surfaces, respectively, indicate the contamination of the surface, e.g. $\alpha = 1$ is a clean surface, while $\alpha = 10^{-4}$ is a highly oxidized surface.

5.5.2 Circulation of the Breeder for Tritium Removal

In order to control the T_2 pressure in the helium coolant, and subsequently the tritium permeation through the SG, we have considered both (1) the circulation rate of the breeder through the blanket and the TRS and (2) the fraction of the coolant which can be diverted to a side-stream for tritium removal. For this study the following assumptions were made: (1) a stream degassing technique[3] was adapted for the liquid metal TRS in which 75% of the tritium is degassed from small droplets (1 mm radius) of the liquid breeder during a fall of 10 m in a vacuum vessel; (2) during the permeation of the tritium from the liquid breeder into the coolant, 99% of the desorbed species were assumed to be T_2O and only 1% as T_2; (3) the exit stream from the helium purification system in which all the tritium is oxidized and collected on a desiccant was considered to contain essentially zero concentration of T_2 while the T_2O pressure was limited to 0.48 Pa, the vapor pressure of ice at -66°C, and (4) only the T_2 species were allowed to permeate the SG.

Based on the above assumptions, a sensitivity analysis was made, as shown in Fig. 5.5-3, in which the tritium permeation rate in the SG was determined as a function of the breeder purification rate and the fraction of the helium coolant diverted for tritium removal. The fraction of the helium flow diverted to the side-stream for purification was kept small, e.g. 0.25, 1 and 4%, so that the size of these components would not be excessive. Typical HTGR fission reactors which release little fission products utilize < 0.1% continuous He purification.[4] The possible flow rates of the liquid breeder through the blanket were limited by the pumping power required to circulate this liquid. As a first approximation the pumping power was related to the pressure required to force the viscous liquid through the Be spheres in the blanket plus the MHD resistance to flow caused by the conductive liquid flowing in the magnetic field, Table 5.5-1. For this calculation all of the liquid breeder was assumed to enter a plenum at the top of the blanket, flow along one-half of the circumference of the blanket and exit at the bottom during residence times of 100 and 1000 s. The residence time of 100 s requires a reasonably low pumping power, 0.5% of the fusion power; consequently, residence times of 100 to 500 s are preferred. The excessively slow residence time of 1000 s would only be used if it were necessary to reduce possible corrosion and mass transfer effects.

Table 5.5-1. Pumping Power for Breeder Circulation

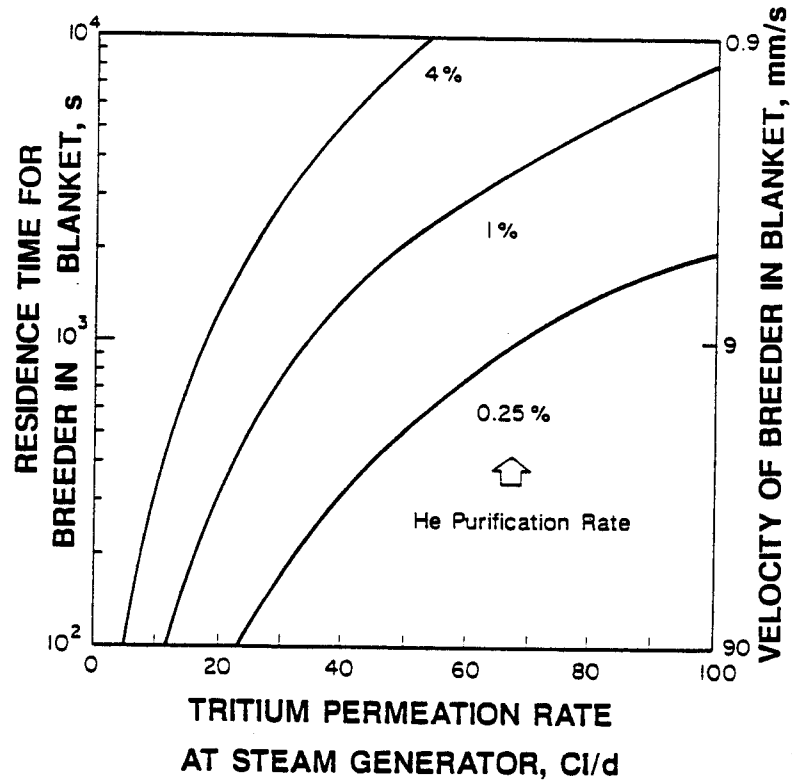|	Residence Time, s	
	100	1000
Velocity, mm/s	90	9
Flow Rate, m^3/s	0.64	0.064
$\Delta P_{viscous}$, MPa	5.5	0.055
ΔP_{MHD}, MPa	24	2.4
ΔP_{total}, MPa	30	2.5
Pumping Power, MW	19	0.16
Pumping Power, % Fusion Power	0.5	0.004

Fig. 5.5-3. Tritium permeation at the steam generator as a function of the residence time in the blanket for the circulating liquid breeder system at three values of the He purification rate.
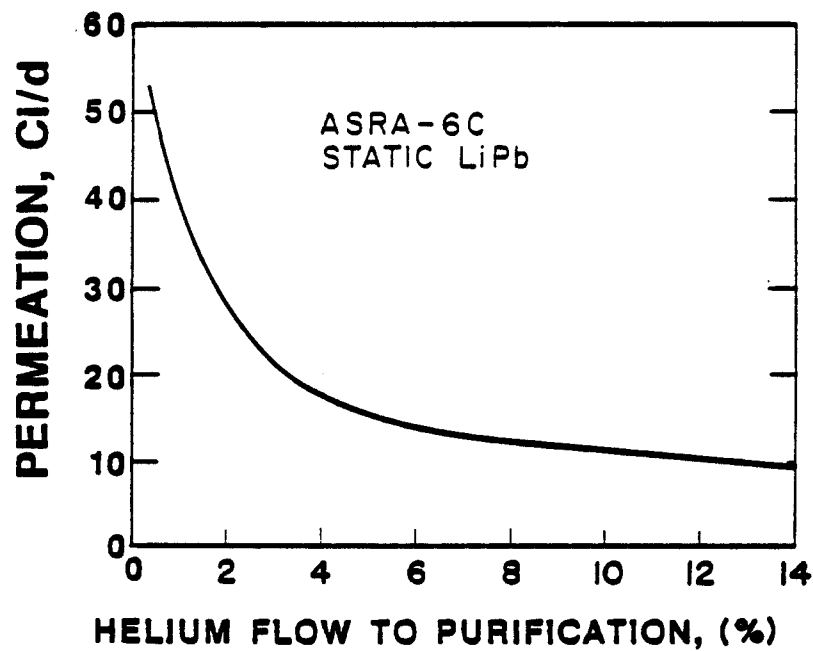

Fig. 5.5-4. T_2 permeation rate at the steam generator as a function of the helium purification rate for the static breeder system.

In order to assess the performance of such a system, we selected the case for 1% helium-purification from Fig. 5.5-3 with a liquid breeder residence time of 320 s in the blanket; the results are shown in Table 5.5-2. The average tritium concentration in the liquid breeder is 3×10^{-9} wt. fraction tritium so that for the total breeder in the blanket, 6.4×10^5 kg, the total inventory is only 1.9 g of tritium. For a Sievert's constant of 1.2×10^{-3} wppm tritium/$Pa^{1/2}$ at 400-500°C the tritium pressure in the blanket is 6.1 Pa. The concentration of T_2O in the helium coolant is 7.2×10^{-8} mole fraction (0.57 Pa) while the T_2 concentration is 1.2×10^{-10} mole fraction (1×10^{-3} Pa), resulting in the permeation of only 20 Ci/d of tritium to the SG. For the entire He circuit, $\sim 2.85 \times 10^4$ kg He, the tritium inventory is 3.2 g, consisting mostly of T_2O.

5.5.3 Noncirculating Breeder System

For the static blanket system, all of the tritium produced in the liquid alloy breeder must be removed either by permeation through the coolant tubes into the helium or by permeation through the cell walls directly into the plasma chamber where it can be processed with the plasma-exhaust gases. Based upon the dimensions of the blanket and the respective barrier factors for tritium permeation, i.e., one for the first wall, 10^2 for the helium coolant tubes and 10^3 for the SG (Fig. 5.5-2), approximately 72% (8.5×10^{-4} moles T_2/s) permeates into the plasma chamber while 28% (3.3×10^{-4} moles T_2/s) permeates into the helium coolant. Of the tritium in the helium only 3.3×10^{-6} moles/s is generated in elemental form, T_2, which can permeate at the SG.

In order to assess the potential for tritium permeation at the SG, the following conditions were examined: a side-stream of the fraction, $\dot{v}$, of the total helium flow was diverted for $T_2O + T_2$ removal, resulting in a steady-state concentration of the tritium in the helium. The concentrations of T_2O and T_2 at the exit of the He purification system are the same as given in Section 5.5.2. The permeation rates of T_2 through the SG were then calculated for this range of T_2 concentrations. The results shown in Fig. 5.5-4 indicate that the tritium release rate decreases rapidly from 54 Ci/d at $\dot{v} = 0.5\%$ to 21 Ci/d at $\dot{v} = 3\%$ and then decreases more slowly as $\dot{v}$ increases.

As an example, the inventories of tritium in the helium coolant and the liquid breeder were calculated for the case of 1% helium purification rate, Table 5.5-2. The tritium inventory in the helium coolant is 4.8 g which exists principally as T_2O at a partial pressure of 0.82 Pa. The steady-state

Table 5.5-2. Comparison of Static Breeder Blanket with
Circulating Breeder Blanket for Tritium Removal

Parameter	Static Blanket	Circulating Blanket
Coolant Purification Rate, %	1	1
Breeder Residence Time, s	∞	320
Oxide Barrier Factor		
Steam Generator	10^3	10^3
Coolant Tubes	10^2	10
T_2/T_2O Ratio Desorbing from Coolant Tubes, %	1	1
Tritium Permeation		
To Coolant, %	28	7
To Plasma, %	72	0
Through Steam Generator, Ci/d	37	20
Tritium Inventory		
In Coolant, g	4.8	3.2
In Breeder, g	340	1.9

partial pressure of T_2 in the coolant is 3.5×10^{-3} Pa, giving a calculated tritium permeation at the SG of 37 Ci/d.

The inventory of tritium within the liquid metal breeder is an important consideration but more difficult to quantify because of conflicting experimental data. In order to obtain a steady-state tritium permeation rate from the blanket modules at the same rate at which it is generated, a partial pressure of T_2 within the blanket of 5.1 kPa (T_2) is required. The concentration of tritium in the liquid alloy at this T_2 pressure is determined by use of the Sievert's constant, K_S; however, two ranges of experimental values for K_S have been reported:[5,6,7,8] (4.6×10^5 and 5.0×10^4) $kPa^{1/2}$/mole fraction T per mole of $Li_{17}Pb_{83}$. Based upon these two values for K_S, the tritium inventory in the entire liquid alloy could be either 50 or 445 g. The lower solubility value is preferred at this time because a very recent determination[9] supports the low solubility value determined by Chan and Veleckis.[5]

The above inventory values are predicted for a well-stirred solution in which the tritium is homogeneously distributed throughout the liquid; however, for the presently proposed blanket the liquid alloy fills only 14% of the volume around the Be spheres. As a result the liquid will not circulate and tritium can migrate to the walls only by the diffusional process. In this case, the inventory of tritium, C_T, is given by the relationship,

$$C_T = \frac{\dot{T} r^2}{4D} + C_0,$$

where, $\dot{T}$ = the tritium generation rate

   r = the radius of the blanket module

   D = the diffusion coefficient of dissolved T in liquid LiPb ($\sim 5 \times 10^{-4}$ cm^2/s)

and C_0 = the gaseous solubility of T_2 in the liquid alloy.

The first-term on the right-hand side of the above equation increases the tritium inventory by an additional 290 g. When combined with the previously determined value for C_0, the total tritium inventory in the blanket would be 340 g, giving a mole fraction tritium concentration of 31 at.ppm. The tritium concentration in this alloy is important because the solubility limit has been reported to be near 10 at.ppm by Wu,[7] > 400 appm by Katsuta[8] and was calculated by Buxbaum to be $\sim$ 48 at.ppm[10] Except for the first value,

apparently, the solubility limit for tritium in this alloy is not exceeded. If the solubility limit were exceeded, the diffusion of tritium through solid LiT would be approximately five-fold slower, thus increasing the tritium inventory.

5.5.4 Comparison Study

In order to gain an appreciation of the advantages and disadvantages of the circulating and noncirculating breeder blanket designs, a comparison study was made at a similar design point for each system. The design point selected was at a 1% helium purification rate following passage of the coolant through the blanket (Table 5.5-2). The relevant values used to calculate the pathways of tritium in the blanket, also given in the table, were utilized to calculate the release of tritium at the SG, e.g. 20 Ci/d for the circulating blanket and 37 Ci/d for the static blanket design.

The significance of these amounts of tritium release to the environment is difficult to quantify at this time because the guidelines for the radio-active discharge from a fusion reactor plant have not been defined. As an indicator of possible limits, 11 different air dispersion models for continual release of HTO at the rate of 100 Ci/d at a height of 20 m were calculated and compared.[11] The chronic dose to an individual at 1 km distance from the release point varied from 0.6 to 14 mrem/yr, with an average of 3.4 mrem/yr. These values compare favorably with the U.S. EPA limit of 10 mrem/yr and the U.S. NRC limit of 5 mrem/yr to a maximum exposed individual.[12] Because the results of the comparison study (Table 5.5-2) are only 20% and 37% of these exposure guidelines such values should be initially conservative and no significance need be attached to the slight difference between them.

The amount of tritium inventory in the coolant, chiefly as T_2O (Table 5.5-2), is similar in each case, i.e., 4.8 g (5 x 10^4 Ci) for the static blanket and 3.2 g (3 x 10^4 Ci) for the circulating blanket. In the most severe accident to the pressurized helium coolant system, all this tritium might be released to the environment. An assessment[11] has been made of the potential radiation dose to an individual residing 1 km from a puff release of 10^4 Ci of HTO at ground level. Nine release models were considered and the radiation dose to the maximum exposed individual varied from 0.05 rem to 1.2 rem with an average of 0.3 rem. Using the average value, we note that the maximum dose caused by tritium in such a potential accident would be 1.5 rem

for our static blanket design. Tritium is expected to cause the largest radiological dose in such an accident.[12] This dose is well within the 25 rem limit suggested in the U.S. NRC Regulation 10 CFR 100.

A chronic radiation dose could be caused by the continual leakage of helium and T_2O from the highly pressurized coolant system. High quality construction and operation of the Dragon Reactor[13] in the U.K. has shown, however, that routine leakage of the helium can be maintained in the range of 0.025 to 0.05% per day; therefore, the maximum expected release in the present case would be only 25 Ci/d and most of it would be within the containment building where it could be recaptured.

The most significant difference between the two types of blankets being considered is in regards to the tritium inventory in the breeder, i.e. 390 g for the static blanket but only 1.9 g for the circulating blanket. Because of this large difference we prefer, at this time, the circulating blanket concept. The static blanket concept should be retained for future consideration, however. Although the static liquid metal breeder has a relatively high tritium inventory, it is much less than in a ceramic breeder such as lithium oxide[4] in which the tritium inventory may exceed 1 kg. Also, because tritium in the liquid metal alloy breeder can permeate directly through its containment capsule, no secondary circuit for T_2O recovery is needed as for a ceramic breeder. As more experience is gained regarding the breeding and diffusion of tritium in this liquid metal breeder the static blanket may become more viable. Then, the helium coolant tubes can be judiciously repositioned to shorten the diffusional paths for heat and tritium removal and, consequently, reduce the tritium inventory.

References for Section 5.5
1. D.F. Holland and G.R. Longhurst, "Modelling and Experiments on Tritium Permeation in Fusion Reactor Blankets," Fusion Tech., 8, 2067 (1985).

2. M.A. Pick and K. Sonnenbeg, "A Model for Atomic Hydrogen-Metal Interactions-Applications to Recycling, Recombination and Permeation," J. Nuclear Materials, 131, 208 (1985).

3. K.E. Plute, E.M. Larsen and L.J. Wittenberg, "Tritium Recovery from Liquid Lithium-Lead by Vacuum Degassing," Nuclear Tech./Fusion, 4, 407 (1983).

4. M.D. Donne and S. Dorner, "Tritium Control in a Helium-Cooled Ceramic Blanket for a Fusion Reactor," Fusion Tech., 9, 484 (1985).

5. Y.C. Chan and E. Veleckis, "A Thermodynamic Investigation of Dilute Solutions in the Liquid Li-Pb Alloys," J. Nuclear Materials, 122 & 123, 935 (1984).

6. G. Kuhlborsch and R. Reiter, "Physical Properties and Chemical Reaction Behavior of $Li_{17}Pb_{83}$ Related to Its Use as a Fusion Reactor Blanket," Nuclear Eng. Design/Fusion, 1, 195 (1984).

7. C.H. Wu, "The Interaction of Hydrogen Isotopes with the Li-Pb Alloys," J. Nuclear Materials, 122 & 123, 941 (1984).

8. H. Katsuta, H. Iwamoto and H. Ohno, "Hydrogen Solubility in Liquid $Li_{17}Pb_{83}$," J. Nuclear Materials, 133 & 134, 167 (1985).

9. G. Casini, "Progress in the Data Base Acquisition for $T/Li_{17}Pb_{83}$/Water Blankets," Abstracts for IAEA Workshop, Yalta, May 1986.

10. R.E. Buxbaum, "A Chemical Theory Analysis of the Solution Thermodynamics of Oxygen, Nitrogen and Hydrogen in Lead-Rich Li-Pb Mixtures," J. Less - Common Metals, 97, 27 (1984).

11. T.F. Kempe, S.B. Russell, K.J. Donnelly and H.J. Reilly, "International Comparison of Computer Codes for Modelling the Dispersion of Tritium Released to the Atmosphere," Fusion Tech., 8 2575 (1985).

12. R. Stasko, Canadian Fusion Fuels Technology Project, unpublished memo regarding MINIMARS Radiological Safety, July 1985.

13. B.G. Chapman, "Dragon Operating Experience," in Proc. Gas-Cooled Reactor Information Meeting, Oak Ridge, TN, April 27-30, 1970, CONF-700401 (1970).

6. SHIELD DESIGN AND OPTIMIZATION

6.1 Neutron Wall Loading Distribution

In toroidal fusion reactors, the neutron wall loading exhibits a poloidal variation that can deviate considerably from the nominal value of the neutron wall loading defined as the neutron fusion power divided by the first wall area. This poloidal variation has an important impact on the first wall lifetime as well as the reactor thermal-hydraulics design. In addition, the wall loading distribution helps identify locations of magnet hot spots and facilitates the design of a magnet shield that satisfies the magnet radiation limits. The poloidal wall loading distribution depends on the aspect ratio, the plasma shape, the neutron source distribution in the plasma and the first wall shape.
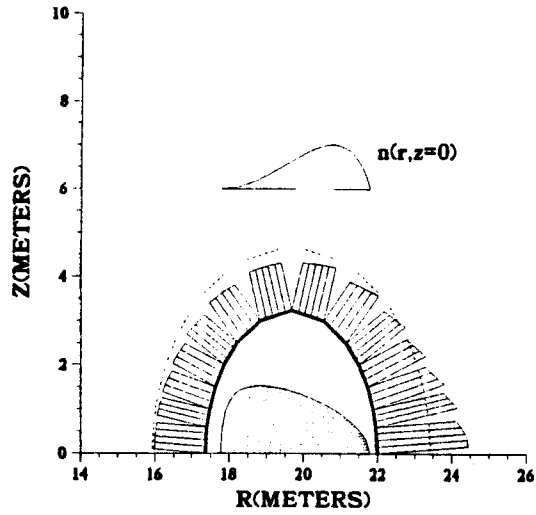
The neutron wall loading distribution in ASRA6C was determined using the NEWLIT code.[1] The code uses ray tracing techniques to determine the extent of the plasma contribution to the neutron current at a given point on the wall. The source distribution within the plasma is taken into account by properly representing the different magnetic surfaces. The boundary of the plasma as well as the first wall can take any shape. The code assumes toroidal symmetry with a symmetric plasma shape about the reactor midplane. Two calculations were performed for the two toroidal locations in ASRA6C where the plasma is horizontal ($\phi = 0°$) and vertical ($\phi = 36°$). The plasma outer boundary was fitted to a D-shape at each of the two toroidal locations. The magnetic shift was taken to be 50% of the plasma radius at the reactor midplane. The neutron source in the plasma was considered to vary with distance from the magnetic axis as $\{1 - (r/r_p)^2\}^2$. The results were normalized to a reactor fusion power of 3.8 GW. The plasma parameters obtained by D-shape fitting at the toroidal locations $\phi = 0°$ and $36°$ are given in Table 6.1-1.

In the final design for ASRA6C, the first wall has the same elliptic shape at all toroidal locations with a = 2.32 m and b = 3.23 m. The center of the ellipse moves in the reactor midplane with the distance from the reactor major axis ranging in each field period from 19.68 m at the toroidal location $\phi = 0°$ to 20.32 m at $\phi = 36°$. The results of the calculations are shown in Fig. 6.1-1. The wall and plasma shapes are indicated as well as the source distribution. The dashed line represents the average wall loading which was

Table 6.1-1. Plasma Parameters at $\phi = 0°$ and $36°$ Obtained by Fitting the Boundary to $R = R_p + r_p \cos(t + C_p \sin t)$ and $Z = r_p \kappa_p \sin t$

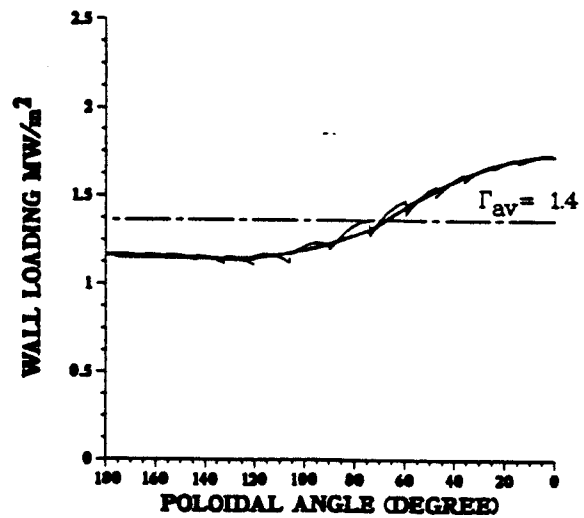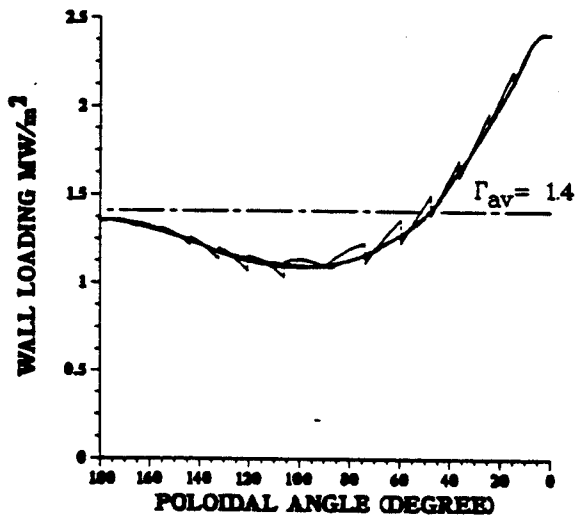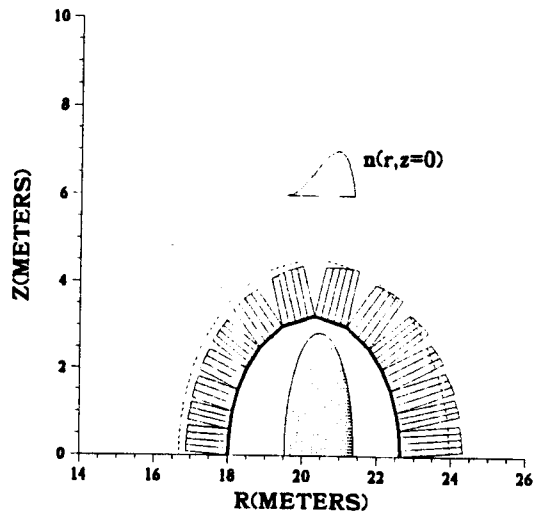|	$\phi = 0°$	$\phi = 36°$
Plasma major radius R_p (m)	19.78	20.46
Plasma minor radius r_p (m)	2	0.93
Plasma elongation factor κ_p	0.765	3.07
Plasma triangularity factor C_p	0.52	0
Magnetic shift ϵ_m (m)	1	0.46

Fig. 6.1-1. Neutron wall loading distribution at the toroidal locations
φ = 0° and 36°. The poloidal angle 0° corresponds to the
outboard side and 180° to the inboard side.

determined to be 1.4 MW/m^2. The results indicate that at all toroidal locations, the peak neutron wall loading occurs on the outboard side at the reactor midplane. The peak neutron wall loading in ASRA6C is 2.4 MW/m^2 and occurs at the five toroidal locations where the plasma shape is horizontal. This peak value calculated by NEWLIT, which assumes axisymmetry, is a good estimate since the peak neutron source is nearly the same distance from the major axis at all toroidal locations. The peak value is 70% higher than the average neutron wall loading of 1.4 MW/m^2. The minimum wall loading is 1.1 MW/m^2 at a poloidal angle of ~ 110°.

Several alternate designs were considered for ASRA6C in which the first wall shape varies as one moves toroidally around the major axis. In these design options the first wall follows closely the plasma boundary shape as explained in Section 5.2. The neutron wall loading distribution calculated using the plasma and wall configuration at the toroidal location ϕ = 0° is shown in Fig. 6.1-2. The peak neutron wall loading is 2.54 MW/m^2 and occurs slightly above the reactor midplane at a poloidal angle of ~ 30°. Because of the reduced total first wall area in this contoured configuration the average wall loading is 1.8 MW/m^2. The minimum wall loading is ~ 1.3 MW/m^2 at a poloidal angle of ~ 140°.

The neutron wall loading distribution calculated here was coupled with the one-dimensional shielding calculations to determine the peak radiation effects in the magnet as well as the total nuclear heating in the ASRA6C magnets. The results were also combined with the poloidal variation of blanket/reflector/shield thickness and composition in the different options to compare the magnet radiation effects obtained in the different design options and the impact on cost as discussed in Section 5.2.

References for Section 6.1

1. H. Attaya and M. Sawan, "NEWLIT - A General Code for Neutron Wall Loading Distribution in Toroidal Reactors," Fusion Technology 8/1, 608 (1985).
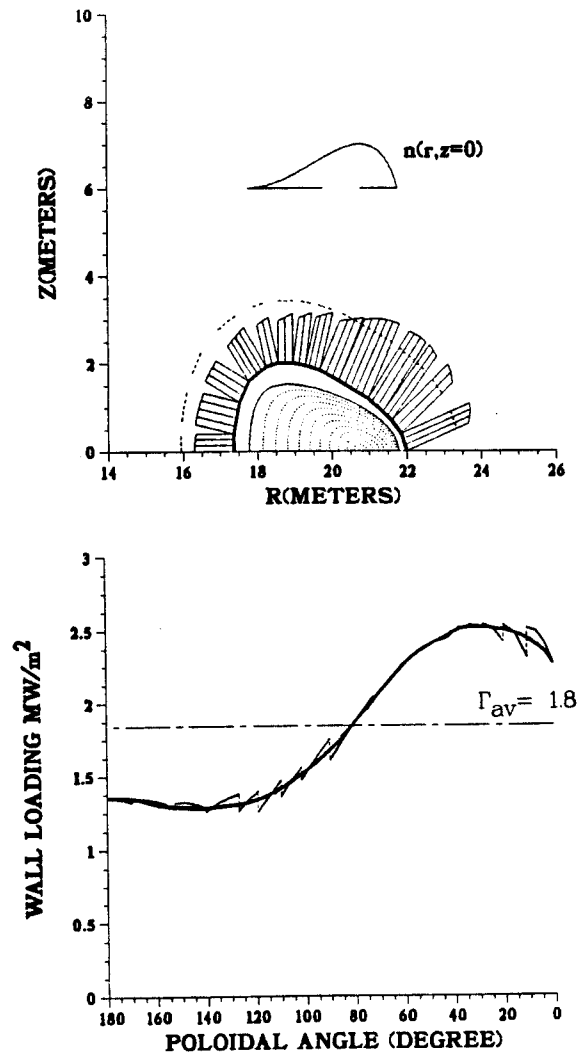
Fig. 6.1-2. Poloidal variation of neutron wall loading in options with first
wall closely following the plasma boundary. The poloidal angle
0° corresponds to the outboard side and 180° to the inboard side.

6.2 Magnet Radiation Limits

The radiation limits for the magnets determine the shield thickness that directly influences the cost of electricity. The superconducting magnet components most sensitive to radiation damage are the superconductor filaments, stabilizer, and electrical and thermal insulators. In addition to its effect on winding temperatures, nuclear heating affects the economic performance of the reactor through increased refrigeration costs. Radiation effects are related as they are determined by the flux level in the magnet. Reviewing previous magnet shielding neutronics calculations for the different conceptual fusion reactor designs, we found a rule-of-thumb relation for radiation effects that holds to within a factor of two. For a 20 full power year (FPY) exposure to the nuclear radiation leaking from the back of the shield, a peak winding pack power density of 1 mW/cm^3 corresponds to $\sim 10^{-3}$ dpa/FPY in the copper stabilizer, $\sim 3 \times 10^{23}$ n/m^2 (E > 0.1 MeV) end-of-life fluence and $\sim 3 \times 10^{10}$ rad end-of-life insulator dose.

Radiation effects on superconductors are related to the damage produced by fast neutrons through the production of defect cascades. The damage is usually measured in damage energy available per atom in eV/atom. Different damage will be produced if the superconductor is exposed to the same neutron fluence with different neutron spectra. Degradation of critical properties is usually related to fast neutron fluence (E > 0.1 MeV). The relative number of neutrons that produces equal damage in superconductors as that produced by one neutron in RTNS-II was calculated by Guinan and coworkers[1-3] to be 4.5, 5.74, 7, 3.68, and 4.7 for IPNS, HFBR, TFCX, STARFIRE and MARS, respectively. We calculated the relative number for ASRA6C and MINIMARS[4] to be 5.1.

The critical properties of A15 compounds are sensitive to nuclear radiation because of the long-range ordered atomic structure. Most experimental data involve irradiation at fission reactor ambient temperatures[3] with limited low fluence 4 K irradiation data.[2] T_c is nearly constant up to a fluence of $\sim 10^{22}$ n/m^2 and drops rapidly at higher fluences.[2] All T_c data from irradiation in different facilities at different temperatures agree when compared on a damage energy basis.[2] Recent data for 19-core and commercial 10,000-filament Nb_3Sn wires[5] agree also very well with previous monofilament data. The drop in T_c is less than 3% up to a fusion reactor fluence (E > 0.1 MeV) of $\sim 5 \times 10^{22}$ n/m^2 and increases to $\sim 20\%$ at $\sim 2 \times 10^{23}$ n/m^2. In general, an initial rise in J_c was observed with a subsequent drop at higher

fluences. The initial rise, which is related to increased H_{c2} with nearly constant T_c at low fluences, increases for larger fields and lower irradiation temperatures.[6,7] H_{c2} was found to vary with fluence in a similar fashion.[5]

Figure 6.2-1 shows the experimental data for the effect of irradiation on J_c compared on a damage energy basis. Comparing the results of high temperature HFBR irradiation[3] with the 4 K irradiation of the nearly identical monofilament sample[2] indicates that high temperature irradiation yields larger J_c degradation. This is due to defect mobility and subsequent cascade collapse during the high temperature irradiation resulting in lower flux pinning. Hence, using the high temperature irradiation data yields conservatively low fluence limits. The commercial 10,000-filament wires[5] have less J_c degradation than the 19-core wires.[3,7] Based on the high temperature irradiation data for multifilamentary wires, a fluence limit of 1.5 x 10^{23} n/m^2 (E > 0.1 MeV) will be assumed in this study. At this fluence T_c drops by ~ 15% from its preirradiation value. This fluence limit needs to be confirmed by 4 K irradiation. Guinan has plans for irradiating multifilamentary Nb_3Sn at low temperatures in the National Low-Temperature Neutron Irradiation Facility (NLTNIF) at Oak Ridge within a year.[8]

Experimental data for fiber-reinforced organic insulators indicate that the mechanical properties degrade at a lower dose than do the electrical ones. Polyimides are 5 to 10 times more radiation resistant than epoxies.[9] Samples of several millimeters-thick cylindrical rods of glass-fiber-filled (gff) polyimide were irradiated by gamma rays at 5 K and tested for flexural and compression strength.[9] More than 65% of the strength was retained up to a dose of ~ 10^{10} rad. The samples are representative of relatively thick sheets of insulators placed between conductors with both compression and interlaminar shear being important. Recently, 0.5 mm-thick disks of gff polyimide (Spaulard-S) were irradiated at 325 K to a mixed gamma and neutron dose of ~ 1.2 x 10^{12} rad with no failures observed in the static compression tests with a 2750 MPa stress level.[10] In these tests essentially no interlaminar shear occurred. Furthermore, this dose corresponds to an excessive fast neutron fluence of ~ 10^{25} n/m^2. In this study we use a dose limit of 10^{10} rad for the electrical insulator. This dose corresponds to ~ 10^{23} n/m^2 fluence and is consistent with the fluence limit used for Nb_3Sn. The aluminized mylar has been used in previous designs as a thermal insulator. However,
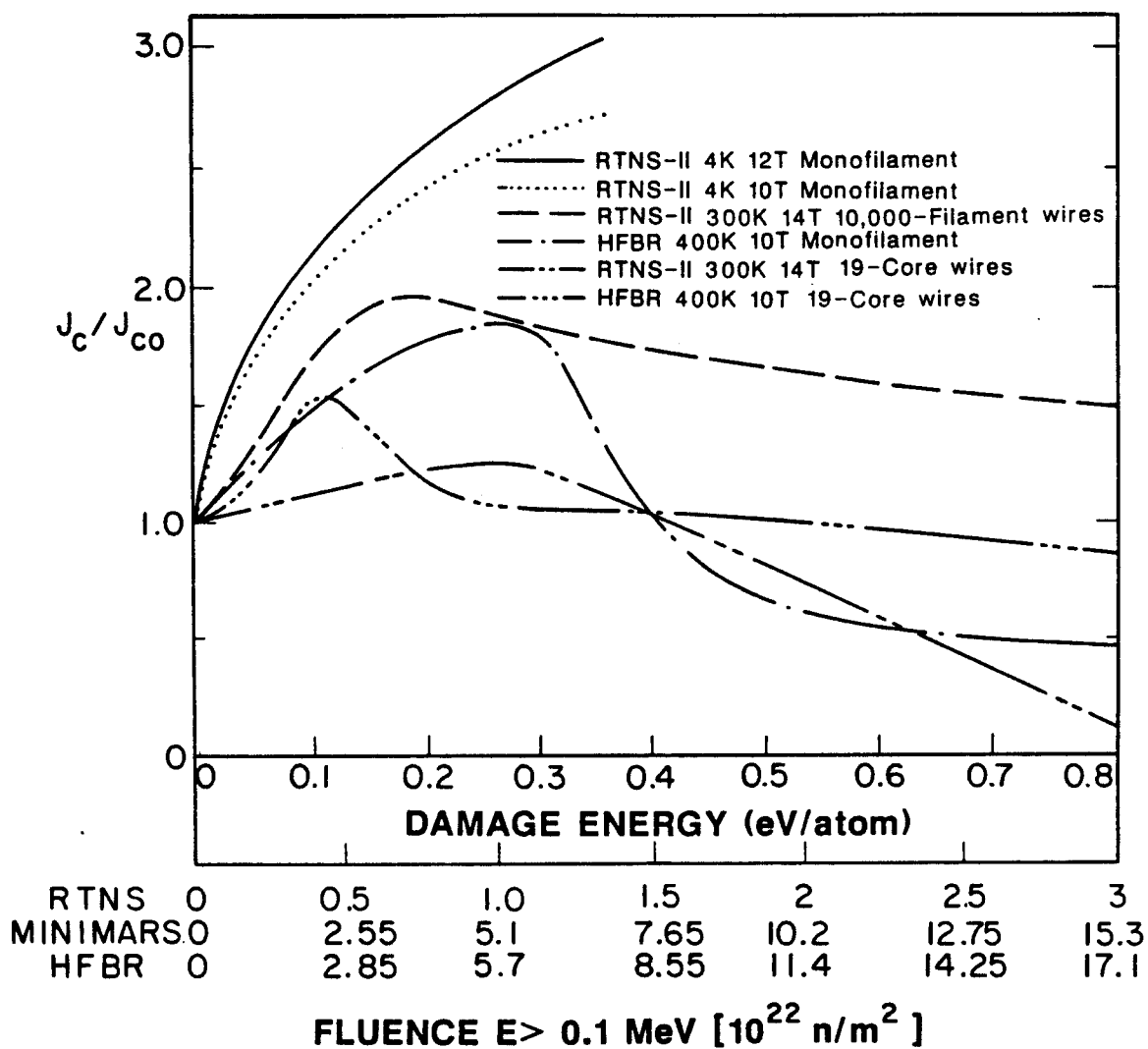
Fig. 6.2-1. J_c changes in Nb_3Sn as function of damage energy and equivalent neutron fluence.

experimental data showed a large drop in its strength after irradiation to 6 x 10^8 rads.[11] No failure of any type was observed in aluminized Kapton up to a dose of 10^{10} rads.[11] The superinsulator located in front of the magnet case is exposed to doses higher than those in the electrical insulators. The more radiation resistant aluminum sheets supported with glass paper will be used in ASRA6C with essentially no practical dose limit.

Neutron irradiation at cryogenic temperature produces immobile point defects in the stabilizer resulting in a zero-field radiation induced resistivity $\Delta\rho_r$ which impacts the total resistivity at field. The relation between $\Delta\rho_r$ and Cu dpa is[12]

$$\Delta\rho_r = 3 \times 10^{-9} \left[1 - e^{-240 \times dpa} \right] (\Omega \ m) \ . \qquad (6.2-1)$$

The resistivity at the operating field ρ_0 depends on $\Delta\rho_r$ and the purity of Cu. Furthermore, partial recovery (80-90%) of radiation induced defects can be achieved by room temperature annealing. Based on Kohler's plot for Cu, we generated a chart relating $\Delta\rho_r$ to ρ_0 given the field B and the residual resistivity ratio RRR of Cu.[13] The dpa rate limit is determined by dividing the dpa limit, from Eq. (6.2-1), by the time before the first magnet anneal. Power reactor availability considerations require at least 4 FPY's before the first magnet anneal.

The effect of stabilizer resistivity increase on both magnet stability and protection is design dependent. If the conservative principle of cryogenic stabilization is adopted, the Cu dpa rate is limited to values as low as ~ 5 x 10^{-5} dpa/FPY[13] for bath-cooled magnets. This is a very restrictive limit that corresponds to an end-of-life neutron fluence of only ~ 10^{22} n/m^2. It is therefore important to consider magnet design approaches that are less sensitive to a stabilizer resistivity increase.[14] The magnet can be designed to be unconditionally cryostable only during the initial charge relying on other stabilization mechanisms later on such as transient stability and end-zone stability. Furthermore, forced-flow magnet designs such as that used in ASRA6C are less sensitive to a Cu resistivity increase. It should be mentioned that if the magnet is designed with adequate stability at the resistivity level corresponding to the saturation radiation induced resistivity (~ 3 nΩ m), the damage in the stabilizer will not be restricted. In this study we do not set a Cu damage limit which is design dependent. It is worth

mentioning that according to the rule-of-thumb relation given in this section, the fluence and dose limits adopted in this study correspond to a maximum Cu radiation induced resistivity of ~ 1 nΩ m.

Although winding pack power densities as high as ~ 1 W/cm^3 can be handled by the liquid helium coolant, the values that can be achieved in practice are much lower because of problems of cryogen replenishment for the He-I cooled magnets and excessive cryoplant cost. The economic optimum nuclear heating level can be determined by a cost tradeoff analysis, where the total cost of items strongly affected by the shield thickness is minimized. In an axisymmetric configuration such as in tandem mirrors, these are the shield itself, the magnets, and the cryoplant. Optimization calculations have been performed for the central cell and choke coil magnets of MINIMARS.[14] The optimum peak winding pack power densities were found to be 0.06 and 0.25 mW/cm^3, respectively. In toroidal devices, practically all major machine components are affected by shield thickness, and the resultant optimum nuclear heating level is higher.

A limit of 0.2 mW/cm^3 on the poloidal average of the winding pack power density in the inner layer of the magnet is used in ASRA6C. This was determined also by requiring that no more than a few percent of the gross electric power be recirculated for the cryoplant. Although this limit is quite small and corresponds to nominal (poloidal average) fluences and doses of only $\sim 6 \times 10^{22}$ n/m^2 and $\sim 6 \times 10^9$ rad, the higher dose and fluence limits used in this study are needed to allow for magnet hot spots as long as the higher nuclear heating at these hot spots does not significantly increase the total cryogenic load.

References for Section 6.2

1. P. Hahn, H. Weber, M. Guinan, et al., "Neutron Irradiation of Superconductors and Damage Energy Scaling of Different Neutron Spectra," UCRL-93186, Lawrence Livermore National Laboratory (1985).

2. M. Guinan, R. Van Konynenburg, J. Mitchell, et al., "Effects of Low-Temperature Fusion Neutron Irradiation on Critical Properties of a Monofilament Nb_3Sn Superconductor," UCID-20048, Lawrence Livermore National Laboratory (1984).

3. C. Snead, D. Parkin, M. Guinan, "High Energy Neutron Damage in Nb_3Sn: Changes in Critical Properties, and Damage Energy Analysis," J. Nucl. Mat. 103 & 104, 749 (1981).

4. J.D. Lee et al., "MINIMARS Final Report," UCID-20773, Lawrence Livermore National Laboratory (1986).

5. F. Weiss, R. Flükiger, W. Maurer, P.A. Hahn and M.W. Guinan, to be published in IEEE Trans. Magn., MAG-23 (1987).

6. H. Weber, "Irradiation Damage in Superconductors," Proc. CEC/ICMC Meeting on Advances in Cryogenic Engineering, Cambridge, MA, August 12-16, 1985.

7. S. Snead, Jr., D. Parkin, "Effect of Neutron Irradiation on the Critical Current of Nb_3Sn at High Magnetic Fields," Nucl. Technology 29, 264 (1976).

8. M. Guinan, Lawrence Livermore National Laboratory, private communications (July 1986).

9. R. Coltman, C. Klabunde, "Mechanical Strength of Low-Temperature-Irradiated Polyimides: A Five-to-Tenfold Improvement in Dose Resistance over Epoxies," J. Nucl. Mat. 103 & 104, 717 (1981).

10. R. Schmunk, EG&G Idaho, Inc., private communication, March 1985.

11. C. Long et al., "Effects of Radiation at 5 K on Organic Insulators for Superconducting Magnets," Special Purpose Materials Progress Report, U.S. DOE Report DOE-ER-004811, p. 73 (1981).

12. M. Guinan, Lawrence Livermore National Laboratory, private communications (June 1983).

13. M. Sawan, "Charts for Specifying Limits on Copper Stabilizer Damage Rate," J. Nucl. Mat. 122 & 123, 1376 (1984).

14. M. Sawan and P. Walstrom, "Superconducting Magnet Radiation Effects in Fusion Reactors," Proc. 7th Topical Meeting on Technology of Fusion Energy, Reno, NV 15-19 June 1986.

6.3 Magnet Shielding

A reduction in the magnet size can be achieved by designing an efficient shield and at the expense of accepting high radiation levels at the magnet. The thickness, composition, and geometric configuration of the shield strongly depend on the allowable radiation limits for the magnet. These limits are based on a number of considerations including the superconductor manufacturing technology, the heat removal requirements, the development in magnet insulation technology, and the coil stability and protection. The adopted radiation limits are summarized here and the reader should refer to the previous section for more thorough coverage. The limit on the end of life peak dose in the boron-free glass-fiber-filled (GFF) polyimide is taken as 10^{10} rads. This allows for possible insulator material improvements. No practical limit is used for the stabilizer damage in the forced-flow magnet design of ASRA6C. The limit on the nuclear heat load in the superconducting (S/C) magnet is design dependent. A limit of 0.2 mW/cm^3 is considered for the average nuclear heating in the inner layer of the magnets to avoid excessively high recirculated power for the cryoplant. The peak neutron fluence ($E_n > 0.1$ MeV) at the S/C magnet should not exceed 1.5 x 10^{23} n/m^2 for Nb_3Sn at the end of 20 full power year (FPY), the design lifetime of the reactor. This is based on reasonable extrapolation of recent experimental data at room temperature.

Considering the magnet radiation limits adopted in this study, we find that the magnet shield is driven by the nuclear heating in the magnet. Hence, the optimum shield composition is determined such that the peak winding pack power density is minimized. We performed a study to optimize the shield behind the thin LiPb/Be blanket using the one-dimensional discrete ordinates code ONEDANT[1] with the XSLIB data library (30 n group + 12 γ group) based on ENDF/B-V, and the P_3-S_8 approximation. We selected the option of alternate materials with a thick layer of Fe-shield (acts also as a reflector) followed by a layer of B_4C-shield and then a layer of Pb-shield. The reflector is helium cooled and the B_4C/Pb shield is water cooled. In all layers, we considered 10 vol% structure and 10 vol% coolant. The material composition for the different zones is given in Table 6.3-1. Figure 6.3-1 shows a schematic of the radial build of the blanket, shield and S/C magnet for a cross section through the midplane on the outboard side at the toroidal location where the plasma is horizontal (at ϕ = 0). At this section, the neutron wall loading peaks at a value of 2.4 MW/m^2, as indicated in Section 6.1.

Table 6.3-1. Material Composition for the Different Zones

Blanket
14 vol% LiPb
55.7 vol% Be (90% d.f.)*
10.3 vol% HT-9
20 vol% He/void

Reflector
90 vol% HT-9
10 vol% He

B_4C Shield
80 vol% B_4C (86% d.f.)*
10 vol% Fe 1422
10 vol% H_2O

Pb Shield
80 vol% Pb
10 vol% Fe 1422
10 vol% H_2O

Cryostat
1 cm Vacuum Vessel (316 SS)
5 cm Thermal Insulation (5 vol% Al)
1 cm LN_2 Radiation Shield
10 cm Coil Case (95 vol% 316 SS, 5 vol% LHe)
1 cm GFF Polyimide (45 vol% poly., 55 vol% S-glass)

S/C Coil
20 vol% 316 SS
40 vol% Cu
12 vol% Nb_3Sn
18 vol% He
10 vol% GFF Polyimide

*d.f. = density factor

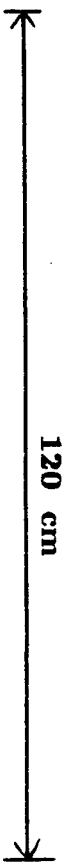| Radius (cm)		Thickness (cm)
0	Plasma	210
210	Scrapeoff Zone ·	22
232	LiPb/Be Blanket	21
253	Clearance	2
255	HT-9 Reflector	44.2
299.2	20 v/o C Insulation	2
301.2	B$_4$C Shield	25.5
326.7	Pb Shield	6.3
333	Clearance	1
334	Cryostat	18
352	S/C Coil	120
472		

120 cm

Fig. 6.3-1. Schematic of blanket, shield, and S/C magnet.

The distance between the first wall and the winding pack is constrained to 1.2 m in ASRA6C. Leaving 21 cm for the LiPb/Be blanket and 18 cm for the cryostat, the space available for the shield is 76 cm. In the optimization study, the three layers of the shield were varied in thickness to reduce the peak nuclear heating in the magnet. The optimum shield was found to consist of 58.1% Fe-shield, 33.6% B_4C-shield, and 8.3% Pb-shield. The peak radiation effects in the magnet are reported in Table 6.3-2. Although the magnet design does not call for a magnet behind the shield at all locations, the radiation effects were calculated assuming that the magnet is everywhere. The radiation effects in the magnet vary poloidally and toroidally according to the variation in the neutron wall loading (see Section 6.1). Figures 6.3-2 and 6.3-3 illustrate the poloidal variation of the nuclear heating and fast neutron fluence at the toroidal location $\phi = 0$ where the most severe radiation effects in the magnet occur.

The mechanical design of the blanket calls for 12 supply and return manifolds to cool the blanket and reflector. Each is 15 cm thick and 40 cm wide. Appropriate reflector cutouts are used to accommodate these manifolds. Our calculations show that the helium manifolds result in local hot spots with a factor of 6-7 higher damage. This effect is shown in Figs. 6.3-2 and 6.3-3. The peak dpa rate in the Cu stabilizer is 5.1×10^{-4} dpa/FPY and this corresponds to 116 nΩ cm radiation induced resistivity after 4 FPY when the first annealing is needed. This is not expected to jeopardize the stability and protection of the forced-flow coils.

The peak radiation effects in the magnets occuring behind the manifolds are given in Table 6.3-2. The manifolds occupy 25% of the back area of the blanket and accordingly the poloidal and toroidal average of the nuclear heating in the front layer of the magnets increases from 0.07 mW/cm^3 to 0.13 mW/cm^3. The nuclear heating per cm toroidal length of the magnet was found to be 2.9 and 5.2 W/cm for the winding pack and coil case, respectively. Since 30 coils each with an axial width of 1 m are used in ASRA6C, the total nuclear heating in the magnets amounts to 24 kW. This requires ~ 7 MW of electric power. Using an energy multiplication of 1.2 and a gross thermal efficiency of 42.7% we estimated the gross electric power to be 1770 MW. This indicates that 0.4% of the gross electric power has to be circulated to remove the nuclear heating from the magnets.
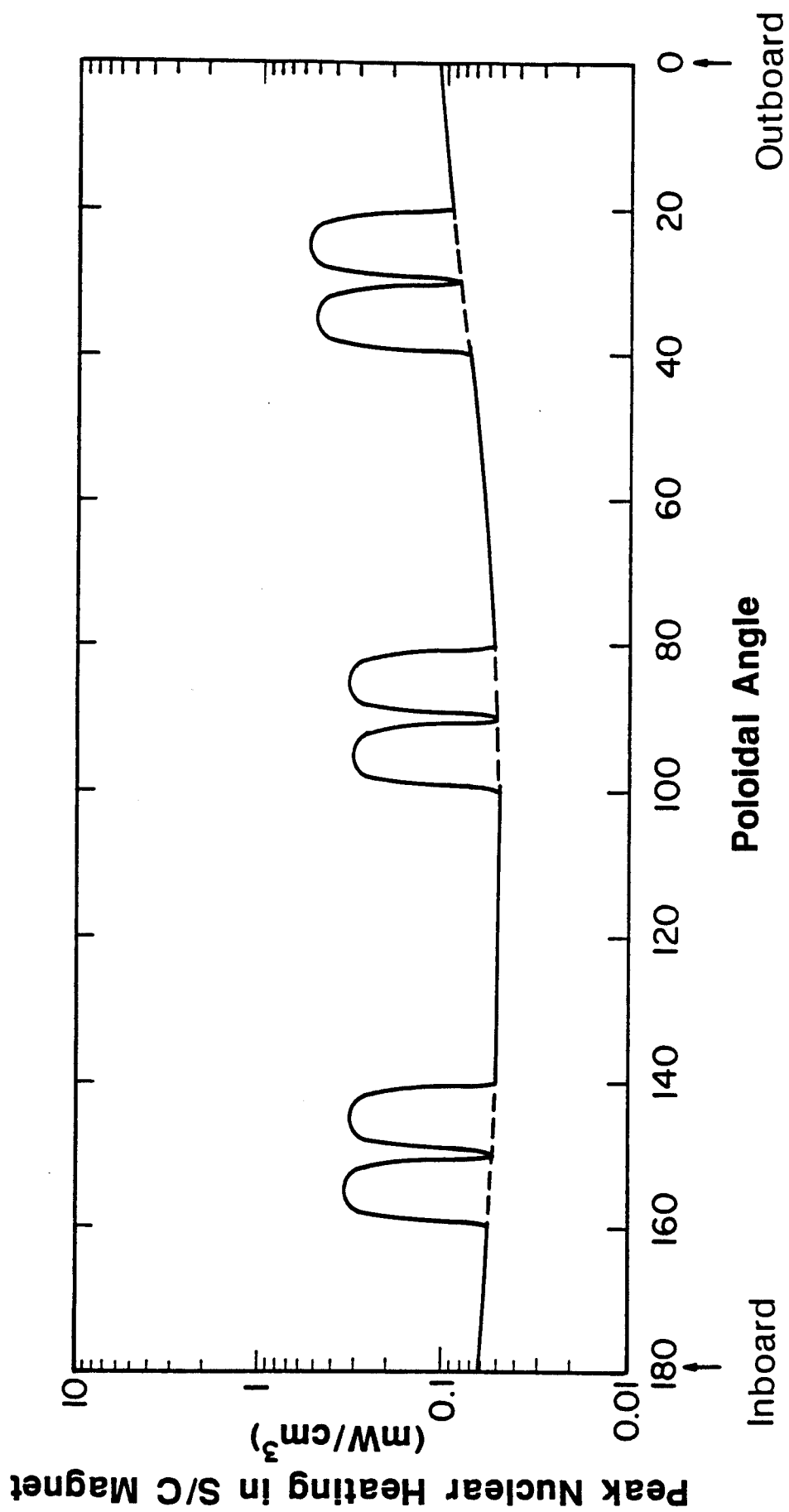
Fig. 6.3-2. Poloidal variation of the peak nuclear heating at toroidal location φ = 0 showing the effect of the He manifolds.

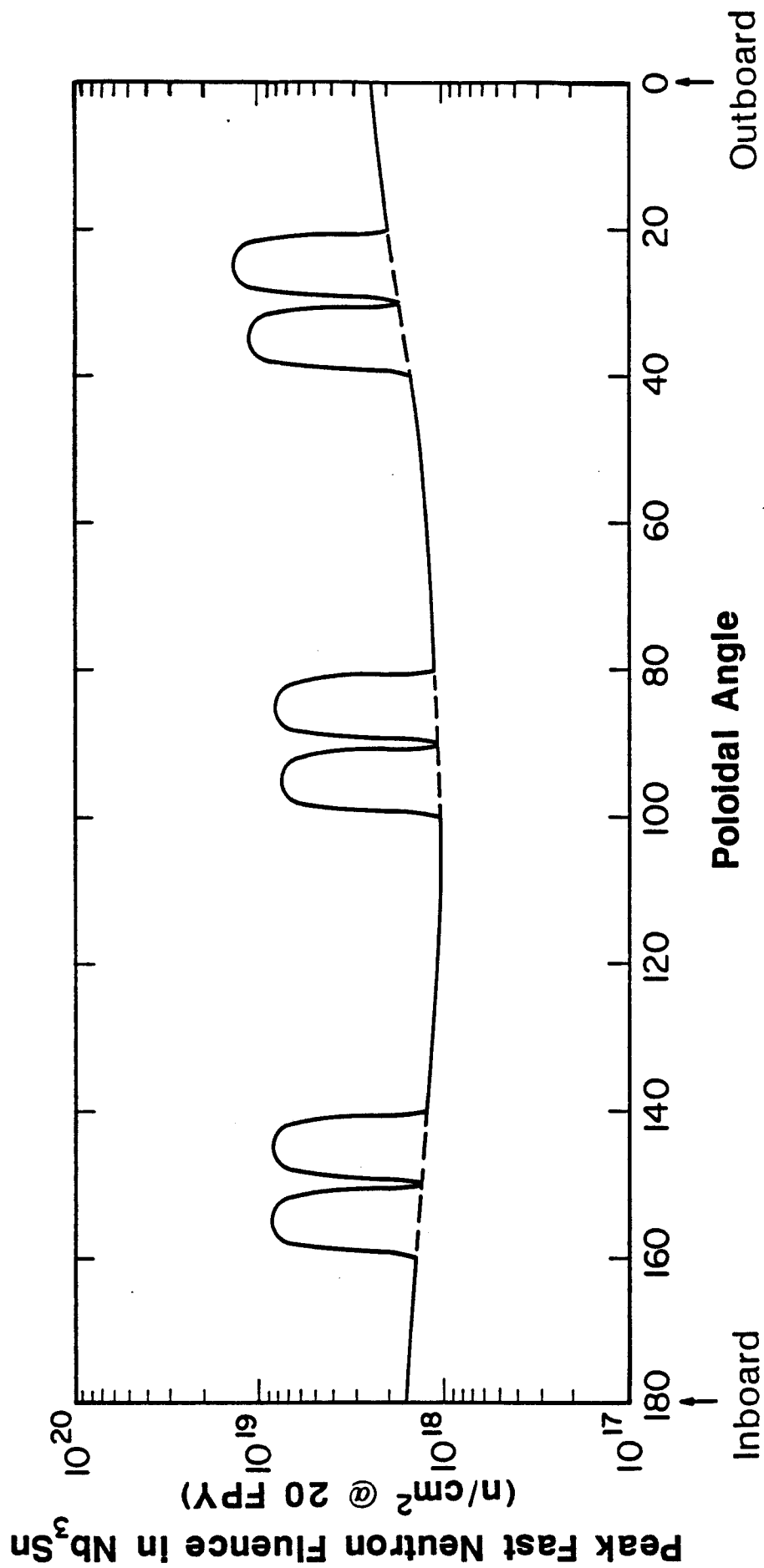Fig. 6.3-3. Poloidal variation of the peak fast neutron fluence at toroidal location φ = 0 showing the effect of the He manifolds.

Table 6.3-2. Peak Radiation Effects in Magnet

	At Midplane (2.4 MW/m^2)	Behind Manifolds
Nuclear Heating (mW/cm^3)	0.11	0.56
Fast Neutron Fluence (n/m^2 @ 20 FPY)	2.5×10^{22}	1.4×10^{23}
Dose in GFF Polyimide (rad @ 20 FPY)	2.2×10^{9}	1.0×10^{10}
dpa rate in Cu Stabilizer (dpa/FPY)	8.4×10^{-5}	5.1×10^{-4}

References for Section 6.3

1. R.D. O'Dell et al., "User's Manual for ONEDANT: A Code Package for One-Dimensional, Diffusion-Accelerated, Neutral Particle Transport," LA-9184-M, Los Alamos National Laboratory (Feb. 1982).

6.4 Penetration Shielding

The presence of the penetrations reduces the effectiveness of the bulk shield as radiation streaming through the penetrations produces hot spots in the S/C magnet and limits its performance. On this basis, some attention was paid to the penetration shield design to insure proper performance of the S/C magnet.

There are four neutral beam injector (NBI) ports (1 x 1.8 m each) located at the outboard side of ASRA6C and 115 pumping ports (each is 1.5 m in diameter) uniformly distributed around the torus. The NBI was chosen for radiation analysis as it has the largest duct opening and thus is expected to result in the highest streaming radiation level at the magnet. The existence of these penetrations indicates that a realistic model to handle the streaming radiation effects on the magnet must be three-dimensional. The Monte Carlo codes are capable of modeling such geometry. However, such calculations are expensive and time consuming. Due to the limited time of the study, we used analytical methods and 1-D models to represent the actual 3-D problem. This approach has been found to be a valuable tool in previous reactor studies.[1-3]

The method[1] consists of computing analytically the neutron wall loading at the penetration wall closest to the coil as a result of neutrons streaming through the penetration, and then performing a 1-D calculation to estimate the radiation effects at the magnet. The wall loading depends on the magnet dimensions, size and shape of the penetration and its location. The W/B_4C shield is used around the perimeter of the penetrations to maximize the attenuation of the streaming radiation. The penetration shielding criterion was set such that the sum of the effects of the radiation penetrating through the duct and the bulk shield should not exceed the radiation limit at the magnet. The results show that the streaming neutron wall loading is 0.2 MW/m^2 and 40 cm of W/B_4C shield (73% W and 27% B_4C) around the NBI duct (in addition to the 20 cm thick coil case) results in peak nuclear heating of 0.6 mW/cm^3 and fast neutron fluence of 1.4 x 10^{23} n/m^2. These calculations are based on an empty NBI. In the actual case, the NBI components attenuate the neutrons and it is expected that this reduces the streaming radiation effects at the magnet by at least a factor of 2. On this basis, adding the radiation effects from both the penetration shield and the bulk shield (see Table 6.3-2) yields peak values of 0.4 mW/cm^3 and 9 x 10^{22} n/m^2 at the outboard side of the torus.

It should be mentioned that a minimum penetration shield thickness of 50 cm should be provided between the penetration walls and the portions of the magnet behind the He manifolds. This is needed to yield a negligible contribution from the streaming radiation at these hot spots.

It is worth mentioning that an attractive solution for the streaming problem is to plug the NBI penetrations with a block of shielding after the startup period and during reactor operation. In this case the shield required around the NBI is reduced considerably. The only concern, however, is that the sides of the S/C magnet closer to the NBI's will be subjected to high nuclear heating levels during the few minutes of startup and the magnet designers should provide special cooling for these sides of the magnet during the startup periods of the reactor.

References for Section 6.4

1. M.E. Sawan, C.W. Maynard, and L.A. El-Guebaly, "Buildup Factors for Magnet Shielding in Tandem Mirror Fusion Reactors," Proceedings of the 6th International Conference on Radiation Shieldings, Tokyo, Japan (1983).

2. M.E. Sawan and L.A. El-Guebaly, "Magnet Shielding in the Compact Fusion Technology Test Facility TASKA-M," Trans. ANS 46, 631 (1984).

3. J.D. Lee et al., "MINIMARS Conceptual Design Final Report," Lawrence Livermore National Laboratory, UCID-20773 (1986).

7. Engineering Consideration of Modular Coils for ASRA6C

7.1. Introduction

The compact system ASRA6C is reduced in size as compared to the preceding data set ASRA6B, or to earlier stellarator fusion reactor coil systems with different numbers of coils per field period, as desribed shortly in chapter 3. The coil systems of ASRA6B and ASRA6C have 6 non–planar coils in each of the 5 field periods. The choice of this coil number is made as a compromise between 'field quality', see [1], and ease of assembly and maintenance of such systems. The main feature of the coils is their identical approximately elliptic coil bore. The uniform shape of the coil bores permits an uncomplicated design of blanket and shield and simplifies maintenance.

The modular coil system ASRA6C is characterized by a major radius $R_o = 20\,m$, an average minor coil radius of $4.6\,m$, and by a distance $\Delta = 1.2\,m$ between the plasma edge and the coils. The coils produce an induction of $B_o = 5.3\,T$ on axis; the total stored magnetic energy amounts to $W_m = 117\,GJ$.

The force distribution within the coils is calculated and yields a local maximum force density of $155\,MN/m^3$. A characteristic feature of non–planar coil systems is that they have lateral forces with local values comparable to the maximum radial component. Within a field period the lateral forces are balanced. The mechanical stress and strain distributions are investigated inside the coils by finite-element calculations, using the SAP V (2) program system. A mutual support between adjacent coils is used. With the orthotropic material data of the Euratom-LCT coil, a maximum equivalent (von Mises) stress of $\sigma_{vM} = 135\,MPa$ is obtained within the coils of ASRA6C, in association with a considerable shear stress, amounting up to $\sigma_{ST} = 50\,MPa$. The tangential strain is about 0.2% for this case.

A short description of the main properties of the coil system ASRA6C as compared to ASRA6B is given in section 7.2. The following section briefly summarizes details of the electromagnetic force distributions present in non–planar coil systems, and compares the results for the two reference systems. In section 7.4, the stress analysis is performed for the coils of ASRA6C. A system of mutual coil support is employed. A summary and conclusions are given in section 7.5.

7.2. Properties of the Coil Systems ASRA6B and ASRA6C

The compact coil system ASRA6C is made possible by introducing a modern design of the blanket and shield (see chapter 5 and 6, and also [2]) which reduces the critical distance Δ between the first wall and the inner contour of the coil winding, from the previous value of $2.1\,m$ to $1.2\,m$. Consequently the major radius can be reduced from $R_o = 25\,m$ in ASRA6B to a value of $20\,m$ in ASRA6C. Fig. 7–1 shows the whole coil configuration of ASRA6C, and Fig. 7–2 shows one field period. There are 6 coils per field period with only three different coil shapes in the complete coil system, if one considers the twofold mirror symmetry. All coil apertures are of the same elliptic cross section with an axis ratio of about 1.17, centered at major radii according to

$R(\varphi) = R_o \left(1 - k\cos(5\varphi) \right)$, where $k = 0.016$ for both cases, and φ is the toroidal angle.

The spatial contours of the non–planar modular coils of ASRA6B and ASRA6C follow an analytical relationship or "winding law", describing the coil centerline for arbitrary position and orientation of the modular coils, as detailed in [3]. The edge contours of the coils are obtained by adding half of the lateral width and shifting by half of the radial height.

The characteristic data of the two coil systems for the Advanced Stellarator Reactors ASRA6B and ASRA6C are given in Table 7–I. Equal values of the effective current density, $j_{eff} = 15\,MA/m^2$, are used in both cases. Here, the effective current density is the total coil current I_c divided by the whole cross section of the coil winding pack, i.e. averaging over the complex structure of superconductor with stabilizer, internal structure, insulation, and helium channels. Because the value of the induction at the axis, $B_o = 5.3\,T$, is the same in both data sets, the total coil current amounts to $I_c = 22.5\,MA$ and $18\,MA$ for ASRA6B and ASRA6C, respectively. The coil current scales proportionally to the major radius. The coil volumes V_c, as given in the table, are estimated including a correction factor f which describes the average toroidal excursion of the coils.

In a toroidal arrangement of non–planar coils a complex distribution of the induction is present, which has components in all spatial directions, and has considerable field gradients. Fig. 7–3 shows the magnitude of the magnetic field in the first quadrant of ASRA6C. The maximum value of the induction is at the coil bore. Due to the non–planar coil shape and the differing coil distances, the maximum field at the coil is different for the three different coils in a field period, and not necessarily at the inner mid–plane. The local maximum values are given in the table and amount to $B_m = 11.0\,T$ and $10.4\,T$ for the two systems, respectively.

Note the remarkable decrease in the stored magnetic energy when the size of ASRA6B is reduced to that of the compact system ASRA6C. On the other hand, the smaller radius of curvature in ASRA6C might influence the material choice and winding techniques for the coil fabrication. The radius of curvature of the 6 coils in one field period is shown in Fig. 7–4 as a function of the coil circumference, measured at the coil corners. The local minimum radius of curvature is given in Table 7–I and amounts to $\rho_c = 0.77\,m$ for ASRA6C.
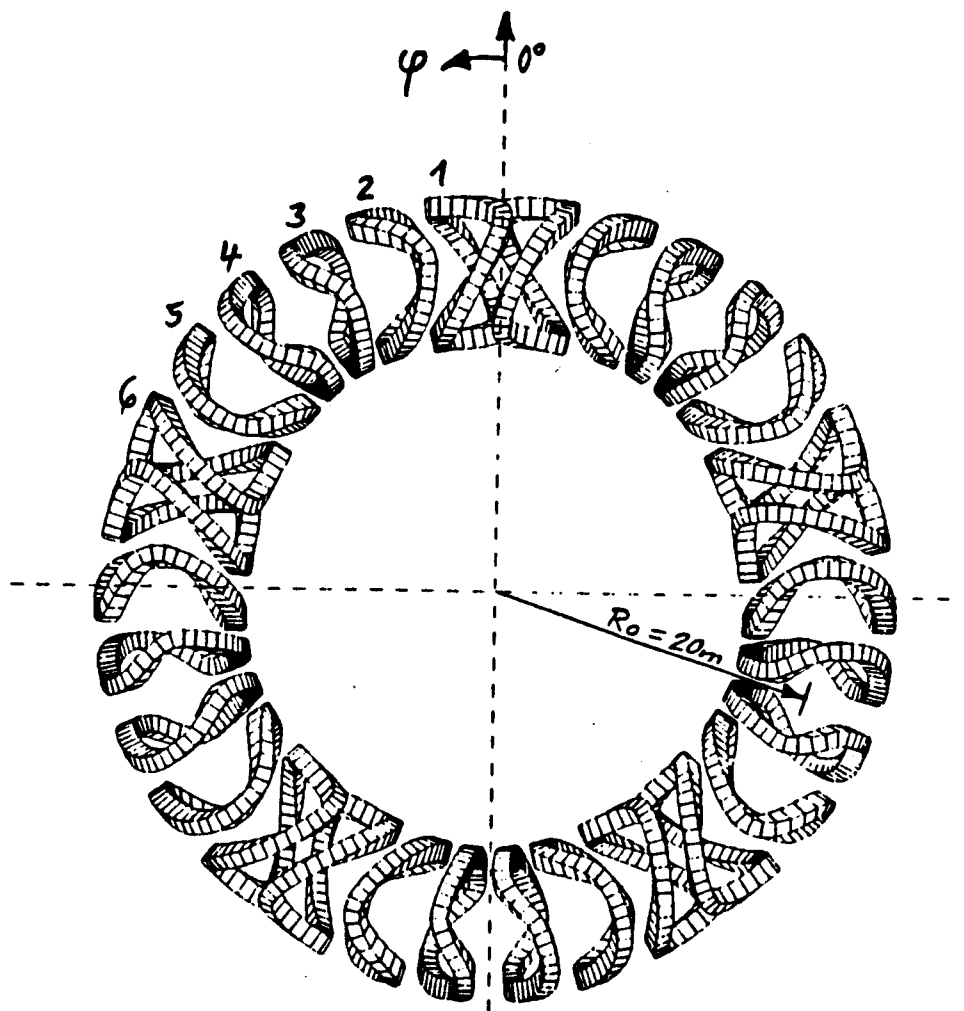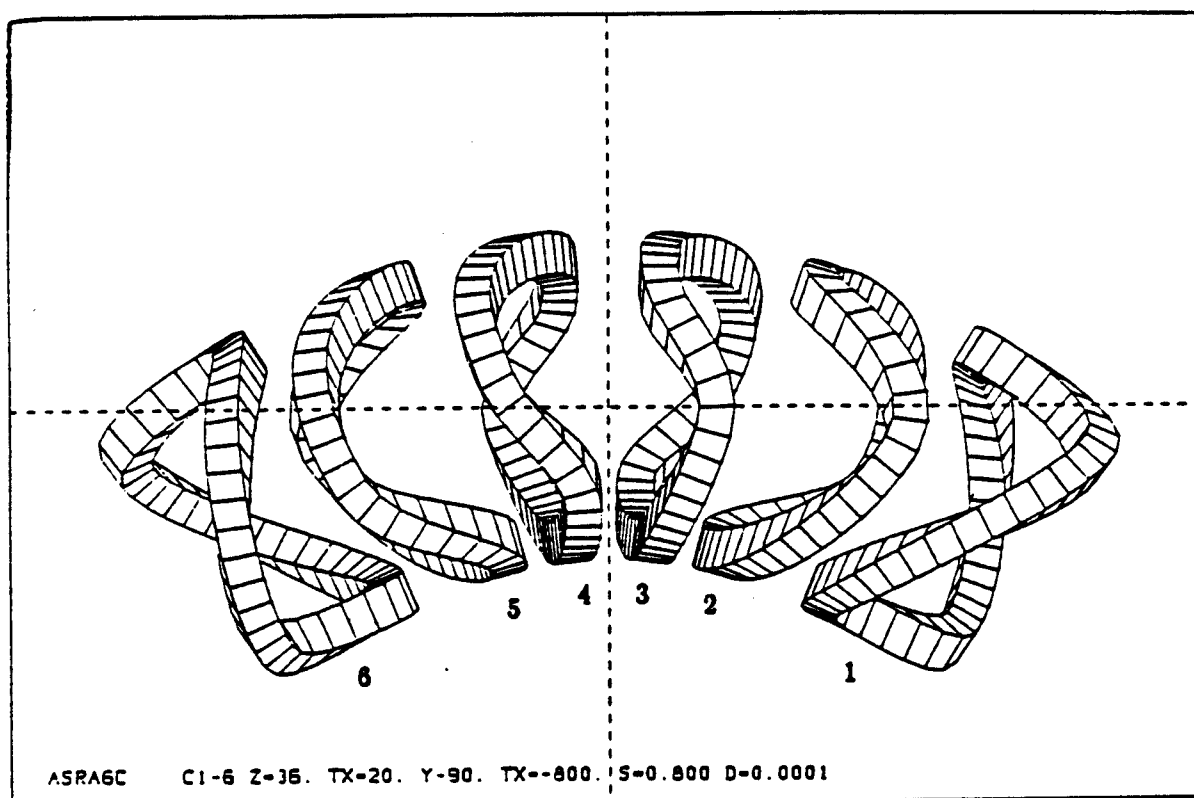
Fig. 7-1: Coil configuration ASRA6C

ASRA6C   C1-6 Z=36. TX=20. Y-90. TX=-800. S=0.800 D=0.0001

Fig. 7-2: Coil configuration ASRA6C, one field period.

TABLE I : Characteristic data of ASRA6B and ASRA6C.

			ASRA6B	ASRA6C
Average major radius	R_o	$[m]$	25.0	20.0
Average coil radius	r_c	$[m]$	5.22	4.57
Radial coil height	w	$[m]$	1.25	1.20
Lateral coil width	t	$[m]$	1.20	1.00
Average coil volume	V_c	$[m^3]$	54.7	40.0
Distance first wall – coil	Δ	$[m]$	2.1	1.2
Min. radius of curvature	ρ_c	$[m]$	1.05	0.77
Coil number total / per FP	n/n_p		30/6	30/6
Total coil current	I_c	$[MA]$	22.5	18.0
Effective current density	j_{eff}	$[MA/m^2]$	15.0	15.0
Self inductance coil 1 (one-turn)	L_{11}	$[\mu H]$	16.9	15.1
Total inductance (one-turn)	L	$[\mu H]$	763.	722.
Total stored magnetic energy	W_m	$[GJ]$	193.	117.
Magnetic induction on axis	B_o	$[T]$	5.3	5.3
Max. induction at coil	B_m	$[T]$	11.	10.4
Rotat. transform on axis	t_o		0.39	0.47
Average plasma radius	r_p	$[m]$	1.6	1.6
Average force density	$\langle F' \rangle$	$[MN/m^3]$	50.	50.
Local max. force density	F'_m	$[MN/m^3]$	165.	155.
Max. net force (one coil)	F_{res}	$[MN]$	$\sim 200.$	$\sim 150.$
Virial stress	σ_V	$[MPa]$	118.	99.

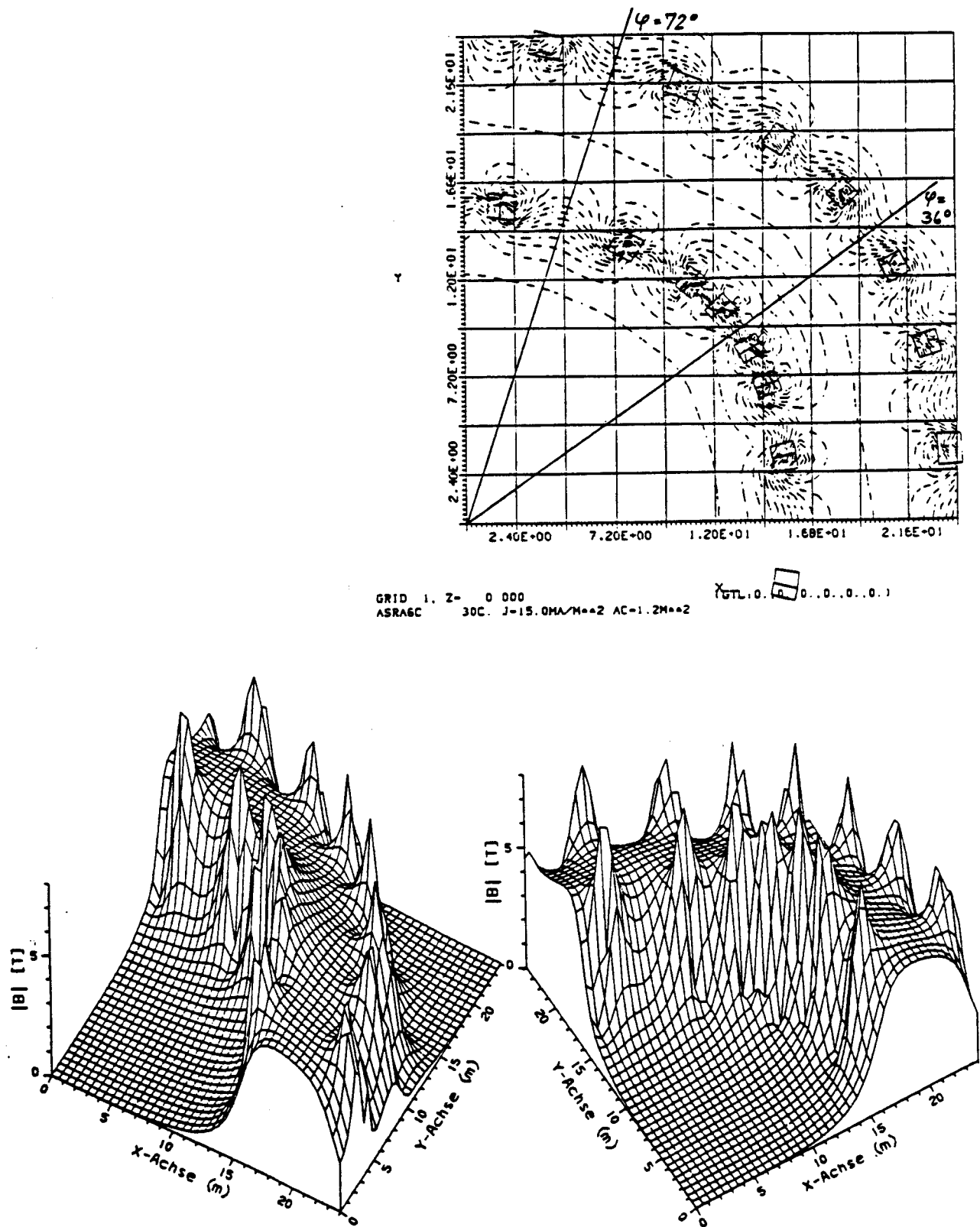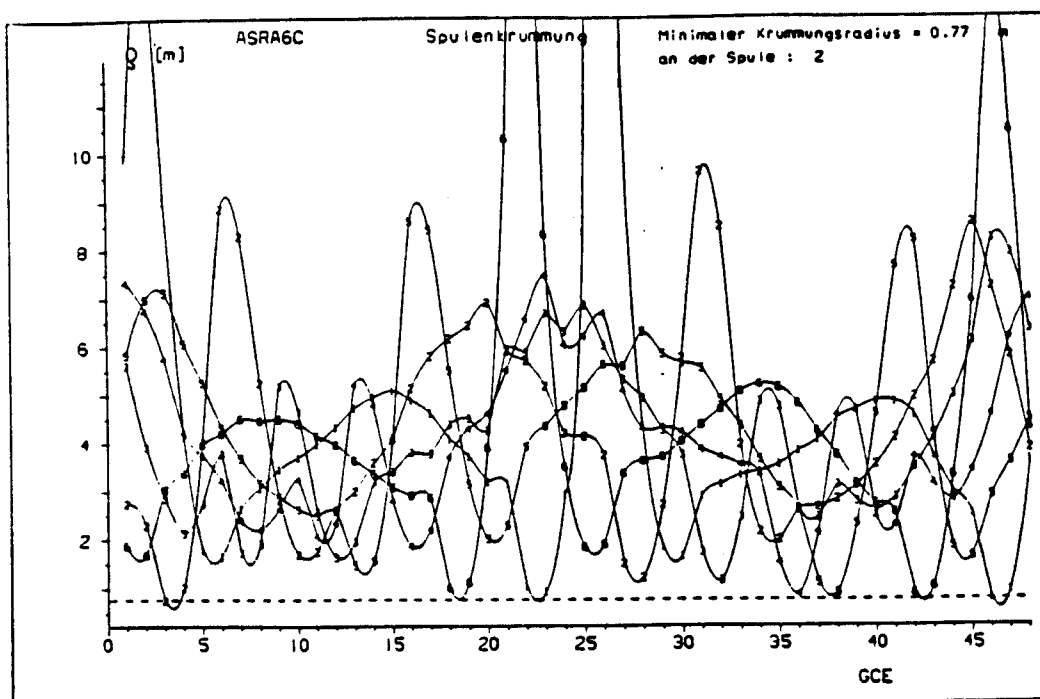Fig. 7-3: Magnitude of the magnetic field in the first quadrant of ASRA6C.

Fig. 7–4: ASRA6C: local radius of curvature of coils 1-6.

7.3. Electromagnetic Forces

In order to describe the distributions of magnetic field, forces, and stresses a local orthogonal coordinate system R, S, T is used, with R indicating the radial, S the lateral, and T the tangential directions, respectively, as shown in Fig. 7-5 (see [4]). Inside the coils all field components B_R, B_S, B_T are present, whereas the current density has only one component in the tangential direction. Hence, according to $\vec{F}' = \vec{j} \times \vec{B}$, there are two components of the force density, namely F_R' and F_S', acting on the twisted coils. These local forces are different for the three differently shaped coils. Thus, considering the twofold mirror symmetry of each field period, the lateral forces are balanced over one field period.

Because of the toroidal arrangement of the system and the relatively small variation of the major radius of the coil centers, a net force exists for each coil of the assembly in the direction towards the torus center. This force amounts to about 150 MN per coil for the ASRA6C configuration, and about 200 MN in ASRA6B, see [5].

In order to obtain the distribution of the force density inside the coils, the cross-section is subdivided into three radial and two lateral "microelements". Earlier studies, given in [4], demonstrate that this rather coarse grid yields a sufficient degree of accuracy.

Fig. 7-6 shows the radial (F_R') and lateral (F_S') components of the force density for coil 1 of ASRA6C versus the coil circumference. All coils in the assembly are energized. The values are computed in the center of the "microelements", as given in the insert of the figure. If coil 1 is treated as a single coil, the values are lower, see Fig. 7-7, but the force density distribution is similarly complex. This is due to the non-planar coil shape.

The average magnitude of the force density is $< F' > = \frac{1}{N} \sum_{i=1}^{N} |\frac{1}{V_i} \int_{V_i} \vec{j} \times \vec{B} \, ds \, dA|$, where ds denotes a line element in the direction of the current, dA an area element perpendicular to ds, V_i the volume of a GCE (general current element), and N the number of the GCE's, respectively. For ASRA6B and ASRA6C, the same value of about 50 MN/m^3 is calculated as an average for all coils in the assembly. The nearly identical result of the two configurations is due to the following facts: the average radial component of the force density in ASRA6B is larger than in ASRA6C, but the lateral component of the force density in ASRA6B is smaller than in ASRA6C, because of the larger lateral radius of curvature in ASRA6B. The local maximum of the magnitude of the force density in ASRA6B is slightly higher than in ASRA6C: 165 MN/m^3 as compared to 155 MN/m^3. It occurs in both systems at coil 2, within GCE number 11, see Fig. 7-8. The five curves of the figure are equally spaced at the coil bore, showing some spread caused by the different local values of the induction, the current density j being a constant across the coils. The ratio of the maximum local force density and the average value is a factor of approximately three. This is caused by the steep field gradients within the coils.

SIDE VIEW

FRONT VIEW

TOP VIEW

cross-section

1.2 m

1.0 m

ASRA6C COIL1 (1)
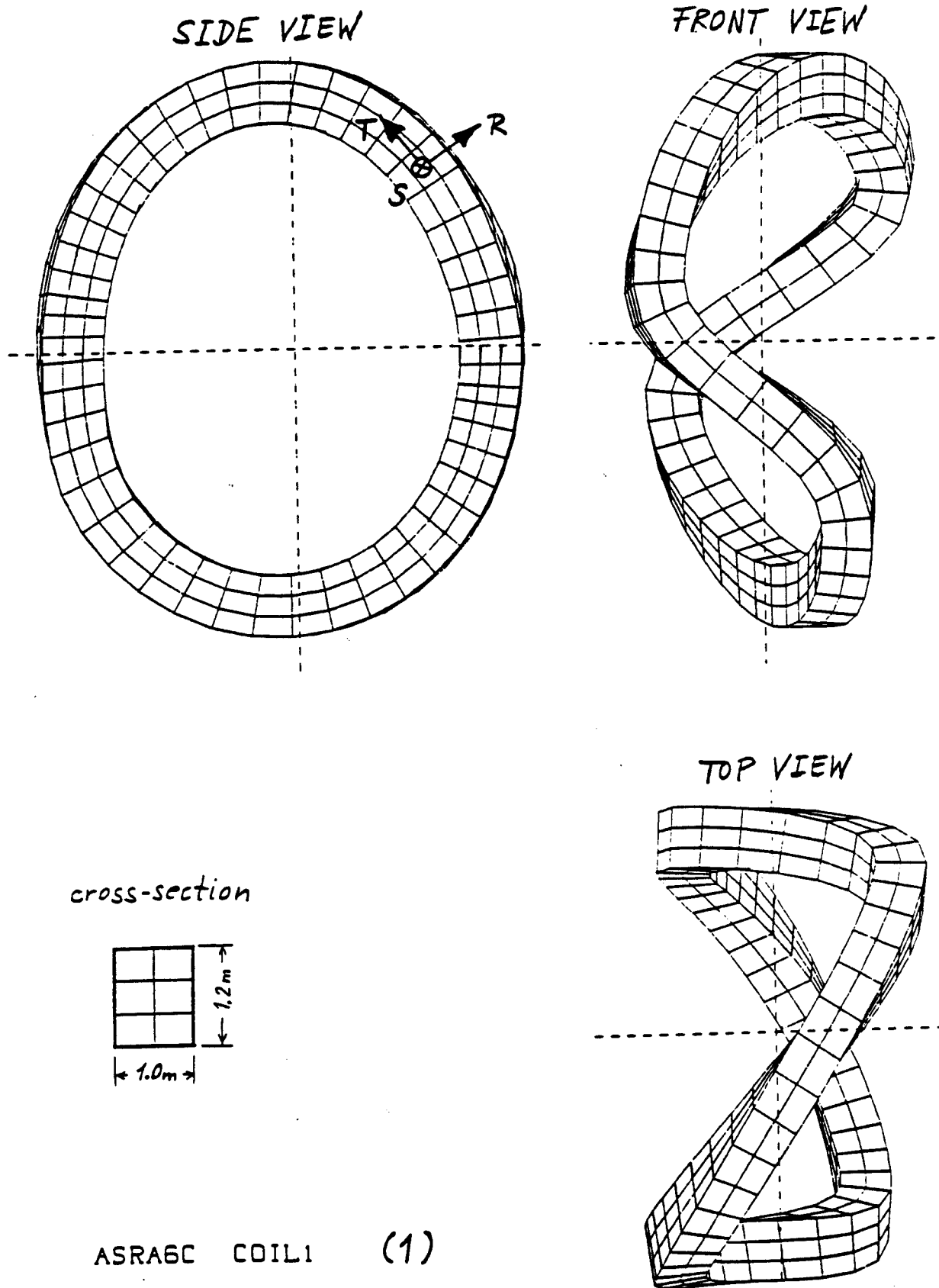
Fig. 7-5: Coil 1 of ASRA6C with the indicated natural coordinate system R, S, T. The cross-section of the coil is subdivided into 6 "microelements".
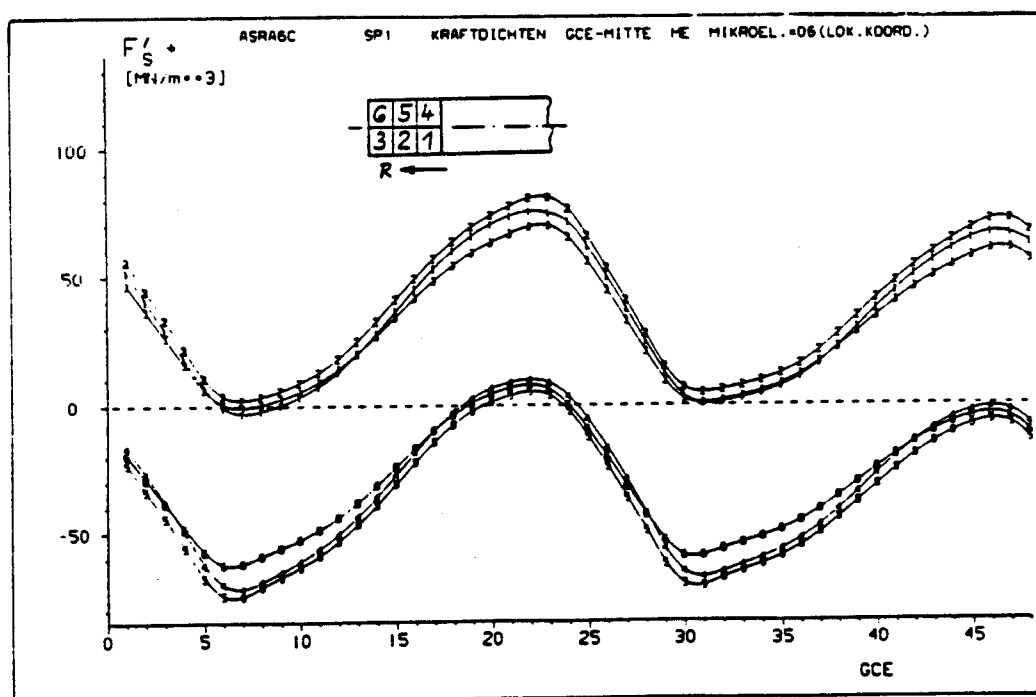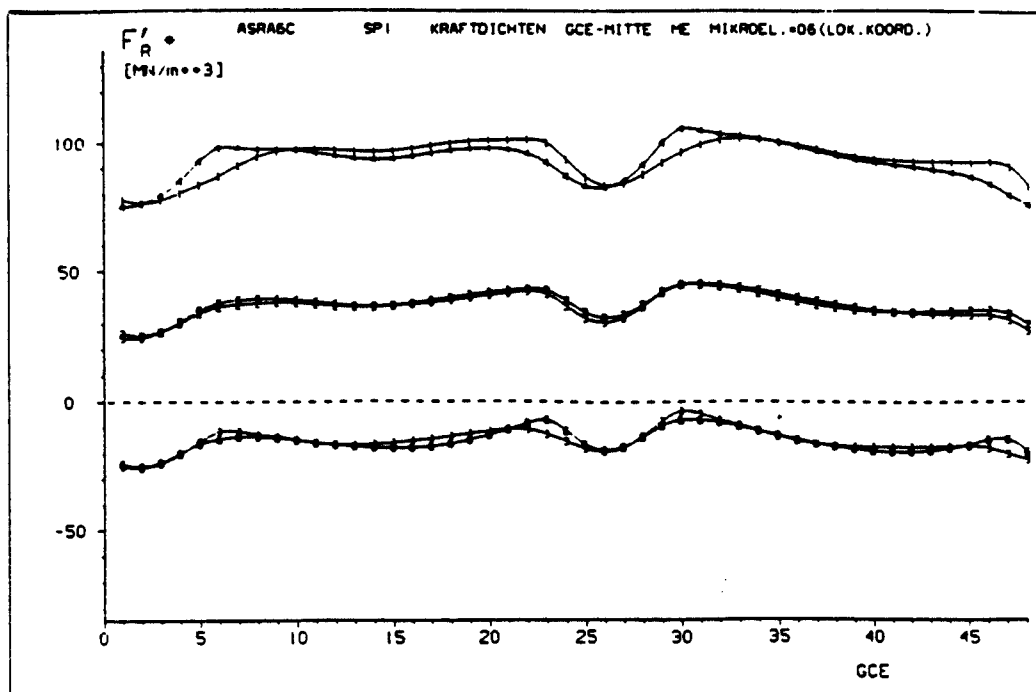
Fig. 7–6: Magnetic force densities in radial and lateral direction of coil 1; all coils in the assembly of ASRA6C are energized.
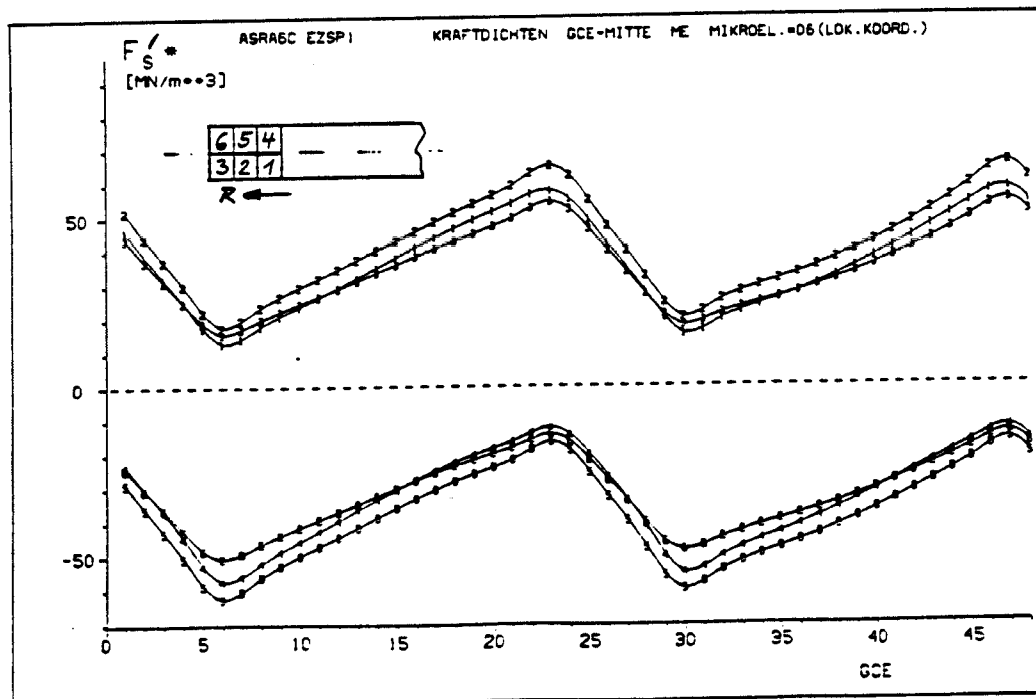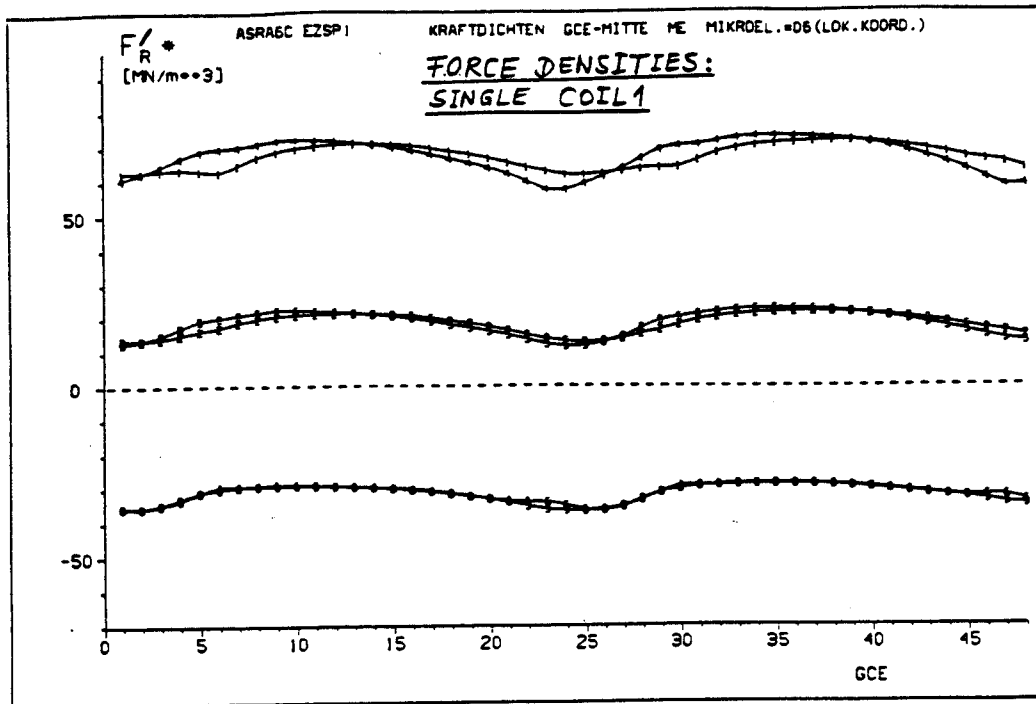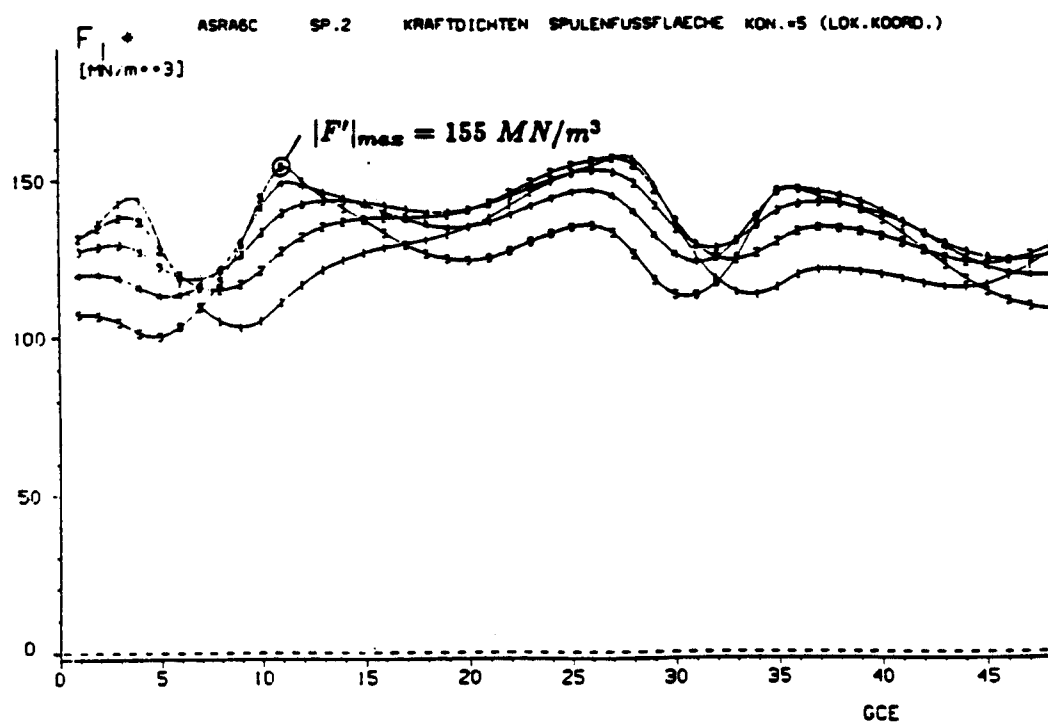
Fig. 7–7: Magnetic force densities in radial and lateral direction of coil 1, the coil is separated from the assembly of ASRA6C.

Fig. 7–8: Magnitude of the force densities calculated at the inner side of coil 2 for 5 contours along the circumference of the coil bore.

7.4. Mechanical Stress Analysis

In order to investigate the mechanical stress and strain distributions, finite-element calculations are performed using the SAP V (2) program system. This is done inside the coils and in some cases within the support structure. The complex coil construction is simplified by using appropriate average values for the material data, as given in [5]. The calculations of stress and strain are performed for coils in the assembly, as well as for a single coil in its own magnetic field.

A single coil separated from the coil assembly is free of a net force, and no external forces are required to support it. The main data for the single coil 1 of ASRA6C at the operating current are listed in Table 7-II.

TABLE 7-II : Characteristic data of single coil 1 of ASRA6C.

Total coil current	I_c	$[MA]$	18.0
Overall current density	j_c	$[MA/m^2]$	15.0
Total inductance (one turn)	L	$[\mu H]$	15.1
Magnetic energy	W_m	$[GJ]$	2.45
Max. induction at coil	B_m	$[T]$	7.7
Local max. force density	F'_m	$[MN/m^3]$	115.
Coil volume (winding pack)	V_c	$[m^3]$	41.0

A single coil without external support shows a complex distribution of the force density, due to the non–planar coil shape. The stress calculations indicate that a coil support similar to that shown in Fig. 7–9 is required, which has a lateral and inside radial thickness of $10\,cm$, and $40\,cm$ at the radial outside. Elastic paddings are included between the coil and the structure. The ratio of structure volume to coil volume amounts to 1.1. Then the bending stresses inside the coil are reduced to acceptable values. The maximum equivalent stress σ_{vM}, as shown in Fig. 7–10, occurs at the centre of the microelements and is about $42\,MPa$ in this case $\big($ using the orthotropic coil data of the WVII-AS coils as given in Table 7–III $\big)$, and the shear stress component σ_{ST} is about $10\,MPa$ under the same conditions, see Fig. 7–11. Fig. 7–12 shows the equivalent stress in the thin structure of the coil housing, as shown in the insert. Because of the high stiffness of the structural material, as compared to the coil material, relatively high stress values occur in the structure material. In the critical part of the structure the maximum value of σ_{vM} reaches $470\,MPa$ at the centre of the microelements. On the surface the absolute maximum value is even higher, but reinforcing the structure at the critical points solves this problem, and the maximum stress values will be well below the stress limit of steel.

TABLE 7–III Orthotropic coil material data, isotropic structure data.

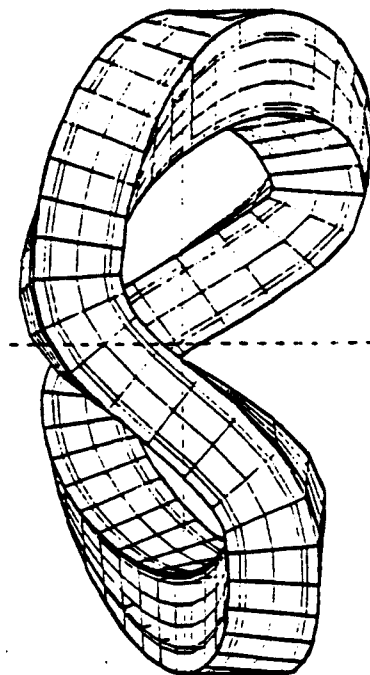|			Coils WVII-AS	Coil LCT-Eur.	Structure Stainless steel
Young's modulus	E_R	$[GPa]$	25.0	62.0	200.0
	E_S	$[GPa]$	25.0	53.0	200.0
	E_T	$[GPa]$	70.0	120.0	200.0
Poisson's ratio	ν_{RS}		0.219	0.198	0.3
	ν_{ST}		0.112	0.126	0.3
	ν_{TR}		0.302	0.298	0.3
Shear modulus	G_{RS}	$[GPa]$	10.7	10.	76.9
	G_{ST}	$[GPa]$	10.7	26.	76.9
	G_{TR}	$[GPa]$	10.7	21.	76.9
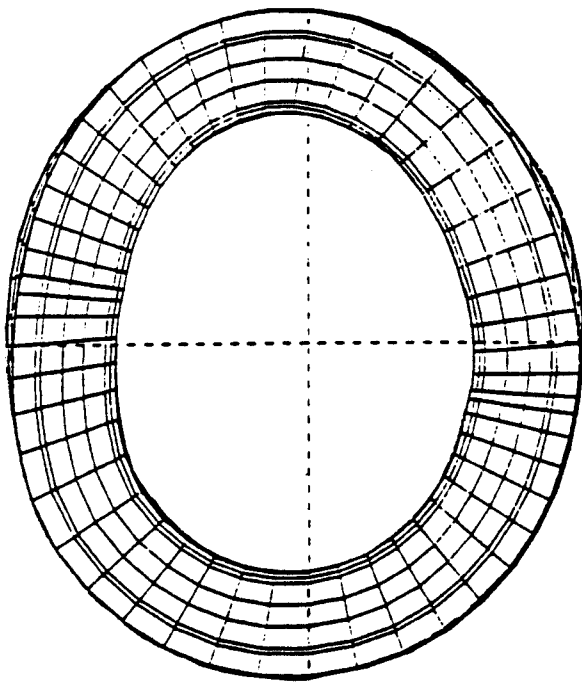
Side view   Front view
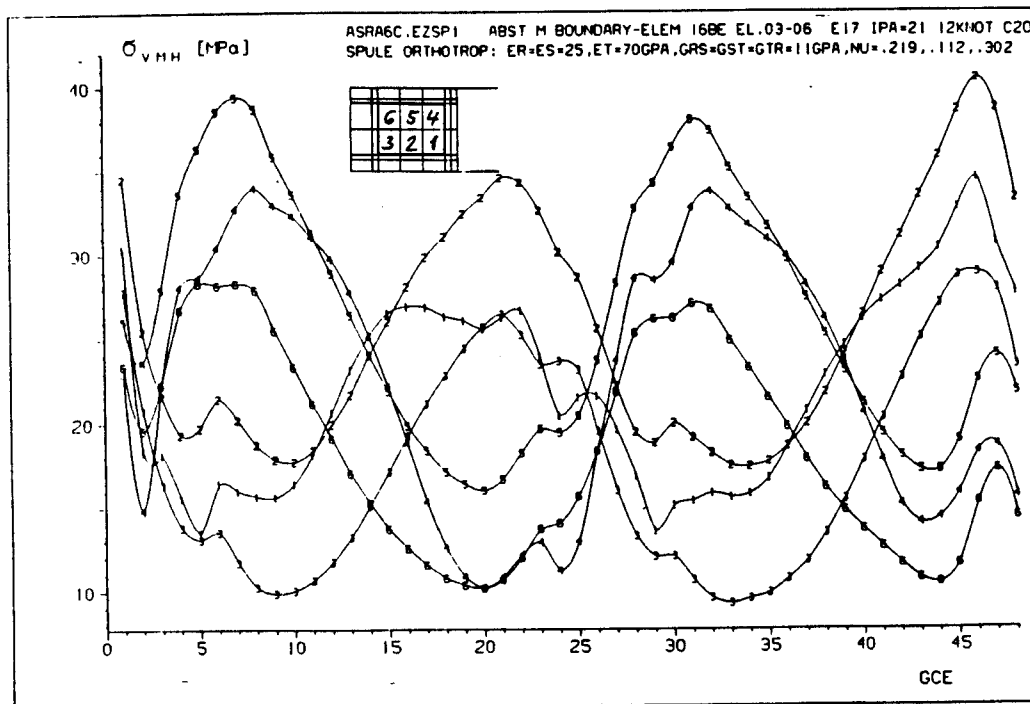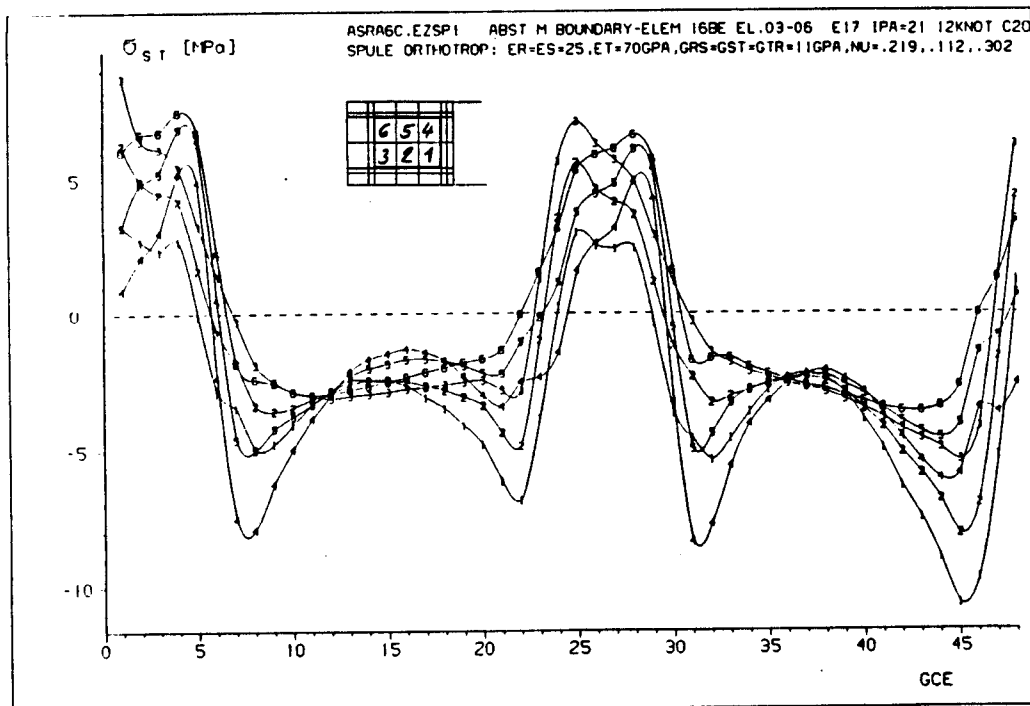

Fig. 7-9: ASRA6C: coil 1 with coil housing.

Fig. 7-10: ASRA6C, single coil 1: equivalent stress σ_{vM}, orthotropic coil data.

Fig. 7-11: ASRA6C, single coil 1: shear stress σ_{ST}, orthotropic coil data.
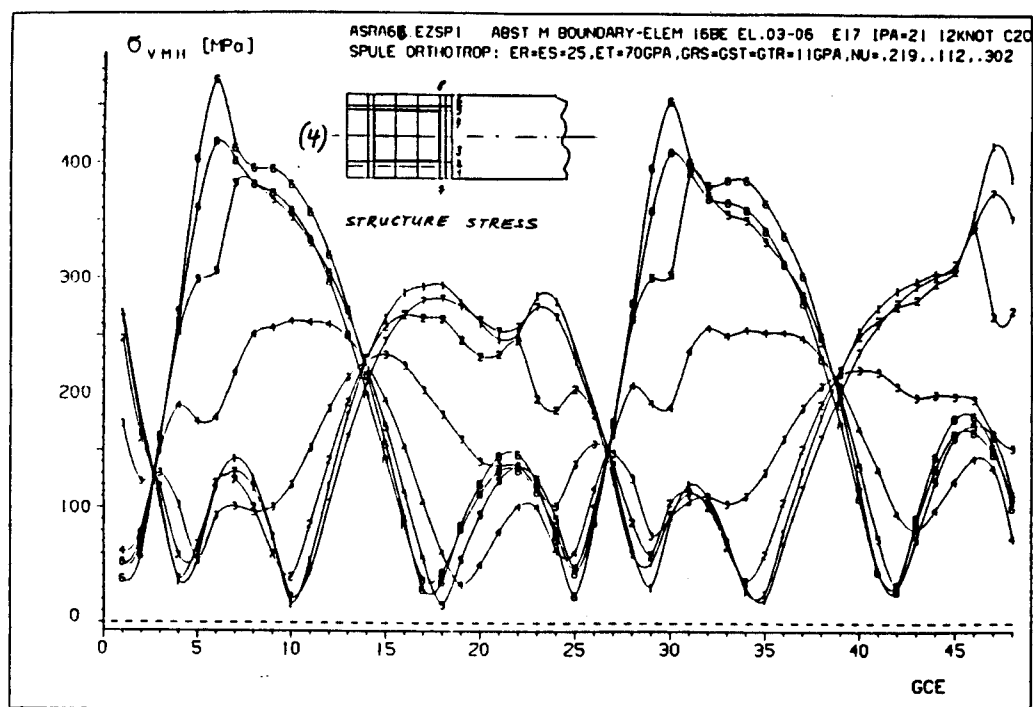
Fig. 7-12: ASRA6C, single coil 1: equivalent stress σ_{vM} in certain parts of the structure, orthotropic coil data.

As support system for the coil assembly of ASRA6C we again use the previously introduced concept of mutual support between adjacent coils, see [5] . Each coil is surrounded by a suitably shaped support structure of stainless steel, consisting of radial and lateral rings. In the development of the support scheme, the rings are completed to a full coil housing, as described in [6]. The housing for the ASRA6C coils has a lateral width of $30\,cm$, a radial inside width of $10\,cm$ and a radial outside width of $60\,cm$. In regions of high curvature of the coils the coil housing is laterally reinforced. The upper part of Fig. 7–13 shows a vertical view on 6 coils, comprising one field period, without mutual support elements. Rigid boundary elements are provided on the outer rings of the arrangement in the region towards the torus center, as shown schematically in Fig. 7–13. In the space between the coils, lateral support elements are located in order to achieve mutual support of the coils, as shown in the lower part of Fig. 7–13 in the $\varphi - \vartheta-$ plane, where φ is the toroidal and ϑ the poloidal angle. The positions of the lateral support elements are varied iteratively in order to minimize the stress and strain values of the coil system. The computations are done for a total number of 4608 nodes and 2922 elements.

The finite element computations are based on orthotropic material data for the coils as given in Table 7–III. Three different cases are investigated:

A : The coils are surrounded with radial and lateral rings, and the coil material data is close to the measured data of the non–planar coils for the Garching Advanced Stellarator experiment WENDELSTEIN VII–AS, as used in [5] .

B : The coils are surrounded with a full coil housing, laterally reinforced at locations of high curvature, as described in [6] , utilizing the coil material data as in case A .

C : Like case B, but with the coil material data of the Euratom–LCT coil as given in [7] .

The results of the stress and strain computations are listed in Table 7–IV.

TABLE 7–IV : Stress and strain calculations for the coils of ASRA6C [*].

			Case A	Case B	Case C
Tangential stress	$|\sigma_T|_{Max}$	$[MPa]$	175.	132.	142.
Shear stress	$|\sigma_{ST}|_{Max}$	$[MPa]$	50.	35.	46.
Equivalent stress	$\sigma_{vM\,Max}$	$[MPa]$	170.	120.	135.
Tangential strain	$|\epsilon_T|_{Max}$	$[\%]$	0.2	0.15	0.17
Shear strain	$|\gamma_{ST}|_{Max}$	$[\%]$	0.5	0.3	0.44

[*] The results include an enhancement factor of 2.5 in cases A and B, and of 2.0 in case C.
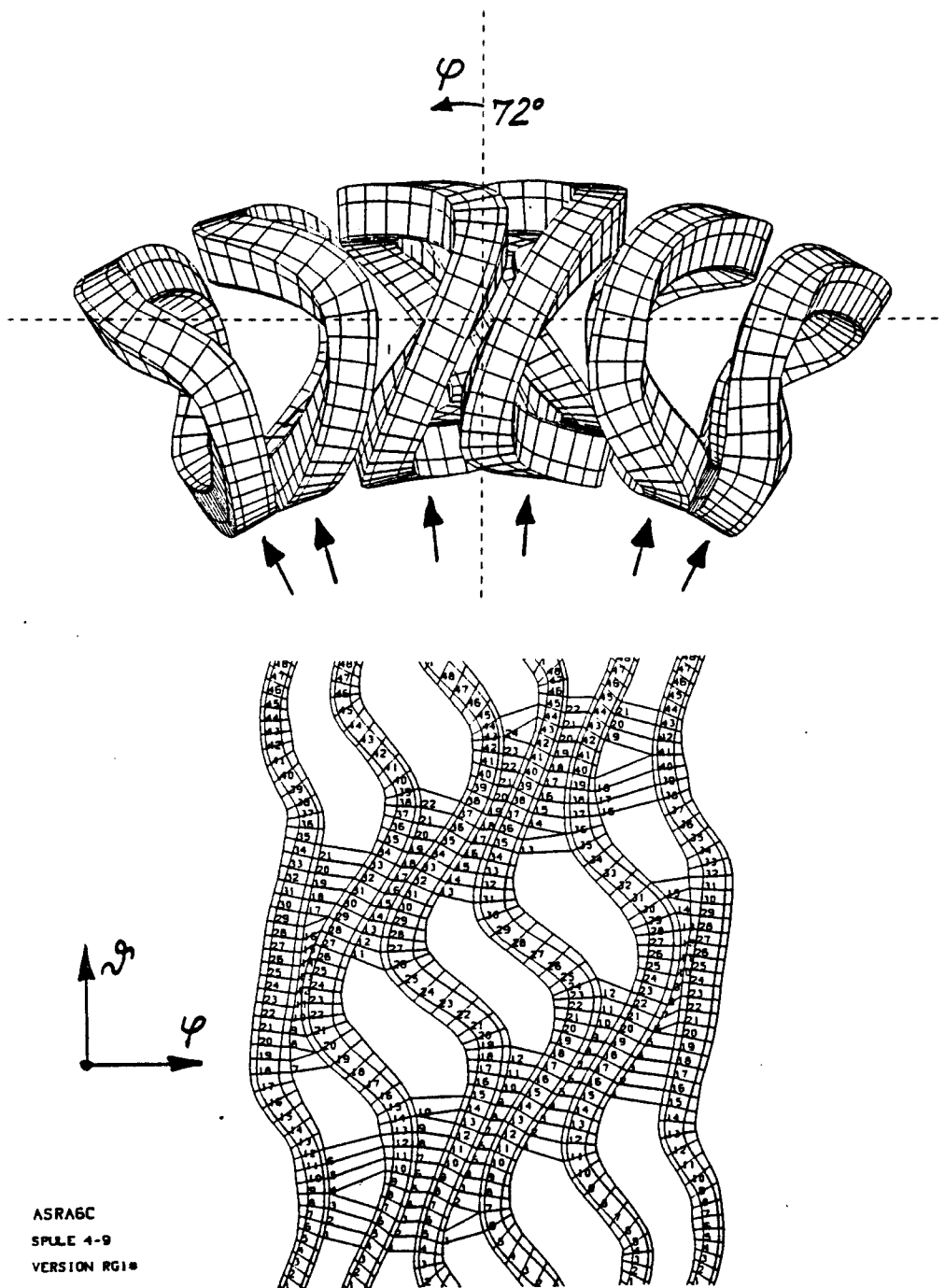
Fig. 7-13: ASRA6C: 6 coils and coil housings, with
dimensions increased at toroidal bending regions.
Mutual support of the coils shown in the lower part
unrolled in the $\varphi - \theta$-plane.

The computation of the load case A for the coils of ASRA6C is performed in order to compare with the stress and strain analysis for the coil arrangement of ASRA6B, as given in [5]. In this larger system, the maximum of the equivalent (von Mises) stress amounts to $180\,MPa$ at a tangential strain of 0.23%. A maximum of the shear stress of $60\,MPa$ is seen in this case. For ASRA6C, slightly lower values are calculated, see Table 7-IV, case A. The similarity of these results can be understood by a comparison of the 'virial stress', the stored magnetic energy normalized by the total coil volume, W_m/nV_c. Here $n = 30$ is the number of coils and $V_c = 2\pi r_c wtf$, where $f > 1$ is a measure of the non-planar coil shape. The quantities w and t are the lateral width and the radial height of the coils, respectively. Inserting the corresponding numbers for ASRA6B and ASRA6C, the virial stresses amount to 120 and 100 MPa; the precise numbers are entered in Table 7-I.

In case B with the relatively weak material data of the WENDELSTEIN VII-AS coils and the complete coil housing the stress and strain values inside the coils of ASRA6C are the lowest.

With the orthotropic material data of the Euratom-LCT coil one obtains in case C a maximum value of about 135 MPa for the von Mises stress, and a maximum tangential strain of about 0.2 % , as shown in Fig. 7-14 and Fig. 7-15, respectively. In these figures, the abscissae are the number of the GCE's, and the different curves apply for the 6 coils treated simultaneously. The equivalent stress contains considerable local maxima of shear stress of about 46 MPa, see Fig. 7-16, which might exceed the permissible stress. These local maxima of the shear stress occur mainly at the edges of the lateral support elements connecting adjacent coils. It is believed that these maxima can be reduced by a smooth shape of the edge of the mutual support elements.

The stress values of Table 7-IV include an enhancement factor in order to take into account local stress maxima and an overall filling factor. In cases A and B this enhancement factor amounts to 2.5, and in case C to 2.0. This is due to a filling factor of 0.8 for cases A and B, and of 1.0 for case C.
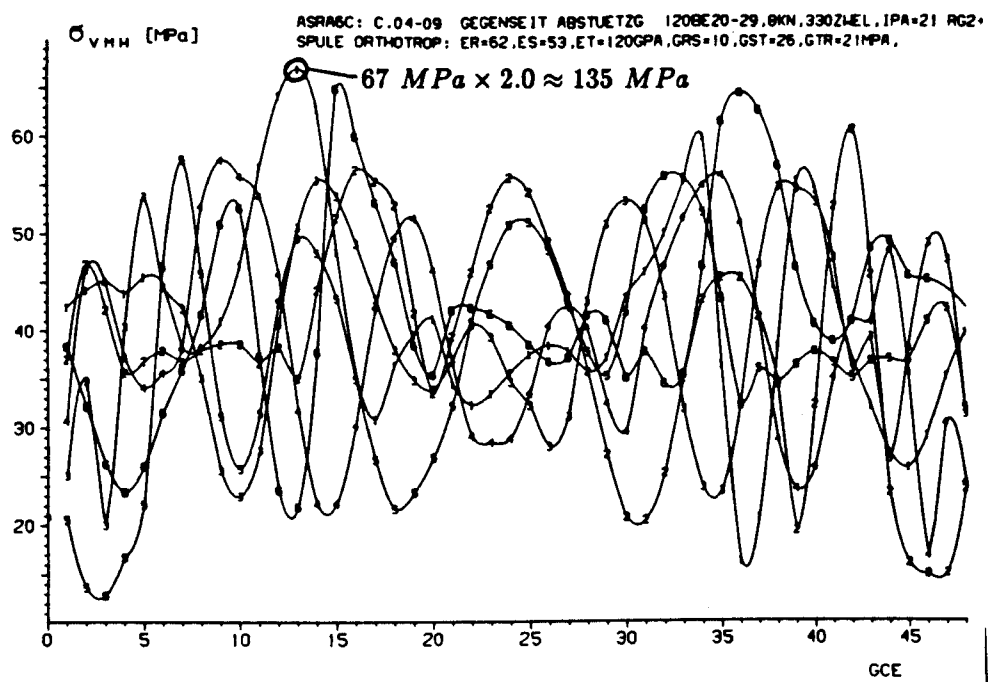
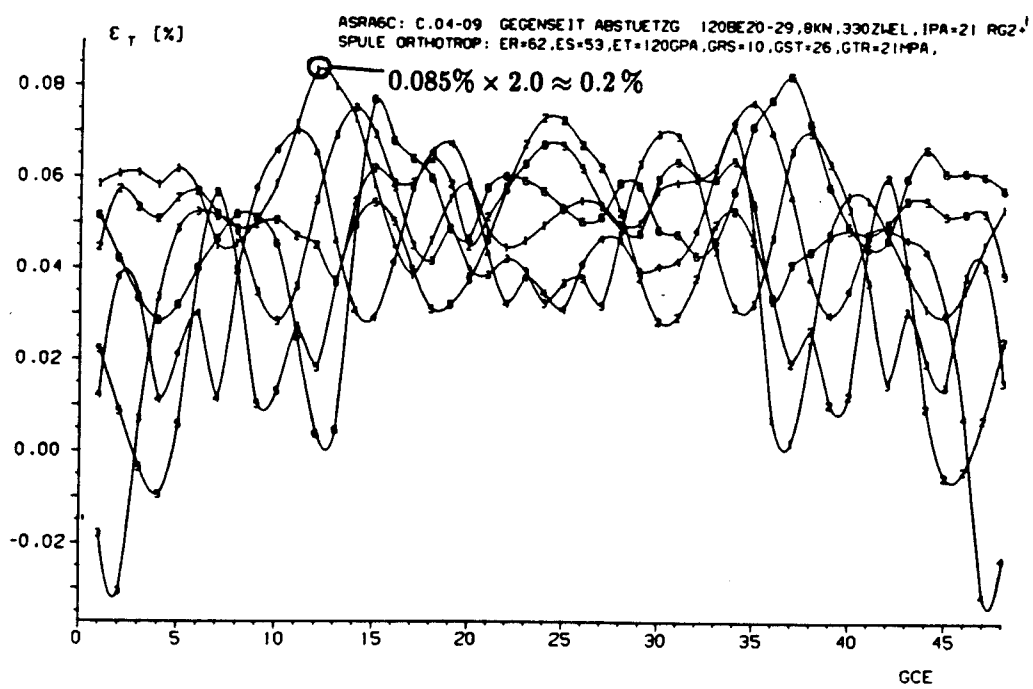Fig. 7-14: ASRA6C: equivalent stress σ_{vM}, orthotropic coil data.

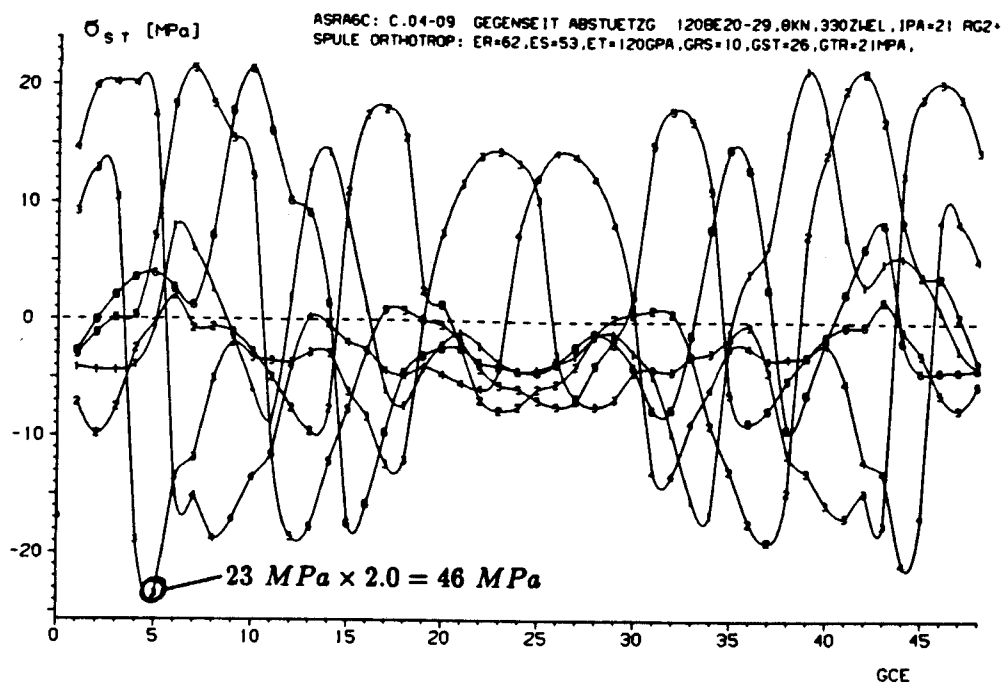Fig. 7-15: ASRA6C: tangential strain ϵ_T, orthotropic coil data.

Fig. 7-16: ASRA6C: shear stress σ_{ST}, orthotropic coil data.

7.5. Summary and Conclusions

The Advanced Stellarator Reactor configurations ASRA6B and ASRA6C with major radii of $R_o = 25$ and $20\,m$, minor coil radii of $r_c = 5.3$ and $4.6\,m$, are characterized by distances of $\Delta = 2.1\,m$ and $1.2\,m$ between the plasma edge and the coil bore. This considerable reduction in size is made possible by the use of a modern thin blanket approach.

For the same values of induction $B_o = 5.3\,T$ at the magnetic axis in both cases, the compact system ASRA6C shows a considerably reduced stored magnetic energy, $W_m = 117\,GJ$, as compared to $193\,GJ$ for the larger system.

Analyzing the distribution of the force densities, with local maxima of around $160\,MN/m^3$ in both cases, and applying the same support scheme and the same orthotropic material data as in the previously published case of ASRA6B, slightly lower values are obtained in ASRA6C, with a maximum of the equivalent (von Mises) stress of $\sigma_{vM} = 170\,MPa$, and a shear stress of $\sigma_{ST} = 50\,MPa$. The tangential strain amounts to 0.2 % for this case. With the orthotropic material data of the Euratom–LCT coil, and the coils surrounded with a full coil housing, laterally reinforced at locations of high curvature, one obtains similar values for the shear stress and the strain, the equivalent stress even decreases to a value of $\sigma_{vM} = 135\,MPa$. From the comparison of stresses we conclude that the coils seem to be feasible for both cases. The shear stresses require some attention in further iterations of the support system, where the mutual coil support elements are to be shaped appropriately.

In the next step, a more detailed analysis is required, which includes the internal stresses caused by the manufacturing of the coils, and those induced during cooldown. Furthermore, more detailed stress computations are necessary with special attention to the details of construction in the regions of maximum load or stress. Such local models would use the global results of the present calculations.

References to Chapter 7

[1]: U. Brossmann, W. Dommaschk, F. Herrnegger, G. Grieger,
J. Kisslinger, W. Lotz, J. Nührenberg, F. Rau, H. Renner,
H. Ringler, J. Sapper, A. Schlüter, H. Wobig,
Concept of an Advanced Stellarator,
Proc. Plasma Phys. and Contr. Nucl. Fusion Research Baltimore,
1982, Vol. III, 141, (1983).

[2]: B. Badger, L. A. El-Guebaly, G. A. Emmert, G. L. Kulcinski,
E. M. Larsen, J. F. Santarius M. E. Sawan, J. E. Scharer,
I. N. Sviatoslavsky, W. F. Vogelsang, P. L. Walstrom,
L. J. Wittenberg,
Annual Report on Contributions to ASRA6C,
a Commercial Stellarator Fusion Reactor,
FPA-85-4 , Madison WI (1985).

[3]: E. Harmeyer, J. Kisslinger, F. Rau, H. Wobig,
A General Winding Law of Modular Stellarator Coils,
IPP Garching Report IPP 2/274 , (1985).

[4]: E. Harmeyer, U. Brossmann, H. Gorenflo, J. Kisslinger,
S. Mukherjee, J. Raeder, F. Rau, H. Wobig,
On Modular Coil Systems of the Wendelstein VII–AS Type
with Reactor Dimensions, IPP Garching Report IPP 2/269 , (1983).

[5]: E. Harmeyer, J. Kisslinger, F. Rau, H. Wobig,
On Modular Coils of a Stellarator Reactor,
Proc. 11th Sympos. on Fusion Engineering,
Austin, TX (USA) , Vol. I, 245 (1985).

[6]: E. Harmeyer, J. Kisslinger, F. Rau, H. Wobig,
Mechanical Behavior of Medium Sized
Modular Stellarator Coil Configurations
Proc. 14th Sympos. on Fusion Technology,
Avignon, France, Vol. 2, 1631 (1986).

[7]: A. Maurer, A. Ulbricht, F. Wüchner,
Effect of Azimuthal Dependence of Radial Young's Modulus
on the Mechanical Behaviour of the European LCT Coil,
Proc. 9th Int. Conf. on Magnet Technology,
Zurich, Switzerland, Vol.1, 428 (1985).

8 Coil Considerations

8.1 General Magnet Considerations

The unique feature of modular stellarator coils is the compound bending, i.e. simultaneous bending in radial (poloidal) and axial (toroidal) direction. This constraint limits not only the thickness but also the width of a compact conductor due to the maximum allowable strain. The strain limitation leads to fairly small conductor cores for compact conductors compared with core sizes for planar coils which are only limited in the radial thickness of the conductor. The consequence of small conductor cores is a low conductor current and a high number of turns. Therefore the inductance of big coils will be very high and there may be problems at the charge and discharge of the coils.

A possible alternative to a compact conductor is the cable-in-conduit conductor, a type of conductor used in the Westinghouse Coil of the LCT project /1/. This type of conductor allows to some extent axial movements of the strands during the winding process. Therefore a strand experiences its "own" strain (ratio of strand diameter to strand bending diameter), if a strand can move freely. In the compacted conductor the movement is prevented to some extent. Thus, the conductor bending strain for cable-in-conduit conductors of the Westinghouse/Airco type is not just the strand diameter divided by the bend diameter, but rather some value between that value and that of the conduit thickness divided by the bend diameter. A conductor of this type is investigated for the Modular Stellarator Reactor ASRA6C. Fig. 7.2-1 shows the coil arrangement. Table 7.2-1 contains the main magnet parameter.

Due to the small distance between first wall and the coil winding pack special attention must be paid to the radiation limits of the materials used in the superconducting magnets. Degradation of physical properties due to radiation has to be taken into account in the design of the conductor itself and also in the design of the whole coil.Special attention has to be focused on the nuclear heating limit.

8.1.1 Strain Limitations

Due to the compound bending, not only the thickness but also the width of the conductor is limited. Fig. 8.1-1 shows this behaviour.
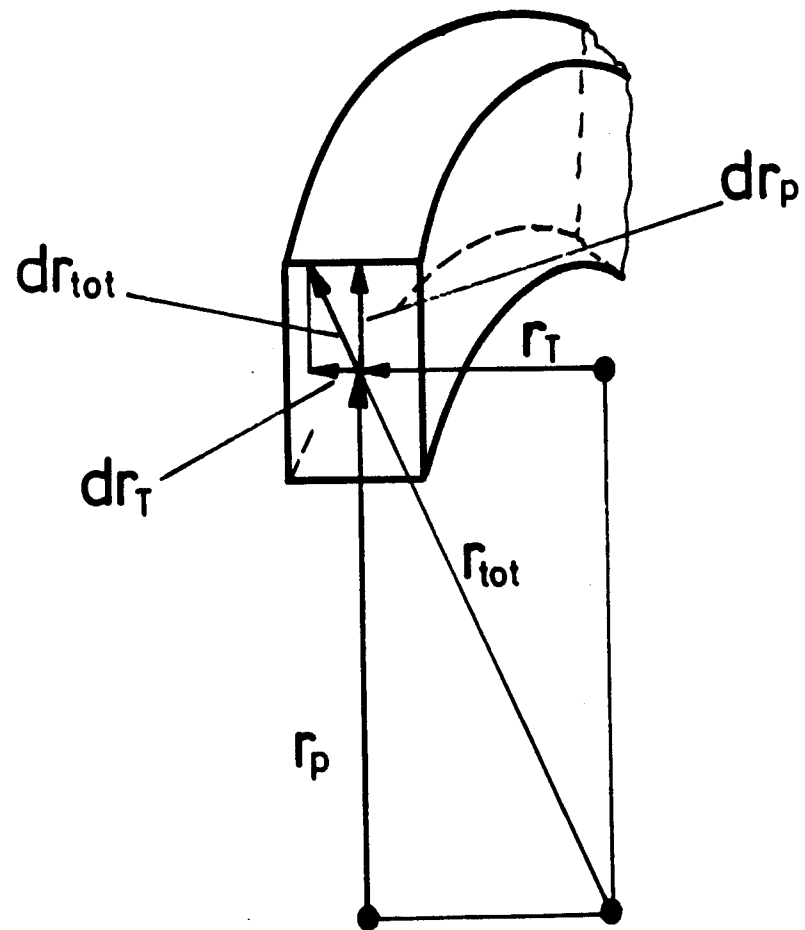
Fig. 8.1-1: Bending behaviour of a compound curve.

To attain the maximum allowable strain ε_{max} for the design the strain figures ε_p for the poloidal bending and ε_T for the toroidal bending have to be taken into account. The definitions of both figures are:

$$\varepsilon_p = dr_p / r_p \quad \text{and} \quad \varepsilon_T = dr_T / r_T$$

(1)

According to Fig. 8.1-1 the total strain is

$$\varepsilon_{tot} = \frac{dr_{tot}}{r_{tot}} = \left\{ \frac{\varepsilon_p^2 r_p^2 + \varepsilon_T^2 r_T^2}{r_p^2 + r_T^2} \right\}^{1/2} \leq \varepsilon_{max}$$

(2)

If $\varepsilon_p = \varepsilon_T = \varepsilon$, then $\varepsilon_{tot} = \varepsilon < \varepsilon_{max}$. In a first approximation the linear relation $\varepsilon_{tot} = \varepsilon_p + \varepsilon_t$ was used for the conductor design. But this strain limitation led to too small conductors, if only compact conductors were considered. For example, if the maximum strain is 0.2 %, then the core of the conductor, which contains the superconductor, would be only on the order of about 10 mm^2. Then the operational current would be only a few kA.

To overcome this strain limit a cable-in-conduit conductor similar to the Westinghouse/Airco concept is investigated. The development and fabrication of this conductor type is described in /1/. A cable-in-conduit conductor allows to some extent axial movements during winding. As a consequence, a strand experiences its "own" strain, i.e. the strain is given by the ratio of conductor diameter d_c to conductor bending diameter d_b. (Vacuumschmelze GmbH, Hanau, FRG, recommends $d_b \geq 150 \ d_c$ /2/.), if the strand can move freely. However, in the compacted conductor the movement is prevented to some extent. Thus the conductor bending strain for cable-in-conduit conductors of the Westinghouse/Airco type is not just the strand diameter divided by the bend diameter, but rather some value between that value and that of the conduit thickness divided by the bend diameter. The exact value is a function of cable compaction, surface conditions of the strands, etc.

8.1.2 Radiation Limits

8.1.2.1 Magnet Materials

The results of a literature study of the radiation effects of neutrons and gammas on the materials used in fusion magnets are given in two KfK reports /3, 4/. The values used for the reactor design are given in the neutronics section 6.2.

8.1.2.2 Nuclear Heat

In /5/ a formula is developed to establish an acceptable nuclear heating limit p_{max}:

$$p_{max} = \frac{T}{\lambda} \cdot f \cdot \frac{x \cdot P_{el}}{N \cdot V_c \cdot (CPC)} \tag{3}$$

for $T >> \lambda$, where:

p_{max} = peak value at the inside of the magnet winding pack,

T = radial thickness of the winding pack,

λ = decay length (an exponential decay of nuclear heat inside the magnet winding pack is assumed),

f = ratio of nuclear heat power to the total power required for removal of all magnet losses at 4 K, (f is not fixed, there must be an assumption)

P_{el} = total electric reactor power,

x = fraction of the total electrical reactor power allowed to remove the magnet losses,

CPC = (cryogenic power coefficient) = ratio of electrical power at 300 K to cooling power at 4 K,

N = number of magnets,

V_c = coil volume.

The average heating limit is related to the maximum by:

$$P_{av} = \lambda / T \cdot p_{max} .$$

Formula (3) assumes nuclear heating to represent a fixed fraction of total losses. As shield thickness changes nuclear heating changes, but other losses remain the same. Therefore

$$p_{max} = \frac{T}{\lambda} \left[\frac{xP_{el}}{NV_c(CPC)} - P_{loss} \right]$$

is more appropriate, where P_{loss} is power loss at 4 K excluding nuclear heating.

For ASRA6C which has about 3800 MW fusion power and about 1700 MW electric power we allow e.g. 1 per cent ($x = 0.01$) of the electric power to be used to remove all magnet losses at 4 K. At a CPC of 500 then the cooling power at 4 K is 24 kW. The number of the coils is 30 and the volume of

one coil is 41 m³. If we assume that the nuclear heat losses are about 50 % (f = 0.5) of the total magnet losses, then we get from Formula (3)::

$$p_{max} = T/ \lambda \cdot 9.756 \cdot 10^{-3} \text{ mW/cm}^3$$

The average nuclear heat power density is therefore about 0.01 mW/cm³. The peak power density with T = 1.2 m and λ = 0.09 m according to /6/ is:

$$p_{max} = 0.13 \text{ mW/cm}^3.$$

This is the nuclear heating limit used for the magnet shield design. Neutronics calculations in section 6.3 indicated that the total nuclear heating in the 30 coils is 24 kW with a peak power density P_{max} = 0.13 mW/cm³ at the magnet winding. The difference is due to the fact that the analytical model here assumes perfect exponential variation and calculates heat only in winding pack. Heating in the case is more than that in the winding pack.

8.1.3 General Features of the ASRA6C Magnets

The overall current density of 15 MA/m² is moderate compared with the current densities in the LCT-coils which are up to 33 MA/m² in the Swiss coil /7/*.

The total coil current is

$$N \cdot I_0 = 18 \text{ MA} \tag{1}$$

where N is the turn number and I_0 the rated current. I_0 will be determined during the conductor design procedure and Eq. (1) gives then the turn number. The (one turn) coil inductance of 15.13x 10⁻⁶ H together with the total coil current of 18 MA gives a stored energy of 2.45 GJ per coil.

The mechanical behaviour of the coils is discussed in chapter, 7.

The maximum field of 10.4 T for the coils is near the limit where ternary NbTi and Helium II cooling are usually considered. Nevertheless, the first choice is a binary Nb₃Sn conductor due to the higher stability margin and lower refrigeration power.

*)LCT (Large Coil Task) is an international magnet test. Six D-shaped coils are tested together at the Oak Ridge National Laboratory in Oak Ridge, Tennessee, USA.

In this case the current density is strongly strain dependent (see e.g. /8/). If a maximum allowable strain for Nb$_3$Sn is set to be in the range of 0.2 % to 0.3 %, the small bending radius in the toroidal direction (r_t = 0.77 m) requires small conductor cores, if a monolithic conductor is to be used. This would allow only low operational currents, typically 5 kA maximum, leading to high inductances of the coils and safety problems, as discussed earlier. Therefore the probability of building modular stellarator reactor coils with monolithic Nb$_3$Sn conductors is low.

For ASRA6C a cable-in-conduit conductor is proposed. The results of the test of the Westinghouse coil in the spring of 1986 in Oak Ridge /9/ show that such a conductor can be used taking into account a sufficient margin for degradation. .

References to Section 8.1

/1/   P. A. Sanger, E. Adam, E. Gregory, W. Marancik, E. Mayer, G. Rothschild, and M. Young, "Developments in Nb$_3$Sn Forced Flow Conductors for Large Magnets", IEEE Trans. on Magnetics, Vol. MAG-15, No. 1, Jan. 1979, p. 789.

/2/   VACUUMSCHMELZE GmbH, Hanau, FRG, sales brochure SL 021, Edition 03/81.

/3/   W. Maurer, "Neutron Irradiaton Effects on Superconducting and Stabilizing Materials for Fusion Magnets", KfK 3733, 1984.

/4/   W. Maurer," Neutron and Gamma Irradiation Effects on Organic Insulating Materials for Fusion Magnets", KfK 3974, 1985.

/5/   W. Maurer, "Limitations in the Conductor Design for Modular Stellarator Coils", 11th Symp. on Fus. Eng., Austin, Texas, Nov. 18-22, 1985.

/6/   R. Flükiger et al., "An A15 Conductor Design and its Implications for the NET-II TF Coils", KfK 3937, 1985.

/7/   I. Horvath et al., "Manufacturing of the Swiss coil", 10th Symp. on Fus. Eng., Philadelphia PA, Dec. 5-9, 1983.

/8/   R. Flükiger et al., "Superconductivity for Fusion: The Materials Development and Testing", Nucl. Eng. and Design, 73 (1982) 153.

/9/   ORNL test team, private communication.

8.2 Conductor Design for ASRA6C Magnets

As basic strand a commercially available Nb_3Sn multifilamentary conductor is chosen. According to /1/ we choose the strand NS 1000 Ta-I with stabilizing copper. (Description: Matrix CuSn with approximately 10,000 Nb-filaments and a central copper-core with a tantalum diffusion barrier, proportion of the area approx. 17 $\pm$ 3 %. The diameter is 0.8 mm and the critical currents at 4 K are 154 A at 12 T, 192 A at 11 T, 243 A at 10 T, 365 A at 8 T, and 664 A at 5 T.)

The cable-in-conduit conductor could be fabricated in the same manner as the Westinghouse conductor /2/.

The first step is the cabling of 3 strands to a triplet (A-cable) . The second step is the cabling of 3 A-cables to a 3^2-cable (B-cable). The third step is the cabling of B-cables to a 3^3-cable (C-cable). The fourth step is the cabling of 3 C-cables to a 3^4-cable (D-cable). The D-cable contains now 81 basic strands. The fifth step is the cabling of 6 D-cables around a central Cu-subcable with resulting 486 basic strands. The sixth step of the fabrication process is the continuous wrapping and welding of a stainless steel sheet of 0.9 mm thickness around the cable. The final step is the compaction to the final dimensions.

After the compaction the cable can be reacted, insulated and wound to the winding package. In this case the insulation is outside of the steel jacket and consists of organic materials. The conductor pack is then inserted in the case, which has to support the magnetic forces. Calculations of the thickness of the casing are reported in the preceeding chapter. The thickness inside of the winding package is 10 cm, on the outside 60 cm, and also 30 cm on both sides of the coil.

The relatively high thicknesses of the casing led to the consideration of an alternative. That would be an inside electrical insulation. In this case the insulation must be out of ceramic material, because it has to withstand the reaction treatment at 700 - 800 °C. As shown in Fig. 8.2-1, a protection sheet of about 0.2 mm is wrapped around after the final cabling step and the following step is now the insulation step, where insulation material (about 1 mm thick) is wrapped around the protection case. The final step is the continuous wrapping and welding of a stainless steel sheet of about 1 mm thickness. Compaction and squaring gives the final shape of the conductor shown in Fig. 8.2-1.

An advantage of this conductor would be the assembly process of the winding pack by laser beam welding as shown in Fig. 8.2-1. Stainless stripes and the welded structure would give an additional support. There are, however, some open questions:

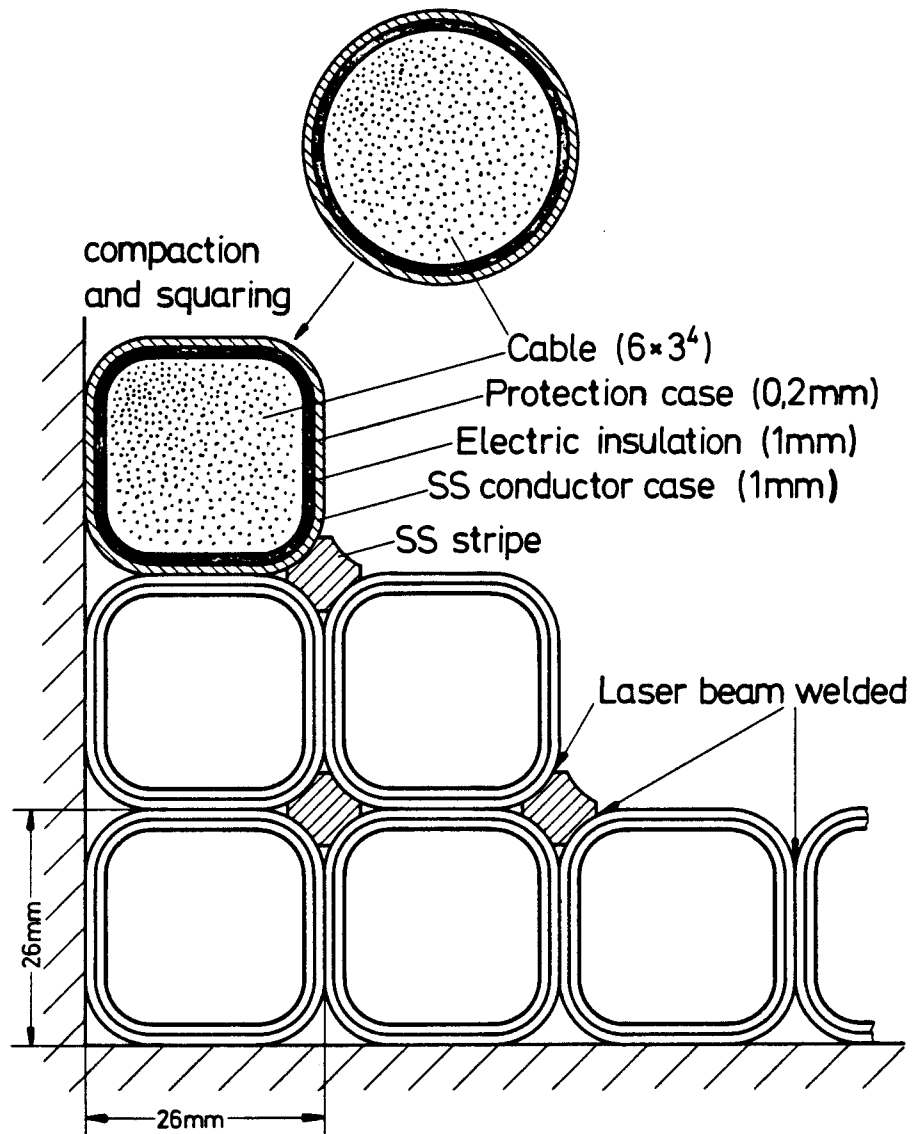# CONDUCTOR AND WINDING SCHEME

Fig. 8.2-1: Cable-in-conduit conductor and proposed coil assembly.

- Are stress concentrations at the welds not too high?
- Is the insulation scheme and welding procedure compatible?
- What influence on the insulation has the bending of the conduit during the winding?
- Is a sliding insulation possible?
- Is a low compaction fraction sufficient?
- Can the inside insulation be made reliable enough to withstand the full dump voltage? The full dump voltage appears everywhere along the conductor across the ceramic insulation.

These question can only be clarified by experimental work.

The calculation with the basic strand diameter of 0.8 mm gives for the cable an area of 475 mm^2 (244.3 mm^2 for the 486 strands, 40,7 mm^2 for the Cu-subcable, and 190 mm^2 for void). This corresponds to a radius of 12.3 mm, if the cable is a circle. Adding 0.2 mm for the protection sheet, 1 mm insulation thickness, and 1 mm conductor case gives a radius of 14.5 mm or an area of about 660 mm^2. After squaring the conductor with rounded corners (5 mm minimum radius of the corner) and after compacting by 4.4 %, the final dimensions of the conductor are 26 mm x 26 mm. The strain of the conductor case for the minimum bending radius of 770 mm is 1.7 %. This is tolerable for stainless steel.

The theoretical critical current of this conductor is 486 x 192 A (at 11 T) = 93.312 kA. The definition of the operational current is governed by other considerations as e.g. turn number and winding cross section or simply costs. Calculations for 10 kA to 40 kA are made. The choice of 18 kA is a compromise between turn number and winding pack cross section and maximum field at the conductor.

The choice of 18 kA offers the possibility to save basic strand material. If we replace in the first cabling step one of the basic strands by a Cu-strand of 0.8 mm, then the theoretical current is 62.2 kA, which is a factor of 3.4 higher than the rated current. Another possibility is to lower the coil cross section, but this leads to higher fields at the conductor.

The Westinghouse coil with the conductor type discussed above became superconducting in February, 1986 and has been tested as a single coil [3]. The tests covered charging to the design current of 17.76 kA and current-sharing tests using the resistive heater. The full design current was achieved in May, 1986. The peak field in this single coil test was 6.2 T at conductor.The current-sharing threshold temperature was measured to determine the strain degradation of the Nb$_3$Sn/Cu conductor after reaction as a result of handling the coil. The results of these measurements show serious degradation in the conductor, but the ratio of I/I_{cb} = 0.3 at 8 T (I = nominal current, I_{cb} = critical current at 4.2 K and in the field B based on short samples tests)

chosen from Westinghouse guaranteed a safe operation in the single coil test. The exact cause of the degradation is not known. It occurs only at particular points in the coil and is not associated with points of smallest winding radius. There is good reason to believe that the degradation could be eliminated with improvements in process control.

The latest information from the ORNL test team on the full six-coil array test is of a successful operation including a dump from full current.

The cooling behaviour for the ASRA6C-conductor is similar to the Westinghouse conductor. The experimental results /4/ show that the pressure drop can be described by a friction factor $f = 64/Re$, where Re is the Reynolds number. The small hydraulic diameter of the spaces between strands leads to high quench pressures and thereby leads to a requirement for short cooling paths. It has to be clarified which cooling length can be tolerated.

References to Section 8.2

/1/   VACUUMSCHMELZE GmbH, Hanau, FRG, sales brochure SL 021, Edition 03/81.

/2/   P. A. Sanger, E. Adam, E. Gregory, W. Marancik, E. Mayer, G. Rothschild, and M. Young, Developments in Nb_3Sn Forced Flow Conductors for Large Magnets, IEEE Trans. on Magnetics, Vol. MAG-15, No. 1, Jan. 1979, p. 789.

/3/   L. Dresner et al., First Tests of the Westinghouse Coil in the International Fusion Superconducting Magnet Test Facility (IFSMTF), Applied Superconductivity Conference, Baltimore, USA, Sept. 28 - Oct. 3, 1986.

/4/   G. Zahn, private communication.

8.3 Summary and Conclusions

The study of the nonplanar coils for a modular stellarator reactor show that the main limitation for the coils is given by the compound bending, which limits the dimension of the conductors. Therefore, the likelihood of building the coils with monolithic Nb_3Sn conductors is low. A cable-in-conduit conductor seems to be a viable solution for nonplanar coils. A conductor design similar to the Westinghouse design is discussed in detail.

9. General Layout and Maintenance

9.1 INTRODUCTION

The configuration ASR 25 T7 was the first to be investigated. The reference case ASRA6C (see Fig. 9.1-1) was the result of an iteration process.
An overview and the description of all configurations are given in Ref. [1].

9.2 OVERALL ARRANGEMENT

All configurations have five field periods, but the total coil number varies from 20 to 50. The major radius is lowest in the reference case ASRA6C. The minor radius is very similar in all cases, as is the average coil radius with the exception of ASRA6C. The magnetic field on axis is 5,3 T with resulting maximum fields of about 11 T on the coil winding.

The resulting reference case ASRA6C was a compromise between plasma physics requirements and requirements of accessibility and maintenance of the super-conducting coils and their cryostats. The layout philosophy was to find a simple geometrical shape for the reaction chamber components. Another goal was to have only one separation area per field period, because each separation area requires demountable cold intermagnetic supports as described in section 9.4.

Fig. 9.2-1 shows a cross section in the polodial plane of ASRA6C at the toroidal angle $\varphi = 0°$, i.e. the beginning of a field period. This cross section shows the blanket option IV as described in section 5.1.2. The other options are similar with respect to the aspects investigated here. The contour of the first wall in option IV follows the contour of the plasma; the plasma cross section changes over a field period from an "egg-like" shape to a nearly elliptic shape and back to an "egg-like" shape at the end of the field period.
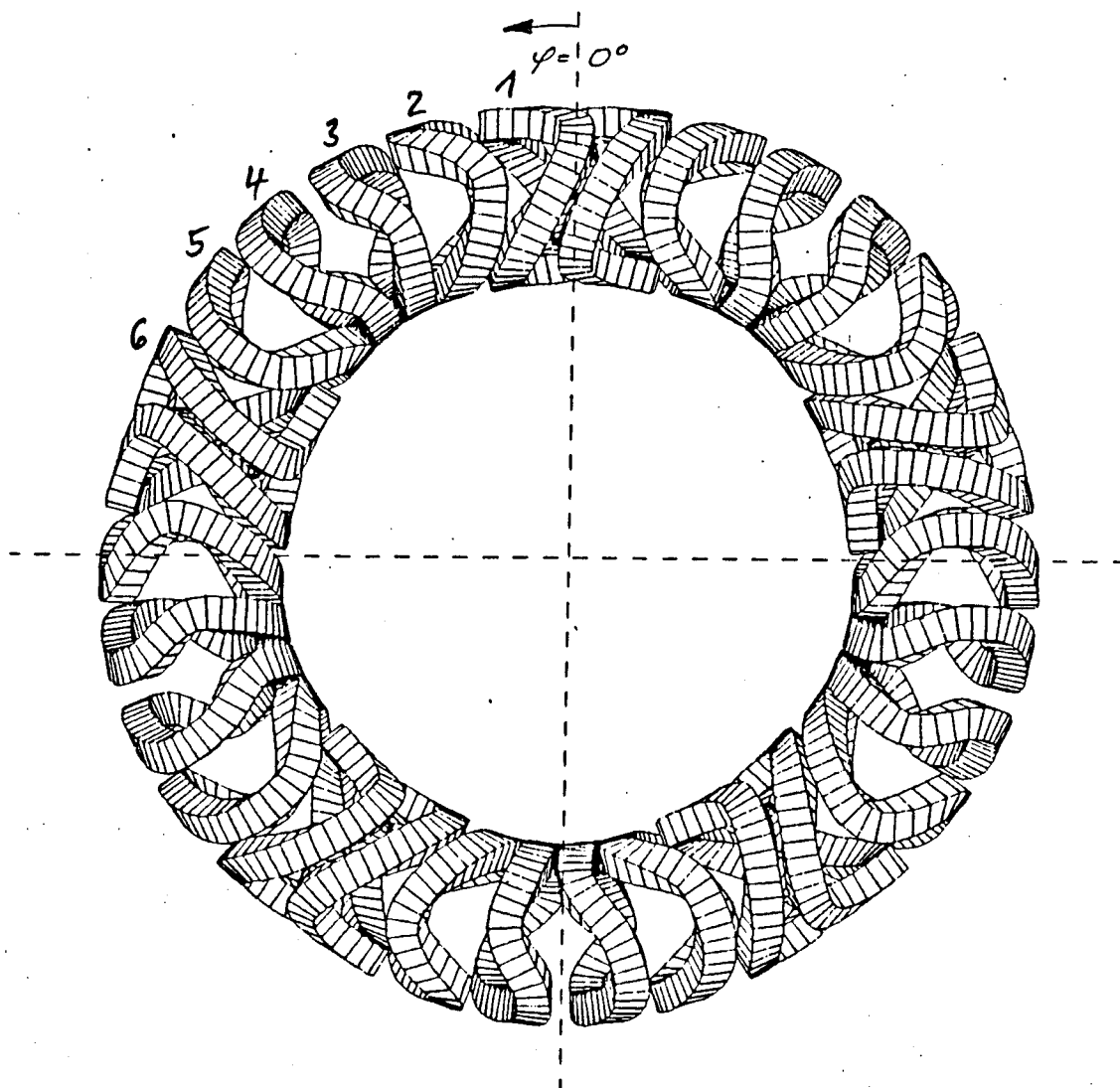
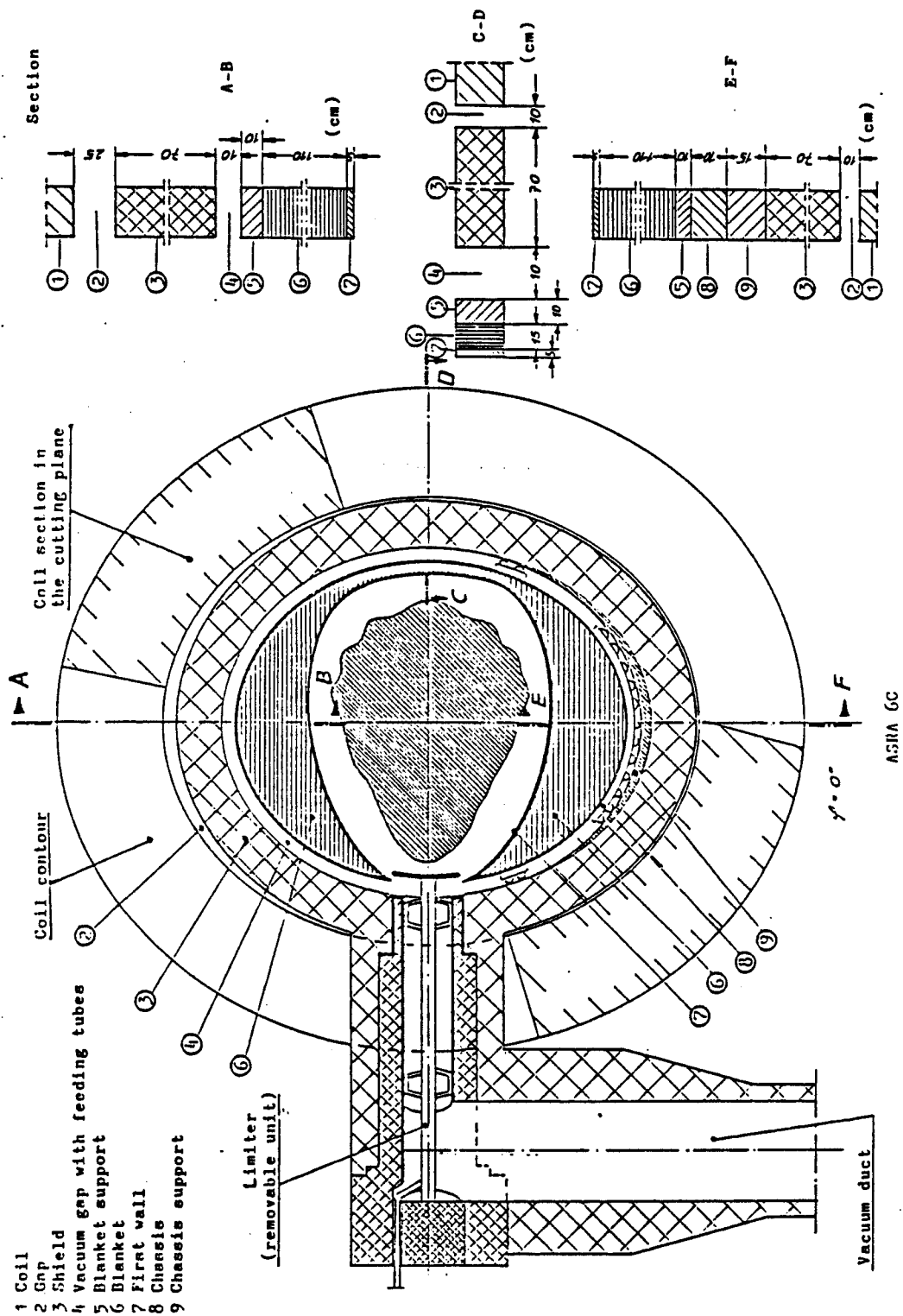Fig. 9.1-1   Configuration ASRA 6C (only winding packs)

Fig. 9.2-1   General layout of the modular stellarator reactor ASRA 6C with Option IV

1 Coil
2 Gap
3 Shield
4 Vacuum gap with feeding tubes
5 Blanket support
6 Blanket
7 First wall
8 Chassis
9 Chassis support

Blanket options I to IV are described in detail in chapter 5. In this chapter option IV is further investigated, because this option can have advantages over the other ones with respect to space for installation of coolant pipes.

For blanket option IV the minimum distance from the first wall to the plasma is about 20 cm. The first wall is integrated into the blanket, and the blanket follows the contour of the plasma, changing its volume and contour. The blanket does not therefore have a constant thickness. The contour of the inner vacuum vessel is nearly elliptical and remains unchanged along the reactor circumference. The shield can be outside of the inner vacuum vessel, with only part of it located inside the separation areas. The minimum shield thickness is 70 cm. The limiter unit is removable, permitting frequent replacement. Additional shielding material is used near the pumping port. The blanket unit is also removable by means of a chassis resting on a chassis support.

Due to the large space requirement by the coolant pipes only a few connections are foreseen for the RBUs (Removable Blanket Units). The big advantage of the blanket option IV is that the supply pipes can be integrated into the blanket which has variable thickness. The best place is the backside of the blanket where breeding is very low.

With such an arrangement of the pipes, the RBUs can be extented to a length of half a field period without difficulty. Consequently, only 10 RBUs are needed for the whole reactor.

If the configuration is subdivided into 5 segments (1 segment = 1 field period) with 2 RBUs in each, the following advantages are obvious:

- Only five separation areas are needed in the reactor hall.

- The number of the cold demountable intermagnetic supports is low, because they are only needed at the separation areas.

- There are only 10 RBUs in the reactor.

- There are only two kinds of RBUs.

A further subdivision of a field period into two halves would be space consuming. Therefore less space would be available for auxiliary equipment.

Fig. 9.2-2 shows a cut in the equatorial plane of ASRA6C at a field period where two (of four) neutral beam injectors are located. One field period (0° to 72°) can be removed as a unit. Both separation areas at 0° and 72° are not planar. The positions of several limiters are given.

The coolant pipes are brought in from the inboard side in order to keep the outboard side clear for maintenance purposes.
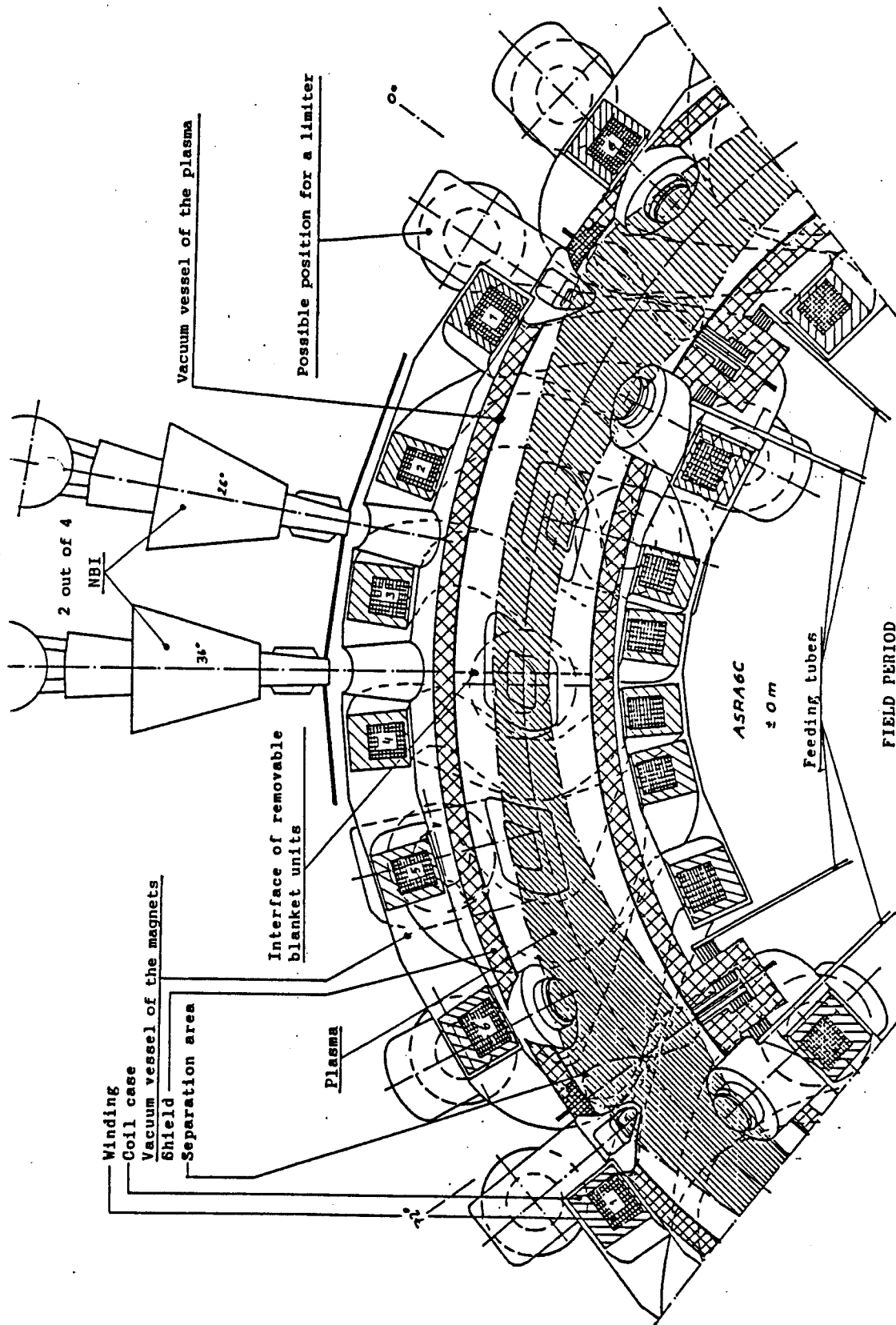
Fig. 9.2-2   Arrangement of one field period

9.3 MAINTENANCE SCHEME

Several possibilities for the maintenance procedure were investigated during the study phase. The main boundary conditions for these possibilities were:

All segments (segment = field period) are removed and the RBUs replaced by new ones during shutdown

or

only one segment is removed and the RBUs are replaced by new ones during shutdown

Fig. 9.3-1 shows the maintenance scheme selected for ASRA6C. The philosophy of this maintenance scheme is the exchange of all removable blanket units (RBUs) in all the field periods during shutdown. One field period segment after another will be removed sequentially from the main ring by the transport vehicle.

This transport vehicle (1) which is located inside the coil circle and moves on tracks and provides the transportation as well as the cooling needed during transport of the segment exchange. The segment is moved out to position (2), where the exchange of the RBUs takes place. The reactor hall has two doors (openings), one for driving out the segment (3), the other for driving in (4).

During blanket replacement the transport vehicle positions itself behind the segment to be exchanged and the cooling pipes to the segment are connected such that cooling is provided by the transport vehicle. The segment is then be separated from the main circle and brought through opening (3) of the reactor hall to positon (2), where the exchange of the RBUs will take place. At that time two stationary manipulators, on each side of the segment swing around to the segment (5), and remove the contaminated RBUs on both sides. The manipulators then swing the RBUs to the storage area for the contaminated RBUs (6) and deposit them there. After this they swing to the storage area for new RBUs (7) and pick up two new ones. They then swing back to the position of the segment (5) and install the RBUs in the segment.

Storage for new RBUs

Storage for
contaminated RBUs

Handling area of
contaminated RBUs

Storage for
new RBUs

Movable adapter

Test

Stationary manipulator
for exanging RBUs

Transport vehicle
for FP segments
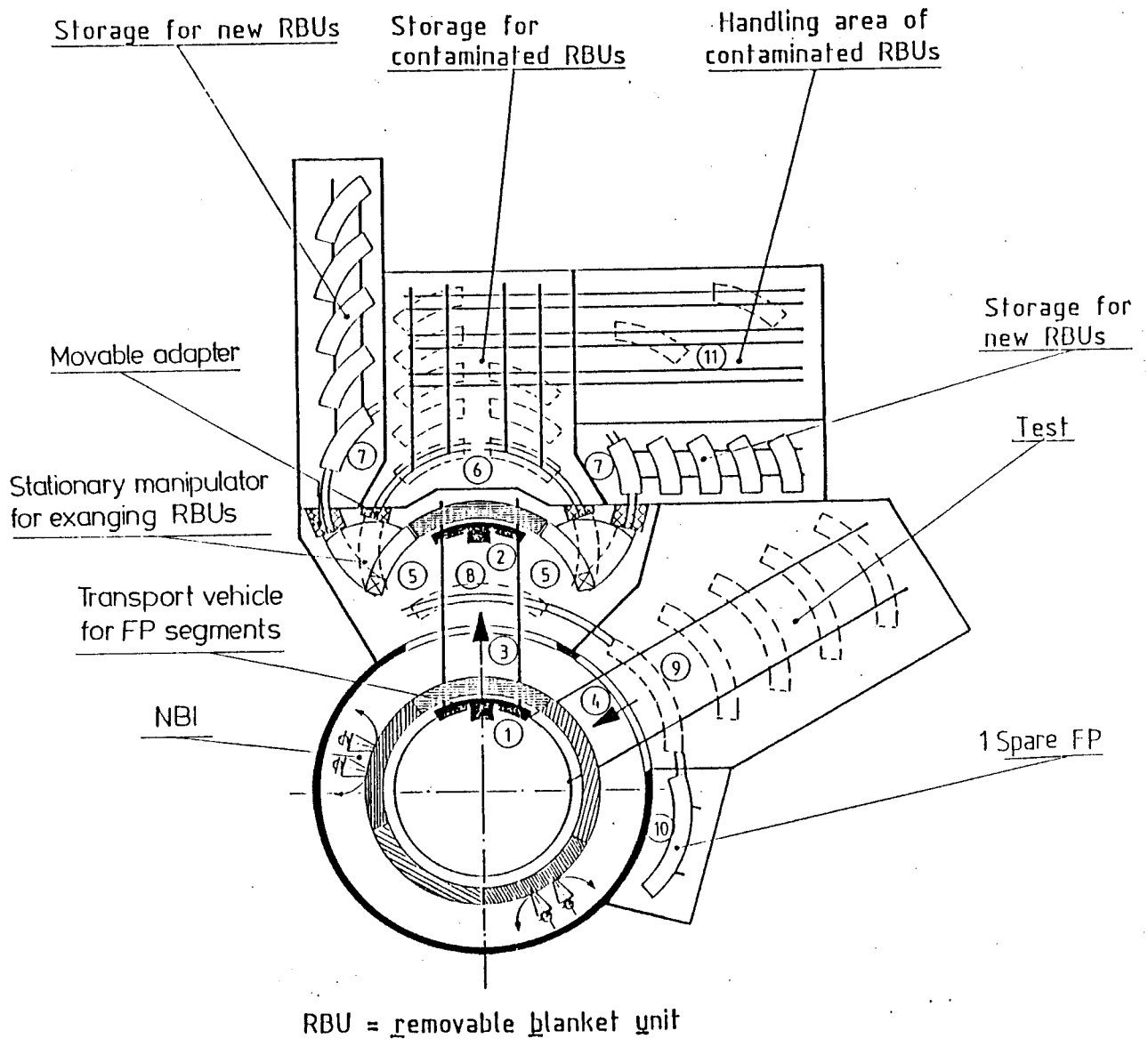
NBI

1 Spare FP

RBU = removable blanket unit

Fig. 9.3-1 Maintenance scheme for ASRA 6C

In the meantime the transport vehicle is separated from the first segment and is driven to the next segment. The cooling of the first segment is taken over by a stationary refrigerator.

The segment with the new RBUs is then brought to position (8) and then to the test laboratory (9). This laboratory is designed for the simultaneous testing of all 5 segments. After the test is completed the segments are brought to their original position in the reactor hall through opening (4) by means of the transport vehicle. During the whole exchange process all the magnets are maintained cold.

A spare segment (10) is made available in case, any of the segments fail during the test.

As shown in Fig. 9.3-1, the reactor hall is designed to fulfill the following tasks and conditions:

- Provide a rotunda with coil arragement and auxiliary equipment

- Have an extension, where RBU exchanges takes place

- Have an excange hall with manipulator devices

- Provide two storage halls for at least 5 new RBUs each

- One storage hall for the contaminated RBUs

- A hall for reprocessing the contaminated RBUs

- A test laboratory, and

- A hall for a spare segment.

In addition several small workshops are needed for preparation and/or rapair work.

9.4 COLD DEMOUNTABLE INTERCOIL SUPPORT

A segment consists of one field period of six coils. Each field period segment will be removed from the main ring in order to exchange the blankets. During this operation the coils must be kept cold. This requirement dictates a special support structure at the interface between segments. The special property of this intermagnetic support structure is (1) to transmit the magnetic forces at a low temperature and (2) to provide an element which can be demounted while the magnets stay cold. This intermagnetic support system can be used for all kinds of superconducting magnet arrangements because no parallel mounting position of magnets is required i.e. the magnets can be prone to each other. Therefore, the demountable cold intermagnetic support described here can be applied for tokamaks, mirrors, modular stellarators as well as magnet systems for special purposes, whenever demountable mechanical support are required.

In the example described, the support is designed for a pressure force of 5 MN (500 t). A minimum distance between the magnets of 0.7 m is required.

9.4.1 DESCRIPTION OF THE INTERMAGNETIC SUPPORT

Certain areas of the magnets must be especially designed in order to enable the transmission of the pressure forces. Figs. 9.4-1 and 9.4-2 show the devices needed for that purpose. The nomenclature of these figures and the following ones are given in Fig. 9.4-1. (1) denotes the outer contour of the coil case, which is considered to be the inner coil support. The coil case is covered with superinsulation (2).

A LN_2 shield is considered as an alternative. A slightly bevelled pressure plate (3) is welded to the coil case at the place where the force is to be transferred. The magnet case is surrounded by the coil vacuum vessel (4) at a distance of about 200 mm. The wall thickness of the vacuum vessel is increased and forms a flange (5) at the intermagnetic support location. An outer pressure plate (7) is connected to this flange by a bellows (6). This plate extends about 5 mm beyond the outer edge of the flange. The cold shield (26) intercepts the heat leak from room temperature to the cold pressure plate (3).
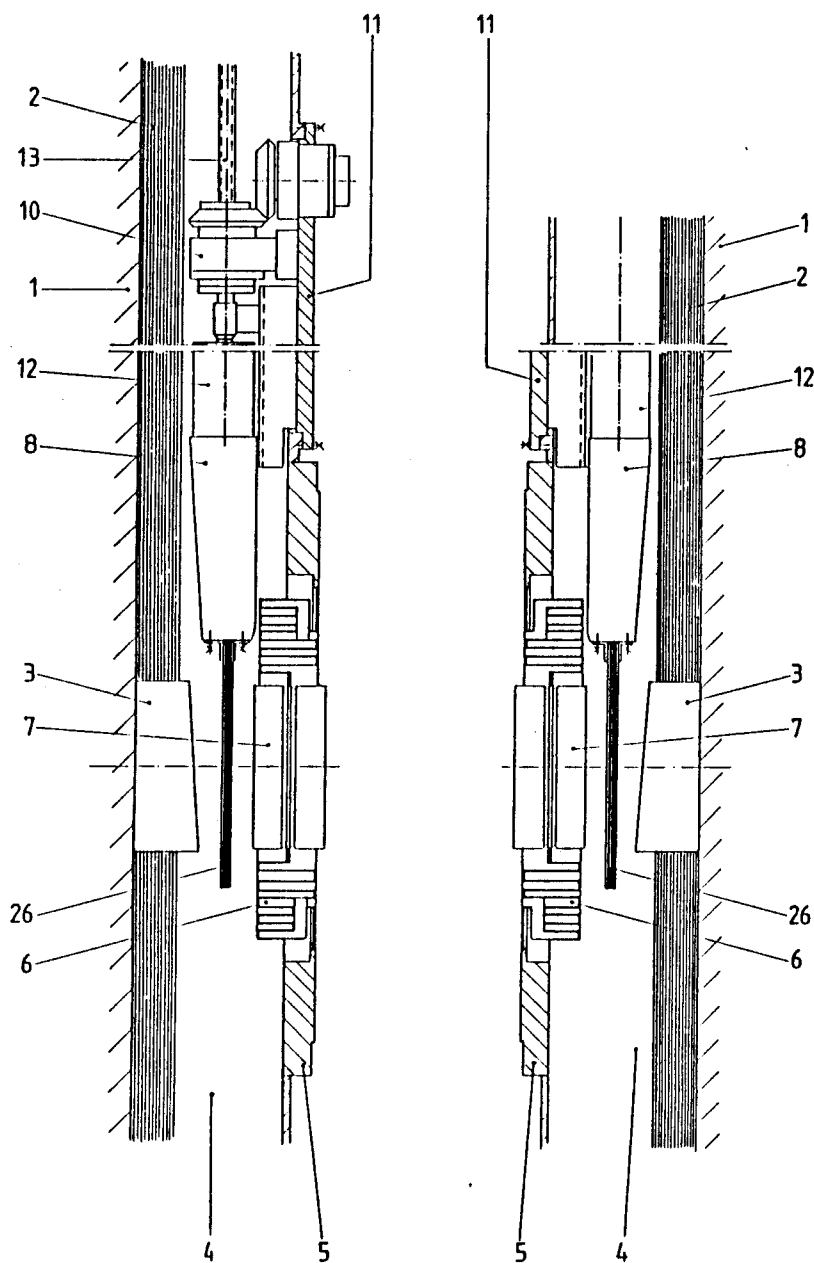
1 Outer contour of coil case	14 Case of the intermediate element
2 Superinsulation	15 Slide bearing
3 Inner pressure plate	16 Movable flange
4 Vacuum Vessel of the coil	17 Bellows
5 Flange	18 Adjustement screw
6 Radial bellows	19 Locating pin
7 Outer pressure plate	20 Central part of the element
8 Wedge	21 Guiding wedge
9 Mount	22 Collar
10 Rack and pinion drive	23 Superinsulation
11 Cover	24 Cap
12 Gilled tube	25 Vacuum connection
13 Threaded spindle	26 Cold shield

Fig. 9.4-1 Starting position for the installation of the
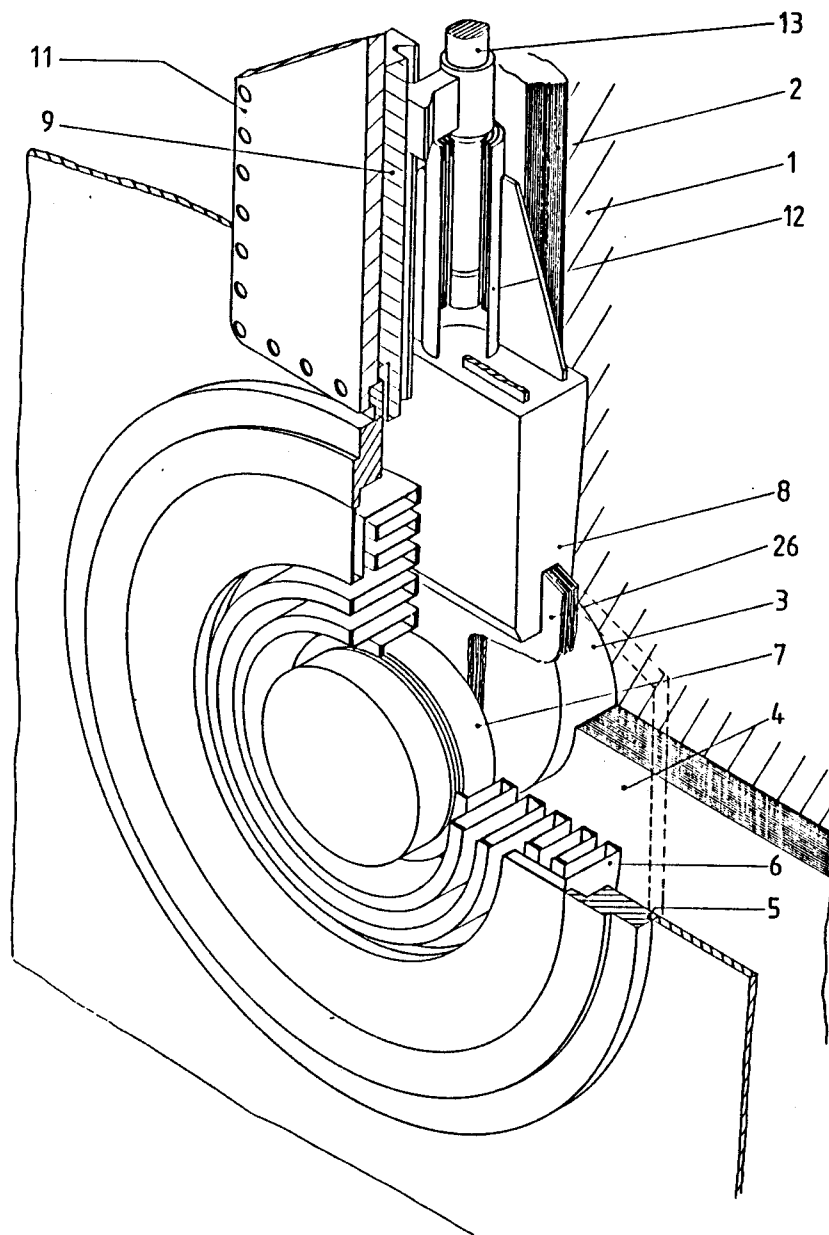intermagnetic support

Fig. 9.4-2 Starting position, perspective view

A wedge (8) together with the mount (9) and drive (10) can be inserted into the vacuum vessel through an opening on the top of the flange. The mount and drive for the wedge are fixed to the cover (11) of this opening. The wedge is connected to the spindle (13) of the drive by a bellows (12). The drive itself can be located on the top or on the side as shown in Fig. 9.4-2. In the latter case the drive must be connected to a bevel gear.

Fig. 9.4-3 shows an alternative design, where the bellows consists of glass fibre reinforced epoxy. The losses in such a system are only 1.5 W compared with 6.5 W for a stainless steel bellows due to the much lower heat conductivity of glass fibre reinforced epoxy. Experience with such bellows is given in Ref. /2/.

Fig. 9.4-4 shows the intermediate part of the support between the magnets. The case (14) of the insert is formed as a flange on one side and as a guiding surface for sliding parts on the other. The flange (16) can be moved into a sliding bearing (15) by means of two adjustment screws (18). A bellows (17) seals the space between the case (14) and the movable flange. Three locating pins at 120 ° intervals align the central part of the insert (20). It has a guide wedge (21) at the bottom on each side and a collar (22) on the top and is wrapped in superinsulation (23) of 50 - 70 mm thickness. Vacuum tight caps (24) cover the locating pins (19) during operation. In addition the case (14) has a vacuum connection (25).
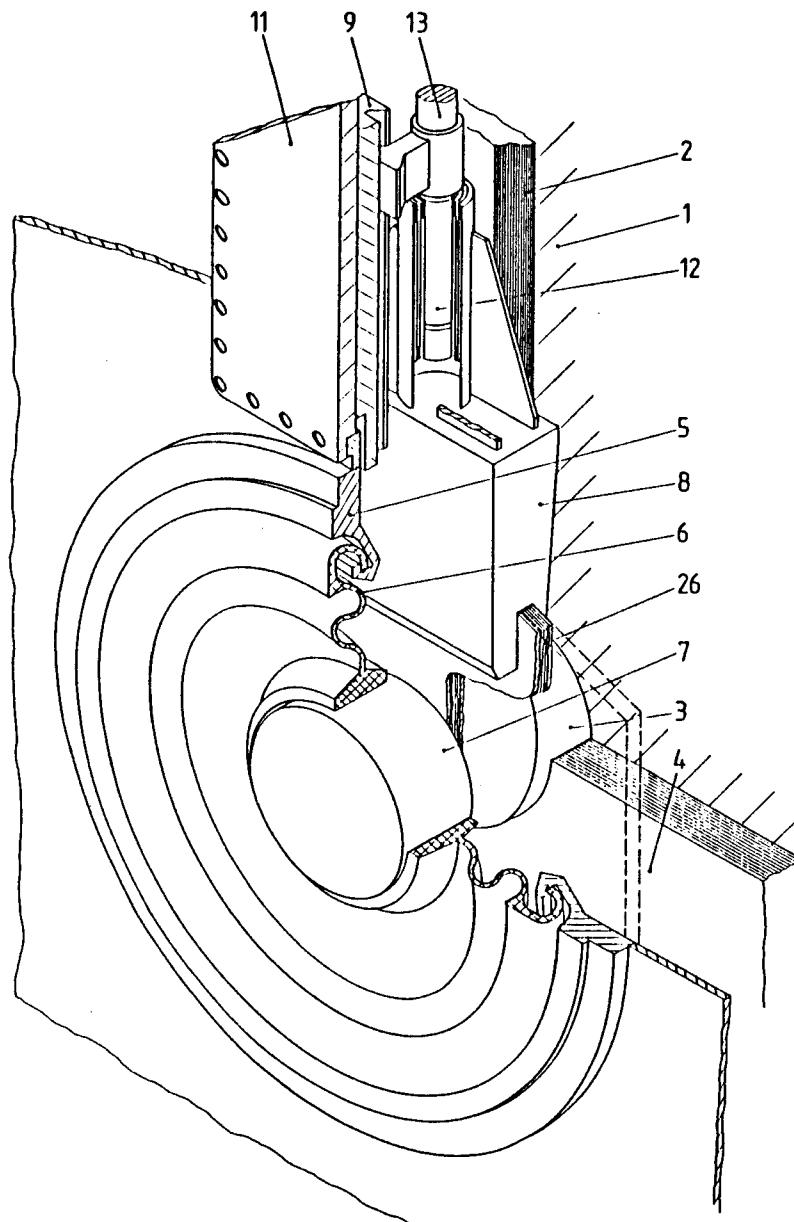
Fig. 9.4-3 Alternative design with glass fibre
reinforced expoxy bellows with 1,5W per bellows
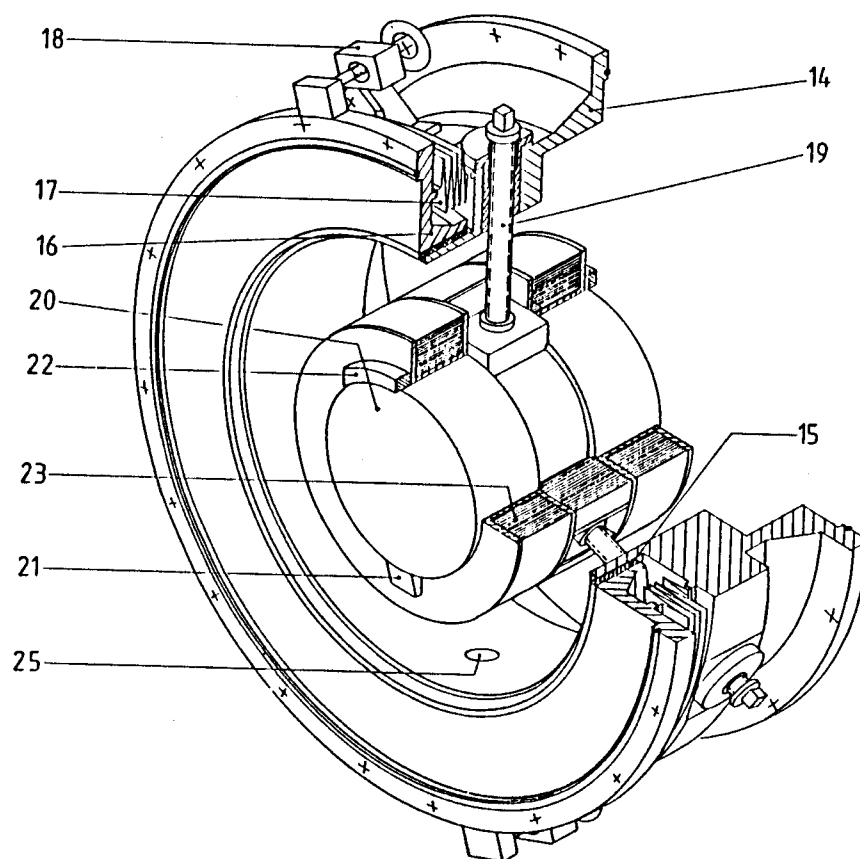(6,5 W for stainless steel bellows)

Fig. 9.4-4   Intermediate element

9.4.2 OPERATION MECHANISM OF THE COLD SUPPORT

Figs. 9.4-1 and 9.4-2 show the starting position for the installation of the cold intermagnetic support. The coils are at operating temperature and the wedges (8) are pulled out. The bevelled inner pressure plate (3) is at a low temperature level also, but is not in contact with the outer pressure plate (7), which is at room temperature. Thus, heat conduction from room temperature to low temperature through the outer plate and the wedge to the inner plate is prevented.

The intermediate element (Fig. 9.4-4) is then placed between the magnets (Fig. 9.4-5). Thus the guiding wedges (21) of the central part of the insert (20) depress the elastically suspended outer pressure plates (7). At this time the element is aligned by the locating pins.

Following this procedure, the case (14) is sealed and tightened to flange (5) of the vacuum vessel (4) of one of the coils. Flange (16) is moved towards flange (5) of the other coil by means of the adjustment screws (18). Then they are sealed and tightened. The three locating pins (19) are retracted and vacuum tightly closed by a cap (24). Then the intermediate element is evacuated.

When the required vacuum level is established, the two wedges are actuated by means of a rack and pinion drive, in order to complete the deployment of the intermagnetic support (Figs. 9.4-6 and 9.4-7). The supporting structure is cooled down by heat conduction. After the required low temperature is reached, the wedges have to be readjusted.
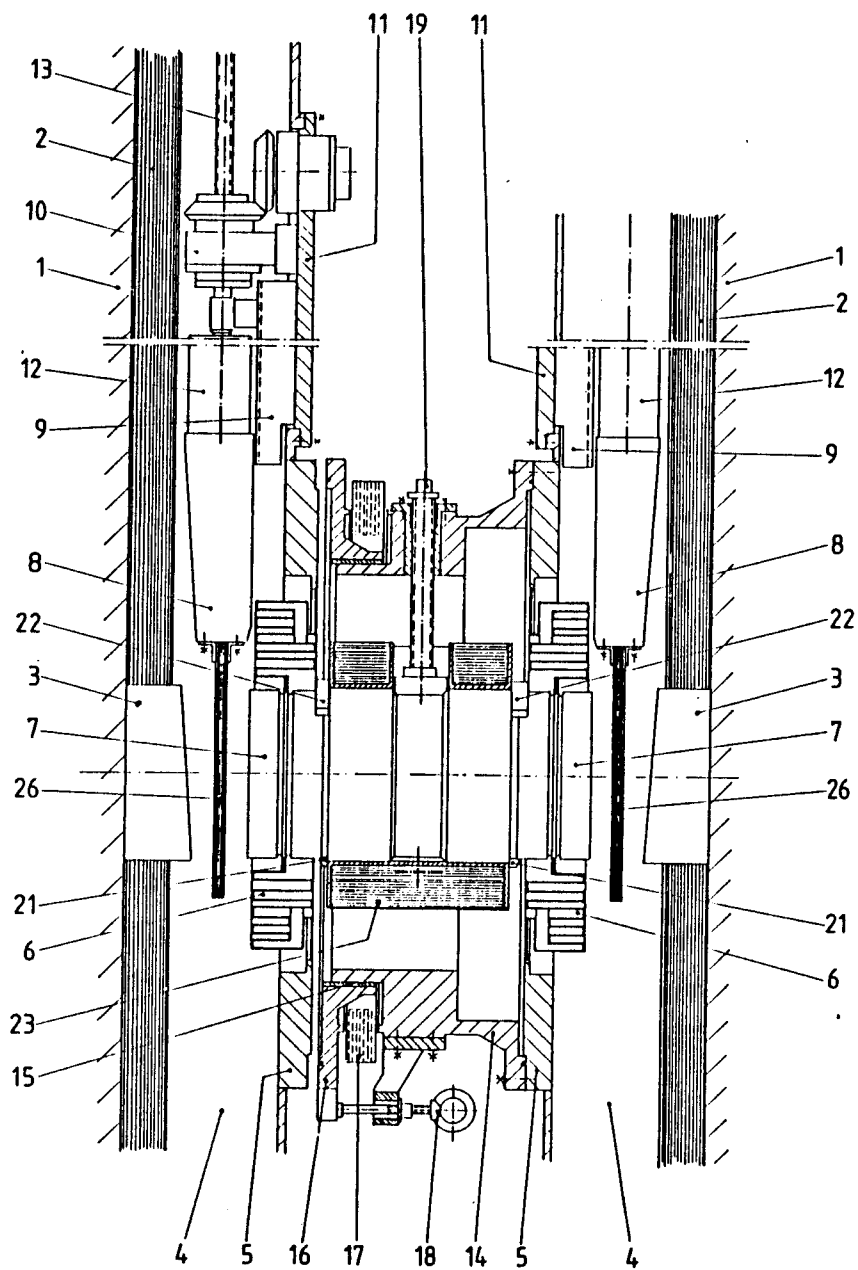
Fig. 9.4-5 Intermediate element placed between
the magnets connected with the flange
of the coil on the right side
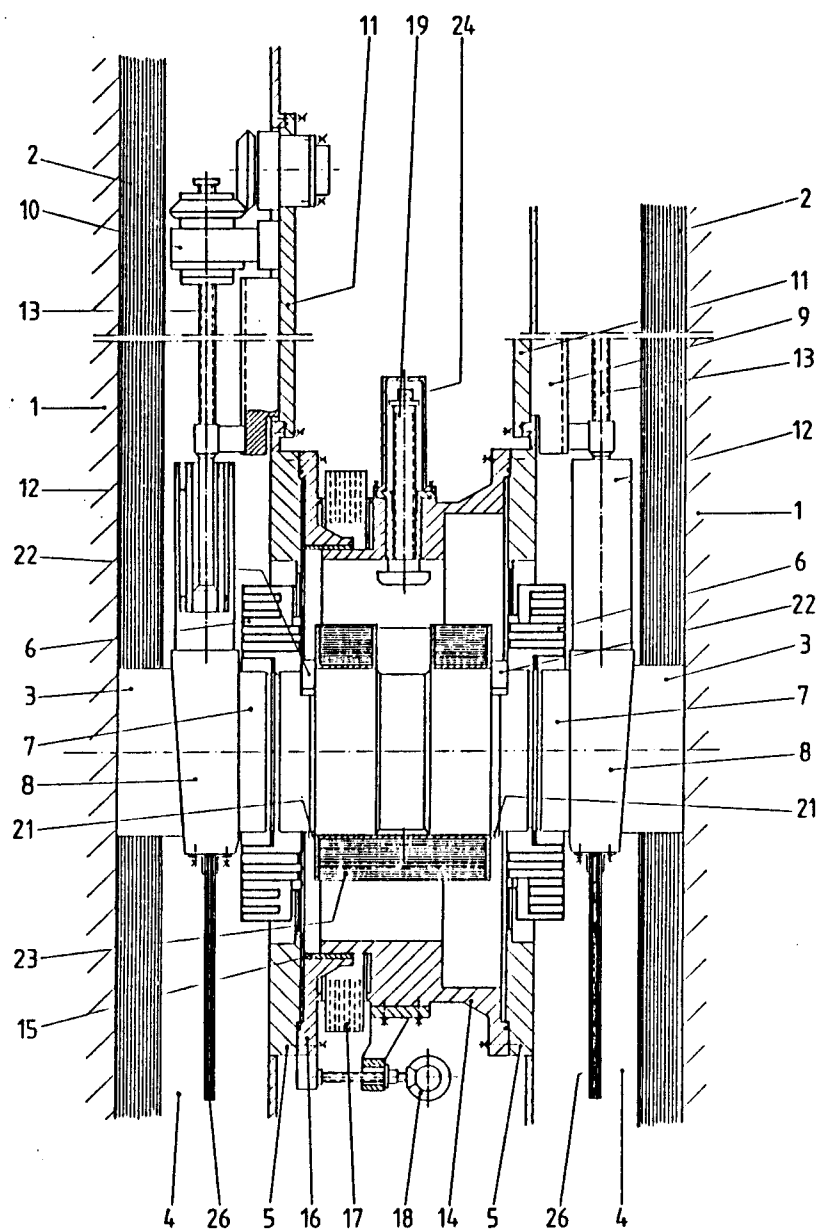
Fig. 9.4-6 Final position after fixing procedure

Fixing procedure:

a) Connection with the flange of the coil on the left side

b) Removal of locating pins

c) Evacuation

d) Fixing of wedges

e) Cool down of support structure

f) Adjustment of wedges
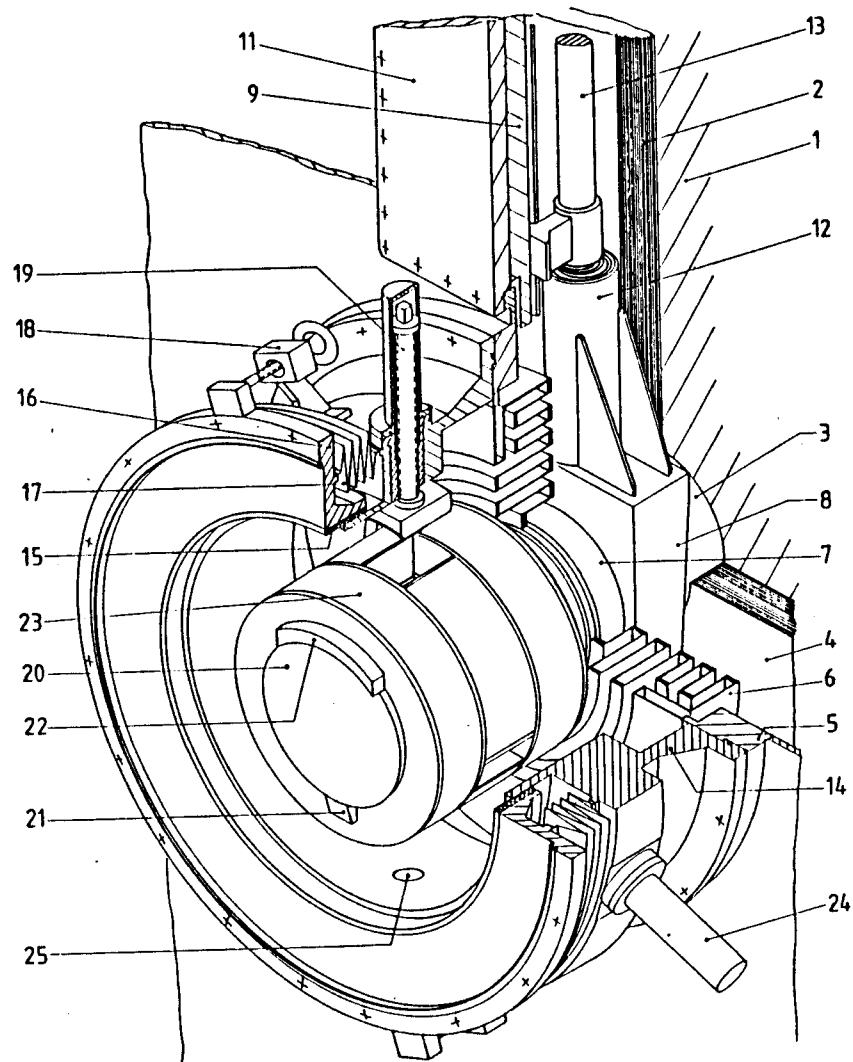
Fig. 9.4-7 Perspective view of support structure ready for
operation

Figs. 9.4-6 and 9.4-7 show that there is no close connection between the parts of the intermagnetic support which are at a low temperature and the parts which are at room temperature. The bellows (6) which support the outer pressure plate (7) and those which support the wedges (12) are at least 800 mm long. Therefore, the heat leak is tolerable.

The demounting of the supports has to be made in reverse order. First, the wedges (8) are removed. The intermediate piece will be warmed up if necessary. Then the three locating pins (19) will be inserted to make contact with the central part of the insert (20). After this the vacuum chamber of the intermediate element will be opened. After this flanges (16) and (14) will be disconnected and the intermediate element is removed.

A description of the demountable cold intermagnetic support is published in /3/.

9.5 SUMMARY AND CONCLUSIONS

A general layout of a modular stellarator reactor is described. The reactor is subdivided into 5 field periods. A blanket option which has variable thickness has been investigated with respect to the arrangement inside the reactor vacuum vessel around the plasma. The advantage of this option is that it provides more space at the backside of the blanket for auxiliary equipment such as coolant pipes.

The maintenance of such a modular stellarator reactor is discussed. The principle idea is the replacement of all removable blanket units in all the field periods during shutdown. The replacement procedure is described and the space requirements for a modular stellarator reactor are listed.

REFERENCES TO SECTION 9

/1/   J. Hübener,
        Vergleich verschiedener Stellarator-Reaktorkonzepte bezüglich
        konstruktiver Realisierung und Handhabung (Teil 1),
        03.01.02 P 15 A, Febr. 1986, unpublished

/2/   D. Evans, J.U.D. Langridge and J.T. Morgan,
        The Manufacture and Properties of a Glass Fabric /
        Epoxy Composite Bellows. Nonmetallic Materials and Composite
        at Low Temperatures. A.F. Clark, R.P. Reed, G. Hartwig (eds.),
        Plenum Press, New York and London, 1979, pp. 365-376

/3/   J. Hübener, G. Böhme and W. Maurer,
        Demountable Cold Intermagnetic Supports for Superconducting Magnets.
        Proc. of the 9th Int. Conf. on Magnet Technology, Zürich (Switzerland),
        Sept. 9-13, 1985, pp. 859-861.

10. Summary and Conclusions

10.1. Summary

An Advanced Stellarator is characterized by a reduction of the secondary plasma currents as compared to those of a standard stellarator, maintaining an average magnetic well in the vacuum fields. In an Advanced Stellarator, the neoclassical particle and energy losses, as well as the shift of the magnetic surfaces by a finite plasma pressure (Shafranov–shift) are reduced, and the deviation of drift surfaces of charged particles from the magnetic surfaces is small, compared to respective results obtained for standard stellarators. This optimization is performed by an appropriate combination of poloidal field components. As typical for an Advanced Stellarator, the shape of the magnetic surfaces varies along the toroidal direction. An example of an Advanced Stellarator is the Garching plasma experiment WENDELSTEIN VII–AS which is under construction and is expected to begin operation in 1987. Advanced Stellarator fields are produced by systems of modular non–planar coils. For a fusion reactor of the Advanced Stellarator type, one set of coils is sufficient in principle, avoiding the problems of linked coils.

In the present report, a survey is given of studies of critical issues concerning Advanced Stellarator Reactors (ASR) and concentrating on the reference data set ASRA6C. This data set features the general properties of such systems but is not optimized with respect to its plasma behaviour under reactor conditions. The magnetic topology is similar to that of the Garching Advanced Stellarator experiment WENDELSTEIN VII–AS. The coil system for ASRA6C is obtained by introducing a modern thin blanket. A low number of 6 coils per field period is chosen as a compromise between 'field quality' and maintainability. In ASRA6C there are three different coil shapes in each of the five field periods. The coils provide an axis field of $B_o = 5.3\,T$; local peak fields of $B_m = 10.4\,T$ are seen at the coils. The magnetic forces of these coils contain appreciable lateral components which are balanced over each field period. By an iterative procedure an appropriate coil support system was developed. The electromagnetic stresses and strains are obtained for single coils and when they are mutually supported. Local maximum values of the equivalent stress $\sigma_{vM} = 135\,MPa$ are seen in the coils at a tangential strain of $\epsilon_T = 0.2\,\%$. Although considerable shear stresses up to $\sigma_{ST} = 50\,MPa$ are present, the coils seem to be feasible. The stresses in the coil housing and the mutual coil support elements are not found to be critical.

Heating and burn scenarios for Advanced Stellarator reactors are established numerically as sequences of equilibria for neoclassical heat conduction and bremsstrahlung as losses, and including electric fields in the 1–D–code. For start–up, an effective heating power of 30 to 50 MW is sufficient. By increased refuelling, ASR is brought to full fusion power of 3.5 to 4 GW, preferentially at a moderate temperature of 12 to 15 keV. In a different example, calculated for ASRA6C with a reduced value of the ripple losses in order to account for the improved confinement properties of an Advanced Stellarator, an additional radiative power loss of 300 MW near the plasma edge can be tolerated at an increased fusion power of 3.9 GW. In this computation the temperature is $T \approx 19\,keV$ and the value of the average β is $<\beta> = 5\,\%$. At this value the magnetic axis is shifted by approximately half of the minor radius. This shift is regarded as determining the critical β for equilibrium. There are theoretical

arguments that the critical β for stability is lower for the above systems. However, innovative stellarator configurations, "HELIAS", with medium aspect ratios were recently published; these are stable up to an average $<\beta>$ up to 9 % according to resistive interchange modes.

From magnetic field studies near the separatrix a system of pumped limiters is chosen for edge control of the plasma in ASRA6C. Because of the ergodic layer of the edge, it appears that the pumped limiters can operate in a high recycling mode with a low plasma temperature at the target plate. The first wall is shaped similar to the contours of the outer magnetic surfaces, or, preferentially, can have identical elliptic cross sections. For a fusion power of 3.8 GW the average neutron load at the first wall is 1.4 MW/m^2 with a local enhancement up to 2.4 MW/m^2. This estimate is obtained by a one–dimensional axisymmetric code . A radially shifted volume source models the Shafranov shift of the finite–β plasma. Depending on the efficiency of the pumped limiters the first wall is also loaded by plasma losses. The effects of trapped α–particles as well as local sputtering remain to be quantified. Furthermore , there is also plasma radiation to the first wall. A radiative layer at the plasma edge would effectively reduce the heat load to the pumped limiters.

A thin blanket of 21 cm thickness is proposed for ASRA6C. It consists of slowly circulating $Li_{17}Pb_{83}$ as breeder with Be as moderator and neutron multiplier, and uses He gas as coolant in a HT–9 ferritic steel structure. An overall breeding ratio of 1.05 including penetrations and an energy multiplication factor of 1.2 are computed. A fraction of 10 % of the 2280 m^2 surface of the first wall is taken into account for port holes. This promising result is made possible by the use of Be in the breeding blanket. This blanket, reflector and shield system provides adequate protection for the superconducting coils.

Further investigations are concerned with the conductor design, and with details of the coil construction. The general layout and the maintenance of the reactor are investigated. One of the options utilizes a blanket with variable thickness, and the contours of the first wall are matched to the shape of the magnetic surfaces near the plasma edge. A demountable cold intermagnetic support is designed for use at the separation areas between the coil modules. These cover one field period in the present reactor lay–out of ASRA6C. Two removable blanket units are foreseen which are replaced from both sides of the module in the maintenance procedure.

10.2.   Critical Issues

For the development of Stellarators towards competitive fusion reactors critical issues exist in the areas of plasma physics and of technology.

Transport (heat conduction and particle losses), as extrapolated from present experiments and theory appears to be tolerable for reactor–grade plasmas, but this needs experimental verification in larger devices. As in the case of other steady state magnetic fusion systems with good confinement, impurities may pose a critical issue. Equilibrium–β values as obtained by modern 3D–codes are adequate for reactor operation, the experimental proof depends on the performance of forthcoming or planned

machines. Regarding stability-β, an innovative configuration, 'HELIAS', is developed which provides a solution, according to theory.

Critical issues regarding technology may arise from the three–dimensional field structure in Stellarators. The influence of ferromagnetic material on the magnetic topology needs to be quantified. First wall, blanket and shield call for more complex structures as compared to those of axisymmetric systems, but this is eased at moderate to large aspect ratio. In modular systems the support between coils might pose a critical issue at separation areas which are necessary for construction and maintenance. Solutions in these fields are proposed or are being developed.

In addition, cost considerations are essential. This is already apparent for the forthcoming generation of larger Stellarators, which aim at exploring their reactor potential, and which will most likely utilize superconducting modular coils.

10.3. Conclusions

From the results obtained in this study it can be stated that the Advanced Stellarator scheme offers interesting prospects regarding its development towards a competitive fusion reactor. For ASRA6C, the approach of a comparatively thin blanket has allowed a considerable reduction of the size as compared to previous systems. For ASRA6C a total fusion power of 3.9 GW is calculated in a scenario with an additional edge radiation of 300 MW. The corresponding β–value of 5 % is about the same as the limiting value for equilibrium, β_{eq}. Regarding the question of the stability-β, theory predicts lower values. An innovative configurations, 'HELIAS', with stable $< \beta >$ up to 9% has been published, and modular coils are being developed.

Modular Stellarators of the types described above with systems of non–planar coils constitute viable options for future development towards fusion reactors. Stellarators, also belonging to the class of toroidal magnetic confinement, have some similarities with Tokamaks, but at the same time they have some distinct and favourable differences.

Start–up from existing magnetic surfaces and the possibility of a steady state burn in the absence of dangerous disruptions are major advantages of Stellarator fusion reactors. Continuous operation allows different approaches for the coil engineering, and avoids problems associated with cyclic loads in the first wall, the blanket, and in the coils with the associated support structure. Furthermore, less circulating power is required in these steady state systems. A moderate aspect ratio alleviates problems regarding the first wall power loading.

All these properties need to be considered when comparing the prospects of Stellarators in comparison to the properties of Tokamaks, the presently favoured system in toroidal magnetic fusion research. From the Tokamak development programmes, on the other hand, a considerable fraction of the data base is also applicable for the development of Stellarator fusion reactors and does not require essential new research and development effort.

During recent years, the reactor studies have focused on the clarification of critical issues. The various Stellarator configurations studied at other institutions lead to

differing approaches, and the results of these investigations are in many ways complementary. Examples are the specific types of coil systems to produce the magnetic fields, the choice of the values for the rotational transform and shear, etc., or the option of using the natural separatrix as divertor, in contrast to pumped limiters or to local divertors.

Therefore it is essential to continue system studies of Advanced Stellarator reactors in order to provide further guidance for research directions, e.g. in the search and development of new configurations, and to contribute important elements to the basis necessary for developing economically competitive fusion power stations of the Stellarator type.

APPENDIX A

A.1 Winding Considerations

In previous work with the twisted coils of stellarator-type devices, various ad hoc winding envelopes have been assumed. In the present work, the techniques of differential geometry are applied to the problem of determining the actual shape of the windings and the orientation of the current filaments in a twisted winding, given arbitrary starting surfaces for the winding. Mathematical formulas were developed for the above quantities in the limit that turns have small transverse dimensions compared to bend radii and envelope dimensions.

A.2   Winding Pack Coordinates and Magnetic Field Calculations

A winding pack is specified by giving the coordinates of points on each winding turn or filament relative to a fixed three-dimensional rectangular coordinate system. The coordinates are conveniently parameterized in terms of two parameters which specify the locations of the turn in the winding pack and of a third coordinate which specifies the length along a particular filament from a starting position. For twisted windings there exists an infinity of different parameterizations that specify the same winding pack in space.

A convenient set of parameters for defining a winding pack is based on the actual sequence in which the winding pack is wound. First, a starting layer surface is specified by a vector function $\vec{R}(p,q)$ of two arbitrary surface parameters (for a toroidal surface, for example, these might be the toroidal and poloidal angles). Successive layers form a family of parallel surfaces with the parametric form

$$\vec{R}_p(p,q,h) = \vec{R}(p,q) + h\hat{N}(p,q) \qquad (8.3-1)$$

where $\hat{N}$ is the outward surface normal at p,q. Individual turns in a layer must then be specified by a relation between p and q, or by separate functions for p and q, in terms of a third parameter, which may be arc length or some other convenient parameter which is a function of arc length.

At this point, a discrepancy between one result of the present work (Eq. 8.3-1) and previously assumed winding pack envelopes is already apparent. If the surface of Ref. 1 (the envelope of surface binormals along a curve lying in a toroidal surface) is taken as a starting surface, the parallel

surfaces calculated by Eq. 8.3-1 do not coincide with the layer surfaces given, i.e., the envelopes of surface binormals transported a constant distance along the normal to the curve. The discrepancy is zero at the middle of the winding pack and increases towards the sides.

Starting turns in each layer are specified by defining a starting turn surface which intersects the family of surfaces parallel to the starting layer surface; starting turns for each layer are the curves of intersection of the above surfaces. In a particular layer, as successive turns are laid down against each other, a family of geodesic parallels is formed. This family is the curved surface analog of parallel curves in the plane. A family of parallel curves in the plane is generated by laying off equal distances along the normals to the starting curve. The locus of the endpoints for a fixed distance is a member of the family of parallel curves. On a curved surface the straight normals of the plane case are replaced by geodesics which intersect the starting curve at right angles; geodesic parallels are the loci of end points of arcs of constant length along these geodesics. The above procedure can be generalized to allow the starting layer and starting turn surfaces to intersect at the center of the pack, in which case turns and layers are "unwound" to get to the actual starting layer and starting turn surfaces.

Determination of the parametric equations for the starting turns requires solution of a set of three coupled transcendental equations, one for each component in the fixed rectangular frame of reference. Geodesics are determined in the general case by integration of second-order non-linear ordinary differential equations. In the present work, explicit formulas for the coefficients of the geodesic equations, called Christoffel symbols, were found for the parallel surfaces in terms of the parameterization of the starting surface, and are given in Ref. 2. The result of the procedure described above is a parameterization of the winding pack of the form

$$\vec{r} = \vec{F}(s_o, h, w) \qquad (8.3-2)$$

where $\vec{r}$ represents the rectangular coordinates of a point in the winding pack, s_o the arc length along the curve of intersection between the starting layer and starting turn surface, h the winding depth, and w the length along orthogonal geodesics from the starting turn in each layer. The sides of the winding pack envelope are the two surfaces

$$\vec{R} = \vec{F}(s_0, h, 0), \quad 0 < h < H, \quad 0 < s_0 < L$$

and
$$(8.3\text{-}3)$$

$$\vec{R} = \vec{F}[s_0, h, \phi(h)], \quad 0 < h < H, \quad 0 < s_0 < L$$

where H is the total winding depth, L the total starting turn arc length, and $\phi(h)$, the value of w for the last turn in a layer, is a continuous function of h. The bottom and top surfaces are

$$\vec{R} = \vec{F}(s_0, 0, w), \quad 0 < w < \phi(o), \quad 0 < s_0 < L$$

and
$$(8.3\text{-}4)$$

$$\vec{R} = \vec{F}(s_0, H, w), \quad 0 < w < \phi(H), \quad 0 < s_0 < L .$$

For magnetic field calculation, the Biot-Savart integral becomes

$$\vec{B}(\vec{X}) = \int\limits_0^L \int\limits_0^H \int\limits_0^{\phi(h)} \frac{J(h,w)[\frac{\partial \vec{F}}{\partial s_0} \times (\vec{X} - \vec{F})](\frac{\partial \vec{F}}{\partial w} \times \frac{\partial \vec{F}}{\partial h}) \cdot \frac{\partial \vec{F}}{\partial s_0}}{|\vec{X} - \vec{F}|^3 \, |\frac{\partial \vec{F}}{\partial s_0}|} \, dw \, dh \, ds_0 \quad (8.3\text{-}5)$$

where $J(h,w)$ is the current density in an infinitesimal area element orthogonal to $\partial \vec{F}/\partial s_0$.

A fundamental difference between flat and twisted windings is evident from the above discussion. Assuming for the moment turns of square cross-section, in flat windings, turn locations and the winding pack envelope are the same regardless of whether the winding pack is made up of n layers with m turns per layer, or of m pancakes or discs with n turns per pancake. For twisted windings, this is not generally true. This can be seen from the fact that while turns in a layer form a family of geodesic parallels, the intersections of successive layers with the starting layer surface do not. Therefore, if the starting layer and starting turn surfaces are exchanged, the resultant turn locations and final winding pack envelopes are different.

Also, in a flat winding, a plane orthogonal to any turn intersects all of the other turns orthogonally. For twisted windings it is, in general, impossible to find a family of surfaces that intersect all of the filaments in the cross-section orthogonally. This is a result of the fact that along a geodesic in a particular layer, the filaments are, in general, rotated with respect to the filaments of the previous layer.

A.3 Use of Developables for Winding Surfaces

Fabrication of surfaces for winding can be considerably simplified if a particular class of surfaces, called developables, is used. Developables are surfaces that can be formed out of plane pieces by bending without stretching. In the present work, the mathematical formulas necessary for finding the flattened shape of the pieces, given the parametric expression for the curved surfaces, were derived.

In addition, methods for approximating developables either by a collection of plane surfaces or by a collection of cone segments and plane surfaces were found. Also, procedures for approximating general curved surfaces by a patchwork of developables were derived. The above work is presented in detail in Ref. 3.

Use of developables for winding surfaces also results in a considerable simplification of the equations for geodesics. Solutions for the geodesics in analytic form were found for the starting surface and its parallels. Closed forms could not be derived for the geodesic parallels themselves. As a result, the following questions remain unanswered: if developable surfaces are taken for the starting layer and starting turn surfaces, can a function $\phi(h)$ be chosen which will result in a developable surface at $w = \phi(h)$? If so, what restrictions are placed on the starting developables? (The top layer surface will automatically be developable if the starting layer surface is developable; as a result, at least three of the four envelope surfaces can be made to be developable.)

Use of a particular developable, called the rectifying developable, for a starting layer surface was also investigated. The rectifying developable, besides having the advantages of general developables for fabrication of the winding surface, has the following additional advantages:

1. The starting turn and all of its geodesic parallels in a layer are themselves geodesics and are of equal length. As a result, if the curvature does not change sign, turns can be wound without continuous clamping because winding tension does not cause the turns to slip sideways.

2. Wide, flat, ribbon-like conductors can be used to minimize conductor strain, while maintaining a large cross-section, because the conductor is bent along an axis lying in local tangent plane. This feature should be particularly useful in windings with strain-sensitive Nb_3Sn superconductor.

Details of the above work are given in Ref. 2.

References
1. E. Harmeyer, J. Kisslinger, F. Rau, and H. Wobig, "A General Winding Law of Modular Stellarator Coils," IPP 2/274, March 1985.

2. P.L. Walstrom, "The Differential Geometry of Twisted Coil Windings," paper presented at the ANS Topical Meeting on the Technology of Fusion Energy, Reno, Nevada, June 1986.

3. P.L. Walstrom, "Approximation of General Curved Surfaces in the Fabrication of Shell Structures," University of Wisconsin Technology Institute Report UWFDM-690, Sept. 1986.